QUANTUM STOCHASTIC COMMUNICATION WITH PHOTON-NUMBER SQUEEZED LIGHT

by

JOSHUA PARAMANANDAM

A thesis submitted to the

Graduate School—New Brunswick

Rutgers, The State University of New Jersey

in partial fulfillment of the requirements

for the degree of

Master of Science

Graduate Program in Electrical And Computer Engineering

Written under the direction of

Professor Michael A Parker

and approved by

____

____

____

New Brunswick, New Jersey

October, 2007

ABSTRACT OF THE THESIS

Quantum Stochastic Communication with Photon-number squeezed light

By Joshua Paramanandam

Thesis Director: Professor Michael A Parker

Squeezed states of light have found importance in quantum cryptography due to the no-cloning theorem which prevents two states from being identical to each other. The quantum state with quadrature operators X1 and X2 can be visualized as a point in phase space with the center being $\langle X1 \rangle$,$\langle X2 \rangle$ surrounded by an error region which satisfies the minimum uncertainty product $\langle \Delta X_1^2 \rangle \langle \Delta X_2^2 \rangle = 1/16$. These states are intrinsically secure since one needs to know which quadrature the measurement is to be made and any attempt to measure the wrong quadratures with arbitrary accuracy would disturb the message. Of course, the eavesdropper cannot simultaneously measure both quadratures with infinite precision for each. This thesis describes a method that not only encodes information in the amplitudes of the quadratures alone but also in the uncertainty of those states. One example of squeezed light is the number-phase squeezed state which satisfying the uncertainity relation $\langle \Delta n^2 \rangle \langle \Delta \phi^2 \rangle = 1/4$. An implementation is demonstrated where the information is encoded only in the photon number uncertainity and the phase variable is ignored.

The barrier regulation mechanisms such as macroscopic coulomb blockade in semiconductor junction diodes are responsible for generating photon fluxes with penetration below the standard quantum limit(shot noise level). The thesis describes a comprehensive quantum mechanical Langevin model which details the various mechanisms responsible for producing photon number squeezing from the thermionic emission to the diffusion current limits. Quantities such as the pump fluctuations and cross correlation spectral densities are studied under constant current and constant voltage conditions. The research investigates the generation of photon number squeezed light from high efficiency light emitting diodes. A measurement setup for subshot noise is constructed and each stage is properly calibrated. Experiments were performed to determine the squeezing spectra and Fanofactors for the L2656 and the L9337 high efficiency LEDs. The L9337 produces a squeezing of 1.5dB below the shot noise level over a bandwidth of 25Mhz, the largest known penetration at room temperature. The quantum stochastic communicator is also demonstrated. The research shows that the switching elements used in the modulation of the electrical bias which in turn affect the regulation mechanisms do not affect the statistics of the emitted light under certain conditions. The decoding of the time varying variances is achieved by using time frequency analysis with the aid of the spectrum analyzer.

Acknowledgements

To start with, I am grateful to my advisor, Dr. Michael A. Parker, who has been a source of constant encouragement and guidance. He has since introduced me to Quantum Optics with one on one sessions, Machining, and Electronics.

I would also like to give a shout-out to my present and past nanolab colleagues, Gunay Akdogan, Mandira Thakedast, HeeTaek Yi, Morris Reichbach for interesting discussions and motivation. I would like to thank Steve Orbine for helping out with quick fix solutions to equipment problems. I would like to thank my family and friends who have supported and believed in me through my research. Most of all, I thank the almighty, who has made this thesis possible

Table of Contents

List of Tables

List of Figures

Chapter 1

Introduction

1.1 Introduction

We start by asking the question 'Is it possible to communicate with noise?'. The neverending quest for nanoscale devices and nanosignals, keeps lowering the signal to noise ratios. One way to combat this is to reduce the noise, such as using squeezed fields for optical or RF signals. But we could consider an alternative: ie. Use the noise itself as the signal. In fact,at this point we may wonder: What is noise? The answer is very subjective. For example, a person may enjoy listening to a certain type of music while others may find it distasteful and noisy. We certainly can encode information in noise itself, and that is the sole purpose of this thesis. However, this thesis approaches the problem from a quantum perspective, using continuous distributions arising from natural sources such as optoelectronic devices, but the same idea can be applied to any classical stochastic process produced using computers.

1.2 The concept of Stochastic Modulation

The premise of the stochastic modulation idea is that the set of statistical moments of a random signal should be modulated independent of one another. The n'th statistical moment of a random variable Z is defined as $< z^n >$ where Z takes on values z and $\langle\rangle$ represents the average with respect to a continuous or discrete probability distribution P(z). The n=1 moment provides the mean. The central moments are defined by removing the mean component of z and can be stated in general as

$$m_n(z) =< (z - z)^n > \tag{1.1}$$

The moments defined in Eq. (1.1) assume that the probability function is known a priori at the transmitter end ie a random signal should be sculpted with these specified statistical moments. For a process, whereby the values of z arrive as a sequence in time at a receiver, the moments must be calculated based on the observed values. For example $z = z(t_i)$ must represent a sequence of voltages generated by a computer every 0.1 nanoseconds. An 'estimator' on the receiving side approximates the statistical moment by averaging over a finite number of observed values. For a communications system, the finite time interval might be attributed to the response time of the electronc circuits or to the number of values a processor samples from the data stream to calculate these estimations. If N samples are obtained the finite time moments are then estimated as

$$< z > \approx \frac{1}{N} \Sigma_{i=1}^{N} z_i \qquad < (z - z)^n > \approx \frac{1}{N} \Sigma_{i=1}^{N} (z_i - z)^n \tag{1.2}$$

Of course as the number of samples N increases, the estimate becomes closer to the actual statistical moments. However this is only true for ergodic processes where the underlying probability distribution does not depend on time ie. p(z,t)=p(z,0) .The moments estimator depends on the original modulation rate(the number of samples produced) and the averaging time of the receiving electronic circuits or processors. The actual averaging of a computer circuit follows a convolution integral and not necessarily a uniform average over a finite time interval. Note that the stochastic modulator intentionally alters the probability distribution in time, and for two different pulses it may be that $p(z, t_1) \neq p(z, t_2)$.However this is very subjective to the receiver side and the concept of non-ergodicity needs furthur clarification. For example consider N ensembles of random processes $z(t)$ where each realization of one ensemble carries the same statistical information. If we pick one element k of the ensemble l ,the different time averages $^{(k,l)}z$ then coincide with the ensemble average $^{(l)} < z >$. The same applies to any other process say m(t) constructed from $^{(l)}z(t)$. This property defines the ergodic nature of the random variable Z. for ensemble l. Now let us define a process z(t) made up of realizations k and l from two ensembles whose finite time average is$^{(k,1),(l,2)}z_T$. Now the ensemble average is defined as

$$<^{(k,1),(l,2)} z_T > = \frac{1}{T} \int_{t-T/2}^{t+T/2} <^{(k,1),(l,2)} z_T > dt \tag{1.3}$$

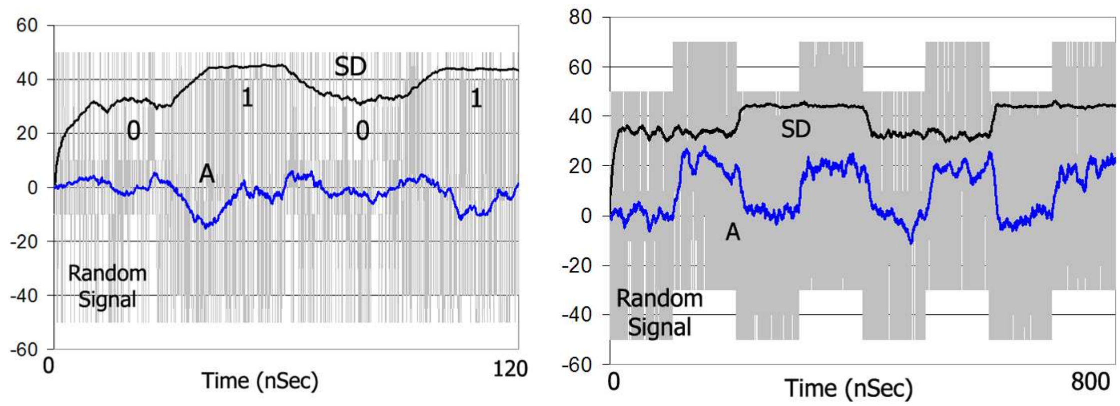

Figure 1.1: (a)The random signal with variable finite time average and standard deviation (b)A modulated average without affecting the standard deviation

When T is short enough that we capture the realization of the first ensemble, we have $<^{(k,1),(l,2)} z_T >=<^{(k,1)} z_T >=^{(1)}< z >$ and the process is certainly ergodic with respect to the first ensemble but when T encompasses both ensembles, we lose ergodicity.

Our first goal was to develop a macroscale version of the communicator where the signals may be in volts and rely on man made distribution rather on the intrinisic distributions of thermal noise or shot noise from resistors and diodes. This was done to verify that the estimations could be performed in the time domain and as a testbed to validate our ideas. In order to illustrate our ideas, we start by considering the simulation performed in Fig.(1.1). It shows a sequence of random values generated by a computer at a rate of 1 value every 0.1 nanosecond(the grey lines in the background) and the detected signal obtained by estimating these random values(thick lines in the foreground). The detection circuits uniformly average over a 10 nanosecond interval. The signal appears to be noise as evident from the finite-time average (A) that fluctuates randomly about the expected value of 0. However, the finite-time standard deviation (SD) shows a sequence of digital values (0101). The rounding of the standard deviation SD near the transitions between 0 and 1 can be attributed to the averaging of the detection circuits.

The random signal in Fig.(1.1a) is generated by two different probability distributions. The distributions operate at different times from each other so that the total process cannot be classified as ergodic. The two probability distributions for the figure differ only in the standard deviation. Distribution 1, which is active in the ranges 0-30 and 60-90 nanoseconds, has probabilities of $P(-50) = P(50) = 0.2$ and $P(-10) = P(10) = 0.3$, while distribution 2, which is active at the other times, has probabilities of $P(-50) = P(50) = 0.2$ and $P(-40) = P(40) = 0.3$. A processor can generate arbitrary probability distributions P(z) for random variable Z in real time using the well known relation $P(z) = k(\frac{dz}{dx})^{-1}$ where x represents the values of the random variable X with uniform probability distribution and the constant k ensures the probability P(z) integrates to unity . As an estimator, the finite-time standard deviation in Fig.(1.1) shows that distribution 1 has a standard deviation of approximately 30 while the second one has an approximate value of 45.

Modulation can also be impressed on the average without affecting the modulation on the standard deviation. Typically most systems modulate the average and keep the standard deviation as small as possible in order to provide a large signal-to-noise ratio; the standard deviation usually characterizes the noise level. However, in this case the standard deviation must be allowed to change since it also represents a signal. Figure (1.1b) shows the signals detected by circuits that uniformly average over 150 nSec. The detected average (A) and standard deviation (SD) appear relatively independent of each other. Normally, slight bumps in the standard SD can appear near the transitions in the average A as a result of the circuits performing a finite time average. In general, all of the statistical moments can be independently modulated.

1.3 Why Quantum Noise?

This thesis deals primarily with nanoscale optical signals. The optical signal can in general be a random variation of amplitude or phase. The noise from the optical sources has magnitudes ranging from picoWatts to nanoWatts. The noise in these sources can be modulated by properly electrically biasing the device or using an optical modulator. Let us consider a single polarized electromagnetic field travelling along the z direction with an electric field of the form

$$E(z,t) = -\sqrt{\frac{h\omega}{\epsilon_0 V}}(P\cos(kz-\omega t) + Q\sin(kz-\omega t)) \tag{1.4}$$

for the quadrature amplitudes P and Q where V denotes the photon modal volume and $h\omega$ represents the photon energy. When we perform repeated measurements of the electric field, we obtain a range of P and Q values that fall within a region of phase space. The points in phase space can be represented by the amplitude

$$|E| = \sqrt{\frac{h\omega}{\epsilon_0 V}}\sqrt{Q^2 + P^2} \tag{1.5}$$

and the phase space angle $\phi = \tan^{-1}(Q/P)$ .The distance from origin to center of the 'circle' represents the average electric field amplitude $\langle |E| \rangle$ and the angle to P-axis represents the average phase $< \phi >$ of the wave. Any experimental setup would have to generate two types of fluctuations:The first a minimum uncertainty state with uncertainty regions represented by the product of the standard deviation of the two quadratures ie. $\Delta Q \Delta P = 1/2$.This type of optical state is the coherent state which is represented by the state vector $|\alpha\rangle$ and if we reduce the uncertainity of one of the quadratures as well as simultaneously increasing the conjugate quadrature such that the minimum uncertainty is preserved, we have the squeezed state represented by $|\alpha, \eta\rangle$.The complex quantity η represents the degree of squeezing and has the property that $|\alpha, \eta\rangle \rightarrow |\alpha\rangle$ as $\eta \rightarrow 0$.The squeezing parameter determines the degree of assymetry of the ellipse or phase angle. The amplitude squeezed state has smaller amplitude fluctuations and for certain cases smaller fluctuations in the photon number than the standard quantum limit. The phase fluctuations are larger than that of the coherent state. Other types of squeezed states are the phase squeezed states(where the phase fluctuations are reduced and the quadrature squeezed states. There is another important state known as photon number squeezed which is the essence of this thesis. This state is produced by LEDs and multimode devices under spontaneous emission, where the photon emissions are highly correlated. Studies of photon number squeezed light, ignore the conjugate phase quadrature, focussing on only reducing the photon number variance to low levels.The phase quadrature may be undefined or rather take any value in phase space with average 0. The average of the photon number can also be modulated.The bias current to the optical device controls the optical power and hence the average electrical field $\langle |E| \rangle$ or photon number. We deal typically with mixed state density operators where instead of writing $\rho = |\alpha, \eta\rangle\langle\alpha, \eta|$,we express in terms of probabilities associated with an ensemble of such systems given by

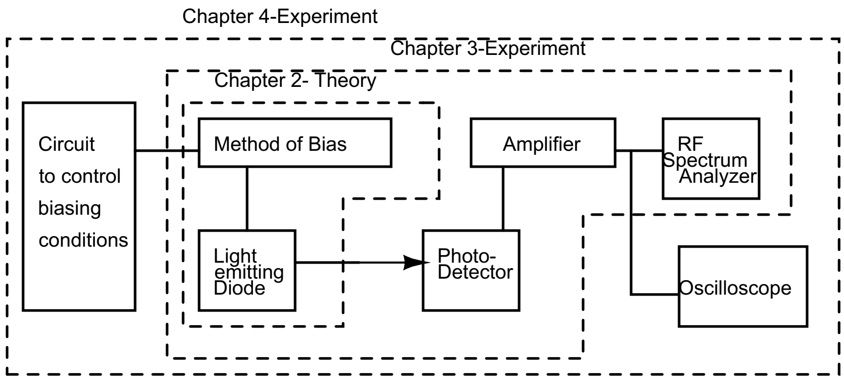

Figure 1.2: Thesis chapter Overview

$\rho = \int d\alpha P(\alpha)|\alpha,\eta\rangle\langle\alpha,\eta|$ .The quantum mechanical aspects of squeezing in photodetected light can be traced back the commutation relations of field operators and to the dynamics of the matter field interaction in the semiconductor carriers.

Quantum states of light provide us the means to send secure information by using the rules of quantum mechanics. The rules of quantum mechanics allows us to create a secure channel that detects the presence of eavesdroppers. The very process of measurement leads to collapse of the wavefunction causing it to be no longer measurable or to affect it in such a way that the uncertainities of the state would reflect the measurement process. Hence the fragile nature of nonclassical light states make it attractive in secure point to point communication systems.

1.4 Thesis Overview

Fig. (1.3) describes the significance of each of the following 3 chapters in this thesis. The central premise is a method of communication by modulating the quantum noise from light emitting diodes(LEDs). The organization of chapters 2 to 4,follows a bottom to top approach designed to answer the following questions:

1)What is shot/subshot noise and how does subshot noise arise in LEDs.

2)Demonstrate subshot noise experimentally and be assured that it is below the quantum noise limit. ie. to show that the LED generates nonclassical(true quantum) light states.

3)To develop a method of controlling and modulating the statistics of emitted quantum light and to demonstrate the quantum stochastic communicator.

1. In Chapter 2, the theoretical models surrounding the LED and methods of controlling the statistics of light from the device are outlined. We review the mechanisms responsible for shot noise generation in light emitting diodes and the methods of suppressing it. The noise model of the LED is sufficient to understand the subshot photon noise generation for diffusion current based devices. However it is not sufficient to explain devices that utilize the thermionic emission model such as double barrier heterojunctions. Since the experiments use both diffusion and thermionic emission limited devices, we derive a general theory using quantum mechanical Langevin equations. The theory re derives the already established photon Fanofactors from a quantum mechanical basis. The central purpose is to obtain analytical results that will be used later in experimental modeling. We also obtain expressions for pump fluctuations, cross correlation of spectral densities and show that the Langevin analysis predicts the same results as the noise equivalent model of the LED in the diffusion regime.

2. In Chapter 3, the experiments required to measure subshot noise in light emitting diodes are devised. Each stage of the measurement chain is properly calibrated. As a fiduciary, we start by studying the L2656 LED which has been well established in the literature. However, most authors have ignored the concept of differential efficiency and non-radiative processes which may affect squeezing. We fit our results to theoretical models with very good accuracies at all frequencies. We also perform such experiments for the L9337 LED.

3. Finally in chapter 4, we discuss the methods of stochastic modulation using quantum light states from the L2656 and L9337 LEDs. A demodulation scheme is developed that performs the decoding in the frequency domain. The idea relies on using the spectrum analyzer to perform a time-frequency analysis of the quantum signals. In order to perform variance modulation,we need to choose proper switching circuits. This requires knowledge of the noise mechanisms in the switching elements with and without the LED inserted. This affects the output spectral densities of light from the

LED. Finally, the modulation circuit(ie. circuit to control the biasing conditions) is combined with the time frequency decoder and the modulation of the average and variance is simultaneously demonstrated using classical signals for the ac channel and quantum signals for the noise channel.

4. Chapter 5 concludes our work where the achievements in this thesis are outlined along with possible future research ideas.

Chapter 2

Quantum Noise from Light emitting diodes

2.1 Introduction

In recent years, squeezed states have attracted great attention with many proposals for its usage in quantum cryptography[2]. However, one would need to resort to nonlinear quantum optical setups such as four wave mixing or second harmonic generation for generating such states of light. They are expensive and difficult to setup and require very precise single mode lasers as the pump source. These systems have demonstrated anywhere from 1-10dB of penetration below the standard quantum limit[3]. Yamamoto and coworkers discovered that amplitude squeezed states which has photon number uncertainty below the standard quantum limit(shot noise level) could be generated easily with light from semiconductor lasers[4]. These observations were made on laser diodes driven with high impedance constant current sources and demonstrated that noise could indeed be suppressed below the shot noise level. The explanation for this behavior relied on an electronic feedback mechanism which was first proposed by Yamamoto for laser diodes[5] and later extended to LEDs by Edwards[6]. Before this discovery, it was a long standing conclusion that the electron-hole recombination noise in a semiconductor junction LED was characterized by the full shot noise level and could not be changed and one paper went as far as to conclude that the effect was only restricted to semiconductor lasers[7]. Our goal in this thesis is to demonstrate a way of communicating using a nonclassical state of light. For this purpose, we have chosen LEDs as it is easy to setup, and large degrees of squeezing have been demonstrated which are comparable to the nonlinear setups. The LED form the crucial transmitter section of our communicator and we would like to modulate the moments of the quantum states such as the photon number average and variance. In order to manipulate the statistics of light from LEDs, it is essential that the LED source actually generates subshot(squeezed) light. There have been examples in the literature[3] where experiments falsely claim subshot characteristics but they are essentially nonlinearities. One way to verify the experimental results is to fit it with well established theoretical models. The experiments in the following chapters are performed using a semiconductor heterojunction diode and a double heterojunction diode. We develop the theoretical models in this chapter corresponding to these two structures and study the pump and photon noise characteristics of these devices. Quantum light from semiconductor diodes are a part of the growing field of semiconductor quantum optics. There are two parts to this problem: (a) An electronic part which involves the carrier continuity equations and current flow in semiconductor junctions and (b)quantum optical part for the photon generation through radiative recombination by means of the light-matter interaction as well as the propagation of the photon states through optical components introducing loss. We are interested in the noise spectra of these electronic and optical processes(rather than their steady state dc quantities) as we shall experimentally verify them in the following chapters. In this chapter we review the mechanisms that are responsible for producing both subshot electrical junction current and optical flux. The need to follow both the electric current and the photon flux is that when the pump electron flows are quieted down, the electron statistics can be transferred to the photons provided the recombination is instantaneous. For example, a shot noise recombination current implies a shot noise limited photon flux.

This chapter deals with the theory of subshot noise from light emitting diodes. In section 2.2, we try to answer the question as to what the nature of the electrical shot noise is and how it arises in semiconductor systems. The most popular interpretation of shot noise in pn diodes comes from the earlier thermionic emission vacuum diodes where if one counts the random passage of carriers from one electrode to another it results in a Poisson electron count distribution. Early authors have applied the same idea to the charge transit across a pn junction diode and this idea has been referred to in recent papers[8]. Of course this interpretation is only partly correct. The electron shot noise at the terminals of the diode appears as it does for the Boltzmann conductors ie. due to the discreteness of electron motion in the bulk regions of the semiconductor. Nevertheless at low injection currents the carrier transport across the depletion region does contribute to the shot noise spectra and at moderate current regimes the current is primarily due to the recombination processes taking place in the bulk. Our focus is only in the low and moderate current injection regimes as they are the conditions under which the experiments are performed in the following chapter. Shot noise suppression was not a new idea when it was first observed in pn junction diodes. As early as the 70s,the vacuum tubes had already shown a small degree of electron noise suppression due to the space charge and memory effects[9]. The suppression from this system depends on the nature of applied bias, ie. constant voltage or constant current. The same bias methods are relevant to pn junction diodes. Also most textbooks[10] make the distinction between thermal and electrical shot noise stating their corresponding formulas. However Landauer has shown[11] that in the quantum regime, for ballistic transport problems and extremely small resistors(where the conductance is quantized) there is no such distinction and both thermal and shot noise are extremes of a more basic result which deals with the discreteness of an electronic charge. So the origin of noise is due to the discrete nature of electrons and both shot and thermal(and even 1/f) arise eventually from this electron motion. This is easily validated in classical Maxwell Boltzmann conductors of finite resistance, where one can prove a rather strange equality: $2qI=4kT/R$. In section 2.3 the origin of shot noise and PN junction diodes is due to random processes taking place in the bulk regions of the diode which is contradictory to the random passage of carriers across the depletion region as presented in most textbooks[10].

Subshot photon generation relies on the presence of a quiet pump, which is established by means of a negative feedback mechanism. Section 2.4 illustrates this idea using the the equivalent noise circuit of the diode. Such a circuit is sufficient to understand the regulation mechanism and the suppressed recombination current but is inadequate when applied to double heterojunction diodes with short active regions where the thermionic emission model dictates the current flow mechanism. In order to explain the squeezing in the thermionic emission regime, a Langevin model was proposed by Kobayashi et al[12] where they obtained a general relationship that allowed one to characterize LED structures that operated from the diffusion to the thermionic emission limits. Such a theory extended earlier results from Kim et al[13]and Fujisaki et al[14]. The most important contribution in [12] was the ratio of the backward to forward pump rates which offered a simple way of representing current mechanism from the diffusion limit (valid for long heterojunction diodes) to the thermionic emission limit(valid for double heterojunction diodes). Typically most LED's are long diodes since the recombination lifetime is small as a result of heavy doping(eg. a diode's physical length could be as small as$1\mu m$ and still be categorized as long diodes due to its short minority carrier lifetime). Section 2.6 discusses the current mechanisms in both these device structures as well as their relation to the Backward Pump(BP) model. The BP model is later used in the quantum mechanical Langevin theory to derive important relations for the photon flux Fanofactors as well as the squeezing bandwidth which are then used to fit the experimental results of chapter 3.

2.2 Origin of Shot Noise

The electric current is defined microscopically as the transport of discrete units of electronic charge(electrons or holes in semiconductors). If we can visualize the electrons regularly spaced in time, then the current is quiet with no noise. Electrons traveling through the semiconductor suffer inelastic collisions with the lattice (which result in loss of coherence), Coulomb interactions between particles and other many body effects. All these are responsible for current noise in the terminals of semiconductor devices. At the macroscopic level or from an experimental point of view, we hardly observe these discrete units but we observe current noise as a continuous quantity. In order to establish the current noise(in particular the shot noise), we need to relate it to the discrete nature of electrons in devices. In the following sections, we show the origin of shot noise is due to passage of carriers in the space charge limited region.There are two important reasons why understanding noise in vacuum diodes is important: (a)The early models of diode noise by Van-der-Ziel[15] extended the analysis of vacuum tubes to semiconductor junctions. This is not entirely correct as was later challenged by Buckingham[16, 17]and Robinson[18] who attributed it to entirely the bulk regions. More recent observations show it to be a combination of both space charge effects and random events in the bulk region. (b)The constant voltage and constant current modes affects the lifetimes of carrier transport and charging. These are directly applicable to PN diodes where the nature of the bias controls the external charging lifetimes which in turn allows one to observe either Poisson or sub-Poisson currents.

2.2.1 Shot Noise from a vacuum diode

One of the earliest observations of shot noise was measured in the thermionic emission diode[18] where the random passage of carriers through the tube produced a Poissonian current. Let us consider such a device which has two infinite plates separated by a distance d. We assume there is no space charge for now, and any electron once it enters the vacuum makes a complete transit without returning. If an electron is emitted from the cathode, the instantaneous current measured in the external circuit according to Ramo's theorem[18, 16] is $i(t) = \frac{qv(t)}{d}$. Even though the electron emissions are discrete events, the current is a continuous quantity as it depends on the time varying velocity. The random emission of electrons from the cathode gives rise to an electric current which is a random pulse train expressed as

$$i(t) = -e \sum_{k=1}^{K} F(t - t_k) \tag{2.1}$$

where t_k is the time at which the k'th electron is emitted from the cathode(where the emissions can be modeled as a Poisson process) and K is the total number of pulses in a time duration T. The pulse $F(t - t_k)$ measured in the external circuit is the response function and can be taken as a delta function if we assume the transit time of the electron is negligible. We can use Campbell's theorem[18] to find the mean as

$$\langle I \rangle = \frac{e\langle K \rangle}{T} \int_{-\infty}^{\infty} F(t)dt \tag{2.2}$$

and from Carson's theorem[18] we obtain

$$S_i(\omega) = 2\nu q^2 |F(i\omega)|^2 + 4\pi I^2 \delta(\omega) \tag{2.3}$$

The first term reduces to 2qI when we assume the $|F(i\omega)|^2 = 1$ which is the shot noise spectral density and is characteristic of any device which at any point receives or sends a random pulse train of the form Eq. (2.1). The diode is connected to a voltage V through a resistor R_s. There are two circuit time constants: $\tau_{tr} = \frac{d}{v}$-transit time of carrier and $\tau_{RC} = R_S C$-circuit relaxation time which determine the shape of the function F(t). We assume that the velocity is a constant. In addition to the following two cases, particles accelerated from 0 at the cathode by an electric field have non constant velocity and have been treated in [19].

Case 1 : $\tau_{tr} << \tau_{RC}$

At $t = 0^-$, the voltage at the anode is $V_A = V$. After an electron transit, the cathode loses a charge and the anode gains a charge immediately. The voltage at the anode is $V_A(t = 0^+) = V - q/C$. An external circuit current flows in order to relax the circuit back to the original voltage $V_A = V$. Using Kirchoff's law we can write

$$\frac{dV_A}{dt} = -\frac{V_A}{\tau_{RC}} + \frac{V}{\tau_{RC}} \tag{2.4}$$

and obtain using the initial condition at $t = 0^+$, $V_A(t) = V - \frac{q}{C} e^{-t/\tau_{RC}}$. The current in the external circuit is

$$i(t) = \frac{V - V_A}{R_s} = \frac{q}{R_S C} e^{-t/\tau_{RC}} \tag{2.5}$$

We could have obtained the above results simply by understanding how a capacitor works ie. the voltage rises with a circuit time constant and similarly current decays until the voltage across the capacitor is constant after which there is no more flow of charge. The response function in this case from Eqs. (2.1) and (3.29) is $F(t) = \frac{1}{R_S C} e^{-t/\tau_{RC}}$. Obtaining the Fourier transform of F(t) and substituting it in Eq. (2.3) we obtain[19]

$$S_i(\omega) = 2qI \frac{1}{1 + \omega^2 R^2 C^2} + 4\pi I^2 \delta(\omega) \tag{2.6}$$

At low frequencies $0 < \omega < 1/RC$, we obtain $S_i(\omega) = 2qI$ which is equivalent to the full shot noise.

Case 2 : $\tau_{tr} >> \tau_{RC}$

When an electron is emitted from the cathode it induces a charge of -q on the anode. However this is not an instantaneous process and the charge q builds up by $\tau_{tr} = \frac{d}{v}$ which is the time it takes to cross the diode. From Ramo's theorem, this leads to a current in the external circuit $i(t) = \frac{qv}{d}$. Note that $i(t)$ is continuous since a current meter at the anode plate will register a continuous value corresponding to the position of the electron at various positions in the tube. This same current flows into the cathode to balance the charge. Initially the surface charge on the cathode is -CV. After electron emission it becomes -CV+q and at the same time it starts charging with the current from the anode. So the surface charge on the cathode can be written as

$$Q_C(t) = -CV + q - \frac{qv}{d}t \quad 0 < t < \frac{d}{v} \tag{2.7}$$

At $t = \frac{d}{v}$ surface charge is restored to $Q_C(t) = -CV$. The response function in this case is $F(t) = q\frac{v}{d}$. Converting F(t) to the Fourier Transform and using Eq. (2.3) we obtain[19]

$$S_i(\omega) = 2qI[\sin c(\omega d/2v)]^2 + 4\pi\nu^2\delta(\omega) \tag{2.8}$$

At low frequencies $0 < \omega < v/d$, we can use the identity $\frac{sinx}{x} = 1$.Thus the current noise spectral density of Eq. (2.8) reduces $S_i(\omega) = 2qI$ which is once again the full shot noise.

Remarks

From the above two cases, we note that the current through the response function depends on the slowest time constant. In the case of $\tau_{tr} \gg \tau_{RC}$ we assume that when an electron is in transit there are no further emissions. Then each transport is completely independent of the other and we have a Poisson point process for which Eq. (2.1) is applicable. Hence the rate of emission from the cathode is $R \ll \frac{1}{\tau_{tr}}$. If $R > \frac{1}{\tau_{tr}}$ there will be more than one electron in transit creating a space charge effect. The potential profile can be obtained by solving the Poisson equation. Each particle will have to cross a potential barrier while contributing to the potential themselves. There is now the probability that the electron returns back to the cathode. Excess electron emission is followed by increasing barrier, which leads to reduced emission in the next instant. In the long time scale the electron emissions are regulated and this is the space charge suppression mechanism. However the regulation mechanism does not greatly suppress the noise, and experimental results have shown the noise current to be only 0.01dB below the shot noise level[9]

In the case of $\tau_{tr} \ll \tau_{RC}$, the electron transport from the cathode to anode is instantaneous, but the voltage recovers very slowly at a time scale of τ_{RC}. In order to ensure statistical independence the emission from the cathode must be on a longer time scale compared to τ_{RC} ie. the rate of emission from the cathode is $R \ll \frac{1}{\tau_{RC}}$. The emission rate that depends on the voltage assumes that the electron emission events are completely independent of each other. In other words, it is a Poisson point process. The rate of emission depends on the voltage applied and is only fully recovered after a time τ_{RC} has elapsed. For the case $R > \frac{1}{\tau_{RC}}$, the slow recovery of the voltage would suppress the rate of subsequent electron emission due to memory effects in the voltage. Both memory effects and space charge suppression lead to subshot noise. When $\tau_{tr} \gg \tau_{RC}$ the voltage recovers immediately and we call this the constant voltage case. The converse is considered as constant current case. The same physics can be observed in pn junction diodes. The Johnson noise from the resistor connected to the vacuum diode is neglected in the above analysis. It causes the charge on the plates to fluctuate about its steady state and its effect is an important contribution in the depletion region charging process and voltage fluctuation of pn diodes.

2.2.2 Noise from Maxwell-Boltzmann conductors

Next we consider the case of noise in Boltzmann conductors which is characterized by thermal noise. The Brownian motion of charge carriers as they interact with the crystal lattice leads to a fluctuating emf at the terminals. This random signal was first observed by Johnson[20] who verified the now famous relation $V_{th}^2 = 4kTRB$. This result was simultaneously developed by Nyquist[21] using a transmission line model which can be described as a macroscopic (or thermodynamic) theory since it linked the macroscopic parameters of the system such as the temperature T, resistance R and the fluctuating current (I_{th}) or voltage(V_{th}) by using two laws from statistical mechanics: second law of thermodynamics and the equipartition theorem. The derivation as such was valid only for a system where the charge carriers approach thermal equilibrium through interaction with the crystal lattice. However this macroscopic description can be quite deceiving as this leads us to believe that thermal noise is quite different from shot noise. Consider a one dimensional conductor of length L with n average(a nonfluctuating quantity) charge carriers per unit length. The shot noise current $\langle i^2 \rangle = 2qI\Delta\nu$ where q is the electronic charge and I is the dc current and $\Delta\nu$ is the bandwidth. The same expression can be written in particulate form using $I = q\frac{dn}{dt} = q\frac{n}{\tau}$ which leads to

$$\langle i^2 \rangle = 2q^2 \frac{dn}{dt}\Delta\nu = 2\langle q^2 \rangle AL\frac{n}{\tau}\Delta\nu \tag{2.9}$$

where A is the area of the semiconductor and τ is the mean free path. A carrier moving with velocity v for a time t will contribute a fractional charge $q(t)$ at the terminating electrodes which is given by[11]

$$q(t) = \frac{evt}{L} \tag{2.10}$$

In the thermionic diode, the noise was due to the random injection of charges and statistical independence of these events. Also each event made a complete transit from one electrode to another. In the case of the conductor, each carrier performs a free flight until a collision with the lattice in which case the velocity becomes randomized which is also the source of noise. This free flight is less than the length of the conductor and hence produces the fractional charge. Since each collision randomizes the velocity and each such collision takes place at random times, the charge $q(t)$ is a doubly stochastic variable in both v and t ie. the joint probability $P(v,t) = P(v).P(t)$ since both velocity and time are statistically independent variables. Eq. (2.9) can now be written as

$$\langle i^2 \rangle = 2\frac{e^2\langle v^2 \rangle\langle t^2 \rangle n}{L\tau}\Delta\nu \tag{2.11}$$

We need to obtain expressions for $\langle v^2 \rangle$ and $\langle t^2 \rangle$.The probability of a flight time between t and $t+dt$ is equal to zero collisions at times $[0,t]$ and one collision in the time interval $[t, t+dt]$ and can be written as the product of a Poisson and Bernoulli probability densities given by

$$\rho(t)dt = p(0,t) * p(1,dt) = \frac{1}{\tau}e^{\frac{-t}{\tau}}dt \tag{2.12}$$

Using Eq.(2.12), we can obtain the second order moment in t as

$$\langle t^2 \rangle = \int_0^\infty t^2\rho(t)dt = 2\tau^2 \tag{2.13}$$

In order to obtain a relation for the velocity fluctuations of an electron $\langle v^2 \rangle$, we resort to the Langevin equation[22] which can written as

$$m\frac{dv}{dt} = -\gamma v(t) + F(t) \tag{2.14}$$

The above equation is quite general as it describes the one dimensional classical Brownian motion of a particle of mass-m immersed in a liquid with temperature T. The degrees of freedom for the particle are represented by the center of mass coordinate at time t which is $x(t)$ and its corresponding velocity $v = \frac{dx}{dt}$. It would be quite difficult to describe the interaction of $x(t)$ with the many degrees of freedom associated with the molecules of the surrounding liquid. It would be easier to treat the surrounding liquid as a singular heat reservoir(which includes the effects of the many degrees of freedom) at absolute temperature T whose interaction with $x(t)$ could be established as a net force F_{net}. The decomposition of F_{net} into the two forces which constitute the two terms in the RHS of Eq. (2.14), requires some clarification. Since we have aggregated the effects of the reservoir into a single F_{net}, we may expect it to depend on the position of many atoms which are in constant motion. Hence F_{net} is a rapidly varying function of time which changes in an irregular manner due to the random motion associated with the atoms. We cannot specify a precise functional dependence of F_{net} on t, but we can give more information about it if the problem is studied from a statistical standpoint. Hence, we must consider an ensemble of similarly prepared systems, each of which consists of a particle and its surrounding medium governed by Eq. (2.14). Since $F_{net}(t)$ is a random force, it follows that $v(t)$ also fluctuates in time. The solution for $v(t)$ is no longer obtained by solving an ordinary differential equation but has to be stated in terms of a probability distribution $P(v, t, v_0)$- which governs the occurrence of velocity v at time t given that $v = v_0$ at $t = 0$. From statistical thermodynamics, we know that the system should tend to a Maxwellian distribution of temperature T of the surrounding liquid, 'independently' of v_0 in long time scales. This implies that any non-zero initial velocity $v \neq 0$ which may be produced by the presence of an external force, requires the velocity to tend to the equilibrium value of $v = 0$ once the external force is removed. If $F_{net} = 0$, Eq. (2.14) then fails to predict this behavior of $v(t)$ and hence the interaction force F_{net} must be affected by the motion of the particle such that it contains a slowly moving force, say $F_{friction}$ which is some function of v, tending to restore the particle to equilibrium. Now $F_{net}(t) = F_{friction}(v) + F(t)$ is decomposed into the slowly moving component and the faster component which is independent of velocity. If v is not too large, we may expand $F_{friction}(v)$ in a power series leading to $F_{friction}(v) = -\gamma v$[1] where γ is also known as the friction coefficient and we see that this force represents the dynamical friction experienced by a particle which tends to reduce $v(t)$ to zero as time increases. The frictional force implies that the energy associated with the degrees of freedom of the particle is dissipated to the other degrees of freedom associated with the reservoir. The concept of dissipation is an important one, and exists only when we treat the particle and reservoir as two separate systems. Once the particle loses energy to the reservoir, it is forever lost. This is different if one were to construct a microscopic equation for the combined particle-surrounding liquid system. In such a case, there are no frictional forces and hence no dissipation ie. the energy has simply been transferred to the reservoir which is still the same system. The total energy is conserved and if the arrow of time were reversed, the particles would retrace their paths backward in time. Since we have separated the slower moving frictional component from the net reservoir interaction force F_{net}, we can say more about the properties of the remaining fluctuating term $F(t)$: (a)It is independent of $v(t)$ and it drives $v(t)$ in such a way that $\langle v(t_1)F(t_2)\rangle = 0$ for $t_2 > t_1$.(b) $F(t)$ is a a Gaussian random process which will has as many positive as negative variations such that $\langle F(t)\rangle = 0$[2]. (c)It varies quite rapidly compared to $v(t)$ ie. there exists a time interval Δt such that the difference between $v(t)$ and $v(t+\Delta t)$ is negligible whereas $F(t)$ may undergo several fluctuations and no correlations between $F(t)$ and $F(t' = t + \Delta t)$ exists[3]. This implies that $\langle F(t)F(t')\rangle = D\delta(t-t')$ where D is

---

[1]One important assumption that we have made is that since F_{net} is a random force, the velocity $v(t)$ must also fluctuate in time and must be decomposed as follows: $v(t) = \langle v\rangle + v'$ ie. into a slow moving component given by the ensemble average of the velocity $\langle v(t)\rangle$ and a faster moving component v'. The faster component can be ignored since the mass of the particle is appreciable which leads to the approximation $\alpha\langle v\rangle \approx \alpha v$. This is important when taking the power series expansion of the velocity.

[2]The formal solution to the Langevin Equation of Eq.(2.14) is $v - v_0 e^{-t/\tau_c} = e^{-t/\tau_c}\int_0^t e^{t'/\tau_c}F(t')dt'$. Applying the ensemble average to the formal solution along with Property (b), we get$\langle v\rangle = v_0 e^{-t/\tau_c}$. The average velocity tends to zero in the long time scales which is the expected result in systems where macroscopic frictional forces are commonplace.

[3]The function $F(t)$ as well as its integral as seen in the RHS of the formal solution has only statistically defined properties. Hence the solution of the Langevin equation is understood as specifying a probability distribution $P(v,t,v_0)$ such that $P(v,t,v_0) = P(\int_0^t e^{(t'-t)/\tau_c}F(t')dt')$. Property (c), allows us to divide

the strength of the Langevin noise force. These three conditions for $F(t)$ are characteristics held by Langevin equations in general and Eq. (2.14) may be considered as a prototype for the expressions used to describe the junction voltage and carrier number fluctuations in pn junction diodes which are encountered later on in this chapter.

We now return to the problem of the noise in a resistor, where the particle which is described by the Langevin equation of Eq. (2.14), is the electron and the heat reservoir is the lattice. Under zero applied bias(thermal equilibrium situation), the average drift velocity is zero. Whenever the electron collides with the lattice, it acquires a non-zero momentum which decays towards zero with a time constant $\tau_c = \frac{m}{\gamma}$. This physics is described by the Langevin equation, where the drift velocity is kicked by the rapidly moving Langevin noise source F(t) (which is due to the interaction of the lattice with the electron) and represents the fluctuation term and the resultant non-zero velocity which is damped at the same time by the slow moving friction component which represents the dissipation term. Taking the Fourier transform of Eq. (2.14) gives us

$$V(i\omega) = \frac{F(i\omega)}{(\gamma + i\omega m)} \tag{2.15}$$

In order to determine the Langevin noise force $|F(i\omega)^2|$, the equipartition theorem is used where for thermal equilibrium, the mean energy of the particle

$$\frac{1}{2}m\langle v^2\rangle = \frac{m}{2}\int_0^\infty S_V(\omega)d\omega = \frac{kT}{2} \tag{2.16}$$

Taking the spectral density of Eq.(2.15) as $S_V(\omega) = \langle V^*(i\omega)V(i\omega)\rangle$ and substituting it in Eq.(2.16), we can obtain, $|F(i\omega)^2| = 4kT\gamma^2/m$. The voltage spectral density is then

$$S_V(\omega) = \frac{4kT}{m(1+\omega^2\tau_c^2)} \tag{2.17}$$

where $\tau_c = \frac{m}{\gamma}$. Taking the Fourier transform of the zero time autocorrelation function of Eq.(2.11), followed by substituting Eq.(2.13) and Eq.(2.17) in it, the power spectral density

---

the interval of time t over which the integration is performed into a large number of subintervals of duration Δt where the velocity or position of a Brownian particle can be treated as constants and only $F(t)$ is time varying. This assumption allows one to derive the solution[22] $P(v,t,v_0) = P(v - v_0e^{-t/\tau_c}) = \left(\frac{m}{2\pi kT(1-e^{-2t/\tau_c})}\right)^{0.5} \exp\left(-\frac{m|v-v_0e^{-t/\tau_c}|^2}{2\pi kT(1-e^{-2t/\tau_c})}\right)$ which leads to a Maxwellian distribution which is independent of v_0 when $t \to \infty$ as expected.

of the current fluctuations becomes

$$S_I(\omega) = \frac{A}{L} e^2 n\tau S_V(\omega) = 4kT/R(\omega) \tag{2.18}$$

where $R(\omega) = \frac{L}{A}\left(\frac{m}{e^2 n\tau}\right)(1 + \omega^2\tau_c^2)$ is the frequency dependent resistance. The current fluctuations power spectral density which is obtained by short-circuiting the terminals produce the familiar Johnson noise result. Since Eq.(2.18) was obtained from the shot noise current of Eq.(2.9), it tells us that there is no difference between the shot and thermal noise quantities and each arise as a result of the discrete nature of electronic charge. This result also allows one to argue that for any device, the origin of shot noise is not only due to the random passage of carriers through the space charge region as analyzed for the thermionic emission diode. In the case of the pn diode, the shot noise arises in the regions far away from the space-charge region(in the bulk) due to small thermal induced electron motion or through random generation or recombination events.

2.3 Shot Noise in PN Junction Diodes

This section discusses the minority carrier transport noise in a one dimensional asymmetrically doped heterojunction barrier diodes. The current noise of a pn heterojunction is solved by combining the small signal Green's function method of Van Vliet[23] with the diffusive treatment of Buckingham[16],thereby consolidating the two approaches. The method is quite general as it treats the processes occurring in the bulk material(away from the depletion region) of the diode and is applicable irrespective of nature of the barrier, be it either heterojunction or homojunction barrier diodes. Numerical solutions for the spatial electron noise densities can be obtained by coupling the analytical Green's function with numerical drift-diffusion simulations and will allow us to study the noise processes in the heterojunction type structures. We can analytically obtain either the voltage or the current fluctuations at the terminals of the device. In order to obtain the current fluctuations, the noise current generator connected to the terminals must be established and no potential fluctuation is allowed on such a terminal which is set by a constant voltage source. This condition will be referred from hereon as the constant voltage case. To obtain the voltage fluctuations, the noise voltage generator is determined with no current fluctuations occur on this terminal and this condition is referred to as constant current case. Constant voltage and constant current cases are two methods of bias which influenced the noise in thermionic diodes and they have the similar interpretation in pn junction diodes.

The focus of noise is on single and double heterojunction diodes as these are the typical light emitting diode structures which are dealt with experimentally in chapter 3, but extensions to homojunctions is straightforward since we assume that the evaluation of the Green's function does not depend on the nature of the barrier. This assumption is true only for constant voltage bias and is validated by numerical simulations performed on pn homojunctions which show that the Green's function tend to zero at the metallurgical junction[24]. Under constant current mode, recent analytical work on n^+n homojunctions show that the transfer impedance[4] produces additional terms due to the coupling between the n^+ and n sides instead of just providing the standard bulk terms corresponding to these regions. This implies that the junction exhibits a long term Coulombic interaction induced by space charge at the junction which has a noise suppression effect. This effect is the space charge suppression mechanism already seen earlier in the thermionic emission diode, and has been referred to by Yamamoto[25] as the Macroscopic Coulomb Blockade effect with respect to p^+n junctions. In this section, the terminal current noise in a p^+N heterojunction under constant voltage mode is established. We do not obtain self-consistent expressions for the Green's functions under the constant current mode(as this still a topic under research) and will not see if the junction effect is manifested as additional terms in the Green's functions. Instead, the extension to constant current case can be obtained by placing the diode noise model obtained from the constant voltage case in a high impedance environment which is determined by a large series resistance in series with the noise model of the diode. The constant current case is the origin of subshot noise in these systems and will be the focus

[4]The propagation of a microscopic noise fluctuation to the device terminals is represented by the gradient of the impedance function-$Z(x)$ also known as the impedance field ∇Z. The spectral density of the voltage fluctuations between the probing terminals under constant current operation is $S_V = A\int_{-L}^{L} |\nabla Z(x)|^2 K(x)dx$ where $K(x)$ is the noise source in slice x and the integration is over the device of length of $2L$. In this section we obtain the spectral density of the current fluctuation under constant voltage condition given by a similar expression$S_I = A\int_{-L}^{L} |\nabla G(x)|^2 K(x)dx$ where ∇G is the gradient of the Green's function. Using the expression for S_I along with circuit analysis of equivalent noise model of the diode, we can obtain the expression for S_V.

of Section 2.3.

The structure considered in the analysis is shown in Fig.(2.1) as an arbitrary(barrier is irrelevant) pn junction with the depletion region width at $x_p + x_n$ and the p and n neutral regions having widths $w_p - x_p$ and $w_n - x_n$. The following assumptions are made in the analysis of the current noise: a)The low frequency spectra is obtained ignoring the cutoff characteristics of the carrier lifetimes. b)The depletion approximation is used in obtaining the Green functions ie. the depletion region has abrupt boundaries and the applied voltage is contained within this region and the semiconductor is charge neutral outside the depletion region. c)The analysis is performed at low to moderate injection conditions where the junction current is expressed as the sum of the minority carrier diffusion current in the two quasineutral regions of the diode. The injected carrier concentrations are much smaller than the majority carrier concentrations which are approximated by their equilibrium values. The depletion region generation-recombination current contribution is neglected. High injection conditions where series resistance effects dominate with the presence of an electric field in the quasi-neutral regions are not treated. d)Green function are obtained by small signal methods based on a perturbation approach to arrive at stationary noise compact device models(compact also means closed-form analytical models used in device design). The small signal method requires linearizing the device equations about the steady state working point and since both the continuity equation as well as the diffusion equation in the quasi-neutral regions are already linear, the Green functions so obtained using these equations are also linear.

Neglecting the electric field in the quasi-neutral regions, the electron continuity equation written on the p side of the junction diode is

$$\frac{\partial n'}{\partial t} = -\frac{n'}{\tau_n} + D_n \frac{\partial^2 n'}{\partial x^2} \tag{2.19}$$

where $n'(x,t) = n(x,t) - n_{p0}$ is the excess electron density, n_{p0} is the equilibrium electron density, D_n is the electric field independent diffusion constant and τ_n is the lifetime of minority electrons. Only the electron noise is studied since a)we consider a p^+N heterojunction where only the electrons contribute significantly to the current because of the heterojunction barrier. This differs for the asymmetrically doped p^+n homojunction where holes would form the majority of the current. b)The same result applies to hole noise on the p side and can be obtained by replacing $n, \tau_n, D_n \rightarrow p, \tau_p, D_p$. In order to evaluate the stationary noise, a small signal analysis must be performed provided the noise perturbation is small enough to warrant a linearized analysis. In order to obtain the frequency dependent Green's functions, we need to take the Fourier transform of Eq. (2.19), which leads to

$$\frac{d^2 n'(x, j\omega)}{dx^2} = \frac{n'(x, j\omega)}{L_n^2} \tag{2.20}$$

where $L_n^2 = L_0^2 (\frac{1}{1+j\omega\tau_n})$ is the ac electron diffusion length and L_0 is its dc quantity. Since the terminal current is calculated from minority carrier diffusion currents at the two depletion region edges $x = x_p$ and $x = x_n$, one may assume that the terminal current noise is also due to the random passage of carriers across the depletion region. This corpuscular treatment was originated by Van-der Ziel[15] by using the thermionic emission diode model of Eq.(2.1), but Faulkner and Buckingham[17] showed that the forward and backward carrier fluxes crossing the junction provide a small contribution to the total terminal current noise, and are unable to explain the measured shot noise results until the fluctuations taking place in regions extending away from the junction are considered. The reason for the noise is due to the relaxation mechanism which return the perturbed minority carriers to equilibrium. The deviation of minority carriers from equilibrium near the junction causes a change in the gradient of the carrier distribution at the edge of the depletion region, which in order to relax to the steady state requires carriers to cross the junction giving rise to a flow of charge around the circuit ie. the terminal current noise is calculated at the depletion region edges as we do for the steady state currents but as a response to events taking place away from the junction. A voltage source is applied across the terminals of the device and the source resistance and the bulk resistance is assumed to be negligibly small when compared with the differential resistance of the diode(constant voltage case). The constant voltage bias fixes the quasi-Fermi levels at the levels set by the applied voltage-V and hence the electron densities at $x = -x_p$(edge of the depletion layer) in Fig. (2.1) are fixed at $n_p(-x_p) = n_{p0} e^{V/V_T}$ and the large recombination velocity at $x = -w_p$(metal contact) sets it at the equilibrium carrier density $n_p(-w_p) = n_{p0}$. These are non-fluctuating quantities and as a result, the electron distribution fluctuates only in the bulk between $x = -x_p$ and

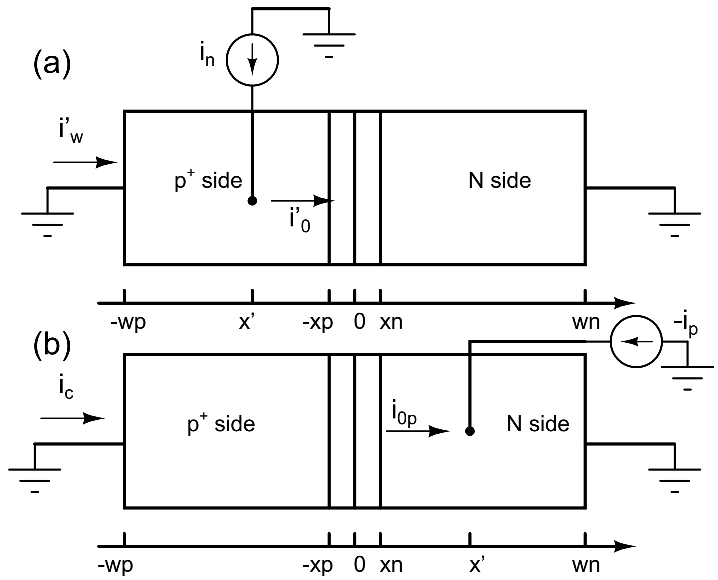

Figure 2.1: Description of the scalar short-circuit current Green 's function. (a)The electron Green's function and (b)The hole Green's function. x_p and x_n indicate the edges of the depletion region and i_n and i_p are the injected electron and hole scalar currents at x'. i'_W,i'_0,i_c and i_{0p} are the output current variations induced in response to the perturbations by the scalar current sources.

$x = -w_p$. In other words, the terminals are 'ac-shorted' and the excess electron densities at the edges of the bulk region should be zero for all frequencies save the dc component. This leaves us with the boundary conditions

$$n'_p(-x_p, j\omega) = n'_p(-w_p, j\omega) = 0 \tag{2.21}$$

The events in the bulk which arises due to action of discrete electronic charges set up fluctuations in electron density which are rapidly relaxed by diffusive current flows in the entire region in order to return the bulk to equilibrium. The relaxation currents are responsible for violation of charge neutrality in this region which induce majority current flow in the external circuit and is the one that leads to the observed current noise in the external circuit.

The noise model can be obtained by following the Green's function approach which has a two step recipe ie. a)The microscopic noise sources are identified inside the device as a function of the steady state working point and b)The noise sources are propagated to the device terminals to evaluate the current noise generators.

There are two microscopic noise sources responsible for the current noise of a constant-voltage driven p^+N heterojunction. One is due to the velocity fluctuation of electron flow(diffusion noise) associated with the Brownian motion of charge carriers or electron-phonon or electron-impurity scattering and the other is the carrier density fluctuation due to transitions between bands and localized states leading to generation-recombination noise of electrons. In this section, we consider only the generation-recombination and diffusion noise in the neutral regions and ignore the noise generated in the depletion region. The propagation of the microscopic noise sources is achieved through a Green's function for each of the carrier species ie. $G_n(x,', \omega)$ for electrons and $G_p(x', \omega)$ for holes. The frequency-dependent 'scalar' Green's function $G(x', \omega)$ can be considered as a current gain which is defined as the ratio of the current variation induced(output variable) at the device anode(p side ohmic contact-(x=W)) or at the edges of the depletion region(x=0) to the electron or hole scalar current excitation(input variable) injected at x' anywhere in the quasi-neutral p^+ or N regions.

The spectrum of the current noise generator is expressed as the sum of the diffusion and GR spectra

$$S_{i_T}(\omega) = S_{i,D}(\omega) + S_{i,GR}(\omega) \tag{2.22}$$

where the expressions for the two terms in Eq.(2.22) are[26]

$$S_{i,D}(\omega) = A \sum_{\alpha=n,p} \int_{\Omega} K_{J_\alpha,J_\alpha} \left| \frac{\partial G_\alpha}{\partial x} \right|^2 dx \tag{2.23}$$

$$S_{i,GR}(\omega) = Aq^2 \sum_{\alpha,\beta=n,p} \int_{\Omega} K_{\gamma_\alpha,\gamma_\beta} G_\alpha G_\beta^* dx \tag{2.24}$$

and the integration is carried out over the entire diode except the depletion regions .ie. $\Omega = \Omega_p \cup \Omega_n$ where the neutral regions are $\Omega_p = [-w_p, -x_p]$ and $\Omega_n = [x_n, w_n]$. Here $K_{J,J}$ and $K_{\gamma,\gamma}$ are the local noise sources due to diffusion and generation recombination noise. The local noise sources can be obtained from the moments of the Fokker-Planck equations(see [23] for a first principles derivation of these moments from the Master equation) and for the case of diffusion noise, the local noise source for electrons is

$$K_{J_n,J_n}(x) = 4q^2 n(x) D_n \tag{2.25}$$

and the local noise source for generation-recombination noise is

$$K_{\gamma_n,\gamma_n}(x) = 2\frac{n_{p0} + n_p(x)}{\tau_n} \tag{2.26}$$

Eqs.(2.23-2.24) can be obtained rigorously by adding scalar impulsive current source as a forcing term in the linearized continuity equations[26]. Let us consider the electron Green's function $G_n(x', \omega) = \frac{i'_W}{i_n}$. From Fig.(2.1a), the Kirchhoff's current law(KCL) for a scalar electron current injection at $x = x'$ where $x' \in \Omega_p$ gives $i'_W + i_n - i'_0 = 0$. On the other hand for $x' \in \Omega_n$, the electrons are majority carriers, and all of the injected current flows through the ohmic contacts in w_n and therefore $i'_W = 0$. Hence

$$G_n(x', \omega) = \begin{cases} 0 & x' \in \Omega_n \\ -1 + G_{n_p} & x' \in \Omega_p \end{cases} \tag{2.27}$$

where $G_{n_p} = \frac{i'_0}{i'_W}$. Consider Fig.(2.1b), the injection of holes in $x' \in \Omega_p$, leads to a flow through the ohmic contacts a $x = -w_p$ and from KCL we have $i_c = i_p$. For $x' \in \Omega_n$, hole injection in minority carrier region leads to $i_{0p} = i_p$. The hole Green's function is defined as

$$G_p(x', \omega) = \frac{i_c}{i_{0p}} = \begin{cases} G_{p_n} & x' \in \Omega_n \\ 1 & x' \in \Omega_p \end{cases} \tag{2.28}$$

where $G_{p_n} = \frac{i_{0p}}{i_p}$. The choice of Green's functions in Eq.(2.27) and Eq.(2.28) are the same expressions used by Bonani et al[26]. Substituting Eq.(2.27) and Eq.(2.27) in Eq.(2.23) and Eq.(2.24) gives us

$$S_{i,D} = A\int_{\Omega_p} K_{J_n,J_n}(x)\left|\frac{\partial G_{n_p}}{\partial x}\right|^2 dx + A\int_{\Omega_n} K_{J_p,J_p}(x)\left|\frac{\partial G_{p_n}}{\partial x}\right|^2 dx \tag{2.29}$$

$$S_{i,GR} = Aq^2\int_{\Omega_p} K_{J_n,J_n}(x)\left|G_{n_p}\right|^2 dx + Aq^2\int_{\Omega_n} K_{J_p,J_p}(x)\left|G_{p_n}\right|^2 dx \tag{2.30}$$

According to the Bonani model, the Green functions have been evaluated using the KCL which may not be entirely correct. For example, according to Eq.(2.28), $i_{0p} = i_p$ in the n side. In fact, injection of a current source at $x = x'$ would establish a concentration gradient, which would lead to different currents along the length of the diode and unless the diode is short, using KCL to evaluate the Green's function is not valid. We shall use the Buckingham diffusion noise theory[16] to see if the choice of Green's function in the Bonani model is correct. Since the noise is studied only in the neutral p^+ region, we can redefine $x = x_p$ as the origin of a new coordinate system and will consider the region from $x = 0$ to $x = W$ where $W = w_p - x_p$.

2.3.1 Generation Recombination Noise

When a generation or recombination event occurs, there is no violation of overall charge neutrality between x=0 and x=W[5]. The majority charge carriers do not have relaxation flows, but there is a perturbation in the minority carrier distribution which cause relaxation flows away from the disturbance to return the system to equilibrium and is responsible for a fraction of the total current noise. Let us consider an electron generation event for which there is an instantaneous appearance or disappearance of an electron at x=x'. This causes an instantaneous current of $i_n(t) = -q\delta(t)$ that flows from 'nowhere' to the x=x' plane in the p^+ region as shown in Fig.(2.2b). The initial and final perturbed electron distribution due to this scalar current source inserted at x=x' is shown also shown in the same figure. Solving the Fourier transformed continuity equation of Eq.(2.20) using the boundary conditions of Eq.(2.21) and $n'(\omega) = n'_1$ at x=x', we obtain

$$n'(x,\omega) = \frac{n'_1}{e^{x'/L} - e^{-x'/L}}(e^{x/L} - e^{-x/L}) \quad , \quad 0 \le x \le x' \tag{2.31}$$

$$n'(x,\omega) = \frac{n'_1}{e^{(W-x')/L} - e^{-(W-x')/L}}(e^{(W-x)/L} - e^{-(W-x)/L}) \; , \quad x' \le x \le W \tag{2.32}$$

The relaxation currents at x=x'+0 and x=x'-0 can be calculated from the diffusion equation and we find the following currents

$$i'_1(\omega) = qD_n\frac{dn'(\omega)}{dx}|_{x=x'-0} = k_1 n'_1 \tag{2.33}$$

$$i'_2(\omega) = qD_n\frac{dn'(\omega)}{dx}|_{x=x'+0} = -k_2 n'_1 \tag{2.34}$$

where we the symbols k_1 and k_2 are defined as

$$k_1 = \frac{qD_n}{L_n}\coth(\frac{x'}{L_n}) \quad , \quad k_2 = \frac{qD_n}{L_n}\coth(\frac{W-x'}{L_n}) \tag{2.35}$$

[5]The charge neutrality is initially observed when the generation or recombination processes produce or remove an electron-hole pair. The holes being majority carriers do not produce concentration gradients or diffusive current flows unlike the minority carrier distributions. After diffusive relaxations flows are setup(almost instantly) charge neutrality is lost.

Since we cannot have any accumulation of charge in the p region, we must maintain current continuity at x=x' which is given by the following jump conditions

$$i'_1(\omega) - i'_2(\omega) + i_n(\omega) = i'_1(\omega) - i'_2(\omega) - q = 0 \tag{2.36}$$

Relation with the KCL of Bonani. Substituting Eqs.(2.33) and (2.34) in Eq.(2.36), we can obtain $n'_1 = \frac{q}{k_1+k_2}$. The relaxation currents evaluated at x=0 and x=W are

$$G_{n_p}(x',\omega) = \frac{i'_0(\omega)}{i_n(\omega)} = \frac{qD_n}{i_n(\omega)}\frac{dn'(\omega)}{dx}|_{x=0} = -\frac{k_0}{k_1+k_2} \tag{2.37}$$

$$G_n(x',\omega) = \frac{i'_W(\omega)}{i_n(\omega)} = \frac{qD_n}{i_n(\omega)}\frac{dn'(\omega)}{dx}|_{x=W} = +\frac{k_W}{k_1+k_2} \tag{2.38}$$

where k_0 and k_W are defined as

$$k_0 = \frac{qD_n}{L_n} cosech(\frac{x'}{L_n}) \quad , \quad k_W = \frac{qD_n}{L_n} cosech(\frac{W-x'}{L_n}) \tag{2.39}$$

The external circuit current due to a single event is given as

$$i'_T(\omega) = i'_0(\omega) - i'_W(\omega) \tag{2.40}$$

and defining the terminal current Green function as $G_{n_T} = \frac{i'_T}{i_n}$ which from Eq.(2.40) gives

$$G_{n_T} = G_{n_p} - G_n \tag{2.41}$$

The average number of generation rate in a small volume $A\Delta x$ is given as $\gamma_G = \frac{n_{p0}A\Delta x}{\tau_n}$ and the average recombination rate is $\gamma_R = \frac{n(x)A\Delta x}{\tau_n}$. Note that each generation and recombination event is uncorrelated, and so the total spectral density includes the sum of all such events in the volume $A\Delta x$ and can be written using Carsons theorem(Eq.(3.27))

$$\begin{aligned} \Delta S_{i,GR}(\omega) &= 2(\gamma_G + \gamma_R)|i'_T(\omega)|^2 \\ &= 2(\gamma_G + \gamma_R)|i_n(\omega)|^2\, |G_{n_T}|^2 \end{aligned} \tag{2.42}$$

The total external circuit fluctuation power spectral density $S_{i,GR}(\omega)$ over the entire base is obtained by integrating Eq. (2.42)

$$S_{i,GR}(\omega) = Aq^2 \int_0^W \frac{2(n(x)+n_{p0})}{\tau_n} \left|G_{n_p} - G_n\right|^2 dx \tag{2.43}$$

where $K_{\gamma_n,\gamma_n} = \frac{2(n(x)+n_{p0})}{\tau_n}$ is the local noise spectral density of the generation recombination noise. Comparing Eq.(2.43) with Eq.(2.30), the choice of Green's function is different by the presence of the additional term G_n. Substituting Eq.(2.37) and Eq.(2.38) in Eq.(2.43) gives us

$$S_{i,GR}(\omega) = \frac{2Aq^2}{\tau_n} \int_0^W [n(x) + n_{p0}] \left| \frac{k_0 + k_W}{k_1 + k_2} \right|^2 dx \tag{2.44}$$

2.3.2 Thermal Diffusive Noise

The topic as it implies refers to thermal noise. But unlike a resistor where the electrons were considered as the majority carriers we consider here the minority carriers in the bulk region(electrons in the p base). The majority carriers by themselves still retain the thermal noise component $4kTR$. Otherwise the same mechanisms are in effect. A single electron due to collision makes a transit of the mean free path l_f and this results in an instantaneous current $q\delta(t)$ at two positions x and $x + l_f$. The electron densities due to this current are perturbed as seen in Fig. (2.2a). We assume that current flows in the positive x direction which implies that electron motion is negative. This sets up a diffusion current(relaxation flows) in accordance with the equations of continuity to return the electron density to steady state(ie. remove this charge). The ac boundary conditions are $n''(j\omega) = 0$ at x=0 and $n''(j\omega) = n_1'$ at $x = x'$. Using the BCs we obtain the following electron concentration

$$n''(x, j\omega) = n_1 \frac{e^{x/L_n} - e^{-x/:_n}}{e^{x'/L_n} - e^{-x'/L_n}} \tag{2.45}$$

The corresponding diffusion current is

$$i_1(\omega) = qD_n \frac{dn'}{dx}|_{x=x'} = \frac{qD_n}{L_n} \coth\left(\frac{x'}{L_n}\right) = k_1 n_1 \tag{2.46}$$

We can similarly obtain for the other side using the BCs $n''(j\omega) = -n_2$ at $x = x' + l_f$ and $n''(j\omega) = 0$ at x=W. The resultant current density is

$$i_2(\omega) = qD_n \frac{dn''(j\omega)}{dx} = -\frac{qD_n}{L_n} coth\left(\frac{x - W}{L_n}\right) n_2 = -k_2 n_2 \tag{2.47}$$

Notice the negative sign, which implies the current is opposite to the direction of flow we chose. However n''_2 is negative which gives the current a net positive flow. At $x = x' + 0$

and $x = x' + l_f - 0$ we can obtain the return currents using the same diffusion equations

$$i_{r1}(\omega) = \frac{qD_n}{L_n \sinh\left(\frac{l_f}{L_n}\right)} \left(-n''_1 \cosh\left(\frac{l_f}{L_n}\right) + n''_2\right) \tag{2.48}$$

Similarly we can define I_{r2}.In fact the return currents can be simplified since the mean free path on the order of nm is less than the diffusion length $l_f \ll L_n$ in which case we obtain

$$i_{r1} = i_{r2} = -\frac{qD_n}{l_f}(n_1 - n''_2) \tag{2.49}$$

If we replace l_f by the width of the depletion region, we obtain the diffusion current for charge carriers crossing the depletion region. In other words,within l_f we have another space charge region or at least devoid of any charge carriers as per our assumption. Since there is no accumulation of charge throughout the bulk, we must have current continuity at x' and $x' + l_f$ which can be written as

$$i''_1(\omega) + i''_{r1}(\omega) = -q\delta(t) \tag{2.50}$$

$$i''_2(\omega) + i''_{r2}(\omega) = -q\delta(t) \tag{2.51}$$

Substituting the results of the currents and simultaneously solving the equations we obtain the expressions for the charge densities

$$n''_1(\omega) = -\frac{l_f k_2}{D_n(k_1 + k_2)} \quad , \quad n''_2(\omega) = -\frac{l_f k_1}{D_n(k_1 + k_2)} \tag{2.52}$$

The circuit current which flows in the external circuit can be determined by the two relaxation currents which flow into the base ie. $i_0(\omega)$ at x=0 and $i''_W(\omega)$ at x=W. Notice that the continuity equation states that there is no violation of charge neutrality. However the resulting relaxation flows which lead to outflow of carriers throughout the region cause the charge imbalance and the violation of neutrality has to be compensated by the external current flow which is made up of a majority carrier hole flow through the contacts and a electron flow across the depletion region. The external circuit current at x=0 is carried by many events of forward and backward injection(through diffusion or thermionic emission) and continuously charge and discharge the region.The same condition applies to holes injected through the contacts. The violation of charge neutrality in the bulk p region is equal to the difference between the currents flowing at x=0 and x=W . This is the terminal current that flows into the junction in response to internal events and is

$$i''_T(\omega) = i''_0(\omega) - i''_W(\omega) \tag{2.53}$$

where

$$i''_0(\omega) = \frac{l_f k_0 k_2}{D_n(k_1 + k_2)} \;\;,\;\; i''_W(\omega) = \frac{l_f k_W k_1}{D_n(k_1 + k_2)} \tag{2.54}$$

We note that i''_T is the Fourier transformed circuit current pulse due to a single electron event. In fact we are closer to using Ramo's theorem now and Eq. 2.3 . The average number of thermal diffusive transits per second in a small volume is $A\Delta x$ is

$$\gamma_T = \frac{n(x)A\Delta x}{\tau_f} = \frac{n(x)A\Delta x}{l_f^2} D_n \tag{2.55}$$

where we have used the Einstein relation for the mean free time between collisions $\tau_f = \frac{l_f^2}{D_n}$ and l_f is the mean free path of the electron in the p region. Since each thermal event occurs independently, this leads to a random pulse train from which the spectral density of current fluctuations due to a small region Δx can be obtained using the Carson's theorem from Eq.(2.3) by replacing $\nu = \gamma_T$ and $|F_T(i\omega)^2| = |i_T(i\omega)^2|$ and ignoring the dc component which gives

$$\Delta S_{i,D}(x,\omega) = 2\gamma_T |i_T(\omega)|^2 = \frac{4An(x)}{D_n} \left| \frac{k_0 k_2 - k_w k_1}{k_1 + k_2} \right| \Delta x \tag{2.56}$$

Note that the expression gives the spectral density of the terminal current which is obtained from a single event multiplied by the total number of average events at each point x of the semiconductor which is simply a dc carrier concentration $n(x)$ which we can easily obtain either by analytical or numerical means. The total current fluctuation spectral density can be obtained by integrating this equation across the entire p region of the diode as

$$S_{i,D}(\omega) = \frac{4A}{D_n} \int_0^W n(x) \left| \frac{k_0 k_2 - k_w k_1}{k_1 + k_2} \right|^2 dx \tag{2.57}$$

The vector Green's function for the diffusion noise can be obtained by comparing Eq.(2.57) and Eq.(2.23) from which $\frac{\partial G_{n_T}}{\partial x} = \frac{\partial G_{n_p}}{\partial x} - \frac{\partial G_n}{\partial x} = \frac{1}{qD} \frac{k_0 k_2 - k_W k_1}{k_1 + k_2}$. The important point to note is that this choice of Green's functions differs from Eq.(2.42) used in the Bonani model. The authors assume that the diode is long, in which case the second term does not have

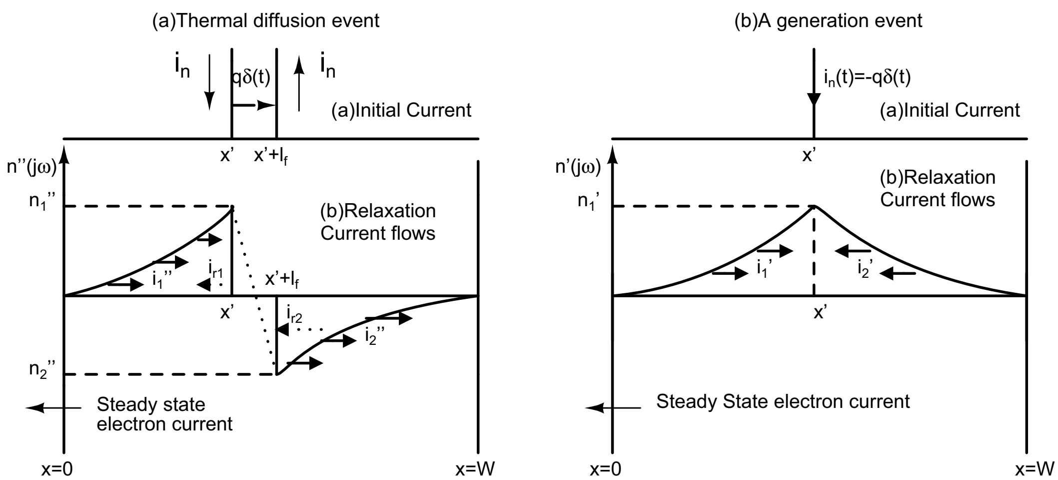

Figure 2.2: The initial current flow followed by the relaxation current flows for (a)a thermal diffusion event and (b)generation process of a minority carrier.

an important contribution. This has been verified by the numerical simulation, but in the case of short diodes, it is essential in setting the thermal noise contribution to zero.

The integrals of Eq.(2.57) and Eq.(2.44) contain various hyperbolic functions in the form of k_0, k_W, k_1 and k_2 which are hard to integrate unless done numerically. To obtain meaningful results we can consider two cases which are useful for the analysis of LEDs, which is the short diode and the long diode. The total noise can be written as the sum of Eq. (2.57) and Eq. (2.44)

$$\begin{aligned} S_{I_T}(\omega) &= S_{i,GR}(\omega) + S_{i,D}(\omega) \\ &= \frac{4A}{D_n} \int_0^W n(x) \left|\frac{k_0 k_2 - k_w k_1}{k_1 + k_2}\right|^2 dx + \frac{2AD_n q^2}{L_0^2} \int_0^W [n(x) + n_{p0}] \left|\frac{k_0 + k_W}{k_1 + k_2}\right|^2 dx \end{aligned} \quad (2.58)$$

Single Heterojunction Long Diode

For a long diode, the bulk p+ region thickness W is much longer than the diffusion length L_n and the upper limit on the integrals can be replaced by infinity. The dc electron distribution as obtained from the continuity equation is

$$n(x) = n_{p0} + (n_p - n_{p0}) exp(-x/L_0) \quad (2.59)$$

and the remaining position dependent terms can be evaluated as follows:

$$\left|\frac{k_0 k_2 - k_w k_1}{k_1 + k_2}\right|^2 \approx \frac{qD_n}{L_n} exp(-2x/|L_n|) \quad (2.60)$$

$$|\frac{k_0 + k_W}{k_1 + k_2}|^2 \approx exp(-2x/|L_n|) \tag{2.61}$$

where we find that $k_2 \approx 1, k_W \approx 0$. Substituting these results in Eq. (2.58), and after performing the integrations,we obtain the spectral density as

$$S_{i_T}(\omega) = \frac{4q^2AD_n}{L_0}(a^2+b^2)[\frac{n_p - n_{p0}}{2a+1} + \frac{n_{p0}}{2a}] + \frac{2q^2AD_n}{L_0}[\frac{n_p - n_{p0}}{2a+1} + \frac{n_{p0}}{a}] \tag{2.62}$$

Taking the low frequency form($\omega\tau_n \ll 1$) for which a=1,b=0 and $L_0 = L$, we get the result,

$$S_{I_T}(\omega) = \frac{4Aq^2D_n}{L_n}(\frac{n_p - n_{p0}}{3} + \frac{n_{p0}}{2}) + \frac{4Aq^2D_n}{L_n}(\frac{n_p - n_{p0}}{6} + \frac{n_{p0}}{2}) \tag{2.63}$$

At zero bias $n_p = n_{p0}$, and using the value of differential resistance at V=0 $R_d = \frac{kT}{eI(V=0)}$,we can simplify Eq. (2.63) as

$$S_{I_T}(\omega) = \frac{4Aq^2D_nn_{p0}}{L_n} = \frac{4kT}{R_d} \tag{2.64}$$

The above expression is the Nyquist theorem for the thermal noise of resistor except we replace the majority carrier resistance with minority carrier junction resistance. It may seem reasonable to invoke Nyquist theorem, whenever the system is in thermal equilibrium. However if we consider the microscopic processes behind Eq.(2.64) , we look towards Eq.(2.63) which shows that there are two equal contributions: from the thermal phonons due to lattice vibrations which cause thermal diffusion noise and from the thermal photon reservoirs which cause g-r noise.

For $V > 0$, Eq. (2.63) reduces to the form

$$S_{I_T} = \frac{2Aq^2D_n}{L_n}(n_p + n_{p0}) = 2q(I_0 + 2I_s) \approx 2qI_0 \tag{2.65}$$

where I_0 and I_S are the forward and reverse saturation currents respectively. This is the standard shot noise current flowing in the external circuit of the diode. Eq.(2.63) has been obtained in the limit of low frequency and of course, the assumption that the diode is long. In Appendix.A we have derived the compact frequency dependent device noise model using the Buckingham's theory which agrees with that obtained in [26], verifying that the Green's function method and Buckingham's diffusion theory are the same when the term G_n is omitted in the calculations.

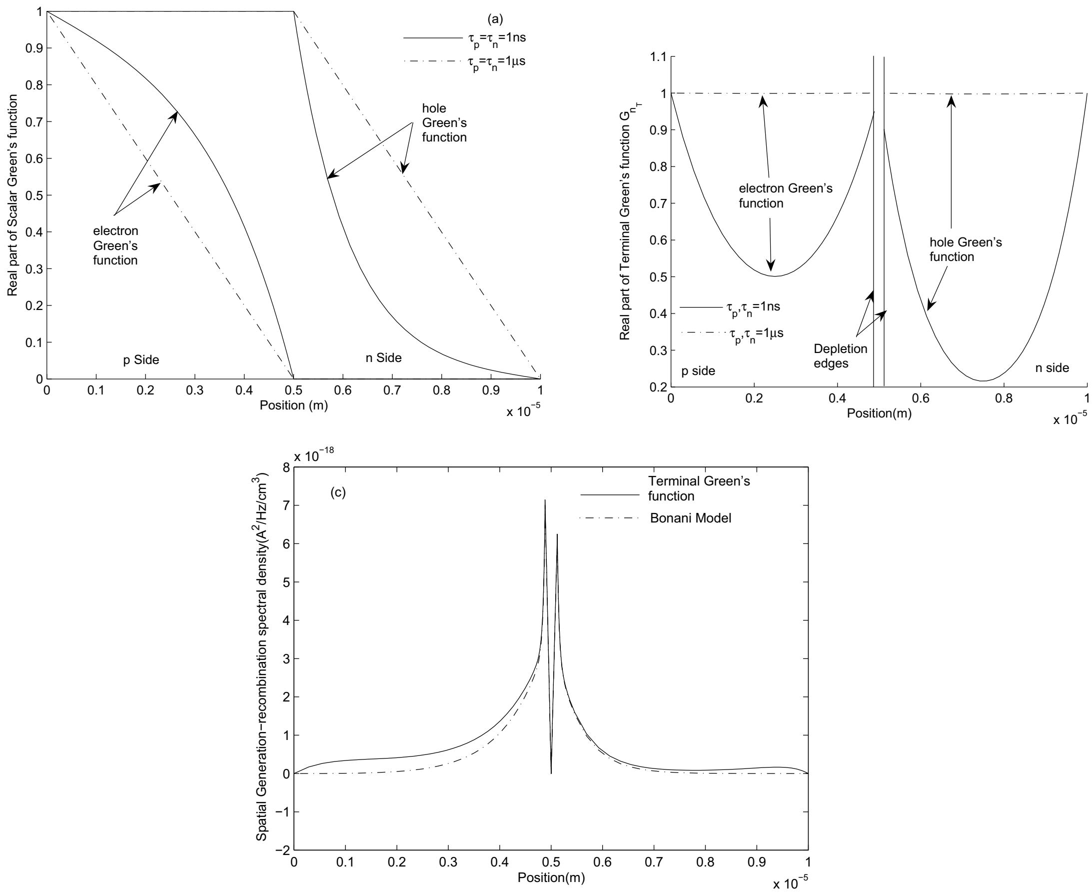

Figure 2.3: (a)Scalar Green's function according to the Bonani model in Eqs.(2.27,2.28) for long($\tau_p = \tau_n = 1ns$) diode and short ($\tau_p = \tau_n = 1\mu s$) diodes (b)The terminal Green's function according to Eq.(2.41) (c)The spatial Generation-recombination noise calculated using the Bonani model versus the terminal Green's function.

Double Heterojunction Diode

An example of a double heterojunction diode is shown in Fig.(2.4). In such structures, the p+ region thickness W is much smaller than the electron diffusion length which makes the diode short. In reality, the diffusion currents are zero since the concentration throughout the p+ region is $n_p = n_{p0}\exp(qV/kT)$ and there are no concentration gradients. The injected current cannot diffuse towards the contacts because of the conduction band discontinuity at p+P heterojunction. We can think of the junction current as electrons crosses an imaginary plane between the conduction and valence bands by radiative or non-radiative processes. If n_c is the total number of carriers in the active region then $I = \frac{en_c}{\tau_n}$ where τ_n is the minority carrier lifetime. Since the diode is small, we can make the following simplifications

$$\frac{k_0 k_2}{k_1+k_2} = \frac{k_W k_1}{k_1+k_2} \approx \frac{qD_n}{W} \quad \frac{k_0}{k_1+k_2} = 1 - \frac{x'}{W}, \frac{k_W}{k_1+k_2} = \frac{x'}{W} \tag{2.66}$$

Using Eq.(2.66) in Eq.(2.54) the noise currents at $x = 0$ and $x = W$, due to the diffusion noise is

$$i_0(\omega) = i_W(\omega) = \frac{ql_f}{W} \tag{2.67}$$

Since i_0 and i_W are identical and positively correlated, the external circuit current fluctuations $_T = {}_W - {}_0$ is zero. The thermal diffusion noise does not cause a departure from charge neutrality in the entire p+ region and hence does not induce external circuit current noise. On the other hand, for g-r noise the currents

$$i_0 = q(1 - \frac{x;}{W}) \;\; , i_W = -q\frac{x'}{W} \tag{2.68}$$

The terminal current is $i_T = i_0 - i_w = q$. Each event of generation and recombination of electrons results in independent current pulses of area q in the external circuit. The low frequency spectra for the forward bias($V > 0$) which is obtained by ignoring the generation events(or n_{p0}) is obtained from Eq.(2.44) as

$$S_{I_T} = 2\int \frac{n_p(x)}{\tau_n}|i_T(\omega)|^2 dx = 2e^2\frac{n_p}{\tau_n} = 2qI \tag{2.69}$$

Hence the total shot noise arises completely from the generation-recombination mechanisms in short base diodes.

Numerical Analysis

In Fig.(2.3a), we have plotted the scalar Green's function according to the Bonani model for the case of short diodes and long diodes which agrees with the results in [24]. The terminal Green's function model according to Eq.(2.41) is plotted in Fig.(2.3b). The terminal Green's function agrees with our previous discussions for both long and short diodes. For the case of short diode, a current injection of a single electronic charge anywhere in the p region produces a terminal current of that electronic charge. Hence the Green's function is one throughout the diode. The spectral density using the Bonani model versus the terminal Green function approach is plotted in Fig.(2.3c) for a symmetrical long diode with doping $N_A = N_D = 10^{16} cm^{-3}$ with a length of $5\mu m$ for the p and n sides. The applied voltage is 0.5V and the lifetime employed is $\tau_p = \tau_n = 1ns$. Since this is a long diode, the difference between the two models is small, since most of the noise appears in the vicinity of the junction. For the short diode case, the Bonani model will neglect the contributions of those events occuring close to the device terminals and will lead to a result which is smaller than predicted by the terminal Green's function model.

2.4 Subshot Noise in pn junction devices

The shot noise current flows into the junction of the diode from the external circuit in response to internal events. The equivalent circuit for noise involves introducing this external current in parallel with the differential resistance of the diode. The noise equivalent circuit is sufficient to explain the regulation mechanisms originally encountered in experiments. In the early 90s, Edwards introduced the 'leaky reservoir' model[6, 27, 28] in order to explain the feedback as well as the noise suppression in the recombination current. He treated the problem electrically by completely relying on the noise equivalent circuit of the LED, and making the assertion that the photon number emitted is equivalent to the carrier number in the active region. The model works quite well but only when describing the moderate injection regime for heterojunction and homojunction based 'long' diodes. In the original paper[6], the regulation mechanism required only the storage of charge carriers in the diffusion capacitance. Later on, Kim et al[13] showed the existence of a depletion

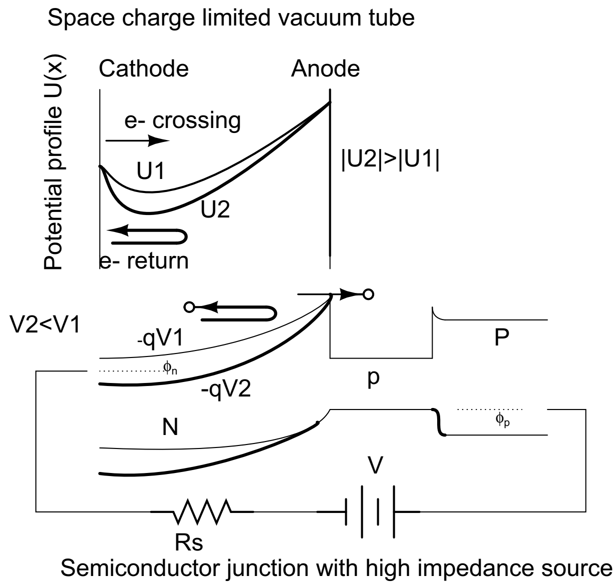

Figure 2.4: Regulated electron emission process in a space charge limited vacuum tube obtained by self-modulation of the potential field profile. The space charge is overlayed with the space charge of the semiconductor junction diode driven by a high impedance current source which also shows the regulated electron emissions through junction voltage modulation.

layer based regulation mechanism quite similar to the space charge mechanism of Fig.(2.4). This required the presence of the depletion capacitance which can be added to the existing equivalent circuit to satisfy experimental observations. Along with the statistical point process for carrier recombination, the process of photon emission-attenuation and photodetection leads to shot noise suppression. Subshot noise relies on the presence of a high impedance current source which establishes a negative feedback and this can be described by the noise equivalent circuit model of LED in Fig. (2.5) which has the following elements: $C = C_{diff} + C_{dep}$ is the sum of diffusion and depletion capacitances, $R_d = (\frac{dI}{dV})^{-1}$ is the differential resistance , v_{sn} is the shot noise voltage associated with R_d , R_S is the source resistance and v_{th} is the thermal noise voltage associated with R_S. Alternatively, we can express all the noise sources in their Norton equivalents in which case $i_{sn} = \frac{v_{sn}}{R_d}$ is the shot noise current and $i_{th} = \frac{v_{th}}{R_s}$. The bias current into the junction is $I_b(t) = I_b + i_n(t)$, the recombination current as $I(t) = I + i_{jn}(t)$, the diode junction voltage as $V(t) = V + v_{jn}(t)$ .The circuit only shows the small signal or noise quantities. The shot noise and thermal noise voltage have the relations $v_{sn}^2 = 2qIR_d^2$ and $v_{th}^2 = 4kTR_S$. Applying nodal analysis to

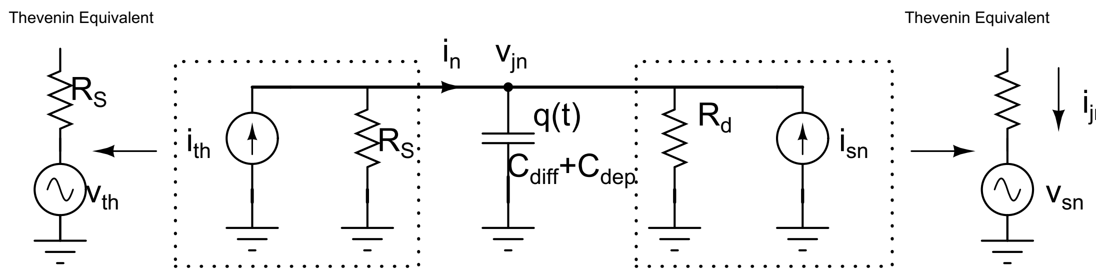

Figure 2.5: Noise equivalent circuit of light emitting diode for long base structures valid under low to moderate injection conditions. The circuit shows the ohmic resistance R_S, dynamic resistance R_d,total capacitance C,stored charge fluctuation q(t),junction voltage fluctuation $v_{jn}(t)$,recombination current i_{jn} junction current i_n and the noise generators v_{sn} and v_{th}.

Fig. (2.5) , the current noise flowing through R_d can be written as

$$i_{jn}(t) = -i(t) + i_n(t) \tag{2.70}$$

where $i(t)$ is the current flowing through the diffusion capacitance and $i_n(t)$ is the current flowing into the junction. Using Eq. (2.70), we can write an expression for the junction voltage fluctuation as

$$C\frac{dv_{jn}}{dt} = \frac{(v_{sn} - v_{jn})}{R_d} + \frac{(v_{th} - v_{jn})}{R_s} \tag{2.71}$$

where $i(t) = C\frac{dv_{jn}}{dt}$. The above equation represents a simple low pass filter. Note that the Thevenin equivalent form for the current sources have been used in obtaining Eq. (2.71) A diode biased with a constant current source has very high source impedance ie. $R_s \gg R_d$, which approximates Eq. (2.71) as $\frac{dv_{jn}}{dt} = \frac{(v_{sn}-v_{jn})}{R_dC}$ .The corresponding voltage transfer function can be written as $\frac{V_{jn}(i\omega)}{V_{sn}(j\omega)} = \frac{1}{1+sR_dC}$. At low frequencies the $V_{jn}(\omega) \approx V_{sn}(\omega)$, which implies junction voltage fluctuations v_{jn} follows the shot noise fluctuations v_{sn}. Beyond the corner frequency $f_c = \frac{1}{R_dC}$, the junction voltage noise decreases by 6dB/octave and is strongly suppressed for frequencies $f \gg f_c$ where it no longer follows the shot noise fluctuations. So at time scale $t \gg R_dC$, a negative feedback mechanism works to suppress the noise below the shot noise level. In state equation terms, the shot noise voltage fluctuation is low pass filtered and fed back to the junction ie. at low frequencies the junction voltage noise follows the shot noise so that the recombination current $i_{jn} = \frac{v_{sn}-v_{jn}}{R_d}$ is reduced. The stored charge fluctuations in the active region $q(t)$ determines the junction voltage fluctuations through $v(t) = \frac{q(t)}{C}$ which implies that any change or suppression of fluctuations in

$v(t)$ in turn affects $q(t)$ and the net recombination process. As the capacitive impedance becomes large at low frequencies, there will be no current flow through this branch. The recombination current through the stored charge in the diffusion capacitance $i = C\frac{dv}{dt}$ should be nearly zero since the junction voltage follows the shot noise fluctuations but,we should not forget the thermal noise in the external circuit which flows into the internal junction deciding the recombination current as $\langle i^2 \rangle = \langle i_n^2 \rangle = 4kT/R$. For large R the noise is sufficiently suppressed. At high frequencies the opposite is true, where the capacitive impedance shorts the shot noise generator and this internal junction noise cannot be extracted into the external circuit to measure. The feedback is essentially broken for frequencies greater than the cutoff of the low pass filter ie. $f_c > \frac{1}{R_d C}$ and the high frequency junction voltage fluctuations v_{jn} and charge recombination noise $q(t)$ are both negligible and the recombination current $i(t) = \frac{v_{sn}-(v_{jn}\approx 0)}{R_d}$ reverts to the full shot noise level. Similar conditions exist for the constant voltage case $R_S \ll R_d$ except in this case the corner frequency is $f_c = \frac{1}{R_s C}$. However we find that $V_{jn}(\omega) \approx V_{th}(\omega)$ which implies the junction noise is the thermal noise of the external resistor and is quite small for all frequencies.

In general,we can establish the noise at low frequencies by removing the diffusion capacitance from the circuit model of Fig. (2.5). Hence,the external circuit current noise and the recombination current noise flowing internally in the junction must be equal to one another. The Fanofactor F can be used to define the degree of suppression/enhancement of the recombination noise with respect to the shot noise spectral density and for the circuit model without the capacitance, we have

$$F_p = \frac{< v_{th}^2 > + < v_{sn}^2 >}{(R_s + R_d)^2 * 2eI} \tag{2.72}$$

For the case of high impedance and noting that the shot noise level is much larger than the thermal noise which can be seen by $2qI = \frac{2kT}{r_d} \gg \frac{4kT}{R_s}$,the Fanofactor is

$$F_p = \frac{4kT/R_s}{2qI} = (\frac{R_d}{R_s})^2 \ll 1 \tag{2.73}$$

The Fanofactors under constant voltage condition where $R_d \gg R_s$ is $F_p = \frac{2qIR_d^2}{r_d^2 * 2qI} = 1$ which agrees with recombination current being shot noise limited. Note that the Fanofactors do not express the noise measured at the photodetector but indicate the noise due to carrier recombination alone. The nature of biasing(constant current or voltage) does not provide us with any new results that may differ with the conventional electrical noise quantities obtained through nodal analysis of equivalent circuits or through numerical means(eg spice simulations), but the nature of bias does affect the photon flux from pn junction diodes.

2.4.1 Photonic Noise

We make the assumption $C_{diff} \gg C_{dep}$ and assume that the overall capacitance $C = C_{diff}$. This is a valid assumption for the moderate injection levels. The reason for not including C_{dep} is that the regulation mechanism that uses the depletion region follows a space charge effect. The equivalent circuit model predicts the same results as the experiments by including C_{dep} as a "fudge factor" into the circuit, but it does not provide the proper physical pictures to explain the mechanism. Then in state variable terms, we can express the junction voltage to the charge stored in C_{diff} as $v(t) = \frac{q(t)}{C}$. Note that this is an important relation since it states that one can measure the photon number of a quantum state without disturbing it. In fact the junction voltage monitors the photon number and feeds it back to reduce the fluctuation under high impedance bias conditions. Such non-destructive measurements are known as quantum nondemolition measurements and have been experimentally verified for semiconductor lasers[4]. Here $R_d C_{diff} = \tau$ is the minority carrier lifetime in the active region of the semiconductor. Rewriting Eq. (2.71) by rearranging terms we obtain

$$\frac{dv_{jn}}{dt} = v_{jn}\left(\frac{1}{R_S C} + \frac{1}{R_d C}\right) + \frac{v_{sn}}{R_d C} + \frac{v_{th}}{R_S C} \tag{2.74}$$

$$\frac{dq}{dt} = -q\left(\frac{1}{R_d} + \frac{1}{R_S}\right) + f_n(t) \tag{2.75}$$

The above equation represents the charge carrier fluctuations in the recombination region and with comparison with Eq. (2.14) resembles a Langevin equation with two relaxation(dissipation) terms and the stochastic thermal equilibrium forcing(fluctuation) terms i_{sn} and i_{th} where

$$< f_n(t)^2 > = < f_{sn}^2 > + < f_{th}^2 > = 2qI + 4kT/R \tag{2.76}$$

We can convert this into a optical rate equation by making the change $q(t) = en(t)$ and grouping external current i_{in} and internal processes $n(t), f_{sn}(t)$ separately gives

$$\frac{dn}{dt} = \frac{i_n(t)}{e} - \frac{n(t)}{\tau} + \frac{f_{sn}(t)}{e} \tag{2.77}$$

The first term describes the fluctuating rate at which the carriers are injected from the external circuit through the depletion region into the active region. The second term describes the net recombination fluctuation events which by itself(by means of feedback) is the response to the pump noise $\frac{i_{in}(t)}{e}$ and the intrinsic stochastic charge recombination process represented by the Langevin term $< f_{sn}^2 >= \frac{2e^2N}{\tau}$. The second and third term completely describe the recombination noise of the active region. The same concepts of constant voltage and constant current are applicable here. In constant voltage case, the junction voltage is pinned which implies the stored electron population is fixed at N(t)=N ie. $\frac{dn}{dt} = n(t) = 0$. The charge carriers recombine randomly as a Poisson point process with mean lifetime τ and we observe the full shot noise in the photon flux. Also since $i_n(t) = f_{sn}(t)$, the shot noise can be observed in the external circuit.

In the constant current case, carrier population $N(t)$ is allowed to fluctuate. If the external junction current noise is suppressed ie. $i_n(t) = 0$, then $\frac{dn}{dt} = -\frac{n(t)}{\tau} + \frac{f_{sn}(t)}{e}$. The corresponding spectral density can be obtained as

$$S_i(\omega) = \frac{2eI\omega^2\tau^2}{1+\omega^2\tau^2} \tag{2.78}$$

This a high pass filter, where the noise at low frequencies is suppressed below the shot noise. From the above equation we note the bandwidth to be $B = \frac{1}{2\pi\tau}$ and is the same as the ac modulation bandwidth of the diode which is incorrect. In actuality we need to consider the depletion capacitance also which becomes more important at weak forward bias and the exact bandwidth is $B = \frac{1}{2\pi(R_dC_{dep}+R_dC_{diff})}$ and is the observed spectrum from experiments. From a small signal standpoint, this may seem obvious,but note that there must be a feedback mechanism in place when the depletion capacitance is included as was the case of the diffusion capacitance. The presence of the depletion capacitance is responsible for regulating the electron flow across the depletion region and is known as the macroscopic Coulomb blockade effect.

Spontaneous emission is an intrinsically Poisson process with mean rate $< \Phi >= \langle N \rangle / \tau$ which is seen when we assume that the junction voltage $V(t) = \langle V \rangle + v(t)$, the charge recombination $Q(t) = \langle Q \rangle + q(t)$ and the recombination number $N(t) = \langle N \rangle + n(t)$ are all held constant. With feedback each of these variables are modulated by the low pass filtering which leads to reduced current noise at frequencies within the feedback loop bandwidth according to Eq. (2.78). Note that there is no optical feedback involved as in the case of amplitude squeezed lasers. The time varying recombination(which is similar to the photon flux and will be shown on a more theoretical basis later on) is a stochastic process given by

$$\Phi(t) = \frac{N}{\tau} + f_{sn}(t)/e = \frac{\langle N \rangle}{\tau} + \frac{n}{\tau} + \frac{i_{sn}}{e} \tag{2.79}$$

The second equality shows three terms which we state from left to right: a)the net recombination rate characteristic of Poisson processes b)the feedback term determined by Eq. (2.77) and gives the response to the stochastic fluctuations in the third term c)the shot noise fluctuations. At constant voltage there is no fluctuation in the electron population $n(t)$ which leads to recombination noise(ie. without the average $\langle N \rangle$) being shot noise limited. As $R_S \gg R_d$,the carrier number $n(t)$ follows the shot noise fluctuations and we can set $\frac{n}{\tau} + \frac{i_{sn}}{e} = 0$. This implies that the flux of photons is suppressed. But we should remember that we are not controlling the spontaneous emission process which is itself a one variable birth-death rate process[23] producing Poisson statistics. What we are affecting is the carrier number and therefore the recombined photon emissions(that follow the carrier statistics) which appear noiseless on time scales much larger than τ. Alternatively, one may consider the following scenario, where the electron crosses the barrier instantly, whereas it takes a longer time for the photons to recombine. In this case, the birth-death rate model is valid. But typically LEDs have heavily doped active regions, where the recombination lifetime is negligible and it is the pump lifetimes that dominate the problem.

2.4.2 Noise Spectral Densities

In section 3, we have seen that the external noise current spectral density S_{I_T} is due to the two processes of thermal diffusive transit of an electron due to collision with the lattice and the generation-recombination of a minority carrier.This is infact the origin of shot noise in constant voltage driven pn junction diodes.Each random event due to these processes sets up a perturbation in the minority carrier region, which in turn leads to relaxation current flows in order to restore the steady state carrier distribution. The departure of minority carrier densities at the depletion layer edge is a side effect of these events and leads to the full shot noise level. For example, a sudden decrease in minority electrons n_c in the p-active region of a p+N heterojunction leads to an reduced recombination rate. The junction voltage being a measure of the active number, also decreases instantly. Since the voltage is to be held constant under constant voltage conditions, it is followed by excess thermionic emission events from the wideband N layer to the p layer thus decreasing the majority carrier electron density n_N in the N layer. The departure of the electron density n_N from the steady state leads to a replenishment of carriers by the majority carrier current flow in the N region and subsequent flows in the external circuit. Note that even though the junction voltage changes from the steady state value,it is immediately relaxed by the external circuit within the R_SC time constant which is much smaller than the internal generation-recombination time constant R_dC. So we can see the junction voltage as being unchanging or constant. A temporal increase of n_c may cause increased backward thermionic emission events causing n_N to increase, followed by a relaxation to steady state by a majority carrier flow in the opposite direction. Following each recombination event which looses an electron hole pair, the external circuit injects carriers into the pn junction in order to restore the steady state carrier density n_c and the junction voltage V_j. The external current noise is thus made of a series of relaxation pulses with the area under each pulse equal to an electron. In this way, the carrier number and voltage recovers to the steady state level before being the next generation/recombination event. In this way, each event is independent of the other or does not have memory of the other event. If the sink for recombination events is through radiative means, a Poisson point Process is seen in the photon flux. The external circuit pulses are also shot noise limited, but it must be pointed out that, the external circuit current is not the origin of the shot noise in the photon flux but is instead the relaxation pulses produced in response to the Poissonian recombination events which is internally generated in the bulk regions of the diode.

$$\begin{array}{ccc} \downarrow & \longleftarrow\!\longleftarrow\!\longleftarrow\!\longleftarrow \; Feedback\,2 \; \longleftarrow\!\longleftarrow\!\longleftarrow\!\longleftarrow\!\longleftarrow & \uparrow \\ n_c(\downarrow) & \Rightarrow V_j(\downarrow) \Rightarrow I_{ext}(\uparrow) \Rightarrow n_N(\uparrow) \Rightarrow V_j(\uparrow) = V_{j0} \Rightarrow n_c(\uparrow) & \\ & \Rightarrow V_j(\uparrow) \Rightarrow I_{ext}(\downarrow) \Rightarrow n_N(\downarrow) \Rightarrow V_j(\downarrow) \Rightarrow & V_{j0} \end{array}$$

We illustrate above the constant voltage operations for two cycles where the first cycle describes the response to the reduction in carrier number and the second cycle attempts to increase the carrier number above the average rate. It may seem that a feedback mechanism is in place but it essentially maintains n_c and V_j at the steady state values of n_{c0} and V_{j0}. It is possible that the feedback mechanism may produce squeezing at frequencies $f < \frac{1}{R_S C}$ which we have already noted earlier. Since the system had negligible source resistance, the circuit relaxation mechanisms were carried out with negligible time delay which is why we could include the external circuit current response in the feedback loop. Each random event whether it be generation recombination or thermal diffusive was not stored in the system memory and occurred independently of one another and this is the origin of shot noise. Note that the system has memory through the storage of carrier concentrations in the diffusion capacitance. If the carriers recombine instantly ie. if the diffusion capacitance is removed from the feedback loop by negligible lifetimes for carriers, the memory effect will cease to exist. In the constant voltage case, the near zero external series forms the sink for shot noise process, bypassing the capacitor which is why we see the shot noise in the external circuit.

In the constant current case, where the source resistance satisfies the condition $R_s \gg 2R_d$, the electron density n_N in the N layer which is modulated by the forward and backward thermionic emission events is not removed immediately by the external circuit current. When compared to the constant voltage case, the external circuit current is relatively fixed but the junction voltage is allowed to fluctuate freely. When the carrier number for electrons in the p region exceeds the average for some reason, the recombination rate also increases. This causes an increased junction voltage and an increase in the thermionic emission events crossing the barrier. The increase of thermionic emission events causes a decrease in the junction voltage as well as a decrease in the the electron density n_N. Since the decrease in both n_N and V_j are not instantly eliminated by the external circuit relaxation currents, the forward thermionic emission rate decreases followed by a reduction in the number of carriers in the active region and the recombination rate. In other words, the deviation of the carrier number from steady state due to the noise events is not eliminated by the external circuit but is done so by the modification of the internal recombination rates which establishes a self-feedback stabilization mechanism regulating the carrier recombinations in the long time scale. Note that each generation-recombination event initiates an external relaxation pulse. But since the time constant for the external relaxation $R_S C$ is much larger than the internal carrier generation-recombination time constant $R_d C$, the external relaxation pulses are smoothed out. In other words, before a external pulse is allowed to die out, another one is initiated and the sum series of these events appears to have an almost dc like quality. Note that both the carrier number and junction voltage fluctuate at the shot noise level whereas it was kept constant in the constant voltage case. The carrier recombination and thus the photon flux is regulated producing a sub-Poisson process. Once again, the external electric current carries the same statistics of the internally regulated photon process and is not the origin of the sub-shot photon flux. The regulated external current noise can also be explained from the equivalent circuit of Fig.(2.5), where we noted that under constant current operation, the internal shot noise is not extracted into the external circuit and the thermal noise current that flows is highly suppressed and very nearly zero. The two modes of operation of the pn junction diode are shown in Fig.(2.6)

The so called 'leaky reservoir' model which employs the equivalent circuit of Fig.(2.5), provided a simple working of subshot noise from a pn junction diode with series resistance R_S connected to the voltage V. We shall now obtain more precise quantities for the spectral densities by writing the the nodal equations using the Norton equivalent forms for the noise sources. Here i_{th} is the thermal current noise associated with R_S and i_{sn} is the shot noise current associated with R_d. The KCL for this noise equivalent circuit is then

$$i_{th} + i_{sn} = \frac{dv_{jn}}{dt} + \frac{v_{jn}}{CR_S} + \frac{v_{jn}}{CR_d} \tag{2.80}$$

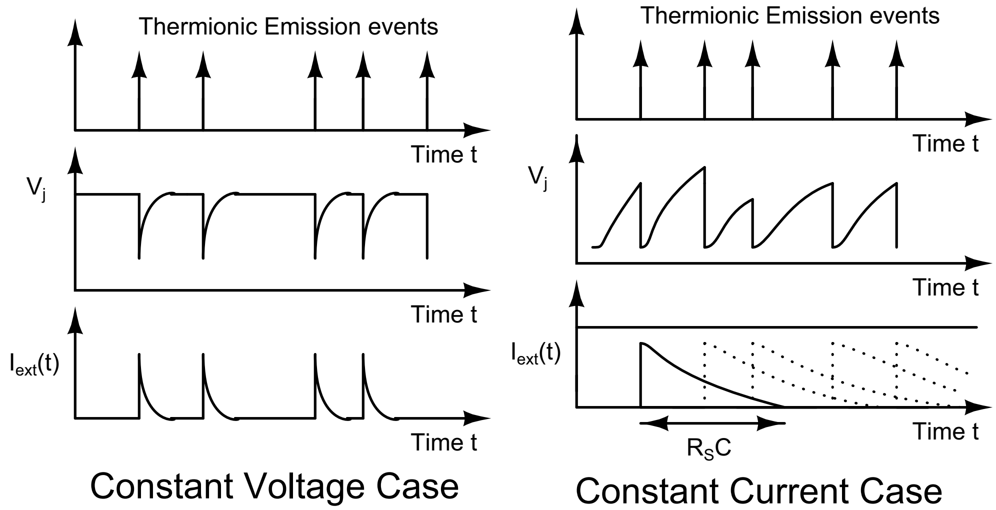

Figure 2.6: The (a)Constant voltage operation and (b)Constant current operation a pn junction diode

where C is the total capacitance and is the sum of the diffusion(C_{diff}) and depletion(C_{dep}) capacitance. The above equation is a Langevin equation with the second term on the right indicating the dissipation of of junction voltage v_{jn} due to external circuit current and the first term on the left as the corresponding external circuit fluctuation. The third term on the right of Eq. (2.80) represents the dissipation of v_{jn} due to carriers crossing the depletion region($C = C_{dep}$) and/or recombination of electrons($C = C_{diff}$) and the second term on the left represents the corresponding fluctuation of v_{jn} due to the thermionic emission/recombination process. For the case of $R_S \gg R_d$, the Langevin equation of Eq.(2.80) becomes

$$\frac{dv_{jn}}{dt} = -\gamma v_{jn} + F(t) \tag{2.81}$$

where $\gamma = \frac{1}{CR_d}$ is the damping constant and the Langevin noise term is $F(t) = i_{sn}$. This formulation is quite similar to Eq.(2.14) and the stochastic trajectories traced by the charge fluctuations(or the junction voltage fluctuations through $v_{jn} = q/C$), the noise source $F(t)$ and the recombination current i_{rec} are plotted in Fig(2.7). For the case of $\gamma = 1000$ in Fig.(2.7c), $F(t)$ gives the junction voltage a kick, but the effect of this force is damped very quickly to zero by the damping term due to the large value of the damping constant. In this case, v_{jn} essentially follows $F(t)$ and the recombination noise given by $i_{rec} = \frac{v_{jn}-v_{sn}}{R_d}$ is zero as indicated by the flat line. For the case of $\gamma = 1$ in Fig(2.7a), $F(t)$ fluctuates

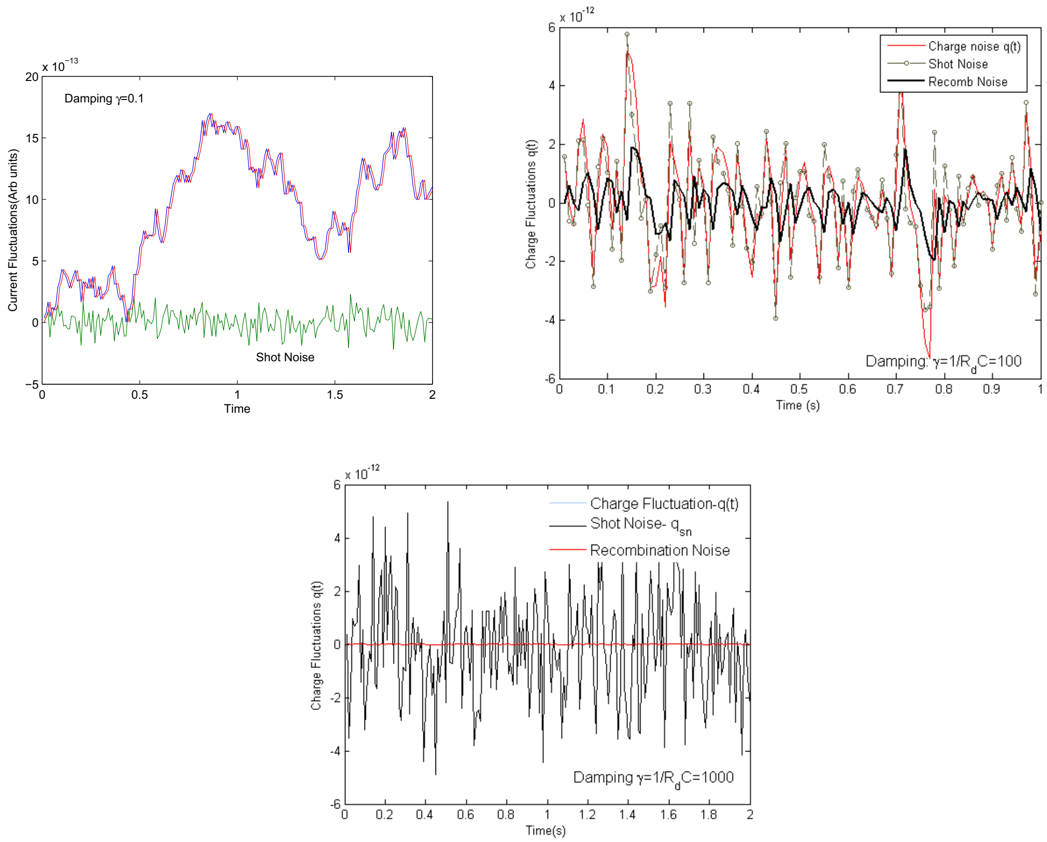

Figure 2.7: Langevin description of damping with the diffusion capacitance and differential resistance of a pn junction diode

v_{jn}, but v_{jn} does not recover immediately and the future $F(t)$ will kick a v_{jn} which has a memory associated with the past value. The case of $\gamma = 100$ lies in between these two cases. It should be mentioned that $\gamma = 1$ is unrealistic, since it implies $R_d \gg R_S$ which is not the condition we started with. In general, for $R_d \gg R_S$(or $R_S \gg R_d$), we can construct a Langevin equation with damping constant $\gamma = \frac{1}{R_S C}$(or $\gamma = \frac{1}{R_d C}$) and noise term $F = i_{th}$(or $F = i_{sn}$) and the junction voltage always follows the Langevin force $F(t)$ whether it be thermal noise or shot noise limited. A complete expression for the spectral densities(without approximations) can be obtained by Fourier transforming Eq.(2.80) and rewriting it to obtain the junction voltage fluctuations

$$V_{jn}(\omega) = \frac{[I_{th}(\omega) + I_{sn}(\omega)]R_d}{1 + \frac{R_d}{R_S} + i\omega C R_d} \tag{2.82}$$

The spectral density is obtained by calculating $\langle V_n^*(\omega)V_n(\omega)\rangle$and is

$$S_{V_{jn}} = \frac{\frac{4kT}{R_S}R_d^2 + 2qIR_d^2}{(1+\frac{R_d}{R_S})^2 + (\omega CR_d)^2} \tag{2.83}$$

In the case of constant voltage which is $R_d \gg R_S$, we see that at low frequencies, the junction voltage spectral density is thermal in nature

$$S_{V_{jn}}(\omega) = \frac{4kTR_S + 2qIR_s^2}{1+(\omega CR_S)^2} \approx \frac{4kTR_S}{1+(\omega CR_S)^2} \tag{2.84}$$

As we remove the series resistance $R_S \to 0$, $S_{V_n}(\omega) \to 0$.In the case of constant current operation, the junction spectral density is at the shot noise level. At very high frequencies, both the constant current and voltage cases, show the same noiseless spectral densities. The external junction current fluctuations are

$$i_n = i_{th} - \frac{v_{jn}}{R_S} \tag{2.85}$$

Fourier transforming the above equations and substituting for $V_{jn}(\omega)$ we obtain

$$I_n(\omega) = I_{th}(\omega) - \frac{V_{jn}(\omega)}{R_s} = \frac{I_{th}(\omega)(i\omega CR_s + \frac{R_s}{R_d}) - I_{sn}(\omega)}{1+\frac{R_s}{R_d} + i\omega CR_s} \tag{2.86}$$

At low frequencies, Eq.(2.86) shows that $I_n \to -I$ which states that the current in the external circuit is equal and opposite to the internal current noise generator. The internal current source I represents the minority carrier noise current from the region between $x=0$ and $x=W$ in the p region(as seen in Section 2), whereas the external current generator I_n represents the majority carrier flow through the metal contacts to restore the charge to equilibrium in this region. The spectral density for current fluctuations using Eq.(2.86) is expressed as

$$S_{I_n}(\omega) = \langle I_n^*(\omega)I_n(\omega)\rangle = \frac{2qI_{sn} + [(\frac{R_S}{R_d})^2 + (\omega R_s C)^2 \frac{4kT}{R_S}]}{1+(\omega CR_s)^2} \tag{2.87}$$

At constant current operation,we have the external current density is at thermal noise limit given by $S_{I_n} = \frac{4kT}{R_S}$ almost independent of frequency. At constant voltage operation, the current spectral density is at the shot noise level at low frequencies, and moves towards the thermal level at higher frequencies.

2.4.3 Macroscopic Coulomb Blockade

In section 3.2, we noted that the regulated emission of photons was due to the modification of recombination rates(by negative feedback) of the charges stored in the diffusion capacitance. But in section 3.1, we noted that the bandwidth for squeezing depended on the sum of the depletion and diffusion capacitance. The thermionic emission diode produces a subshot noise current by modification of the space charge region, which may indicate that such a similar condition exists for the pn junction diode through its depletion capacitance. The terminal current of a strongly biased pn diode is the difference between a forward and backward injection current(which will be detailed in section 4). These currents are individually quite large, but the difference current is the very small diffusion current used in diode analysis. Due to the large forward injection current, Buckingham introduced the forward differential resistance[16] $r_{fi} = \frac{kT}{eI_{fi}}$ in order to account for the voltage drop across the junction and this resistance represents the relaxation mechanism by which equilibrium is restored after a carrier crosses the depletion layer. This differential resistance is much smaller than the differential resistance of the junction R_d simply because because of the much larger I_{fi}. Since the crossing of carriers across the depletion layer is random, this leads to a Poissonian injection events with shot noise given by $4kTr_{fi}$ which is much smaller than than the total shot noise of the diode $2kTR_d$ produced by sum of the generation-recombination and diffusion noise in the bulk of the diode. In other words,the noise due to carriers crossing the depletion region is not the principal reason for the observed shot noise in the macroscopic diffusion limit. However Imamaglo and Yamamoto pointed out that at very low injection currents, the forward emission dominates and the injection of carriers across the junction does provide a shot noise contribution, not at the external terminal current, but in the emission of photons. Under high impedance conditions, the photon emission was subPoissonian, which could only be explained by means of pump noise suppression ie. the injection current induced junction voltage fluctuations worked to provide a negative feedback to regulate the carrier injection rate as in the vacuum diodes of Section 2.1. The central idea used was the Coulomb blockade, a term borrowed from mesoscopic junctions[29, 30], where a single electron crossing the junction prevents further electrons from crossing over, if the electron charging energy due to a single transit e^2/C_{dep} is much larger than the thermal energy kT . This regulates the electron injection process, but in the macroscopic junction case, the junction voltage after each injection drops by e/C_{dep}, the depletion layer charging energy is much smaller than kT and each microscopic event is unregulated and completely random. The macroscopic junction voltage only drops after the injection of N_i carriers to provide $\Delta V_j = \frac{N_i e}{C_{de[}}$. As a result, the forward current will on average decrease to a factor $\exp(-e\Delta V_j/kT) = \exp(-e^2 N_i/kTC_{dep})$ of its initial value. When $e^2 N_i/kTC_{dep} \approx 1$, the collective regulation effect will be active for carrier number $N_i = \frac{kTC_{dep}}{e^2}$. Since the mean injection rate is I/e, this establishes a time scale $\tau_{te} I/e = N_i$ on which the junction voltage provides negative feedback to regulate the carrier injection rate and

$$\tau_{te} = \frac{kTC_{dep}}{e^2}\tau = \frac{kTC_{dep}}{eI} = R_d C_{dep} \tag{2.88}$$

When N_i electrons are injected, the charging energy is $N_i e^2/2C_{dep}$ is larger than kT (the condition is now similar to the mesoscopic Coulomb blockade case) which leads to reduction of junction voltage and raises the barrier against further injection. It results in antibunched electrons on a time scale associated with τ_{te} which is known as the thermionic emission time . As the injection current is lowered, τ_{te} increases, and may exceed the recombination lifetime in which case there is negligible charge storage. Each injection event leads to an instantaneous recombination, and the statistics of pump determines the subshot nature of the photon flux. For measurement times smaller than τ_{te}, the negative feedback mechanism is broken and we don't observe subshot photon features, which is why the bandwidth of suppression is upper limited at $B = \frac{1}{2\pi\tau_{te}}$. Combining the two effects of thermionic emission regulation and spontaneous emission regulation treated in Section 4.2, the total effective squeezing bandwidth $B = \frac{1}{2\pi(\tau_{te}+\tau_r)}$

2.5 Pump Current Mechanisms

From our discussion of depletion capacitance, we note that the junction physics plays an important role in shot noise suppression and we are inclined to consider two types of junctions ie. p^+N heterojunction and a p^+N double heterojunction based upon experiments carried out in the following chapter. Each of these are popular examples of light emitting diodes. The p^+ region is the active region where recombination takes place. The population inversion is the total excess electron carrier density compared to the equilibrium value in the active region. The electron reservoir serves as the pump which injects electrons across the depletion region into the active region. In the case of the heterojunction barriers, the heavily doped p regions have a smaller band gap(GaAs) than the n-type semiconductor(AlGaAs). The current injection is primarily due to electrons because of the bandgap discontinuity of ΔE which reduces hole injection. In the case of pn homojunctions,most of the junction current is due to holes,we follow the electron injection process, effective mass.

2.5.1 From Thermionic emission to Diffusion

The important current conduction mechanisms are thermionic emission and diffusion. The thermionic emission current density is given by the concentration of all electrons with energy sufficient to cross the barrier from the N side to p side. Bethe derived this theory with two important assumptions 1.The barrier height is much larger than kT and 2.even though electrons are lost to the neighboring material at a very high rate, the electron distribution still says Fermi or Maxwell like. The current density from AlGaAs to GaAs is given as[10, 31]

$$J_{N\to p} = (\frac{m*}{h})^3 \frac{e}{4\pi^3} \int_{v_x,v_y} dv_x dv_y \int_{v_z>v_{z0}} dv_z v_z f(v) \tag{2.89}$$

where $f(E) = exp(\frac{E_F-E_c}{kT})exp(-\frac{E-E_c}{kT})$ is the Boltzmann approximated Fermi-Dirac distribution. If we assume that all the electrons above the conduction band have kinetic energy then $E - E_c = \frac{1}{2}m(v_x^2 + v_y^2 + v_z^2)$. Then $f(v) = exp(\frac{E_{Fn}-E_c}{kT})exp(-\frac{m(v_x^2+v_y^2+v_z^2)}{2kT})$. Also we assume that the minimum energy required by an electron to surmount the barrier is $\frac{1}{2}m * v_{z0}^2 = qV'_{Jn} \approx q(V_{bi} - V_a)$, where V_{Jn} is the amount of voltage dropped across the N region. We approximate V_{Jn} to $V_{bi} - V_a$ since the p region is more heavily doped and most of the voltage drops across the N region. The steady state forward injection of electrons by thermionic emission from the widebandgap N region to the narrow gap p region(ie. $I_{fi0} = I_{N\to p}$) can be expressed as

$$I_{fi0} = \frac{ek^2T^2m^*}{2\pi h^3} exp(\frac{E_{Fn} - E_c - qV_{bi} + qV_a}{kT}) \tag{2.90}$$

Using the relations for the conduction band density of states $N_c = 2(\frac{2\pi m^* kT}{h^2})^{3/2}$ and the Richardson thermal velocity $v_{Rth} = \sqrt{\frac{kT}{m^* 2\pi}}$ we can simplify the above relation to

$$I_{fi0} = ev_{th} N_c exp(\frac{E_F - E_c - qV_{bi}}{kT}) exp(qV_a/kT) \tag{2.91}$$

where A^* is the Richardson constant and V_{bi} is the built in voltage given by From Eq. (2.91) and using the Boltzmann relation for the electron concentration at the interface ie. $n(x=0) = N_C exp(\frac{E_C(0) - E_{Fn}}{kT})$ where $E_C(0) - E_{Fn} = q(V_{bi} - V_a) + E_c(\infty) - E_{Fn}$ we obtain the much simpler relation

$$I_{fi0} = \frac{1}{2} ev_{th} n(0) \tag{2.92}$$

This above simple form implies all the electrons at the in the interface spill into the p-side with a thermal velocity which contribute to current. The factor of 1/2 accounts from the difference between the thermal and Richardson's version of the thermal velocity. This can be traced to Eq. (2.89) where we consider only positive velocities or rather the positive part of the Maxwellian. This accounts for $n_{N0}/2$ particles traversing the +x direction. Then $N_C exp - (\frac{E_c(\infty) - E_F}{kT}) exp(-qV_{bi}/kT) = n_{N0} exp(-qV_{bi}/kT) = n_{p0}$.

$$I_{fi0} = \frac{1}{2} ev_{th} n_{p0} exp(qV_a/kT) \tag{2.93}$$

At the edge of the depletion region at x=0(note that $x_{p0} \approx 0$) the current density is $n(0)$. Since these electrons are distributed in a Maxwellian velocity distribution half of them can return back to the N region.

$$I_{bi0} = \frac{1}{2} ev_{th} n(0) \tag{2.94}$$

The difference between the two currents should be the net current into the p region. If we assume the typical result $n_p(0) = n_{p0} exp(qV_a/kT)$ we would get a current of zero. This implies that the value of $n(0)$ should be different. Once the electrons are in the p-type region they diffuse towards the contacts and are

$$J_{diff} = \frac{qD_n}{L_n}(n_p(0) - n_{p0}) \tag{2.95}$$

We can set $J = J_{N \to p} - J_{p \to N} = J_{diff}$ from which we find the value of $n_p(0)$ to be

$$n_p(0) = \frac{1}{1 + \frac{l_f}{L_n}} n_{p0}(exp(qV_a/kT) + \frac{l_f}{L_n}) \tag{2.96}$$

$n_p(0) - n_{p0} = \frac{1}{1+\frac{v_{diff}}{v_{Rth}}} n_{p0}(exp(qV_a/kT) - 1)$. The current can be written as

$$I_0 = qv_{diff} \frac{1}{1 + \frac{v_{diff}}{v_{Rth}}} n_{p0}(exp(qV_a/kT) - 1) \tag{2.97}$$

For $v_{Rth} \gg v_{Diff}$, the electron current is by diffusion ie. electrons diffuse much slowly in the neutral p regions compared to the rate of injection by thermionic emission and hence diffusion is the rate limiting step. In the case $v_{Rth} \ll v_{Diff}$,the carriers diffuse or recombine immediately and are able to follow the thermionic emission events. The current in this case is by thermionic emission. This is seen in metal semiconductor structures due to short dielectric relaxation time or in our case if the width of the base is made small compared to the mean free path ie $W \approx l_f$ or the diode base is short by having a negligible recombination time($\tau \rightarrow 0$). For pn heterojunctions the same arguments hold where the diffusion currents can be obtained by noticing that

$$n_{p0} = Xn_{n0}exp(-qV_{bi}/kT) \tag{2.98}$$

where X is the transmission coefficient of the electrons crossing the heterojunction interface. Using this, the same steady state carrier concentration of a pn junction is applicable ie. $n_p(x) = n_{p0} + (n_p - n_{p0})e^{-x/L_n}$ and the diffusion current is obtained from Eq. (2.95). The Langevin analysis which is to be discussed treats particularly the pn heterojunction from the thermionic emission to diffusion regime. The regime in between the diffusion and thermionic emission limits, are possible because of carrier hot electron effects and different barrier structures. In order to account for them, the forward/backward pump model was developed which relates the pump currents in between these two limits, to experimentally observed quantities in typical photodetection experiments.

2.5.2 The forward/backward pump model

Fig.(2.8) describes the variables used in the description of the foward/backward pump model for a double heterojunction diode. For light emitting diodes, the total current which is the difference between the backward and forward thermionic emission currents is equivalent to

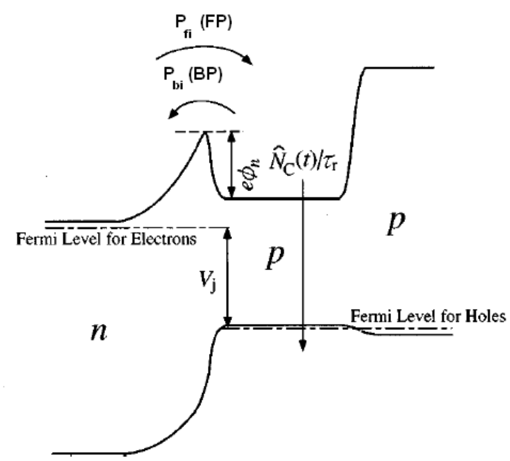

Figure 2.8: The band-diagram of a typical double heterojunction LED under forward bias condition. Here V_j is the applied bias, P_{fi} and P_{bi} denote the forward and backward pump rates and n_c/τ_r denotes carrier recombination in the active region.

the total recombination in the active region. The net current is

$$I_0 = I_{fi0} - I_{bi0} = e(P_{fi0} - P_{bi0}) = e\left(\frac{n_{c0}}{\tau_r} + \frac{n_{c0}}{\tau_{nr}(n_{c0})}\right) \tag{2.99}$$

where $n_{c0} = \int n_p(x)dx$ is the total minority carrier density in the entire active p region, τ_r and τ_{nr} are the radiative and non-radiative lifetimes, P_{fi0}, P_{bi0} correspond to the forward and backward pump rates instead of their currents. The inclusion of non-radiative processes affects the photodetection process the rough the efficiencies. The DC efficiency can be defined as the ratio of current at photodetector I_{PD} to the current flowing in the LED and is

$$\eta_0 = \frac{I_{PD}}{I_O} = \frac{N_0}{P_0} = \frac{\eta_c(1/\tau_r)}{1/\tau_r + 1/\tau_{nr}} \tag{2.100}$$

Here η_c is the finite collection efficiency which represents the photons lost in the photodetection process through beam splitter losses and coupling. The differential efficiency can be defined as the differential ratio of the radiative recombination to the total recombination rate and may take on constant values.In other words,we can use the dc values itself to calculate these quantities, since any change in the frequency population Δn_c around the dc value is followed by immediate reordering of the Fermi-Dirac distributions due to the short time scale over which the reservoir of phonons interact with the electrons and holes. In fact,Δn_c follows quasi-steady state the steady state values and we can instead treat it as small perturbation of the dc steady steady state as Δn_{c0} without requiring a frequency dependent solution. This approximation may be valid to about 100Mhz and is written as

$$\eta_d = \frac{dI_{PD}}{dI_0} = \frac{dN}{dP} = \frac{\eta_c \frac{d}{dn_c}(\frac{n_c}{\tau_r})|_{n_c=n_{c0}}}{\frac{d}{dn_c}(n_c/\tau_r(n_c) + n_c/\tau_{nr}(n_c))|_{n_c=n_{c0}}} \tag{2.101}$$

Introducing efficiencies, allows a simple way of including experimentally measurable quantities into the definitions of the backward to forward pump rate ratio α_0 as

$$\alpha_0 = \frac{I_{bi0}}{I_{fi0}} = \frac{P_{bi0}}{P_{fi0}} \tag{2.102}$$

The current can then be written in terms of only the FP rate from Eq. (2.99) $I_0 = (1-\alpha_0)I_{fi0}$ which leads to

$$I_{fi0} = \frac{1}{1-\alpha_0}\frac{en_{c0}}{\tau_r} \quad , \quad I_{bi0} = \frac{\alpha_0}{1-\alpha_0}\frac{en_{c0}}{\tau_r} \tag{2.103}$$

We can also define the differential ratio of BP to FP rates, which can be defined in the dc limit as

$$\alpha_d = \frac{dI_{bi0}}{dI_{fi0}} = \frac{dP_{bi0}}{dP_{fi0}} \tag{2.104}$$

The defined values of α_0 and α_d are valid irrespective of the presence of the nonradiative processes. Electrons injected into the p region with energies in excess of the barrier height are assumed to have fast energy relaxation times to quickly establish the Fermi-Dirac distribution of elevated temperature T_e. Such short relaxation times justifies the independence of the differential ratio α_d with respect to frequency over the range of device operation. The small signal change in forward or backward currents can be expressed on the basis of the differential ratios as

$$\Delta I_{fi0} = \frac{1}{1-\alpha_d}\frac{e\Delta n_{c0}}{\tau_r} \quad , \quad \Delta I_{bi0} = \frac{\alpha_d}{1-\alpha_d}\frac{e\Delta n_{c0}}{\tau_r} \tag{2.105}$$

The small signal changes are equivalent to fluctuations around the steady state and can be applied equally to ac and noise problems. Due to the continuity of particle flow, the net fluctuations in current can be obtained from Eq. (2.105) as

$$\Delta I_0 = \Delta I_{fi0} - \Delta I_{bi0} = \frac{d}{dn_{c0}}(\frac{n_{c0}}{\tau_r})\Delta n_{c0} = \frac{e\Delta n_{c0}}{\tau_r} \tag{2.106}$$

In obtaining the above equation, we have ignored non-radiative process and hence the expression may be considered ideal. Including τ_{nr} we can obtain the FP current from Eqs. (2.99) and (2.103) as

$$I_{fi0} = \frac{1}{1-\alpha_0}(\frac{n_{c0}}{\tau_r}) + \frac{n_{c0}}{\tau_{nr}(n_{c0})} \tag{2.107}$$

An important assumption we make in arriving at Eq. (2.107) is that the dc and small signal values of the BP processes- I_{bi0} and ΔI_{bi0} are proportional to the average and the fluctuation of the electron population in the active regions and are considered independent of the junction voltage fluctuations. Also the BP rates are valid regardless of the existence of the non-radiative process which is why only I_{fi0} given by Eq. (2.107) is a function of $\tau_{nr}(n_{c0})$ whereas I_{bi0} is given by Eq. (2.103). With the presence of the non-radiative lifetimes, we can define an effective dc BP to FP rate from Eqs. (2.103) and (2.107) as

$$\alpha_{0,eff} = \frac{I_{bi0}}{I_{fi0}} = \frac{\alpha_0}{1+(1-\alpha_0)\frac{\tau_r}{\tau_{nr}}} = \frac{\alpha_0}{1+(1-\alpha_0)(\frac{\eta_c}{\eta_0}-1)} \tag{2.108}$$

The net change in fluctuation in current including the non-radiative processes are

$$\Delta I_0 = \Delta I_{fi0} - \Delta I_{bi0} = \frac{d}{dn_{c0}}(\frac{n_{c0}}{\tau_r} + \frac{n_{c0}}{\tau_{nr}(n_{c0})})\Delta n_{c0} = \frac{\eta_c}{\eta_d}\frac{\Delta n_{c0}}{\tau_r} \tag{2.109}$$

The forward current fluctuations are then expressed as

$$\Delta I_{fi0} = \frac{\alpha_d}{1-\alpha_d}\frac{\Delta n_{c0}}{\tau_r} + \frac{\eta_c}{\eta_d}\frac{\Delta n_{c0}}{\tau_r} \tag{2.110}$$

We can also define an effective differential BP to FP rate ratio at the dc limit using the non-radiative non-ideality which leads to

$$\alpha_{d,eff} = \frac{dP_{bi0}}{dP_{fi0}} = \frac{\alpha_d}{1+(1-\alpha_d)(\frac{\eta_c}{\eta_d}-1)} \tag{2.111}$$

Substituting these results,we can obtain a semi-qualitative expression for the dc currents as

$$I_0 \quad = \quad I_s(\exp(\frac{eV_{j0}}{nkT})(1-\alpha_{0,eff}(V_{j0}))-1) \tag{2.112}$$

where $\alpha_{0,eff}$ can take values from 0 to 1. When $\alpha_{0,eff} = 1$, we obtain the diffusion case where the forward and backward currents are large and equal to each other and the difference current is the small diffusion current. When $\alpha_{0,eff} = 0$, we obtain the thermionic emission case, where the forward electron current is large and the reverse electron current is very small as a result of the large barrier or bandgap discontinuity which prevents the reverse electron flow. This implies that the diffusion current is one limit to the thermionic emission current flows. The more exact analytical value of $\alpha_{0,eff}$ can be proven by comparing Eq. (2.112) with Eq. (2.97). The effective differential efficiency of an LED is defined as

$$\begin{aligned} r_{dj,eff} &= (\frac{dI_0}{dV_j})^{-1} = \frac{kT}{eI_{fi0}}(\frac{1}{1-\alpha_{0,eff}-\frac{kT}{e}\frac{d}{dV_{j0}}\alpha_{0,eff}(V_{j0})}) \\ &= \frac{kT}{eI_0}\frac{1-\alpha_{0,eff}}{1-\alpha_{d,eff}} \end{aligned} \tag{2.113}$$

where we have used $I_{fi0} = \frac{1}{1-\alpha_{0meff}} I_0$ and defined $\alpha_{d,eff}$ as

$$\alpha_{d,eff} = \alpha_{0,eff}(V_{j0}) + \frac{nkT}{eI_0}\frac{d\alpha_{0,eff}(V_{j0})}{dV_{j0}} \tag{2.114}$$

where Eq. (2.114) has been shown to be equivalent to Eq.(2.111)[32]. We shall employ the BP rates in the Langevin model treated in the following section.

2.6 Langevin Analysis of shot noise suppression in LEDs

Typically most semiconductor models utilize a semiclassical rate equation to determine the time evolution of the total carrier density. For an LED where the gain is very small, we can write

$$\frac{dN}{dt} = \frac{J\eta}{ed} - BNP + \frac{n_0}{\tau_r} - \frac{\Delta n}{\tau_{nr}} \tag{2.115}$$

where the first term indicates the pumping process into the active region with current J and d is the thickness of the active region,$N = n_0 + \Delta n$ and $P = p_0 + \Delta p$ are the active region carrier concentration and $\Delta n = \Delta p$ are the nonequilibrium excess carrier density of electrons and holes generated by current.B is the bimolecular radiative recombination coefficient and τ_{nr} is the non-radiative lifetime. The second term indicates the radiative recombination, the third represents generation and the fourth represents the nonradiative channel. First the equation can be written phenomenologically with additional terms such as gain for laser oscillation added easily but it also represents the state equation for the total charge stored in the diffusion capacitance under high bias and can be obtained using the circuit of Fig.(2.5) . This recombination term may be simplified by the $BNP = Bn_0p_0 + B\Delta n(n_0 + p_0 + \Delta n) =$

$\frac{n_0}{\tau_r} + \frac{\Delta n}{\tau_r}$ where $\tau_r \approx \frac{1}{Bp_0}$.

$$\frac{d\Delta n}{dt} = \frac{J\eta}{ed} - \frac{(n_0 + \Delta n)}{\tau_r} + \frac{n_0}{\tau_r} - \frac{\Delta n}{\tau_{nr}} \tag{2.116}$$

The simple equation may in itself be sufficient to describe the subshot characteristics(as we did in the intuitive model) of photon flux provided we add the necessary Langevin forces.We also need to decompose the current into the forward and backward pump process across the semiconductor junction which in turn are effected by another semiclassical rate equation involving the time evolution of junction voltage fluctuations. Usage of such semiclassical equations are justified since there was no optical mechanisms responsible for generating phase coherent light as in semiconductor lasers. This led Kim et al[33] to obtain the optical noise spectra in the the macroscopic diffusion limit. The diode current in their analysis was split into a current fluctuated by the junction voltage fluctuations and another which is the Langevin or Markovian carrier injection process. The current flowing in the external circuit was the junction charging current plus the net diffusion current. The analysis is also applicable to the thermionic emission limit but the authors have made the assumption that the forward and backward carrier lifetimes are negligible which automatically implies the diffusion limit. The analysis was constrained to a long diode such that the difference between the forward and backward currents result in the net diffusion current seen in homojunctions.

The pump process depends on the nature of the device structure. For example, the diffusion model is applicable to homojunctions whereas in heterojunctions the thermionic emission model is applicable. Recently Kobayashi et al investigated the current dependence of squeezing bandwidth in a heterojunction LED and found that a low injection currents the thermionic emission model was valid and at high injection currents, the diffusion model was valid. In intermediate current regimes they found that could not be fit their experimental data with either theories, since there would be some amount of backward carrier injection causing a situation between the two models. By taking into account the ratio of the BP rate to the FP pump rate,they were able to account for the experimental results for squeezing bandwidth over the entire range of currents. Even though there is a barrier to prevent the backward flow of carriers from the active region, the BP process cannot be prevented since the injected electrons may not thermalize to the lower states because of band-tail states and hot carrier effects. Also in order to describe the pump process for a myriad of possible device structures, the phenomenological ratio of the BP to FP processes(α_0, α_d) was introduced in section 2. The case of $\alpha_d = \alpha_d = 1$ restores the diffusion limit and since the carriers move across the junction quickly compared to the other time constants in the system, we cannot make the distinction between recombination and forward injection since they are strongly coupled with one bandwidth given by $f_{3dB} = \frac{1}{2\pi(\tau_r+\tau_{te})}$ .In the case of $\alpha_0 = \alpha_d = 1$ where the back current is zero and the forward current in non-negligible we reach the thermionic emission limit where carrier injection and recombination are viewed as cascaded processes. Another important point is that from a circuit perspective, the external circuit current noise must be suppressed if the recombination noise is to be suppressed because any current variations would affect the carrier number and the recombination rate. ie the low frequency terminal current is related to the recombination in the absence of the capacitance as $I(t) = \frac{eN(t)}{\tau}$. When the external current noise is shot noise limited, it implies that the photon flux emitter is also shot noise limited. However we saw earlier that the sub-shot(or shot) external current noise is not the origin of the photon flux noise but the result of self-regulated(or lack of) photon emission process. Suppression of the external terminal current noise may be a necessary but not sufficient condition ,since the dynamics of the carrier injection into the active region as well as recombination may affect the degree of shot noise suppression. For example, even if the terminal current is highly suppressed, the junction voltage fluctuations which are shot noise at low frequencies, become zero and pin the voltage at higher frequencies leading to a shot noise photon flux. Another example is the generation of sub-Poisson states from pn junction driven under constant voltage source[] .In this case the sub-Poisson external circuit current cannot be assumed, and its the internal junction dynamics responsible, in particular the non-linear microscopic relation between FP and BP process that is responsible for squeezing.

Finally Fujisaki et al[14] studied the quantum noise of LEDs under low injection levels.They treated the case of many photon modes excited in the cavity and found disagreements with the simpler theories which claimed that $F_{ph} = 1 - \eta + \eta F_{dr}$. The reasoning was that the non-radiative processes and carrier number dependence on lifetimes could affect the efficiencies such that the quantum efficiency η_0 differs from the differential quantum efficiency η_d . In the experiment carried out by, it has been reported that $\eta_d > 2\eta_0$ under low current conditions and the simpler theories are infact valid only in the case of high injections where $\eta_0 = \eta_d$. The authors used the quantum mechanical Langevin equations(QLE) to obtain the semiconductor and optical QLEs at low injection conditions. They did this by extending the Chow,Koch and Sargent[34] analysis for the case where many photon modes are present inside the cavity of the LED. However they did not include the effects of pumping such as BP and FP processes seen in the semiclassical theories. Note that we don't distinguish between microscopic and semiclassical, since one deals with currents and the other with particles. A quantum mechanical theory is also microscopic in description but the equations of motion regarding the electron and photon number are strictly derived from Heisenberg's equation of motion. But for the QLE such as electron number, the pump does not have a formal derivation, and has to be included phenomenologically since we are using theα parameters.

In this section we closely follow the Chow,Koch and Sargent theory to derive an expression for the photon Fanofactor which includes the pump statistics, the efficiencies η_0 and η_d , the ratio of the BP to FP process α_0 and α_d as well as parameters related to multimodeness of the LEDs. The expression also agrees with the expressions given by semiclassical theories under large injection conditions from the thermionic emission to the diffusion limit. We investigate the squeezing dependence on bandwidth in these two limits as well squeezing under constant voltage conditions using the nonlinear BP process and the extension of cutoff frequency due to this process. The crosscorrelations between LED quantities are also obtained in these limits. The photon Fanofactors are essential as they allow us to verify the validity of the subshot noise experiments detailed in chapter 3. We shall now discuss the Langevin formalism, which starts with the definition of the total Hamiltonian which includes the contribution of the electron carriers(electrons and holes), the many-body interactions among particles(Coulomb scattering), the dipole polarization, the field modes inside the cavity, the reservoir of modes outside the cavity and the interaction between the reservoir and the cavity field modes.

$$H_{total} = H_{carriers} + H_{many-body} + H_{dipole} + H_{field} + H_{bath} + H_{field-bath} \tag{2.117}$$

The total Hamiltonian of Eq.(2.117) is derived in Appendix.A but the terms of interest are

$$H_{carriers} = \sum_k ((\frac{\hbar^2 k^2}{2m_e} + E_{g0})c_k^\dagger c_k + (\frac{\hbar^2 k^2}{2m_h} + \Delta E_{ch})d_{-k}^\dagger d_{-k}), H_{dipole} = \hbar \sum_{l,k} (g_{l,k}^0 a_l c_k^\dagger d_{-k}^\dagger + g_{l,k}^{\star 0} a_l^\dagger d_{-k} c_k) \tag{2.118}$$

$$H_{field} + H_{bath} + H_{field-bath} = \sum_l \hbar\Omega_l a_l a_l + \sum_j \hbar\omega_j b_j b_j + \hbar \sum_{l,j} (\mu_{lj} a_l^\dagger b_j + \mu_{lj}^* b_j^\dagger a_l) \tag{2.119}$$

The variables appearing in the Hamiltonian are as follows: a_l is the annihilation operator for mode l, Ω_l is the field oscillation frequency for mode l, c_k and d_{-k} are the annihilation operators for electrons and holes, E_{g0} is the bandgap, m_e and m_h are the electron and hole effective mass, $g_{l,k}^0$ represents the coupling constant between the dipole and mode of the field, b_j is the annihilation operator for the reservoir modes and μ_{lj} is the coupling constant describing the interaction between the modes of the bath and the field. The other Hamiltonian terms, such as many body Hamiltonian, lead to complicated expansions in the equations of motion such as four operator products whose effects can be explained by simple handwaving. The Heisenberg equations of motion for any operator O which is part of this entire system is

$$\frac{dO}{dt} = \frac{i}{\hbar}[H_{total}, O] \tag{2.120}$$

2.6.1 Semiconductor Bloch-Langevin Equations

The equation of motion for the dipole operator(which is also referred to as the spin-flip or raising or lowering operator-since it removes an excited state $|11\rangle$ which represents the presence of an electron-hole pair to the ground state $|00\rangle$) in the rotating frame $\sigma_k(t) = d_{-k}c_k \exp(i\Omega_l t)$ is [34]

$$\frac{d\sigma_k}{dt} = -i_k - \Omega_l)\sigma_k - i\sum_{l,k} g_{lk}[c_k d_{-k}, \sigma_k]a_l + [\frac{d\sigma_k}{dt} - \frac{d\sigma_k}{dt}|_{HF}] \tag{2.121}$$

where the renormalized transition energy is $h\omega_k$ which includes a density dependent contribution from the many-body Hamiltonian and whose details are found in Chapter 4 of Ref.[34]. The term in the bracket represents the effect of the Coulomb interaction which couples the two operator terms to four operator terms and $\frac{d\sigma_k}{dt}|_{HF}$ is the Hartree-Fock contribution which is essentially the first two terms of Eq.(2.121). The net effect of the terms within the square bracket is to to produce collision terms which result from the many body interactions ie. $\frac{d\sigma_k}{dt}|_{coll} = \frac{d\sigma_k}{dt} - \frac{d\sigma_k}{dt}|_{HF}$. The following commutator is useful in and represents in some sense the probability of filled valence and conduction band k state minus the probability of an empty valence and conduction band states.

$$[c_k d_{-k}, d_{-k} c_k] = n_{ek} + n_{hk} - 1 \tag{2.122}$$

Substituting Eq.(2.122) in Eq.(2.121), the equations of motion for dipole operator is

$$\frac{d\sigma_k}{dt} = -i_k - \Omega_l)\sigma_k + i\sum_l g_{lk}(n_{ek} + n_{hk} - 1)A_l + \frac{d\sigma_k}{dt}|_{coll} \tag{2.123}$$

Similarly we can write an equation of motion for the electron number operator, where we have added the pumping term A_{ek} and the formal collision term which arises from the many body Hamiltonian

$$\frac{dn_{ek}}{dt} = A_{ek} + i\sum_l (g^*_{lk} A_l \sigma_k + H.C) - \frac{n_{ek}}{\tau_{nr}} + \frac{dn_{ek}}{dt}|_{coll} \tag{2.124}$$

Note that the coupling constant g_{lk} is renormalized from g^0_{lk} defined in Eq.(2.118) as it includes the effect of the many body Hamiltonian. Eq.(2.123) and Eq.(2.124) are the semiconductor Bloch equations and they reduce to the case of an undamped inhomogeneously broadened two level Bloch equation(for a two level atom) when all the Coulomb potential contributions are dropped. In Eq.(2.124), τ_{nr} is the non-radiative decay constant due to capture by vacancies due to defects in the semiconductor and is an implicit function of the total carrier density. The simplest approximation of the collision contribution in the polarization equation of Eq.(2.123) describes the dipole dephasing which is $\frac{d\sigma_k}{dt} = -\gamma\sigma_k$ and the net contribution of the intraband scattering is to return the electron and hole distribution to equilibrium which leads to $\frac{dn_{ek}}{dt} = -\gamma(n_{ek} - f_{ek})$ where f_{ek} is the quasi-Fermi distribution satisfying the condition $\Sigma_k f_{ek} = \Sigma_k n_{ek} = n_c$ where n_c which is the total particle density is conserved. In fact, the intraband scattering part does not play a part in the equations of motion for the total carrier density as it vanishes as seen by summing Eq.(2.124) for all modes. The dipole interacts with the other carrier scattering reservoirs(such as phonon interactions) which could complicate the problem, but we can treat them by adding the Langevin noise operator $F_{\sigma,k}$ to Eq.(2.123). Similarly the electron number is fluctuated by pump processes which are included as the Langevin operator F_{ek} in Eq(2.124). The resultant equations are the semiconductor Bloch-Langevin equations

$$\frac{d\sigma_k}{dt} = -(\gamma + i(\omega_k - \nu_l))\sigma_k + i\sum_{l'} g_{l'k}(n_{ek} + n_{hk} - 1)A_{l'} + F_{\sigma k} \tag{2.125}$$

$$\frac{dn_{ek}}{dt} = A_{ek} + i\sum_{l}(g^*_{lk}A_l\sigma_k + H.C) - \frac{n_{ek}}{\tau_{nr}} - \gamma(n_{ek} - f_{ek}) + F_{ek} \tag{2.126}$$

The rate of change in the carrier density and the electric field envelope vary very little in the dipole lifetime $1/\gamma$ and hence the dipole operator can be eliminated from the field and carrier density equation by using the quasi-equilibrium approximation which assumes that it has reached steady state. The carrier density n_c varies significantly only over relatively long times such as the interband relaxation time. Multiplying Eq.(2.125) by the integrating factors $e^{(\gamma+i(\omega_k-\nu_l)t)}$ leads to

$$\frac{d(\sigma_k e^{(\gamma+i(\omega_k-\nu_l)t)})}{dt} = \sum_l (ig_{l,k}A_l(n_{ek} + n_{hk} - 1) + F_{\sigma k})e^{(\gamma+i(\omega_k-\nu_l)t)} \tag{2.127}$$

The above equation can be integrated to give

$$\sigma_k = \int_{-\infty}^{t} \sum_l (ig_{l,k}A_l(n_{ek} + n_{hk} - 1) + F_{\sigma k})e^{(\gamma+i(\omega_k-\nu_l)(t-t'))}dt' \tag{2.128}$$

We now take the rate-equation approximation by assuming that the carrier densities n_{ek} ,n_{hk} and the mode amplitude A_l are constant over the integration, can be evaluated at time t and taken out of the integral. Next the integration is performed leading to two terms of exponentials. We use the rotating wave approximation, where one of the terms is neglected since it leads to a very large denominator. The final result is

$$\sigma_k \approx \frac{i\Sigma_{l'} g_{l'k}(n_{ek} + n_{hk} - 1)A_{l'} + F_{\sigma k}}{(\gamma + i(\omega_k - \nu_l))} \tag{2.129}$$

The total carrier density $n_c = \sum_k n_{ek}$is obtained from Eq.(2.124) as

$$\frac{dn_c}{dt} = P - \frac{n_c}{\tau_{nr}} + i\sum_{k,l}(g^*_{lk}A_l\sigma_k + H.C) + \sum_k F_{ek} \tag{2.130}$$

We shall return to simplify the above equation after we discuss the field Langevin equations and define the noise operators.

2.6.2 Field Langevin Equations

Each mode of the cavity inside the LED are coupled to the many modes of free space through mirrors of finite transmission. The Langevin method simplifies the analysis by considering that each mode is coupled to a reservoir which is essentially unperturbed by the internal mode(also known as the system) dynamics. The reservoir(or bath) being large(due to many available modes) has a very large bandwidth whereby it is responds much faster than the system variable and is indifferent to the system changes. Using Eq.(2.120) , the annihilation operator for the cavity system obeys the equation of motion,

$$\frac{da_l}{dt} = \frac{i}{\hbar}[H_{tot}, a_l] = \frac{i}{\hbar}[H_{dipole} + H_{field-bath} + H_{field}, a_l] \tag{2.131}$$

The total Hamiltonian is expanded to include only the dipole, field and field-bath coupling terms since only these terms contain the mode operators of the field. Using the bosonic commutator $[a, a^\dagger] = 1$ and an extended result $[a_l^\dagger a_l, a_l] = -a_l$, the equations of motion can be solved as

$$\frac{da_l}{dt} = -i\Omega_l a_l - i\Sigma_j \mu_{l,j} b_j - i\Sigma_k g_{l,k} d_{-k} c_k \tag{2.132}$$

Similarly, the equation of motion of the annihilation operator for the bath is obtained from Eq.(2.120) as

$$\frac{db_j}{dt} = \frac{i}{\hbar}[H_{tot}, b_j] = \frac{i}{\hbar}[H_{field-bath} + H_{bath}, b_j] \tag{2.133}$$

The bath obeys the same commutation relations as the field system $[b_j, b_j^\dagger] = 1$ and $[b_j, b_j] = 0$. Using these properties in Eq.(2.133), we find

$$\frac{db_j}{dt} = -i\omega_j b_j - i\mu_{lj}^* a_l \tag{2.134}$$

Eq.(2.133) and Eq.(2.134) show that the system and the reservoir are linked by nature of interaction Hamiltonian which create an infinite set of coupled Heisenberg equations of motion. The coupled equations can be simplified by adiabatically eliminating the reservoir variables-$b_j(t)$ by using a Wigner-Weisskopf approximation[35], thereby obtaining a modified equation of motion for the system variable a_l. Integrating Eq.(2.134) from t_0 to t we obtain

$$b_j(t) = b_j(t_0)e^{-i\omega_j(t-t_0)} - i\int_{t_0}^{t} \mu_{l,j}^* a_l(t')e^{-i\omega_j(t-t')}dt' \tag{2.135}$$

In the above equation, the first term on the right represents the solution of the Heisenberg equation without the effects of the interaction Hamiltonian and thus describes the free evolution of the $b_j(t)$. Note that this free evolution satisfies the commutation relation as $[b_j(t), b_j^\dagger(t)] = [b_j(t_0), b_j^\dagger(t_0)]$ which shows that equal time commutation relations remains unchanged at all instants of time. The second term describes the perturbation of the free evolving mode amplitudes by the modes inside the cavity, by altering the number of photon in the modes of the reservoir as can be seen by its dependence on $a_j(t)$. Substituting Eq.(2.135) in Eq.(2.132) gives us

$$\frac{da_l}{dt} = -i\Omega_l a_l - i\sum_j \mu_{l,j} b_j(0) e^{-i\omega_j t} - \sum_j \int_0^t \mu_{l,j}^* \mu_{l,j} a_l(t') e^{-i\omega_j(t-t')} dt' - i\sum_k g_{l,k} d_{-k} c_k \tag{2.136}$$

The first term of Eq.(2.136) is the free evolution of the mode inside the cavity. The second term indicates the fluctuations in the reservoir affecting the system. The third term gives the radiation reaction which may be considered as a back-action from the reservoir on the system. This can be inferred by noticing that both Eq.(2.135) and Eq.(2.136) have a similar term. The system first polarizes the reservoir affecting the field modes as shown by the second term Eq.(2.135). The net change of all the reservoir field modes in turn affect the system inside the cavity according to second term of Eq.(2.136). We can move the operator a_l into the Heisenberg interaction picture by removing the fast moving frequencies associated with the various system Hamiltonians as

$$\begin{aligned} A_l(t) &= e^{\frac{i}{\hbar}(H_{field}+H_{bath})t)} a_l e^{-\frac{i}{\hbar}(H_{field}+H_{bath})t)} \\ &= e^{i(\Sigma_m \Omega_m a_m^\dagger a_m)t} a_l e^{-i(\Sigma_m \Omega_m a_m^\dagger a_m)t} \end{aligned} \tag{2.137}$$

Eq.(2.137) can be solved by differentiating $A_l(t)$ leading to

$$\frac{dA_l}{dt} = i\Omega_l e^{i(\Omega_l a_l^\dagger a_l)t}(a_l^\dagger a_l - a_l a_l^\dagger) a_l e^{-i(\Omega_l a_l^\dagger a_l)t} = -i\Omega_l A_l \tag{2.138}$$

This differential equation is easily solved to obtain

$$A_l(t) = A_l(0)\exp(-i\Omega_l t) = a_l \exp(-i\Omega_l t) \tag{2.139}$$

where the equal time commutation relations $[A_l(t), A_l^\dagger(t')] = \delta(t-t')$ are once again preserved. In essence, going into the interaction picture causes $A_l(t)$ to contain, the much slower time dependence of the interaction energy. Substituting Eq.(2.139) in Eq.(2.136) and choosing $t_0 = 0$ gives

$$\frac{dA_l}{dt} = -\int_o^t \sum_j |\mu_{l,j}|^2 A_l(t') e^{-i(\omega_j - \Omega_l)(t-t')} dt' - i \sum_k g_{l,k} d_{-k} c_k + F_l(t) \tag{2.140}$$

where $F_l(t)$ is the noise operator associated with damping the cavity mode l and is given by

$$F_l(t) = -i \sum_j \mu_{l,j} b_j(0) e^{i(\Omega_l - \omega_j)t} \tag{2.141}$$

The noise operator contains all the mode frequencies of the reservoir and varies rapidly with time, affecting the field system within the cavity. The first integral of Eq.(2.140) can be simplified by interchanging the sum and integral and noting that[35]

$$\lim_{t \to \infty} \int_0^t d\tau e^{-i(\omega - \omega_0)\tau} = \pi \delta(\omega - \omega_0) + i \frac{P}{\omega_0 - \omega} \tag{2.142}$$

where P indicates the Cauchy principle value. In Eq.(2.140), we note that the t integration is performed on a time scale commensurate with the inverse of the reservoir bandwidth. $A_l(t)$ varies very little in this timescale allowing it to be taken out of the integral followed by extending the limit of integration to infinity. We can then substitute Eq.(2.142) into Eq.(2.140) as follows

$$\sum_j |\mu_{l,j}|^2 A_l(t') \lim_{t \to \infty} \int_0^t e^{-i(\omega_j - \Omega_l)(t-t')} dt' = \pi \sum_j |\mu_{l,j}|^2 A_l(t') \delta(\omega_j - \Omega_l) \tag{2.143}$$

The Cauchy principal value is responsible for the Lamb shift in the harmonic oscillator[36] but this frequency shift is small and has been neglected in Eq.(2.143). Next we replace the sum over j in Eq.(2.143) with an integral which also introduces the density of states $D(\omega)$ in the integrand which identifies the degree of degeneracy for each frequency. This step followed by further simplification with the delta function which is given by

$$\pi \int |\mu_l(\omega)|^2 D(\omega) A_l(t) \delta(\omega - \Omega_l) d\omega = \pi D(\Omega_l) |\mu_l(\Omega_l)|^2 A_l(t) \tag{2.144}$$

If the the decay constant is chosen as $\kappa_l = 2\pi D(\Omega_l)|\mu_l(\Omega_l)|^2$, along with Eq.(2.141), Eq.(2.140) becomes

$$\frac{dA_l}{dt} = -\frac{\kappa_l}{2} A_l - i\Sigma_k g_{lk}^* \sigma_k + F_l(t) \tag{2.145}$$

Except for the second term, Eq.(2.145) resembles the classical Langevin equation of Eq.(2.14), where the first term represents the drift term and the third term the stochastic forcing term responsible for the fluctuations. We started with a coupled supersystem(system+reservoir) given by Eqs.(2.132) and (2.134), decoupled the reservoir from the system by only including its effects on the system which is to fluctuate and damp the modes inside the cavity. The net effect of this process, is to lose precision which leads to noise. Unlike classical systems, the presence of fluctuation term$F_l(t)$ is required in order to prevent the commutators from decaying to zero. We can further simplify Eq.(2.145) by inserting the expression for the spin flip operator obtained by the quasi-equilibrium approximation in Eq.(2.129) to give

$$\frac{dA_l}{dt} = -\frac{\kappa_l}{2}A_l + \sum_{l',k} g^*_{l,k} g_{l',k} \frac{n_{ek}+n_{hk}-1}{\gamma + i(\omega_k - \nu_l)} A_{l'} - i\sum_k g^*_{lk} \frac{1}{\gamma + i(\omega_k - \nu_l)} F_{\sigma,k} + F_l \tag{2.146}$$

For convenience, we define a fluctuation operator $F_{\sigma,l}(t)$ associated with the carrier scattering reservoirs

$$F_{\sigma,l} = -i\sum_k g^*_{lk} \frac{1}{\gamma + i(\omega_k - \nu_l)} F_{\sigma,k} \tag{2.147}$$

which is associated with the coupling between the electron-hole dipoles and the fields inside the cavity. Also we make the following expansion $n_{ek}+n_{hk}-1 = n_{ek}n_{hk}-(1-n_{ek})(1-n_{hk})$. Eq.(2.146) now becomes

$$\frac{dA_l}{dt} = -\frac{\kappa_l}{2}A_l + \sum_{l',k} g^*_{l,k} g_{l',k} \frac{n_{ek}n_{hk}}{\gamma + i(\omega_k - \nu_l)} A_{l'} - \sum_{l',k} g^*_{l,k} g_{l',k} \frac{(1-n_{ek})(1-n_{hk})}{\gamma + i(\omega_k - \nu_l)} A_{l'} + F_{\sigma,l} + F_l \tag{2.148}$$

We can now determine the quantum Langevin equation for the photon number operator $n_l = A_l^\dagger A_l$ using $\frac{dn_l}{dt} = \frac{dA_l^\dagger}{dt}A_l + A_l^\dagger \frac{dA_l}{dt}$ and Eq.(2.148) which gives us

$$\begin{aligned} \frac{dn_l}{dt} &= -\kappa_l n_l + \sum_k |g_{l,k}|^2 \frac{2\gamma n_{ek}n_{hk}}{\gamma^2 + (\omega_k - \Omega_l)^2} A_l^\dagger A_l + \sum_k |g_{l,k}|^2 \frac{2\gamma(1-n_{ek})(1-n_{hk})}{\gamma^2 + (\omega_k - \Omega_l)^2} A_l^\dagger A_{l'} \\ &\quad + [F^\dagger_{\sigma,l} A_l + H.C] + [F_l^\dagger A_l + H.C] \end{aligned} \tag{2.149}$$

The spontaneous emission is noted as a consequence of vacuum fluctuations stimulating the excited states to recombine. This should be readily explainable with the quantum theory. In Appendix.A, we determine the spontaneous emission (or absorption) operator which determines the emission rate of carriers into mode l(or absorption rate of photons from mode l) which are

$$R_{sp,l} = \sum_k |g_{l,k}|^2 \frac{2\gamma}{\gamma^2 + (\omega_k - \Omega_l)^2} n_{ek} n_{hk} \tag{2.150}$$

$$R_{abs,l} = \sum_k |g_{l,k}|^2 \frac{2\gamma}{\gamma^2 + (\omega_k - \Omega_l)^2} (1 - n_{ek})(1 - n_{hk}) \tag{2.151}$$

Using Eq.(2.150) and Eq.(2.151) in Eq.(2.149), we obtain Eq.(2.152) as

$$\frac{dn_l}{dt} = -\kappa_l n_l + (R_{sp,l} + R_{abs,l}) n_l + [F^\dagger_{\sigma,l} A_l + H.C] + [F^\dagger_l A_l + H.C] \tag{2.152}$$

Next we add and subtract two terms, $R_{sp,l}$ and $\kappa_l \bar{n}(\nu_l)$ which is followed by rearranging the terms giving us

$$\frac{dn_l}{dt} = -(\kappa_l - R_{sp,l} + R_{abs,l}) n_l + R_{sp,l} + \kappa_l \bar{n}(\nu_l) + [F^\dagger_{\sigma,l} A_l + H.C - R_{sp,l}] + [F^\dagger_l A_l + H.C - \kappa_l \bar{n}(\nu_l)] \tag{2.153}$$

We can now define the following fluctuation operators

$$F_{r,l} = F^\dagger_{\sigma,l} A_l + H.C - R_{sp,l} \tag{2.154}$$

$$F_{\kappa,l} = F^\dagger_l A_l + H.C - \kappa_l \bar{n}(\nu_l) \tag{2.155}$$

where $F_{r,l}$ is the noise operator associated with conversion of carriers to photons, and $F_{\kappa,l}$ is the noise operator associated with photons escaping the cavity. We note that the noise operator $F_{r,l}$ is present in equations for carrier number(Eq.(2.130)) and photon number(Eq.(2.153)) but are negatively correlated which implies that any fluctuation which leads to the loss of electrons in mode k is reflected in addition of photons to mode l. The motivation behind adding and subtracting terms in Eq.(2.153) is to add these terms to the noise operators $F_{r,l}$ and $F_{\kappa,l}$ such that the average of these noise operators(which will be evaluated in the following section) evaluate to zero ie.$\langle F_{r,l} \rangle, \langle F_{\kappa,l} \rangle = 0$. Using Eq.(2.154) and Eq.(2.155) along with the assumption $R_{sp,l}, R_{abs,l} \ll \kappa_l$ in Eq.(2.153) affords us the following compact representation.

$$\frac{dn_l}{dt} = -\kappa_l n_l + R_{sp,l} + F_{r,l} + F_{\kappa,l} \tag{2.156}$$

The condition $R_{sp,l}, R_{abs,l} \ll \kappa_l$ is an important assumption for LEDs. This implies that the rate at which photons leave the cavity is higher than the rate at which the photons are created inside the LED cavity. In fact, the steady state result of Eq.(2.156) is $_{l})_{ss} = \frac{R_{sp,l}}{\kappa_l} \ll 1$, ie. the photon number in each mode is negligible. In order to verify that $R_{sp,l}$ is indeed smaller than κ_l, we note that $R_{sp,l}$ depends on the coupling term $|g_{lk}|^2$which is proportional to $1/V_{cavity}$(where V_{cavity} is the volume of the LED cavity and appears through the electric field of a single photon) and the sum over the k modes Σ_k which is proportional to the volume of the active region $V_{active.}$. Hence we can write $R_{sp,l} \propto \frac{V_{active}}{V_{cavity}}$. The active region volume is the region where photons are generated. In the case of the LEDs, most modes of the photons are not confined to the cavity region. In fact, these modes are not separated from the modes of free space outside the cavity, since the transmission coefficient of the mirrors is assumed to be maximum. The cavity volume can be redefined to be a cube on which the detector's surface is located. The volume of this cube is quite large and since $\kappa_l \propto \frac{1}{(V_{cavity})^{1/3}}$ we can determine $R_{sp,l}/\kappa_l \ll 1$ which validates our assumption. At this stage, we can also further simplify Eq.(2.130) by substituting Eq.(2.129) in Eq.(2.130), followed by assuming that $\sum_k F_{ek} = F_P + F_{nr}$ and finally using Eqs.(2.150,2.151,2.154) to arrive at the equation of motion for the total carrier density in the active region.

$$\frac{dn_c}{dt} = P - \frac{n_c}{\tau_r} - \frac{n_c}{\tau_{nr}} + F_P + F_{nr} + F_r \qquad (2.157)$$

2.6.3 Noise Correlations

In order to determine the fluctuation spectra of the photon number noise, the noise correlations among the various noise operators associated with the equations of motion must be determined. These are $F_{r,l}$,$F_{\kappa,l}$ in Eq.(2.156) and F_r,F_P and F_{nr} in Eq.(2.164) respectively which we refer to as the principal operators of the problem. Since the various reservoirs are not related to each other, we assume that the correlations between different reservoir noise operators are zero(eg. $\langle F_l^\dagger F_{\sigma_k}\rangle = 0$). Also the correlation between different modes of photon and wavenumbers of carriers can be neglected[35] which provides for

$$\langle A_l^\dagger A_{l'}\rangle = \langle n_l\rangle\delta_{ll'}, \langle\sigma_k^\dagger\sigma_{k'}\rangle = \langle n_{ek}n_{hk'}\rangle\delta_{kk'}, \langle\sigma_k\sigma_{k'}^\dagger\rangle = (1-n_{ek})(1-n_{hk'})\delta_{kk'} \qquad (2.158)$$

For a general quantum mechanical Langevin equation $\dot{A}_\mu = D_\mu + F_\mu$ with system operator $A_\mu(t)$ coupled to an arbitrary Markovian reservoir F_μ, the diffusion coefficient satisfies the generalized Einstein relation

$$2\langle D_{\mu\nu}\rangle = \frac{d}{dt}\langle A_\mu A_\nu\rangle - \langle A_\mu D_\nu\rangle - \langle D_\mu A_\nu\rangle \tag{2.159}$$

Eq.(2.159) comprises a quantum fluctuation dissipation theorem which relates the drift component-D_μ,D_ν with the diffusion coefficient $D_{\mu\nu}$. From the diffusion coefficient, the noise operator correlation function is determined as

$$\langle F_\mu(t)F_\nu(t')\rangle = 2\langle D_{\mu\nu}\rangle\delta(t-t') \tag{2.160}$$

The general advantage of using Eq.(2.159) to determine Eq.(2.160) is that one does not need to specify the noise operator F_μ. For example, the effect of the carrier scattering reservoirs are included in the equation of motion for dipole operator in Eq.(2.125) as $F_{\sigma,k}$ without knowing its explicit form. Hence in order to determine $\langle F^\dagger_{\sigma_k}(t)F_{\sigma_k}(t')\rangle$, we determine the diffusion coefficient

$$2\langle D_{\sigma_k^\dagger\sigma_k}\rangle = \frac{d}{dt}\langle\sigma_k^\dagger\sigma_k\rangle + (\gamma+i\omega_k-i\nu_l)\langle n_{ek}n_{hk}\rangle + (\gamma-i\omega_k+i\nu_l)\langle n_{ek}n_{hk}\rangle \approx 2\gamma\langle n_{ek}n_{hk}\rangle \tag{2.161}$$

where $\frac{d}{dt}\langle\sigma_k^\dagger\sigma_k\rangle = \langle\frac{d\sigma_k^\dagger}{dt}\sigma_k\rangle + \langle\sigma_k^\dagger\frac{d\sigma_k}{dt}\rangle$ contains terms such as $\langle F^\dagger_{\sigma_k}\sigma_k\rangle$ which are unknown at this point, making the usage of $\langle D_{\sigma_k^\dagger\sigma_k}\rangle$ for finding noise correlations difficult. However for this case, we can use the quasi-equilibrium approximation $\frac{d}{dt}\langle\sigma_k^\dagger\sigma_k\rangle \approx 0$ which allows for the approximate result of Eq.(2.161). Substituting Eq.(2.161) in Eq.(2.160) gives us

$$\langle F^\dagger_{\sigma_k}(t)F_{\sigma_{k'}}(t')\rangle \approx 2\gamma\langle n_{ek}n_{hk}\rangle\delta_{kk'}\delta(t-t') \tag{2.162}$$

$$\langle F_{\sigma_k}(t)F^\dagger_{\sigma_{k'}}(t')\rangle \approx 2\gamma\langle(1-n_{ek})(1-n_{hk})\rangle\delta_{kk'}\delta(t-t') \tag{2.163}$$

We need to establish the correlations between the noise operators for $F_{\sigma,k}$ and F_l since, the principal noise operators are expressed in terms of them. We first start with the principal operator $F_{r,l}$ which requires evaluation of noise correlations

$$\begin{aligned}
\langle F^\dagger_{\sigma,l}(t)F_{\sigma,l}(t')\rangle &= \sum_{kk'} g^*_{lk}g_{lk'}\frac{1}{\gamma-i(\omega_k-\Omega_l)}\frac{1}{\gamma+i(\omega_{k'}-\Omega_l)}\left\langle F^\dagger_{\sigma,k'}F_{\sigma,k}\right\rangle \\
&= \sum_k |g_{lk}|^2\frac{2\gamma}{\gamma^2+(\omega_k-\Omega_l)^2}\langle n_{ek}n_{hk}\rangle\,\delta(t-t') \\
&= \langle R_{sp,l}\rangle\delta(t-t') \qquad (2.164)\\
\langle F_{\sigma,l}(t)F^\dagger_{\sigma,l}(t')\rangle &= \langle R_{abs,l}\rangle\delta(t-t') \qquad (2.165)
\end{aligned}$$

where we have used Eq.(2.162) and Eq.(2.163) in obtaining the results. The average of the noise fluctuations vanishes which motivated us to define $F_{r,l}$ and $F_{\kappa,l}$ according to Eq.(2.154) and Eq.(2.155) which we can now verify. Consider the following noise operator-system operator correlation function whose system operator can be expanded as

$$\begin{aligned}\langle F^{\dagger}_{\sigma,l}(t)A_l(t')\rangle &= \langle F^{\dagger}_{\sigma,l}(t)A_l(t-\Delta t)\rangle + \int_{t-\Delta t}^{t}\langle F^{\dagger}_{\sigma,l}(t')\frac{dA_l(t')}{dt}\rangle dt' \\ &\approx \int_{t-\Delta t}^{t}\langle F^{\dagger}_{\sigma,l}(t')F_{\sigma,l}(t')\rangle dt' = \frac{1}{2}\langle R_{sp,l}\rangle \end{aligned} \tag{2.166}$$

In the first equality of Eq.(2.166), the first term is zero, since a fluctuation in the future cannot affect an operator in the past. Here Δt is a time interval which is shorter than the decay time of the cavity mode $t = 1/\kappa$ but much longer than the correlation time of the reservoir. We encounter the correlation$\langle F^{\dagger}_{\sigma,l}l(t')\rangle$which is non-zero only at $t = t'$ and can be ignored. The final result in Eq.(2.166) is obtained by substituting Eq.(2.164) followed by an integration over half the delta function at $t = t'$ which leads to the factor of 1/2. We can also evaluate the Hermitian conjugate similarly and establish that $\langle F^{\dagger}_{\sigma,l}A_l + H.C\rangle = \langle R_{sp,l}\rangle$ and $\langle F_{r,l}\rangle = 0$. On the other hand, for the case of an oscillator coupled to a reservoir of oscillators, the precise form of $F_l(t)$ is given by Eq.(2.141) and Eq.(2.159) need not be applied. In this case

$$\langle F^{\dagger}_l F_l\rangle = \kappa_l\langle b^{\dagger}_j(0)b_j(0)\rangle\delta(t-t') = \kappa_l n_{th}(\nu_j)\delta(t-t') \tag{2.167}$$

where the average number of photons per mode in the reservoir is given by a thermal distribution $n_{th}(\nu_j) = \frac{1}{e^{\frac{\hbar\omega_k}{kT}}-1}$. The motivation for the choice of the principal operator $F_{\kappa,l}$ in Eq.(2.155) is such that the average of the principal operator vanishes ie. $\langle F_{\kappa,l}\rangle = 0$. This can be seen by obtaining $\langle F^{\dagger}_l A_l + H.C\rangle = \kappa_l n(\bar{\nu_l})$ by the same methods used in evaluating Eq.2.166 . The correlation function for principal operator $F_{r,l}$ is

$$\langle F^{\dagger}_{r,l}(t)F_{r,l}(t')\rangle = \langle F^{\dagger}_{\sigma,l}(t)F_{\sigma,l}(t')\rangle\langle A_l(t)A^{\dagger}_l(t')\rangle + \langle A^{\dagger}_l(t)A_l(t')\rangle\langle F_{\sigma,l}(t)F^{\dagger}_{\sigma,l}(t')\rangle + cross.terms \tag{2.168}$$

In Eq.(2.168), the cross terms have terms like $\langle A^{\dagger}_l A^{\dagger}_l\rangle$ or $\kappa_l\langle F_{r,l}\rangle$ and these are zero. Substituting Eq.(2.164) and Eq.(2.165) in Eq.(2.168), we obtain

$$\langle F^{\dagger}_{r,l}(t)F_{r,l}(t')\rangle = [(\langle R_{sp,l}\rangle + \langle R_{abs,l}\rangle)\langle n_l\rangle + \langle R_{sp,l}\rangle]\delta(t-t') \approx \langle R_{sp,l}\rangle\delta(t-t') \tag{2.169}$$

We also establish in the following step that the correlation between the two noise operators $F_{r,l}$ and $F_{\kappa,m}$ which are associated with the conversion of carriers to photons and escape of photons from the cavity vanish since fluctuations in different reservoirs are typically uncorrelated.

$$\langle F^{\dagger}_{r,l} F_{\kappa,m} \rangle = \langle F_{\sigma,l} \rangle * (Term1) + \langle F^{\dagger}_{\sigma,l} \rangle * (Term2) - R_{sp} \langle F_{\kappa,m} \rangle = 0 \qquad (2.170)$$

where the averages of the noise operator $\langle F_{\sigma,l} \rangle = \langle F^{\dagger}_{\sigma,l} \rangle = \langle F_{\kappa,m} \rangle = 0$. The correlation function of the principal operator $F_{\kappa,l}$ is

$$\langle F^{\dagger}_{\kappa,l} F_{\kappa,l} \rangle = \langle (A^{\dagger}_l F_l + H.c)(F^{\dagger}_l A_l + H.c) \rangle = 0 \qquad (2.171)$$

The above result can be explained by simple handwaving. These are expectation values of 4 operator products with terms like $\langle A^{\dagger}_l F_l F^{\dagger}_l A_l \rangle$. An exact solution can be obtained by substituting for A_l in a manner similar to Eq. (2.166), except we have double integrals and summations. If we look past the integrals and summations, all the four terms take the form $\langle b^{\dagger}_j b_j b^{\dagger}_j b_j \rangle$. These terms which are the averages of four operator products, can be evaluated using the density matrix for the thermal distribution, but its simpler to use Wick's theorem[] where the operator products decompose as

$$\langle n_j^2 \rangle = \langle b^{\dagger}_j b_j \rangle \langle b^{\dagger}_j b_j \rangle + \langle b^{\dagger}_j b^{\dagger}_j \rangle \langle b_j b_j \rangle + \langle b^{\dagger}_j b_j \rangle \langle b_j b^{\dagger}_j \rangle = \overline{n_{th}}(\nu_l)(1 + \overline{n}_{th}(\nu_l)) \qquad (2.172)$$

Since we assume that there are no thermal photons at optical frequencies these correlations in Eq.(2.172) are evaluated to zero. We now summarize the non-zero correlation functions of the principal operators.

$$\langle F^{\dagger}_{r,l}(t) F_{r,l'}(t') \rangle = \langle R_{sp,l} \rangle \delta_{ll'} \delta(t-t') = \left\langle \frac{n_c}{\tau_{r,l}} \right\rangle \delta_{ll'} \delta(t-t') \qquad (2.173)$$

$$\langle F^{\dagger}_r(t) F_r(t') \rangle = \sum_l \langle F^{\dagger}_{r,l}(t) F_{r,l}(t') \rangle = \left\langle \frac{n_c}{\tau_r} \right\rangle \delta_{ll'} \delta(t-t') \qquad (2.174)$$

The correlation function for the principal operators associated with pump and non-radiative processes F_P, F_{nr} cannot be directly evaluated since $\Sigma_k F_{ek} = F_P + F_{nr}$ has not been specified precisely(we have to assume that $\langle F_{ek} \rangle = 0$) but we can use the generalized Einstein relation of Eq.(2.159) to obtain the diffusion coefficient which leads to the noise correlation function for F_{ek} as $\langle F_{ek}F_{ek'}\rangle = (\langle P_{ek}(1-n_{ek})\rangle + \langle\frac{n_{ek}}{\tau_{nr}}\rangle)\delta_{kk'}\delta(t-t')$. Summing over all modes we get $\Sigma_k\langle F_{ek}F_{ek}\rangle = (\langle P\rangle + \langle\frac{n_c}{\tau_{nr}}\rangle)\delta(t-t')$ from which the following decompositions are valid

$$\langle F_{nr}^{\dagger}(t)F_{nr}(t')\rangle = \left\langle\frac{n_c}{\tau_{nr}}\right\rangle\delta(t-t') \tag{2.175}$$

$$\langle F_P^{\dagger}(t)F_P(t')\rangle = \langle P\rangle\delta(t-t') \tag{2.176}$$

2.6.4 Photon Number Noise with a c-number Pump

The total flux detected at the photodiode surface needs to be determined. In order to do this, we must first relate the photon number inside the cavity to the photon flux outside the cavity. The modes inside the cavity can be linked to the modes outside the cavity using the input-output formalism first introduced by Gardiner[37]. The total number of photons outside the cavity from mode 'l' is obtained from the mode operator outside the cavity-$A_{l,out}$ which is $V_l = A_{l,out}^{\dagger}A_{l,out}$. Then the relation between V_l and n_l follows

$$V_l = \kappa_l n_l - F_{\kappa,l} \tag{2.177}$$

Here $n_l = A_l^{\dagger}A_l$ and $F_{\kappa,l} = F_l/\kappa$. Note that the cross terms lead to zero, since they are uncorrelated. Next, the photon flux outside the cavity needs to be related to the total photon number N detected at the photodetector(PD) surface. The photons outside the cavity will be further subject to loss mechanisms, such as imperfect transmission, loss at the PD surface and coupling of the LED to the PD through optical elements. These effects can be suitably represented by introducing a beam splitter between the output of the cavity and the input of the PD. Now, the relation between the mean flux at the detector surface N_0 and that of the average photon number V_0 outside the cavity through the beam splitter can be written as

$$N_0 = \langle N\rangle = \sum_l \theta_l\langle V_l\rangle = \eta_c\langle V\rangle = \eta_c V_0 \tag{2.178}$$

where $V = \Sigma_l V_l$ is the total photon flux from the cavity. Here θ_l is the coupling or transmission coefficient of mode 'l' through the beam splitter. As all the modes are summed at the PD, we obtain a photon number, whose average N_0 is related to the total flux V_0 through a 'net' coupling efficiency $\eta_c = \frac{N_0}{V_0}$ which includes all the loss mechanisms represented by the beam splitter. As the average has been established, the mean photon number fluctuations at the PD surface next needs to be determined. The PD detects N_l photons that pass through the beam splitter as

$$N_l = \theta_l V_l + F_{p,l} \tag{2.179}$$

Here $F_{p,l}$ represents the additional partition noise introduced into the unused portion of the beam splitter. Hence there are two components :(a) the attenuated photon flux outside the cavity, which passes through one port of the beam splitter as given by term 1 of Eq. (2.x) and (b) the vacuum fluctuations (that permeate all space and is present even under no-light conditions) which enter into the second unused port of the beam splitter as given by $F_{p,l}$. The vacuum fluctuations serve to introduce a stochasticity to the beam splitter which randomly deletes the photons at its output with probability θ_l. The cross-correlation associated with $F_{p,l}$ can be determined from the number fluctuations in mode 'l' obtained from Eq. (2.179) using $\Delta N_l = N_l - \langle N_l \rangle$and calculating $\langle \Delta N_l \Delta N_{l'} \rangle$ as

$$\langle \Delta N_l \Delta N_{l'} \rangle = \langle N_l N_{l'} \rangle - \langle N_l \rangle \langle N_{l'} \rangle = \theta_l (1 - \theta_l) \langle V_l \rangle \delta_{ll'} \tag{2.180}$$

where we have used $\langle N_l \rangle = \theta_l \langle V_l \rangle$. Eq.(2.180) describes the fluctuation aspects and is the noise correlation function for $F_{p,l}$

$$\langle F_{p,l}^{\dagger} F_{p,l} \rangle = \theta_l (1 - \theta_l) \langle V_l \rangle \delta_{ll'} \delta(t - t') \tag{2.181}$$

The total spectral density of the photon number fluctuations at the PD(since the quantity is to be observed on a spectrum analyzer) needs to be obtained. A relation between total photon fluctuation and V_l can be obtained by linearizing Eq. (2.179), taking its Fourier transform and adding all the modes to obtain

$$\Delta N(\omega) = \sum_l \theta_l \Delta V_l(\omega) + \sum_l F_{p,l}(\omega) \tag{2.182}$$

where $N_l(\omega), V_l(\omega)$ and $F_{p,l}(\omega)$ are the Fourier components of $N(t), V_l(t)$ and $F_{p,l}(t)$ respectively. The flux correlation of N is obtained from Eq. (2.182) using $\langle \Delta N(\omega)^* \Delta N(\omega) \rangle$ as

$$\langle |\Delta N(\omega)|^2 \rangle = \Sigma_{ll'} \theta_l \theta_{l'} \langle \Delta V_l^*(\omega) \Delta V_{l'} \rangle + \sum_{ll'} \langle F_{p,l}^{\dagger} F_{p,l} \rangle + \langle cross.terms \rangle \tag{2.183}$$

The cross terms are of the form $\langle \Delta V_l \rangle \langle V_l \rangle$ and since the average of the fluctuations is zero these terms can be ignored. Hence the photon fluctuation spectral density can be obtained as

$$\langle |\Delta N(\omega)|^2 \rangle = \sum_{ll'} \theta_l \theta_{l'} \langle \Delta V_l^* \Delta V_{l'} \rangle + \sum_l \theta_l (1-\theta_l) \langle V_l \rangle \tag{2.184}$$

We adopt the small signal methods used in Ref.[38] for the radiative and non-radiative lifetimes since they are dependent on the nonequilibrium carrier concentration n_c. We linearize them to order $\Delta n_c = n_c - n_{c0}$ by performing a Taylor's series expansion and for the single mode lifetime

$$\tau_{r,l}(n_c) = \tau_{r,l}(n_{c0}) + \frac{d\tau_{r,l}(n_c)}{dn_c}|_{n_c=n_{c0}} \Delta n_c \tag{2.185}$$

We set $K_{r,l} = -\frac{\partial \tau_{r,l}}{\partial n_c}|_{n_c=n_{c0}} \frac{n_{c0}}{\tau_{rl,}(n_{c0})}$ which indicates the strength of the nonlinearity or the sensitivity of the lifetime to the carrier number fluctuations and allows us to reexpress Eq.(2.185) as

$$\tau_{r.l}(n_c) = \tau_{r,l0}(1 - K_{r,l} \frac{\Delta n_c}{n_{c0}}) \tag{2.186}$$

The total effective radiative carrier lifetime is $\frac{1}{\tau_r} = \Sigma_l \frac{1}{\tau_{r,l}}$ and performing a similar Taylor's series expansion on this variable we have

$$\tau_r(n_c) = \tau_{r0}(1 - K_r \frac{\Delta n_c}{n_{c0}}) \tag{2.187}$$

The effect of the linearized lifetimes can be included in the equations of motion. For example, the fluctuation in carrier density obtained by considering only the second term of Eq.(2.164) (since it depends on the radiative lifetime) is

$$\frac{d\Delta n_c}{dt} = \frac{dn_c}{dt} - \frac{d(n_c)_0}{dt} \rightarrow \frac{n_c}{\tau_r} - \frac{n_{c0}}{\tau_{r0}} = \Delta n_c \frac{(1+K_{r,l})}{\tau_{r0}} = \frac{\Delta n_c}{\tau_r'} \tag{2.188}$$

where we have used Eq.(2.188) to construct the redefined lifetime τ_r'. Note that there are three lifetimes: the carrier dependent lifetime τ_r, the DC lifetime associated with steady state τ_{r0} and finally the redefined lifetime τ_r' which is expressed in terms of the DC lifetime and the strength of the carrier fluctuations. From now on, we work with the redefined lifetimes and for the nonradiative term in Eq.(2.164) and the second term in Eq.(2.156), we can obtain similar definitions for the redefined lifetime as

$$\tau_{r,l}' = \frac{\tau_{r,l0}}{1+K_{r,l}}, \quad \tau_r' = \frac{\tau_{r0}}{1+K_r}, \quad \tau_{nr}' = \frac{\tau_{nr0}}{1-K_r} \tag{2.189}$$

The total effective lifetime can be expressed in terms of the radiative and the nonradiative lifetime as

$$\frac{1}{\tau''} = \frac{1}{\tau'_r} + \frac{1}{\tau'_{nr}} \tag{2.190}$$

Linearizing Eqs. (2.156),(2.164) and (2.177) in terms of $\Delta n_n = n_c - n_{c0}, \Delta n_l = n_l - n_{l0}$ and $\Delta V_l = V_l - V_{l0}$ and using Eqs. (2.189) and (2.190) in them leads to

$$\frac{d\Delta n_c}{dt} = \Delta P - \frac{\Delta n_c}{\tau''} + F_p + F_r + F_{nr} \tag{2.191}$$

$$\frac{d\Delta n_l}{dt} = -\kappa_l \Delta n_l + \frac{\Delta n_c}{\tau'_{r,l}} + F_{\kappa,l} + F_{r,l} \tag{2.192}$$

$$\Delta V_l = \kappa_l \Delta n_l - F_{\kappa,l} \tag{2.193}$$

Taking the Fourier transforms of Eq. (2.191) and (2.192), followed by eliminating the carrier number fluctuation $\Delta n_c(\omega)$ from the expression for the photon number fluctuation inside the cavity($\Delta n_l(\omega)$) leads to

$$\Delta n_l(\omega) = \frac{\tau''}{\tau_{r,l}} \frac{(\Delta P + F_p(\omega) + F_r(\omega) + F_{nr}(\omega))}{(1 + i\omega\tau'')(\kappa_l + i\omega)} + \frac{(F_{\kappa,l}(\omega) + F_{r,l}(\omega))}{(\kappa_l + i\omega)} \tag{2.194}$$

Similarly, taking the Fourier transform of Eq. (2.193), followed by substituting of $\Delta n_l(\omega)$ in the resultant equation gives

$$\Delta V_l(\omega) = \frac{\tau''}{\tau_{r,l}} \frac{\kappa_l(\Delta P(\omega) + F_p(\omega) + F_r(\omega) + F_{nr}(\omega))}{(1 + i\omega\tau'')(\kappa_l + i\omega)} + \frac{\kappa_l(F_{\kappa,l}(\omega) + F_{r,l}(\omega))}{(\kappa_l + i\omega)} - F_{\kappa,l}(\omega) \tag{2.195}$$

We drop the $\omega$from the noise operators with the assumption that we are referring from there on to the Fourier transforms of the time domain operators. The cross correlation between modes l and l' of the photon flux fluctuation is obtained as

$$\begin{aligned} \langle \Delta V_l^* \Delta V_{l'} \rangle \quad = \quad & \frac{\tau''}{\tau'_{r,l}} \frac{\tau''}{\tau'_{r,l'}} \frac{(\langle |\Delta P_{tot}|^2 \rangle + S_{F_r} + S_{F_{nr}})}{(1 + \omega^2 \tau''^2)} + \frac{\tau'' \langle F_r^*(\omega) F_{r,l'}(\omega) \rangle}{\tau'_{r,l}(1 - i\omega\tau'')} \\ & + \frac{\tau'' \langle F^\dagger_{r,l} r(\omega) \rangle}{\tau_{r,l'}(1 + i\omega\tau'')} + \langle F^\dagger_{r,l} r_{,l'}(\omega) \rangle + coeff * \langle F_{\kappa,l}(\omega) X(\omega) \rangle \end{aligned} \tag{2.196}$$

where $S_{F_r} = \langle |F_r|^2 \rangle$ and $S_{F_{nr}} = \langle |F_{nr}|^2 \rangle$ which are the power spectral densities obtained by taking the Fourier transform of Eq.(2.174) and Eq.(2.175). The total pump fluctuations is grouped together as $\Delta P_{tot} = \Delta P + F_p$ and its spectral density can be greater or smaller than $\langle_p(\omega)|^2 \rangle = \langle P \rangle$ depending on the modulation of the pump ΔP. $X(\omega)$ in Eq. (2.196) can be replaced by $F_{r,l}, F_r$ or $F_{\kappa,l}$. In all these cases the correlations evaluate to zero. The pump is included only as a c-number in these equations and represents the net forward injection events. The pump can be either noiseless($\Delta P_{tot} = 0$) or at the full shot noise level. For the time being, we ignore the negative feedback mechanism that serves to suppress the pump fluctuations below the shot noise level to establish the condition $\Delta P_{tot} = 0$. The purpose is to obtain a general expression that studies the effects of non-radiative mechanism ie. the presence of differential efficiencies and the nature of emission lifetimes on the squeezing characteristics. The pump regulation when properly included, tends to change only frequency dependent squeezing spectra but predicts the same result as the untreated pump case at low frequencies. The reason for investigating the role of differential efficiencies, is that the simple relations for the photon noise used in the early experimental observations of subshot noise were not very accurate. This is validated in the squeezing spectra for the LEDs in chapter 3. It is useful to redefine the correlation terms of Eq.(2.173-2.175) in terms of the pump factor$P$. In order to do this, the equation relating the variables V_0,P_0 and N_0 where N_0 is the number of photons detected at the photodetector surface, V_0 is the number of photons emitted from the cavity and P_0 is the number of electrons pumped into the active region is given by Eq.(2.99) which can be written as $\frac{N_0}{P_0} = \frac{\eta_c n_{c0}/\tau_{r0}}{n_{c0}/\tau_{r0}+n_{c0}/\tau_{nr}} = \frac{\eta_c V_0}{P_0}$ from which the following relations for the spectral densities can be inferred

$$S_{F_r} = \frac{n_{c0}}{\tau_r} = \frac{\eta_0}{\eta_c} P_0 \ \ , \ \ S_{F_{nr}} = \frac{n_{c0}}{\tau_{nr}} = (1 - \frac{\eta_0}{\eta_c}) P_0 \tag{2.197}$$

Substituting Eq.(2.197) in Eq.(2.196) gives us

$$\begin{aligned} \langle |\Delta N(\omega)|^2 \rangle &= \sum_l \theta_l (1-\theta_l) \langle V_l \rangle + \sum_{ll'} \theta_l \theta_{l'} \{ (\frac{\tau''^2}{\tau'_{r,l}\tau'_{r,l'}} \frac{\langle |\Delta P_{Tot}|^2 \rangle + P_0}{(1+\omega^2 \tau''^2)}) - \\ & (\frac{\tau''}{\tau'_{r,l}} \sum_l \frac{n_{c0}}{\tau_{r,l'_0}(1-i\omega\tau'')} \delta_{ll'} + \frac{\tau''}{\tau'_{r,l'}} \sum_{l'} \frac{n_{c0}}{\tau_{r,l_0}(1-i\omega\tau'')} \delta_{l'l}) + \langle V_l \rangle \delta_{ll'} \} \end{aligned} \tag{2.198}$$

The above expression has many unknowns associated with the lifetime and carrier numbers such as $\theta_l, \tau_{r,l}, \tau_r, \tau'', n_{c0}, V_L$,etc. We need to convert it to an experimental observable related to parameters that can be extracted from measurements. As a first step we note that

$$\frac{d}{dn_c} (\frac{n_c}{\tau_r(n_c)})|_{n_c = n_{c0}} = \frac{1}{\tau_r(n_{c0})} (1 - \frac{n_{c0}}{\tau_r(n_{c0})} \frac{\partial \tau_r}{\partial n_c}) = \frac{1}{\tau_{r0}} (1 + K_r) = \frac{1}{\tau'_r} \tag{2.199}$$

which allows us to re-express the differential efficiency(Eq.(2.101)) as

$$\eta_d = \frac{\eta_c(1/\tau_r')}{1/\tau_r' + 1/\tau_{nr}'} \tag{2.200}$$

The total lifetime is then expressed in terms of the radiative lifetime using $\tau'' = \frac{\eta_d}{\eta_c}\tau_r'$ which when substituted in Eq.(2.198) gives us

$$\left\langle |\Delta N(\omega)|^2 \right\rangle = \sum_l \theta_l \left\langle V_l \right\rangle + \eta_d^2 \sum_{ll'} \theta_l \theta_{l'} \frac{\tau_r'^2}{\eta_c^2 \tau_{r,l}' \tau_{r,l'}'} \frac{\left\langle |\Delta P_{Tot}|^2 \right\rangle + P_0}{(1+\omega^2\tau''^2)} - 2\eta_d \sum_l \frac{\tau_r'\theta_l^2}{\eta_c \tau_{r,l}' \tau_{r,l0}} \frac{n_{c0}}{1+\omega^2\tau''^2} \tag{2.201}$$

The photon Fanofactors which are normalized to a calibrated shot noise level and detected at the PD surface is $F_{ph} = \frac{\left\langle |\Delta N(\omega)|^2 \right\rangle}{N_0}$ and can be obtained in terms of the normalized pump Fanofactors which are defined as $F_p = \frac{\langle |\Delta P_{tot}|^2 \rangle}{P_0} = \eta \frac{\langle |\Delta P_{tot}|^2 \rangle}{N_0}$. Eq.(2.201) now becomes

$$F_{ph}(\omega) = 1 + \frac{\eta_d^2}{\eta}\xi_1 \frac{F_p(\omega)+1}{(1+\omega^2\tau''^2)} - 2\frac{\eta_d \xi_2}{(1+\omega^2\tau''^2)} \tag{2.202}$$

where we have collected the remaining variables under $\xi_1 = \Sigma_{ll'}\theta_l\theta_{l'}\frac{\tau_r'\tau_r'}{\eta_c^2\tau_{r,l}'\tau_{r,l'}'}$ and $\xi_2 = \left(\Sigma_l \frac{\tau_r'\theta_l}{\eta_c\tau_{r,l}'}\right)^2$ and we have used $\frac{n_{c0}}{N_0} = \frac{\tau_{r0}}{\eta_c}$. Note that ξ_1, ξ_2 represent the multimode properties of the cavity and are equal to each other when $l = l'$. Eq.(2.202) can be rearranged by separating out the pump Fanofactors as

$$F_{ph}(\omega) = 1 - \frac{1}{(1+\omega^2\tau''^2)}\frac{\eta_d^2}{\eta}\xi_1(\frac{2\xi_2\eta}{\xi_1\eta_d} - 1) + \frac{\eta_d^2}{\eta}\xi_1\frac{F_p(\omega)}{(1+\omega^2\tau''^2)} \tag{2.203}$$

The photon Fanofactors obtained are a function of the normalized(and controllable) pump fluctuations, the cutoff frequency $1/\tau''$ (where τ'' is the net lifetime of radiative and non-radiative processes) and parameters which are related to cavity properties such as ξ_1, ξ_2 and the electronic to optical conversion efficiencies including beam splitter loss through η_d, and η_0. We now discuss a few cases to illustrate Eq. (2.203)

Case 1:The low frequency limit of Eq. (2.203) can be obtained by setting $\omega = 0$. This case is generally applicable, irrespective of pump conditions(which is still untreated at this point), since the pump serves to change the cutoff frequencies and along with the recombination process is not a concern at lower frequencies. This allows us to obtain

$$F_{ph}(0) = 1 - \frac{\eta_d^2}{\eta_0}\xi_1(\frac{2\xi_2\eta_0}{\xi_1\eta_d} - 1) + \frac{\eta_d^2}{\eta_0}\xi_1 F_p(0) \tag{2.204}$$

When the photons are emitted into each mode as well as detected homogeneously, ie. under the same conditions for each mode. This leads to the conditions that $\theta_l = \theta_m$ and $K_r = K_{r,l}$ which also sets $\xi_1 = \xi_2$. Eq. (2.204) further reduces to

$$F_{ph}(0) = 1 - \frac{\eta_d^2}{\eta_0}(\frac{2\eta_0}{\eta_d} - 1) + \frac{\eta_d^2}{\eta_0}F_p(0) \tag{2.205}$$

Eq. (2.205) is valid for most macrojunction LEDs. The presence of ξ_1 and ξ_2 is valid for microcavities where vacuum fluctuations influence the cavity emission and absorption rates. When the non-radiative processes cease to exist and/or the carrier number dependence of the lifetimes is zero, ie. $\tau_{nr} \to \infty$ or $K_r + K_{nr} = 0$, this leads to the condition $\eta_d = \eta_0$, which reduces Eq. (2.205) to the familiar Fanofactor expression obtained in early experiments[28]

$$F_{ph} = 1 - \eta_0 + \eta_0 F_p \tag{2.206}$$

When the pump currents are Poissonian, $F_p = 1$ and the detected photon Fanofactors are also Poissonian ie. $F_{ph} = 1$. When $F_p = 0$ the photon Fanofactors are limited by the total efficiency of the system as $F_{ph} = 1 - \eta_0$. Any values of F_p in between 0 and 1 create values such as $F_{ph} = 1 - \frac{\eta_0}{c}$ where c tends to ∞ as $F_p \to 1$.

Case 2:Subpoisson light from cavity due to multimodedness of cavity: We assume that there are no non-radiative processes ie. $\eta_d = \eta_0$ which leads to

$$F_{ph} = 1 - \eta_0\xi_1(\frac{2\xi_2}{\xi_1} - 1) + \eta_0\xi_1 F_p \tag{2.207}$$

For $F_p = 1$, we have $F_{ph} = 1 - 2\eta_0(\xi_1 - \xi_2)$. If $\xi_1 - \xi_2 = \frac{1}{2\eta_0}$ then we can establish $F_{ph} = 0$ even when the pump is Poissonian. For $F_p = 0$, we have $F_{ph} = 1 - \eta_0(2\xi_2 - \xi_1)$ and we see that to get $F_{ph} = 0$ we need to set $2\xi_2 - \xi_1 = \frac{1}{\eta_0}$. Hence even when the pump noise is zero, we can still see Poisson outputs and the $F_p = 1$ and $F_p = 0$ cases are completely independent of one another. For eg. if we set $\xi_1 = 0.7$ and $\xi_2 = 0.2$ we have $F_{ph} = 1 - \eta_0$ for $F_p = 1$ but $F_{ph} = 1 + 0.3\eta_0$ for $F_{ph} = 0$ which is clearly superPoisson.

Case 3:Nonradiative process: Now we shall see if subshot noise is possible from the nonlinearity associated with the efficiencies. We assume homogeneous conditions ie. $\xi_1 = \xi_2 = 1$. This leads to

$$F_{ph} = 1 - \frac{\eta_d^2}{\eta_0}(\frac{2\eta_0}{\eta_d} - 1) + \frac{\eta_d^2}{\eta_0}F_p \tag{2.208}$$

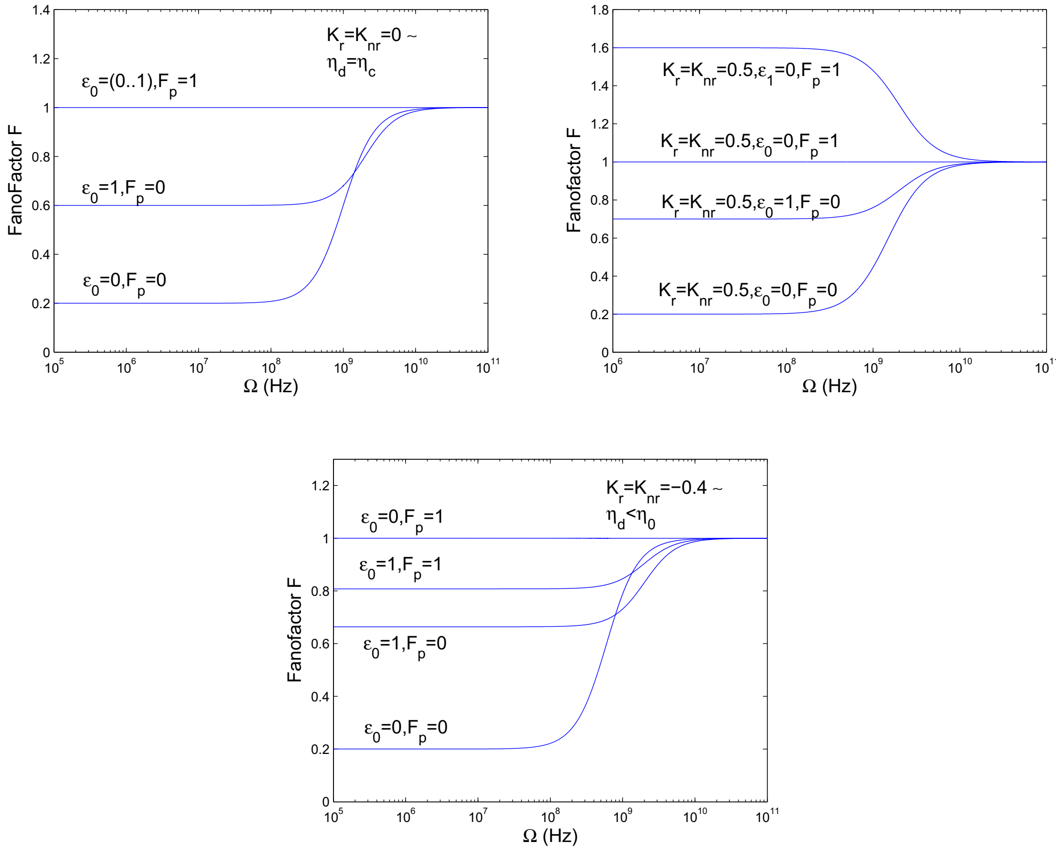

Figure 2.9: Photon Fanofactors for Poisson and Subpoisson pump noise considering the effects of non-radiative mechanisms. Here $\epsilon_0 = \frac{\tau_{r0}}{\tau_{nr0}}$. The three cases treated are a)$K_r = K_{nr} = 0$ b)$K_r = K_{nr} = 0.5$ and $K_r = K_{nr} = -0.4$

For $F_p = 1$ we have $F_{ph} = 1 - \frac{2\eta_d^2}{\eta_0}(\frac{\eta_0}{\eta_d} - 1)$. When $\frac{\eta_0}{\eta_d} = 1$ we have Poisson, for $\frac{\eta_0}{\eta_d} > 1$ superPoisson and for $\frac{\eta_0}{\eta_d} < 1$ subPoisson. For $F_p = 0$, we have $F_{ph} = 1 - \frac{\eta_d^2}{\eta_0}(\frac{2\eta_0}{\eta_d} - 1)$ where we have $\frac{\eta_0}{\eta_d} = 1/2$ for Poisson and $\frac{\eta_0}{\eta_d} > 1/2$ for subPoisson and $\frac{\eta_0}{\eta_d} < 1/2$ for superPoisson.

Case 4:Finite frequency case: The frequency dependent photon Fanofactors of Eq.(2.203) have been plotted in Fig.(2.9). Homogeneous emission conditions have been assumed and we define $\epsilon_0 = \frac{\tau_{r0}}{\tau_{nr0}}$. Figs.(2.9a,b,c) represent the three cases of $K_r = K_{nr} = 0$, $K_r = K_{nr} = 0.5$ and $K_r = K_{nr} = -0.4$. The first two cases do not show the typical relationships between the pump and emitted photons, ie. when the pump is Poisson the emitted photons are Poisson or superPoisson and when the pump is suppressed, the emitted photons are subPoisson. The third case of $K_r + K_{nr} < 0$, corresponds to the situation where $\eta_d < \eta_0$ which can be seen from Eq.(2.200) and Eq.(2.189). In this case, it is possible to achieve a subshot noise even with a Poissonian pump.

2.6.5 Pumping mechanisms

So far we left the pump $P(\omega)$ untreated mainly because, when properly treated it serves to either enhance or reduce the other lifetimes in the problem contributing to variations in squeezing spectra as well as reducing the lower limit to the degree of pumping noise. For example, treating a noiseless pump $\Delta P = 0$ is not acceptable, and we can obtain more precise relationships for it in terms of circuit time constants. One of the most straight forward methods is to add $P = \frac{\eta J}{ed}$ as in Eq.(2.116). Here η is the total charge carrier injection efficiency, J is the current density and d is the thickness of the active region. Another important assumption is that the pump electrons go through enough collisions in the active region to maintain quasi Fermi-Dirac statistics. The current can be treated similar to the Fermi golden rule transitions between two states,ie. we need one k state empty in the active layer and another filled in the pump reservoir. This leads to[34]

$$P_{ek} = \frac{\eta_{tr} J}{edN_0} f_{ek0}(1 - n_{ek}) \tag{2.209}$$

where η_{tr} is the transport factor which indicates the efficiency with which the carrier makes it into the active region and f_{ek0} and N_0 are the Fermi probability and total carrier densities in the absence of an perturbation such as the electromagnetic field. The most important thing to realize is that each quantum state which can be occupied by only one carrier gets filled, $P_{ek} = 0$. This is also known as pump blocking and only the higher energy particles can enter the active region or if the existing carriers thermalize or recombine. The total pump carrier rate is given as $P = \Sigma_k P_{ek}$.This pumping method is popular in the treatment of lasers but it is not strongly applicable to LEDs since the active region is not in a state of inversion. Nevertheless, in high injection conditions it should be included. We assume that most of the currents are in the low to moderate injection regime. We may draw comparison to the backward flow of carriers which take place from the active region to the pump reservoir and is seen at moderately high currents. This is a different effect where the active region carriers do not recombine fast enough and have energies to

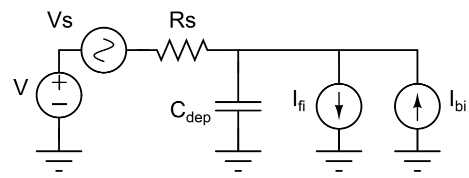

Figure 2.10: The pump equivalent circuit model which describes the charging and discharging of the pn junction by the stochastic forward and backward injection currents

surmount the barrier in the reverse direction. Let us consider Fig.(2.10) where the junction voltage $V_j = V_{bi} - V_a$ is the difference between the Fermi levels between the n and p side of the junction.This is the voltage across the depletion layer capacitance C_{dep} . This circuit diagram is different from the one of Fig.(2.5) which included the diffusion capacitance and the noise terms. The difference stems from the fact that we have constructed a rate equation for carrier densities in the active region as in Eq.(2.164) and this accounts for the effect of recombination and generation through the diffusion capacitance. The pump currents $I_{fi}(t)$ and $I_{bi}(t)$ charge and discharge the junction capacitance and hence this circuit may be called a 'pump' equivalent circuit. There are three mechanisms responsible for changing the depletion layer width x_n . : 1)The external circuit current which pushes the electron cloud forward thus forward biasing the junction and decreasing x_n until steady state is reached. 2)The forward injection of carriers across C_{dep} which causes uncovering of charges and increasing the space charge layer which leads to reverse bias and an increase in x_n. 3)The backward injection current which recovers the ionized charges and decreases the depletion region width x_n. One important assumption here is that $C_{dep} = \frac{\epsilon_o A}{x_n}$ is not affected by the changes in x_n and is assumed constant. This is true since current changes don't affect the capacitance as much as voltage changes which enjoys a $1/\sqrt{V_j}$ relationship. These effects can be added together with appropriate signs to obtain the rate of change of junction voltage.

$$\frac{C_{dep}}{e}\frac{dV_j}{dt} = \frac{I_{ext}}{e} - P_{fi}(t) + P_{bi}(t) \tag{2.210}$$

This is the only expression which does not have a quantum mechanical underpinning but nevertheless the electron FP rate P_{fi} and electron BP rate P_{bi} are treated as operators similar to the pump term of Eq.(2.164). Since the injection process is stochastic, we can split the FP and BP rates into two parts:an average rate which varies according to the time dependent junction voltage $V_j(t)$ and stochastic part which is due to the random carrier injection events and is reduced to zero when averaged ie. $P_{fi}(t) \rightarrow P_{fi}(V_j(t)) + F_{fi}$ and $P_{bi}(t) \rightarrow P_{bi}(n_c(t)) + eF_{bi}$ Here F_{fi} and F_{bi} are the Langevin noise operators. The external circuit current is expressed as $I_{ext} = \frac{V-V_j}{R_S}$. Since the resistor is a source of thermal fluctuations of $V_{Rs} = \sqrt{4kTR_s}$, we can define the 'current' Langevin operator associated with it as $F_{rs_I} = V_{Rs}/R_s$ with associated Markoffian correlation function $< F^{\dagger}_{rs_I} F_{rs_I} >= \frac{4kT}{R_s}$.This is the stochastic part of the external current which is $I_{ext}(t) \rightarrow \frac{V-V_j}{R_s} + eF_{rs}$.Substituting these relations in Eq.(2.210) we get

$$\frac{C_{dep}}{e}\frac{dV_j}{dt} = \frac{V - V_j}{eR_s} - P_{fi}(V_j) + P_{bi}(n_c) - F_{fi} + F_{bi} + F_{rs_I} \tag{2.211}$$

Note that the FP and BP rates also give us the forward and backward currents $I_{fi}(t) = eP_{fi}(t)$ and $I_{bi}(t) = eP_{bi}(t)$ flowing across the junction. In the steady state ie.setting $\frac{dV_j}{dt} = 0$ we obtain

$$\frac{V - V_{j0}}{eR_s} = P_{fi}(V_{j0}) + P_{bi}(n_{c0}) \tag{2.212}$$

where the subscript 0 indicates the steady state values.We can now linearize Eq.(2.211) by expanding about its steady state values ie $V_j = V_{j0} + \Delta V_j$ and $n_c = n_{c0} + \Delta n_c$.We substitute these relations in Eq.(2.211) taking into consideration Eq.(2.212) to obtain the junction voltage fluctuation rate as

$$\frac{C_{dep}}{e}\frac{d\Delta V_j}{dt} = -\frac{\Delta V_j}{eR_s} - \Delta P_{fi} + \Delta P_{bi} - F_{fi} + F_{bi} + F_{rs_I} \tag{2.213}$$

where $\Delta P_{fi} = P_{fi}(V_{j0} + \Delta V) - P_{fi}(V_{j0})$ and $\Delta P_{bi} = P_{bi}(n_{c0} + \Delta n_c) - P_{fi}(V_{j0})$ .Taking the Fourier transform of Eq.(2.213) and using F_{rs_V} which is the voltage variant of the Langevin force with Markoffian correlation $< F_{rs_V} F_{rs_V} >= 4kTR_s$ instead of F_{rs_I} we obtain

$$\Delta V_j(\omega) = -\frac{e}{C_{dep}}\frac{\tau_{RC}}{1 + i\omega\tau_{RC}}(\Delta P_{fi} + \Delta P_{bi} - F_{fi} + F_{bi} + \frac{C_{dep}}{e\tau_{RC}}F_{rs_V}) \tag{2.214}$$

Eq.(2.214) can be now shown to satisfy the microscopic pulse description shown in Fig.(2.6). When an electron crosses the depletion region at a random time t_i,it creates +e at the n-depletion region edge and -e in the active region and the sum FP rate is $P_{fi}+F_{fi} = \Sigma_i \delta(t-t_i)$ .Integrating this expression and using the integral definition $u(x) = \int_{-\infty}^{x} \delta(t)dt$

$$\int (P_{fi}(t) + F_{fi}(t))dt = \Sigma_i u(t - t_i) \tag{2.215}$$

where $u(t)$ is the unit step function.This gives us the total number of such pulses N in some interval and resembles the typical Poisson staircase. Each FP event results in the in the change of junction voltage by $-e/C_{dep}$.The FP events tend to bring in charges from the external circuit with a time constant $\tau_{RC} = R_S C_{dep}$ in order to restore the junction to its stead state value.The external current is made up of the same number of FP events given by $I_{ext} = \frac{e}{\tau_{RC}} \Sigma_i \exp[-(t-t_i)/\tau_{RC}] u(t-t_i)$.The pulses can be integrated as

$$\int I_{ext} dt = e \sum_i (1 - e^{-(t-t_i)/\tau_{RC}}) u(t-t_i) \tag{2.216}$$

Adding Eq.(2.215) and Eq.(2.216) we obtain the resultant junction voltage fluctuations induced by the FP process and the subsequent recharging by the external circuit as

$$\Delta V_{j1} = \frac{-e}{C_{dep}} \sum_i e^{-(t-t_i)/\tau_{RC}} u(t-t_i) \tag{2.217}$$

Applying the Fourier transform to the above equation gives

$$\Delta V_{j1}(\omega) = -\frac{e}{C_{dep}} \frac{\tau_{RC}}{1 + i\omega\tau_{RC}} \Sigma e^{-i\omega t_i} \tag{2.218}$$

If we apply the Fourier transform to the FP rate and the Langevin term we see that $FT(P_{fi} + F_{fi}) = FT(\Sigma_i \delta(t - t_i)) = \Sigma_i e^{-i\omega t_i}$.This gives us

$$\Delta V_{j1} = -\frac{e}{C_{dep}} \frac{\tau_{RC}}{1 + i\omega\tau_{RC}} (\Delta P_{fi} + F_{fi}) \tag{2.219}$$

We can obtain a similar expression for the junction voltage fluctuations induced by the BP rate and the Langevin force as

$$\Delta V_{j2} = \frac{e}{C_{dep}} \frac{\tau_{RC}}{1 + i\omega\tau_{RC}} (\Delta P_{bi} + F_{bi}) \tag{2.220}$$

The last contribution is the thermal noise of R_S which fluctuates the junction voltage. This is seen as an additional noise component in the external circuit pulses that affects the junction voltage even if there is no current and in thermal equilibrium. It can be written as

$$\Delta V_{rs} = \frac{1}{C_{dep}} \int i(t) dt = \frac{F_{rs}}{1 + i\omega\tau_{RC}} \tag{2.221}$$

Adding Eqs.(2.219-2.221) together we obtain the net junction voltage fluctuations caused by the FP and BP rates, subsequent circuit responses and the thermal noise current of R_s and we see that summed result shows us that the pulse description of Fig.(2.6) satisfies Eq.(2.214) since they are similar.

2.6.6 Field Langevin Equation under Homogeneous emission conditions

In typical macroscopic LEDs, we can make a few simplifying assumptions: The transmission coefficients for each mode are equal and we can set $\theta_l = \eta_c$. Also the radiative lifetime in each mode is assumed to be the same ie. homogeneous emission conditions where each photon is emitted and detected in the same manner which leads to $\xi_1 = \xi_2 = 1$. Summing all the modes of photons inside the cavity ie.$n = \Sigma_l n_l$, Eq.(2.156) then becomes

$$\frac{dn}{dt} = -\kappa n + \frac{n_c}{\tau_r} + F_r + F_k \tag{2.222}$$

where $F_\kappa = \Sigma_{ll} F_{\kappa,l}$ and $F_r = \Sigma_l F_{r,l}$ and the decay constant κ_l for each mode is the same. The total number of photons outside the cavity can be obtained by summing Eq.(2.177) over all modes which leads to $\Sigma_l V_l = V = \kappa n - F_\kappa$. Since $\omega \ll \kappa$ under typical experimental conditions, we can assume Eq.(2.222) reaches steady state, ie. $\frac{dn}{dt} = 0$ which gives $\kappa n = \frac{n_c}{\tau_r} + F_r + F_k$ from which $V = \frac{n_c}{\tau_r} + F_r$. Linearizing V, followed by taking the Fourier transform gives us

$$\Delta V(\omega) = \frac{\Delta n_c(\omega)}{\tau_r} + F_r = \Sigma_l \Delta V_l(\omega) \tag{2.223}$$

where the last equality states that the total fluctuation is equal to the fluctuation in each mode. However note that $\Delta V^2 \neq \Sigma_l \Delta V_l^2$ from which $\langle \Delta V^\dagger \Delta V \rangle = \Sigma_{ll'} \langle \Delta V_l \Delta V_{l'} \rangle$. The homogeneous emission conditions play an important part in writing the equation in this form. Otherwise the multimoded-ness will stand out. Eq.(2.184) now becomes

$$\langle |\Delta N|^2 \rangle = \eta_c (1 - \eta_c) \sum_l \langle V_l \rangle + \eta_c^2 \langle \Delta V^\dagger \Delta V \rangle \tag{2.224}$$

In order to distinguish Eq.(2.224) from Eq.(2.184), we replace $\langle |\Delta N|^2 \rangle = \langle \Delta \Phi^\dagger \Delta \Phi \rangle$ which is the spectral density of the flux at the photodetector due to all modes. Substituting the first equality of Eq.(2.223) in Eq.(2.224) gives us

$$\langle \Delta \Phi^\dagger \Delta \Phi \rangle = \eta_c (1 - \eta_c) \frac{n_{c0}}{\tau_r} + \eta_c^2 (\frac{\Delta n_c^\dagger \Delta n_c}{\tau_r^2} + \langle \Delta n_c^\dagger F_r \rangle + \langle F_r^\dagger \Delta n_c \rangle + \langle F_r^\dagger F_r \rangle) \tag{2.225}$$

The reason we arrived at Eq.(2.225) is two fold: a)For LED structures, the modes inside and outside the cavity can be considered as continuous, allowing us to consider a cavity as big as the cube on whose edges the detector is placed. This allows us to state that the radiative recombination rate $\frac{n_{c0}}{\tau_r}$ is the same as the photodetector current in a unity efficiency detector. So we do not need to deal with the multimodedness of the cavity. b)We have added another equation of motion to describe the junction voltage fluctuations, which in turn modulates the pump rate. This requires us to solve rate of change of junction voltage fluctuation, carrier number, photon number inside the cavity and finally photon number outside the cavity which makes the problem more complex. By making the assumption that photons inside are equal to photons outside the cavity, we do not need Eq.(2.177) leaving only three equations to solve. We shall next obtain Eq.(2.225) by including the pump regulation mechanisms such as the macroscopic Coulomb blockade and non-linear backward pump processes.

2.6.7 Photon Number Noise with Regulated Current flows

The linearized small signal equation of motion for the carrier densities in Eq.(2.191) is modified to include the effects of the FP and BP rates as discussed in Section.5.5 to give

$$\frac{d\Delta n_c}{dt} = \Delta P_{fi} - \Delta P_{bi} - \frac{\Delta n_c}{\tau''} + F_{fi} - F_{bi} + F_r + F_{nr} \tag{2.226}$$

where the single c-number pump operator P has been replaced by operators which increase and decrease the carrier densities of the active region by the process of forward($P_{fi} + F_{fi}$) and backward injection($P_{bi} + F_{bi}$). Since the FP rate is modulated by the junction voltage fluctuation, it is a function of V_j which allows us to write

$$\Delta P_{fi} = \frac{dP_{fi}(V_j)}{dV_j}|_{V_j=V_{j0}} \Delta V_j = \frac{C_{dep}}{\tau_{fi}} \Delta V_j \tag{2.227}$$

where $\tau_{fi} = C_{dep}(\frac{dI_{fi}}{dV_j})^{-1}$ is the forward injection time or the time taking a single carrier to transit across the junction in the forward direction. The BP rate is assumed to depend only on the carrier number at that instant of time(Note that n_c is in turn dependent on the junction voltage fluctuations) which allows us to write

$$\Delta P_{bi} = \frac{dP_{bi}(n_c)}{dn_c}|_{n_c=n_{c0}} \Delta n_c = \frac{\Delta n_c}{\tau_{bi}} \tag{2.228}$$

where $\tau_{bi} = (\frac{dP_{bi}(n_c)}{dn_c})^{-1}$ is the backward injection lifetime. Using the definitions of Eq.(2.227) and Eq.(2.228) in Eq.(2.226) and Eq.(2.213), we obtain

$$\frac{d\Delta n_c}{dt} = \frac{C_{dep}}{\tau_{fi}}\Delta V_j - \frac{\Delta n_c}{\tau_{bi}} - \frac{\Delta n_c}{\tau''} + F_{fi} - F_{bi} + F_r + F_{nr} \tag{2.229}$$

$$\frac{C_{dep}}{e}\frac{d\Delta V_j}{dt} = -\frac{\Delta V_j}{eR_s} - \frac{C_{dep}}{\tau_{fi}}\Delta V_j + \frac{\Delta n_c}{\tau_{bi}} - F_{fi} + F_{bi} + F_{rs_I} \tag{2.230}$$

Taking the Fourier transform of the above equations we get

$$\frac{C_{dep}}{e}\Delta V_j = \frac{\tau_{fi}\tau_{RC}}{\tau_{fi} + \tau_{RC} + i\omega\tau_{fi}\tau_{RC}}(\frac{\Delta n_c}{\tau_{bi}} - F_{fi} + F_{bi} + F_{rs}) \tag{2.231}$$

$$\Delta n_c = \frac{\tau''\tau_{bi}}{\tau'' + \tau_{bi} + \imath\omega\tau''\tau_{bi}}(\frac{C_{dep}\Delta V_j}{e\tau_{fi}} - F_r + F_{fi} - F_{bi}) \tag{2.232}$$

Solving the above two equations algebraically we get

$$C_{dep}\Delta V_j = \frac{1}{A+iB}(-\frac{\tau''\tau_{fi}}{\tau_{bi}}F_r - \tau_{fi}(1 + i\omega\tau'')(F_{fi} - F_{bi}) + \tau_{fi}(1 + i\omega\tau'' + \frac{\tau''}{\tau_{bi}})F_{rs_I}) \tag{2.233}$$

$$\Delta n_c = \frac{1}{A+iB}\tau''(-(1 + \frac{\tau_{fi}}{\tau_{RC}} + i\omega\tau_{fi})F_r + (\frac{\tau_{fi}}{\tau_{RC}} + i\omega\tau_{fi})(F_{fi} - F_{bi}) + \frac{C_{dep}}{e\tau_c}F_{rs_V}) \tag{2.234}$$

where

$$A = 1 - \omega^2\tau''\tau_{fi} + \frac{\tau_{fi}}{\tau_{RC}}(1 + \frac{\tau''}{\tau_{bi}}) \tag{2.235}$$

$$B = \omega(\tau_{fi} + \tau'' + \frac{\tau_{fi}\tau''}{\tau_{bi}} + \frac{\tau_{fi}\tau''}{\tau_{RC}}) \tag{2.236}$$

The spectral density of the photon flux is obtained by substituting Eq.(2.233) and Eq.(2.234) in Eq.(2.225) to give

$$\begin{aligned} S_{\Delta\Phi} = {} & \eta_c S_{F_r} - \frac{\eta_c^2}{A^2+B^2}[\{2A(1 + \frac{\tau_{fi}}{\tau_{RC}}) + 2B\omega\tau_{fi}\}S_{F_r} - \{(1 + \frac{\tau_{fi}}{\tau_{RC}})^2 + \omega^2\tau_{fi}^2\}S_{F_r} \\ & - \frac{C_{dep}^2}{e^2\tau_c^2}S_{F_{rs}} - \{(\frac{\tau_{fi}}{\tau_{RC}})^2 + \omega^2\tau_{fi}^2\}(S_{F_{fi}} + S_{F_{bi}})] \end{aligned} \tag{2.237}$$

where $S_{F_{fi}}$ and $S_{F_{bi}}$ are the spectral densities of the forward and backward processes which are defined from Eq.(2.103) as $S_{F_{fi}} = \frac{1}{1-\alpha_{0,eff}}P_0$ and $S_{F_{bi}} = \frac{\alpha_{0,eff}}{1-\alpha_{0,eff}}P$ where the substitution $\alpha_0 \rightarrow \alpha_{0,eff}$ has been made to include the effect of non-radiative processes. One does not need Eq.(2.159) to arrive at the pump spectral densities. They can be obtained by noting that the forward and backward events are shot noise process, and the spectral density of shot noise process is equal to the DC average value. The photon Fanofactor is obtained from Eq.(2.237) as

$$\begin{aligned} F_{ph} &= \frac{S_{\Delta\Phi}}{\eta_0 P_0} = 1 - \frac{\eta_c}{A^2+B^2}[\{2A(1+\frac{\tau_{fi}}{\tau_{RC}}) + 2B\omega\tau_{fi}\} - \frac{\eta_c}{\eta_0}[\{(1+\frac{\tau_{fi}}{\tau_{RC}})^2 + \omega^2\tau_{fi}^2\} \\ &+ \frac{1}{(1-\alpha_{0,eff})(1-\alpha_{d,eff})}\frac{2}{n}\frac{R_s}{R_d} + \{(\frac{\tau_{fi}}{\tau_{RC}})^2 + \omega^2\tau_{fi}^2\}\frac{1+\alpha_{0,eff}}{1-\alpha_{d,eff}}]] \end{aligned} \tag{2.238}$$

Eq.(2.77) is the central equation in this chapter which describes the photon emission statistics for a LED based upon the following time constantsτ_{fi},τ_{bi},τ_{RC},τ_r. The expression is independent of the nature of the junction as the specific choice of a junction simply redefines τ_{fi} and τ_{bi} For our homo/heterojunction case, the forward emission time is obtained from Eq.(2.109) as $\tau_{fi} = \frac{kTC_{dep}}{eI_{fi}} = \frac{kTC_{dep}}{eI_{)}}(1-\alpha_{0,,eff}) = C_{dep}r_{dj,eff}$ where $r_{dj,eff}$ has been defined in Eq.(2.113). Also an expression for τ_{bi} can be obtained by comparing Eq.(2.228) with Eq.(2.105) to obtain $\tau_{bi} = \frac{1-\alpha_d}{\alpha_d}\tau_r'$. Substituting $\tau'' = \frac{\eta_d}{\eta_c}\tau_r$, $\tau_{bi} = \frac{1-\alpha_d}{\alpha_d}\tau_r$ and choosing $r = \frac{\tau_{RC}}{\tau_{fi}}$, we can temper Eq.(2.238) to the form

$$\begin{aligned} F_{ph} &= 1 - \frac{\eta_c}{A'^2+B'^2}[\{2(1-\alpha_d)\{A(1+r) + 2B\omega\tau_{RC}\} - \frac{\eta_c}{\eta_0}(1-\alpha_d)^2[\{(1+r)^2 + \omega^2\tau_{RC}^2\} \\ &+ \frac{1}{(1-\alpha_{0,eff})(1-\alpha_{d,eff})}\frac{2}{n}\frac{R_s}{R_d} + \{1 + \omega^2\tau_{RC}^2\}\frac{1+\alpha_{0,eff}}{1-\alpha_{d,eff}}]] \end{aligned} \tag{2.239}$$

where

$$A' = \frac{\eta_c}{\eta_d}(1-\alpha_d)(1+r) - \omega^2\tau_{RC}\tau_r(1-\alpha_d) + \alpha_d \tag{2.240}$$

$$B' = (1-\alpha_d)(1+r)\omega\tau_r + \frac{\eta_c}{\eta_d}(1-\alpha_d)\omega\tau_{RC} + \alpha_d\omega\tau_{RC} \tag{2.241}$$

Based on the modes of operation of the diode, we can study Eq.(2.238) under the following cases:

a)High impedance conditions: Here $R_d \ll R_s$ which leads to $\tau_{te} \ll \tau_{RC}$. We also assume that there are no non-radiative process and Eq.(2.239) becomes

$$\begin{aligned} F_{ph} &= 1 - \eta_c\frac{1 - 2\omega^2\tau_{fi}^2(\frac{\alpha_0}{1-\alpha_0}) + 2\omega^2\alpha_d\tau_{fi}\tau_{te}}{1 + 2\alpha_d(\omega\tau_r)(\omega\tau_{te}) + (1-\alpha_d)^2(\omega\tau_r)^2(\omega\tau_{te})^2 + (\omega\tau_{te})^2 + (\omega\tau_r)^2} \\ &= 1 - \eta_c\frac{1 + 2\omega^2\tau_{te}^2(1-\alpha_d)\frac{(\alpha_d-\alpha_0)}{1-\alpha_0}}{1 + 2\alpha_d(\omega\tau_r)(\omega\tau_{te}) + (1-\alpha_d)^2(\omega\tau_r)^2(\omega\tau_{te})^2 + (\omega\tau_{te})^2 + (\omega\tau_r)^2} \end{aligned} \tag{2.242}$$

where $\tau_{fi} = (1-\alpha_0)\frac{kT}{eI_{LED}} = (1-\alpha_0)\tau_{te,0}$. For the thermionic emission case($\alpha_0, \alpha_d \to 1$) Eq.(2.242) gives

$$F_{ph} = 1 - \eta_c \frac{1}{(1+\omega^2\tau_{te}^2)(1+\omega^2\tau_r^2)} \tag{2.243}$$

For the diffusion case, Eq.(2.242) gives

$$F_{ph} = 1 - \eta_c \frac{1}{1+\omega^2(\tau_{te}+\tau_r)^2} \tag{2.244}$$

b) Constant Voltage conditions: Here $R_d \gg R_S$ which also implies $\tau_{te} \gg \tau_{RC}$. Eq.(2.239) is now

$$F_{ph} = 1 - \frac{2\eta_c(1-\alpha_d)\{\frac{\eta_c}{\eta_d}(1-\alpha_d)+\alpha_d\} - \frac{\eta_c^2}{\eta_0}(1-\alpha_d)^2\frac{2}{1-\alpha_{0,eff}}}{\{\frac{\eta_c}{\eta_d}(1-\alpha_d)+\alpha_d\}^2 + (1-\alpha_d)^2\omega^2\tau_r^2} \tag{2.245}$$

Let us first consider the thermionic emission case($\alpha_0 = \alpha_d = 0$)

$$F_{ph} = 1 - \frac{\frac{2\eta_d^2}{\eta_0}\{\frac{\eta_0}{\eta_d} - 1\}}{1+\omega^2\frac{\eta_d^2}{\eta_c^2}\tau_r^2} \tag{2.246}$$

Eq.(2.246) agrees with Eq.(2.205) for the case $F_p = 1$. This similarity tells us that by leaving the pump untreated, the Fanofactors obtained are for the thermionic emission case. The pump being at the shot noise level translates to the shot noise for the photon flux as expected for the constant voltage case. For the diffusive case of $\alpha_0 = \alpha_d \to 1$, Eq.(2.245) provides $F_{ph} \approx 1$. This may be explained as follows: In the case of thermionic emission, the pump current does not include the backward recombination current and hence the radiative processes. So the Fanofactors essentially decouple into the pump and radiative mechanisms separately each of them Poisson processes. But since the recombination is instantaneous, the pump shot noise process is the one observed in the photon flux. But in the case of diffusion, the recombination and pump processes becomes tightly coupled. For example an electron may return to the pump reservoir before recombining changing the simple Poisson recombination statistics. We can however attempt to treat the problem by considering three random processes which are all Poisson a)the forward pump b) the backward pump and c)the recombination. The forward and backward pump events take place on the time scales of $\tau_{fi} \approx \tau_{bi} = 0$ compared to the radiative lifetime τ_r. This causes the forward and backward current to monitor each each, reducing the net current noise and what is left is the random recombination process. Hence the noise is Poissonian.

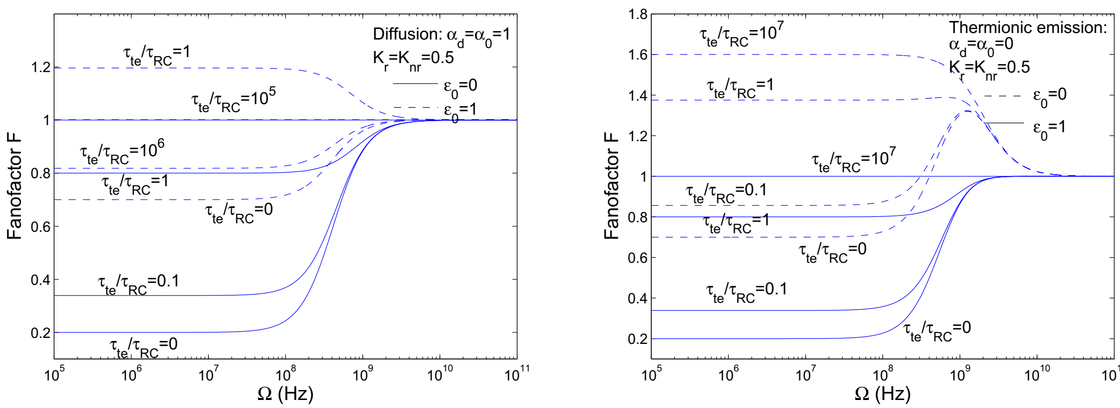

Figure 2.11: Photon Fanofactors under constant voltage and constant current conditions for the thermionic emission and the diffusion regime pump models. Constant current case is reached when $\tau_{RC} \gg \tau_{te}$ and the constant voltage case is true when $\tau_{RC} \ll \tau_{te}$ is satisfied.

Now let us assume that there are no non-radiative processes which implies $\eta_d = \eta_0 = \eta_c$. Eq. (2.245) then gives us

$$F_{ph} = 1 - \frac{2\eta_c(1-\alpha_d)\{\frac{\alpha_d-\alpha_0}{1-\alpha_0}\}}{1+(1-\alpha_d)^2\omega^2\tau_t^2} \tag{2.247}$$

From Eq.(2.247), we see that for thermionic emission or diffusion we end up with $F_{ph} \approx 1$. For the condition $\alpha_d > \alpha_0$, we see that there is subshot behavior. We can obtain a subPoisson case under constant voltage conditions itself. This is the regime of squeezing due to the nonlinear backward pump model. This case is not studied in our experiments as it creates a situation where both constant voltage and constant current produces subshot noise. In the noise modulation experiments of chapter 4, it is a requirement to switch between constant voltage and constant current modes and expect shot and subshot noise respectively. This controls the variance of noise and is the essence of the stochastic communication method. In Fig.(2.11), we plot the finite frequency photon Fanofactors of Eq.(2.238) for the diffusion and thermionic emission case under constant voltage and constant current operations. We see that the results of Fig.(2.11) agree with each of the simple cases discussed above.

2.6.8 Pump rate fluctuations

We would also like to determine the pump fluctuations independently of the detected Fanofactors. The net current fluctuations can be rewritten as

$$\Delta P_{fi}(\omega) = P_{fi} - P_{fi0} = P_{fi0}\frac{q\Delta V_j}{kT} \tag{2.248}$$

The pump fluctuations can be obtain from the voltage fluctuations of Eq.(2.214) as

$$\Delta P_{fi} = -\frac{1}{\tau_{te,fi}}\frac{\tau_{RC}}{1+i\omega\tau_{RC}}(\Delta P_{fi} + F_{fi} - \Delta P_{bi} - F_{bi} - \frac{C_{dep}}{e\tau_{RC}}F_{rs}) \tag{2.249}$$

where $\tau_{fi} = \frac{kT}{eI_{fi0}}C_{dep} = (1-\alpha_{0,eff})\frac{kT}{eI_0}C_{dep} = (1-\alpha_{d,eff})\tau_{te,eff}$. The net forward injection process with the Langevin term gives

$$\Delta P_{fi} + F_{fi} = \frac{F_{fi}(1+i\omega\tau_{RC}) + \frac{\tau_{RC}}{\tau_{fi}}(\Delta P_{bi} + F_{bi} + \frac{C_{dep}}{e\tau_{RC}}F_{rs})}{1+\frac{\tau_{RC}}{\tau_{fi}} + i\omega\tau_{RC}} \tag{2.250}$$

Similarly one can write an expression for the backward injection events as

$$\Delta P_{bi} + F_{bi} = \frac{\alpha_{d,eff}}{1-\alpha_{d,eff}}\frac{\eta_c}{\eta_d}\frac{\Delta n_c}{\tau_r} + F_{bi} \tag{2.251}$$

The net fluctuations can be obtained as $\Delta P_{net} = \Delta P_{fi} + F_{fi} - \Delta P_{bi} - F_{bi}$ from which

$$\Delta P_{net} = \frac{F_{fi}(1+i\omega\tau_{RC}) + r\frac{C_{del}}{e\tau_{RC}}F_{rs} - (1+i\omega\tau_{RC})(\frac{\alpha_{d,eff}}{1-\alpha_{d,eff}}\frac{\eta_c}{\eta_d}\frac{\Delta n_c}{\tau_r} + F_{bi})}{1+r+i\omega\tau_{RC}} \tag{2.252}$$

where for simplicity r is the ratio τ_{RC}/τ_{fi}. We note that the above equation is dependent of Δn_c which is in turn coupled to two other equations. Substituting Eq.(2.234) in Eq.(2.252) and grouping together the various terms we end up with the following result for the pump fluctuations

$$\begin{aligned}\Delta P_{net} \quad &= \quad \frac{1}{(A+iB)(1+r+i\omega\tau_{RC})}\{[(A-\alpha') + i(B-\omega\alpha'\tau_{RC})]((1+i\omega\tau_{RC})(F_{fi}+F_{bi}) \\ &\quad + F_{rs}\frac{rC_{dep}}{e\tau_{RC}}) + \alpha'(1+r+i\omega\tau_{RC})(1+i\omega\tau_{RC})(F_r+F_{nr})\}\end{aligned} \tag{2.253}$$

where $\alpha' = \frac{\alpha_{d,eff}}{(1-\alpha_{d,eff})}\frac{\eta_c}{\eta_d}(1-\alpha_d)$. We can calculate the spectral fluctuations as $\langle\Delta P^{\dagger}_{net}\Delta P_{net}\rangle$ and obtain the Fanofactor as $F_p = \frac{\langle\Delta P^{\dagger}_{net}\Delta P_{net}\rangle}{P_0}$ .The resulting expression after substituting the necessary correlations are

$$F_p = \frac{1}{(A^2+B^2)((1+r)^2+\omega^2\tau_{RC}^2)}\{((A-\alpha')^2+(B-\omega\alpha'\tau_{RC})^2)(1+\omega^2\tau_{RC}^2)\frac{1+\alpha_{0,eff}}{1-\alpha_{0,eff}} + \frac{1}{(1-\alpha_{d,eff})(1-\alpha_{0,eff})}\frac{2R_s}{nr_{dj,eff}}) + \alpha'^2((1+r)^2+\omega^2\tau_{RC}^2)(1+\omega^2\tau_{RC}^2)\} \quad (2.254)$$

We shall consider only the low frequency case ie. $\omega\tau_{RC} \ll 1, \omega\tau_r \ll 1$ and ignore non-radiative recombination which sets $\alpha_{0,eff} = \alpha_0$ and $\alpha_{d,eff} = \alpha_d$. For constant voltage case, we obtain

$$F_p = (1-\alpha_d)^2\frac{1+\alpha_0}{1-\alpha_0} + \alpha_d^2 \quad (2.255)$$

The first term is due to the forward and backward emission processes and the second term is due to recombination induced fluctuations. The reason why the recombination noise affects the net pump noise is that the backward injection events are dependent on the electron population in the active region Δn_c and is affected by F_r which fluctuates the carrier number due to recombination. If we assume the linear relationship$\alpha_0 = \alpha_d$, we have $F_p = (1-\alpha_0^2) + \alpha_0^2$ which is true for either thermionic emission or diffusion conditions. For the case of diffusion($\alpha_0 = 1$), the first part which is due to the forward and backward injection events, is completely suppressed below the full shot noise by the linear correlation between the forward and backward injections but the negative feedback caused by the backward pump events is completely removed by the recombination induced noise. For the thermionic emission case($\alpha_0 = 0$), the recombination noise does not affect the pump since the backward injection events do not exist. In [32], the researchers have found that the nonlinear case $\alpha_d > \alpha_0$, provides a stronger negative feedback due to the BP process which overcomes recombination induced noise producing a subshot pump even under constant voltage conditions. Under constant current conditions, we see from Eq.(2.254), that under thermionic emission or diffusion conditions the low frequency pump Fanofactor is

$$F_p \approx (\frac{\tau_{te}}{\tau_{RC}})^2 \quad (2.256)$$

and hence $F_p \ll 1$. This is the same result predicted by the simple equivalent circuit model in Eq. (2.73).

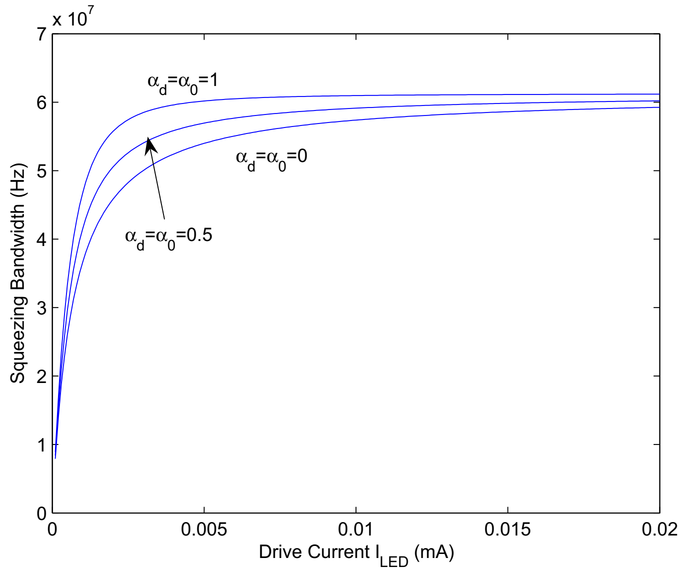

Figure 2.12: 3dB Squeezing bandwidth as a function of LED drive current for the pump model evaluated from the thermionic emission to the diffusion limits.

2.6.9 Squeezing Bandwidth

The squeezing bandwidth is defined as the frequency at which the frequency dependent Fanofactor is reduced by a factor of 2 compared to the Fanofactor at the dc frequency limit. This can be calculated from Eq. (2.242) by setting

$$1-\eta_c\frac{1+2\omega^2\tau_{te}^2(1-\alpha_d)\frac{(\alpha_d-\alpha_0)}{1-\alpha_0}}{1+2\alpha_d(\omega\tau_r)(\omega\tau_{te})+(1-\alpha_d)^2(\omega\tau_r)^2(\omega\tau_{te})^2+(\omega\tau_{te})^2+(\omega\tau_r)^2}=1-\frac{\eta_c}{2} \quad (2.257)$$

The frequency ω which satisfies the above condition is the cutoff frequency of the squeezing(subshot noise) and we can denote it as $\omega=\omega_c$ which is determined as

$$\omega_c=\sqrt{\frac{1}{2(1-\alpha_d)^2\tau_r^2\tau_{te}^2}\left\{-(C)+\sqrt{C^2+4(1-\alpha_d)^2\tau_r^2\tau_{te}^2}\right\}} \quad (2.258)$$

where $C=\tau_r^2+\tau_{te}^2+2\alpha_d\tau_r\tau_{te}-4\frac{(1-\alpha_d)}{(1-\alpha_0)}(\alpha_d-\alpha_0)\tau_{te}^2$. In the case of the thermionic emission limit obtained by setting $\alpha_d,=\alpha_0=0$, the cutoff frequency is given by

$$\omega_c=\sqrt{\frac{1}{2\tau_{te}^2\tau_r^2}\left(-(\tau_r^2+\tau_{te}^2)+\sqrt{\tau_r^4+\tau_{te}^4+6\tau_r^2\tau_{te}^2}\right)} \quad (2.259)$$

In the case of the diffusion limit ie. $\alpha_d=\alpha_0=1$, we obtain the limit

$$\omega_c=\frac{1}{\tau_{te}+\tau_r} \quad (2.260)$$

which is the bandwidth predicted by the equivalent noise circuit model of the pn diode. Fig.(2.12) plots the functional dependence of squeezing on the LED drive current which is varied through the parameter $\tau_{te} = kTC_{dep}/eI_0$ .The squeezing dependence is plotted for three different constant values of 0,0.5 and 1 for α_0 and α_d but with the same values for C_{dep} and drive currents. Kobayashi et al[12] have shown that as the drive current is increased for a double barrier heterojunction diode, the experimental results start from the thermionic emission limit, followed by gradual changes in α_0, α_d until it reached the diffusion limit. In other words, the BP rates are functions of increasing drive current. So in the case of homojunction and heterojunctions where diffusion is the current mechanism, the injected electrons may easily go back whereas for heterojunction diodes at low current levels, the presence of large barrier(conduction band discontinuity) prevents this backward flow of electrons. Both these mechanisms affect the frequency dependent squeezing characteristics as seen in Fig. (2.12). Also we can see that both the thermionic emission and diffusion models predict the same cutoff frequency at high currents. In fact, this is a problem experimentally, as one needs to perform experiments at low drive currents to determine the squeezing bandwidths in order to ascertain if the device falls within the thermionic emission or diffusion model or in between. Note that even homojunction based diodes can have thermionic emission if the diffusion velocity is much larger than the thermal velocity $v_{diff} \gg v_{Rth}$ according to Eq. (2.109). At the present, the BP parameter is dependent on the electron population n_c in the active region which is in turn affected by the carrier dependent velocities.

2.6.10 Correlations between the fluctuation quantities

Correlation between junction voltage and carrier number

The normalized correlations between the junction voltage fluctuations and the carrier number are defined as

$$|C_{n,v}|^2 = \frac{\langle \frac{C_{dep}}{e} \Delta n_c^*(\omega) \Delta V_j(\omega) \rangle^2}{\frac{C_{dep}^2}{e^2} \langle \Delta n_c^*(\omega) \Delta n_c(\omega) \rangle \langle \Delta V_j^*(\omega) \Delta V_j(\omega) \rangle} \tag{2.261}$$

For the case of diffusion $\alpha_d, \alpha_0 \rightarrow 1$, which leads to the following definitions

$$\langle\frac{C_{dep}}{e}\Delta n_c^*(\omega)\Delta V_j(\omega)\rangle = \frac{\tau_{te}\tau_r}{A^2+B^2}(S_{F_r}+S_{F_{rs}}) \ , \ \langle\Delta n_c^*(\omega)\Delta n(\omega)\rangle = \frac{\tau_r^2}{A^2+B^2}(S_{F_r}+S_{F_{rs}})$$
$$\langle\frac{C_{dep}^2}{e^2}\Delta V_j^*(\omega)\Delta V_j(\omega)\rangle = \frac{\tau_{te}^2}{A^2+B^2}(S_{F_r}+S_{F_{rs}})$$

which causes $|C_{n,v}|^2 = 1$. In the case of the thermionic emission limit $\alpha_0, \alpha_d \rightarrow 1$, which leads to the following definitions

$$\langle\frac{C_{dep}}{e}\Delta n_c^*(\omega)\Delta V_j(\omega)\rangle = \tfrac{\tau_{te}\tau_r}{A^2+B^2}(S_{F_{rs}}) \ , \langle\Delta n_c^*(\omega)\Delta n(\omega)\rangle = \frac{\tau_r^2}{A^2+B^2}(S_{F_r}+S_{F_{rs}})$$
$$\langle\frac{C_{dep}^2}{e^2}\Delta V_j^*(\omega)\Delta V_j(\omega)\rangle = \frac{\tau_{te}^2}{A^2+B^2}(S_{F_{fi}}+S_{F_{bi}}+S_{F_{rs}})$$

which leads to $|C_{n,V}|^2 \approx 1$. What we see is that irrespective of the constant voltage or constant current biasing conditions(irrespective of the value of τ_{RC}) or whether the device has diffusion limited or thermionic emission limited current, the correlations between junction voltage and carrier number approach unity. The reason behind this is that any changes in carrier number due to forward and backward injection of carriers which move rapidly back and forth across the junction with time constants τ_{fi}, τ_{bi} establishing the correlation between the junction voltage and carrier number. Any recombination will cause a reduction in carrier number and a corresponding decrease in the junction voltage of e/C_{dep} which are directly correlated or can be seen by noting that the charge fluctuations in the capacitor is related to voltage fluctuations ie.$\Delta Q = C\Delta V$ provided the capacitance is constant.

Correlation between junction voltage and photon flux

The analytical relation for the correlation function between the junction voltage and photon flux has been obtained in [33] for the diffusion case. We shall describe the effects here qualitatively. Irrespective of the bias conditions, there is near perfect correlation between the carrier number and the junction voltage. The photon flux is related to the carrier number by a coupling efficiency. If the efficiency is 1, then we will observe a perfect correlation(correlation is 1) between the photons and the junction voltage. When the efficiency is reduced, photons may be deleted but carriers are still emitted which is reflected in the junction voltage which then results in the loss of the correlation. The value of this correlation coefficient is the same as the coupling efficiency at high frequencies(or short counting times) since each each photon counted or not is equivalent to a junction voltage drop of e/C_{dep}. Along with the decreasing coupling efficiency, if the measurement time is long, then many photons may be emitted and detected, and this destroys the correlation between the junction voltage and photon flux further.

2.6.11 Validity of the Equivalent circuit model in the diffusion limit

Finally, we shall now see if the Langevin model supports the small signal equivalent model laid out in the intuitive description of noise in the beginning of the chapter as well the noise spectral densities obtained when we discussed the Buckingham's diffusion noise model, for the simpler case of long diodes. We obtain the carrier spectral densities from Eq.(2.234) as

$$S_{\Delta n_c} = \langle \Delta n_c^\dagger \Delta n_c \rangle = \frac{1}{A^2+B^2}\tau_r^2((1+\frac{\tau_{fi}}{\tau_{RC}})^2+\omega^2\tau_{fi}^2)S_{F_r}+((\frac{\tau_{fi}}{\tau_{RC}})^2+\omega^2\tau_{fi}^2)(S_{F_{fi}}+S_{F_{bi}})+S_{F_{rs_I}}) \tag{2.262}$$

The forward injection current is modeled as a thermionic emission current from n-layer to p-layer with an average which varies as a function of the time dependent junction voltage and a stochastic random injection events with zero average. Using Eq.(2.93), with $v_{th} = \frac{l_f}{\tau_f}$ and $D_n = \frac{l_f^2}{2\tau_f}$ we obtain

$$I_{fi}(t) = \frac{en_{p0}D_nA}{l_f}e^{\frac{eV_j(t)}{kT}} + eF_{fi} \tag{2.263}$$

where l_f is the electron mean free path and $D_n = \frac{l_f^2}{2\tau_f}$. Since the thermal motion is random, electrons at a distance of $-l_f$ from the edge of the junction, reach the edge of the junction and cross back into the p region. The backward injection current as a function of its time varying average and stochastic term evaluated at $x = -l_f$ is

$$I_{bi}(t) = eD_n\frac{dn}{dx}|_{x=-l_f} = \frac{eD_nA}{l_f}[n_{p0} + \frac{N}{AL_n}e^{-l_f/Ln}] + eF_{bi} \tag{2.264}$$

In the previous sections, the diffusion model was established with the BP rates $\alpha_0, \alpha_d = 1$ but the total current in Eq.(2.112) became zero. This is not incorrect, but simply states, that the diffusion current is very small when compared to forward and backward injection currents where $I_0 = I_{fi} - I_{bi}$ is the difference between the average forward and backward currents and can be verified to be the diffusion current equation of a diode $I_0 = I_s(exp(eV_j/kT) - 1)$. To complete the picture, the pn junction is connected to a constant voltage source with a series resistor that carries voltage noise which is responsible for the external terminal current

$$I_{ext}(t) = \frac{V - V_j}{R_s} + eF_{rs} \tag{2.265}$$

At steady state, the diffusion current balances the external current as $V - V_{j0}/eR_S = I_{fi}(V_{j0}) - I_{bi}(n_{c0})$. Since the backward injection current depends on the carrier number n_{c0}, the backward lifetimes are redefined from the pump rates of Eq. (2.228) to currents using Eq. (2.264) as

$$\frac{1}{\tau_{bi}} = \frac{1}{e}\frac{dI_{bi}(N)}{dN}|_{N=N_0} = \frac{I_{bi}(N_0)}{e(N_0 + n_{p0}AL_n e^{l_f/L_n})} \tag{2.266}$$

Since the electron mean free path is much smaller than the diffusion length, at a high bias, we obtain $I_{fi}, I_{bi} \gg I_0$ which implies that the time constants τ_{fi} and τ_{bi} are the smallest time constants in this problem which leads to the following condition $\tau_{fi}, \tau_{bi} \ll \tau_r, \tau_{te}, \tau_{RC}$. The currents expressed in terms of the LED diffusion current and the lifetimes are

$$I_{fi}(V_0) = I(1 + \frac{\tau_r}{\tau_{bi}}) + \frac{\tau_r}{\tau_{bi}}I_0 \quad , \quad I_{bi}(N_0) \approx \frac{\tau_r}{\tau_{bi}}(I + I_0) \tag{2.267}$$

The spectral densities are redefined, according to the new pump or current definitions as

$$S_{F_r} = \frac{2}{e}(I + 2I_o) = \frac{2I}{e} + \frac{4kT}{e^2 R_{d0}} \;, S_{F_{rs}} = \frac{4kT}{e^2 R_s} = \frac{4(I + I_0)}{e}\frac{\tau_{te}}{\tau_{RC}} \tag{2.268}$$

$$S_{F_{fi}} = \frac{2I_{fi}(V_0)}{e} \quad , \quad S_{F_{bi}} = \frac{2I_{bi}(N_0)}{e} \tag{2.269}$$

Substituting the various noise correlation terms in the obtained expression for the spectral density we obtain

$$\begin{aligned} S_{\Delta n} &= \frac{1}{A^2 + B^2}\tau_r^2((1 + \frac{\tau_{fi}}{\tau_{RC}})^2 + \omega^2\tau_{fi}^2)(\frac{2I}{e} + \frac{4kT}{e^2 R_{d0}}) \\ &\quad +((\frac{\tau_{fi}}{\tau_{RC}})^2 + \omega^2\tau_{fi}^2)(\frac{2I}{e}(1 + \frac{2\tau_r}{\tau_{bi}}) + \frac{4}{e}\frac{\tau_r}{\tau_{bi}}\frac{kT}{eR_{d0}}) + \frac{4(I + \frac{kT}{eR_{d0}})}{e}\frac{\tau_{te}}{\tau_{RC}}) \end{aligned} \tag{2.270}$$

Eq.(2.270) can be applied to a wide range of conditions, but since we are interested in the diffusion limit case we set $\tau_{fi}, \tau_{bi} \to 0$. Under strong bias conditions where $I \gg I_0$ the above equation is greatly simplified to

$$S_{\Delta n} = \frac{\tau_r^2}{A''^2 + B''^2}(\frac{2I}{e} + \frac{4kT}{e^2 R_s}) \tag{2.271}$$

where the denominator $A''^2 + B''^2 = (1 + \frac{\tau_{te}}{\tau_{RC}})^2 + \omega^2(\tau_r + \tau_{te})^2$.

Constant Current Case

In the constant current case $\tau_{te} \ll \tau_{RC}$ and the denominator terms are $A''^2 + B''^2 = 1 + \omega^2(\tau_r + \tau_{te})^2$. Eq.(2.271) now reduces to

$$S_{\Delta n} = \frac{\tau_r^2 \frac{2I}{e}}{1 + \omega^2(\tau_r + \tau_{te})^2} \tag{2.272}$$

The current noise can be obtained from the carrier spectral density by $S_{\Delta I} = e^2\omega^2 S_{\Delta n}$ which leads to

$$S_{\Delta I} = \frac{2eI\omega^2\tau_r^2}{1 + \omega^2 R_d^2 C^2} \tag{2.273}$$

where $C = C_{diff} + C_{dep}$. Note that Eq.(2.273) represents the 'recombination' current noise which was obtained in Eq.(2.78) using the equivalent circuit model and not the external circuit current noise of Eq.(2.87) Since $I = C_{diff}\frac{dV}{dt}$, the voltage spectral density across the capacitance can be obtained as$S_{\Delta V} = \frac{1}{\omega^2 C_{diff}^2} S_{\Delta I}$ from which

$$S_{\Delta V} = \frac{2eIR_d^2}{1 + \omega^2 R_d^2 C^2} \tag{2.274}$$

and agrees with the macroscopic theory of Eq.(2.83) under constant current case.

Constant Voltage Case

Under the constant voltage case, the series resistance is removed producing the condition $\tau_{te} \gg \tau_{RC}$. The denominator terms then become $A''^2 + B''^2 = (\frac{\tau_{te}}{\tau_{RC}})^2(1 + \omega^2(\frac{\tau_{RC}}{\tau_{te}}\tau_r + \tau_{RC})^2)$ and Eq.(2.271) now reduces to

$$S_{\Delta n} = \frac{\tau_r^2 \frac{4kT}{e^2 R_S}(\frac{\tau_{RC}}{\tau_{te}})^2}{1 + \omega^2(\frac{\tau_{RC}}{\tau_{te}}\tau_r + \tau_{RC})^2} \tag{2.275}$$

The current noise spectral density and voltage spectral density are obtained similar to Eq.(2.273) and Eq.(2.274) to obtain

$$S_{\Delta I} = \frac{\tau_r^2 4kT\omega^2 \frac{R_S}{R_d^2}}{1+\omega^2 R_S^2 C^2} \ , \ S_{\Delta V} = \frac{4kTR_S}{1+\omega^2 R_S^2 C^2} \tag{2.276}$$

which once again agrees with the macroscopic theory in the diffusion limit for long diodes.

External Circuit Fluctuations

Linearizing Eq.(2.265) followed by taking the Fourier transform provides the external circuit current as

$$\Delta I_{ext} = -\frac{\Delta V_j}{R_S} + eF_{rs} \tag{2.277}$$

The external current spectral density is obtained from Eq.(2.277) using $\langle \Delta I_{ext}^* \Delta I_{ext} \rangle$ as

$$S_{\Delta I_{ext}} = \frac{1}{A^2+B^2}\{(\frac{\tau_{te}}{\tau_{RC}})^2(2e(I+2I_0)) + (1+\omega^2(\tau_r+\tau_{te})^2)\frac{4kT}{R_s}\} \tag{2.278}$$

With a little simplification we see that at low frequencies.the above expression is equal to the shot noise under constant voltage conditions and is at the thermal noise limit at the constant voltage conditions. The origin of noise in the external circuit can be obtained by recognizing which variables appear in Eq.(2.278). The forward and backward currents introduce effective resistances $\frac{kT}{eI_{fi}}, \frac{kT}{eI_{bi}}$ across the junction layer which is the related to the time constants $\tau_{fi} = \frac{kTC_{dep}}{eI_{fi}}, \tau_{bi} = \frac{kTC_{dep}}{eI_{ni}}$. Since the currents is so much larger than the differential resistance $\frac{kT}{eI_0}$ established by the diffusion currents, the junction voltage dropped by forward(or backward injection) event are immediately relaxed by a backward(or forward) injection rather by the current through the external circuit. This implies that the noise due to stochastic injection events across the junction are not seen in the external circuit, and all the noise comes from the recombination events in the active region as seen earlier in the circuit analysis.

2.7 Summary

The mechanisms responsible for subshot noise generation have been reviewed in this chapter. Analytical expressions for the photon Fanofactors are obtained using the quantum mechanical Langevin model. The theory obtains expressions from the thermionic emission limit to the diffusion limit corresponding to a long base heterojunction and short active region double heterojunction diodes since these structures are typical of LEDs used in the following chapter. The Fanofactors for the pump have been determined as well as cross-correlation spectral densities between junction voltage and carrier number as well as carrier number and photon numbers. Finally we also show the validity of the Langevin model to predict the same results as the simple equivalent noise model of the LED under moderate injection conditions.

Chapter 3

Experiments on Subshot Noise

3.1 Introduction

In recent years there have been numerous experiments that verified reduced intensity noise in semiconductor laser diodes(LD) and LEDs. This suppression has so far been the largest in LD with nearly 4.5dB below the SQL which has been demonstrated from pump noise suppressed quantum well lasers[39]. LEDs, since they are thresholdless have an advantage over the LD for generating low intensity subpoisson light since they have very high efficiency compared to LD at low injection currents. The largest intensity squeezing reported so far is 3.1dB at 77K[40] and squeezing over the broadest frequency range of nearly 1.5Ghz[41] has been reported using an integrated LED-Photodetector(PD) system with Be heavily doped active region of $3.5 * 10^{-19} cm^{-3}$. The lowest current range over which squeezing has been demonstrated runs in a few microamperes[42]. Also the ease in showing subshot characteristics with LEDs have included them in many nonclassical light experiments such as quantum non-demolition(QND) devices[43], optoelectronic amplifiers and quantum correlated light beams using series and shunt coupled devices[44]. In each application requiring the generation of nonclassical light, the LEDs have to been operated under constant current operation where the squeezing is essentially limited by two factors: 1)The response time of the pn junction(also known as the thermionic emission time $\tau_{te} = R_d C_{dep}$) which determines the cutoff frequency for the pump noise suppression due to the macroscopic Coulomb blockade effect and 2)The carrier lifetime τ_r which determines the cutoff frequency for suppression of recombination noise. These issues have already been dealt with theoretically in chapter 2. It is important to note that the constant current biasing mechanism is not sufficient to explain the subshot experimental results. For example having a high impedance constant current bias does not imply regulation of carriers across the depletion region into an active region,since unlike a mesoscopic junction the carriers do not block the successive carrier injection(single electron coulomb blockade). The random stochastic process of injection cannot be suppressed just by quieting the pump. There must a collective coulomb blockade regulation which involves many carriers and takes place on a time scale of τ_{te} and for observation times smaller than this value we would still observe shot noise irrespective of high impedance pump suppression. If a LED does not regulate well, it will not demonstrate squeezing and this is characteristic of low efficiency generic diodes. Hence we need to use high efficiency heterojunction structures and this narrows the study of the optical noise spectra to the L2656 LED which has been shown previously to produce a squeezing of about 0.7dB[45] as well as the L9337 LED for which the results have not been previously reported.

Our principle goal in this chapter is to construct a measurement setup to observe optical noise spectra of sub-Poisson light and to achieve maximal squeezing, with suppression greater than 1dB over a frequency range of several Mhz at room temperature. The measured photon Fanofactors play an integral role in the communication experiments of chapter 4. In order to be sure that the shot noise suppression is valid, the measured spectral density of the noise from the photodetector and the corresponding Fanofactors are fit to the analytical expressions that have been developed in chapter 2. Section 3.2 details the thermal and electrical shot noise measurements performed. The shot noise of the optical noise spectra will have to surpass the electrical shot noise from the photodetector and the thermal noise from the resistors in order to be displayed. Section 3.3 details the experimental setup to measure shot and subshot noise spectra. Each stage of the setup, which includes the LED, photodetector, amplifier and the spectrum analyzer are calibrated and the parameters which may affect subshot noise are studied. In Section 3.4, experiments are carried out to verify that the optical noise spectra from the lamp are at the shot noise level. It is important that the shot noise levels are well calibrated. Otherwise the degree of suppression for subshot noise will not be established without the reference shot noise level and the measured Fanofactors would be in error casting doubt on all experiments. In Section 3.5, the subshot experiments are performed for the L2656 and L9337 LEDs. Even though the noise spectra under high impedance pump suppression and constant voltage bias conditions are well understood from a theoretical point of view, experiments are performed to demonstrate the physics of these biasing mechanisms. We also observe certain anomalous behavior in some experiments, where the frequency dependent Fanofactors show increased squeezing at certain frequencies instead of the expected low pass characteristic and provide possible explanations for this behavior. The noise squeezing bandwidth as a function of drive current is also obtained. This describes the maximum 'noise modulation' bandwidth in the communication setup of chapter 4.

3.2 Thermal and electrical shot noise Measurements

The first experiments we performed was to characterize the electrical thermal noise voltage and shot noise current. The thermal noise is associated with the resistor and shot noise appears as the photocurrent noise in the experimental setup used to measure subshot optical spectra(which appears in the following section). It is important to make sure that the subshot/shot optical noise is much larger than the electrical and thermal noise spectra in order to be measured. The quantities measured in this section are integrated over a certain bandwidth and did not deal with spectral densities(noise measured over 1Hz). In order to measure the noise over a 1Hz resolution(such as the optical noise spectra for subshot measurements), the experimental setup required a high gain, low noise amplifier and a low noise spectrum analyzer, the choice of which became clearer once the electrical noise measurements were completed and the lower limits of electrical noise quantities were established.

Thermal noise is due to electron agitations which give rise to random voltage fluctuations in the terminals. The particles perform random motion and suffer collisions in the lattice. The velocity and the consequent current due to this particle motion is described by a Langevin equation. We would now like to experimentally verify the variation of noise voltage with resistance. The thermal noise formula can be obtained using the transmission line method of Nyquist[21] which is an important quantity that can be measured. Consider two resistors of equal resistances R at temperature T connected by a transmission line of characteristic impedance of R. Conductor 1 produces a current I equal to the emf due to thermal agitation divided by the total resistance 2R. Power transferred to conductor 2 is this current squared times the resistance. Because the two resistors are at the same temperature, the second law of thermodynamics requires that the power flow in one direction is equal to the power flow from the opposite direction. We may imagine this as a voltage wave $V = V_0 \exp i(kx - \omega t)$ traveling with a velocity $v = \frac{\omega}{k_x}$ where $k_x = \frac{2\pi}{\lambda}$. By shorting the two resistors and trapping the wave on the transmission line, we can obtain the power or the energy transferred per second which Nyquist derived to be

$$P = \frac{Energy}{Length} * \frac{Length}{Time} = \frac{\frac{L}{v} * kT * B}{L} * v = kTB \tag{3.1}$$

The power transferred is the maximum noise power since the load is matched to the transmission line(no losses). The circuit can be represented as a noise generator(voltage source) connected to a resistor. The mean-square voltage amplitude at the destination resistor is then V^2/R which gives

$$< V^2 >= 4kTRB \tag{3.2}$$

It is important to note that when one resistor drives another noiseless resistor and the two resistors are matched to each other, the net power developed is kT for a bandwidth of 1Hz. This is equal to -174dBm for T=293K where the dBm is decibels referred to 1mW power. A measuring instrument with sensitivity to very small signals would measure this value if we terminated its input with a 50Ω resistor but most instruments do not have such sensitivity which is why we need good amplifiers which raise the noise to appreciable levels. If the resistor is connected across the input of a high gain amplifier whose voltage gain as a function of frequency is $G(f)$, the mean square output voltage of the amplifier which is the sum of resistor(R) and amplifier noise(A) is

$$< V_o^2(R+A) >= 4kTR\int_0^{\infty} |G(f)|^2 df + < V_o^2(A) >= 4kTRG(0)^2 B_N + < V_o^2(A) > \tag{3.3}$$

where $V_o(A)$ is the amplifier noise referred to the output and $B_N = \frac{1}{G(0)^2}\int_0^{\infty} |G(f)|^2 df$ is the effective noise bandwidth(ENB). For a simple first order low pass gain characteristic we can evaluate ENB to be $B_N = 1.57 f_{3dB}$.Normally, the bandwidth of a system(eg. amplifier)

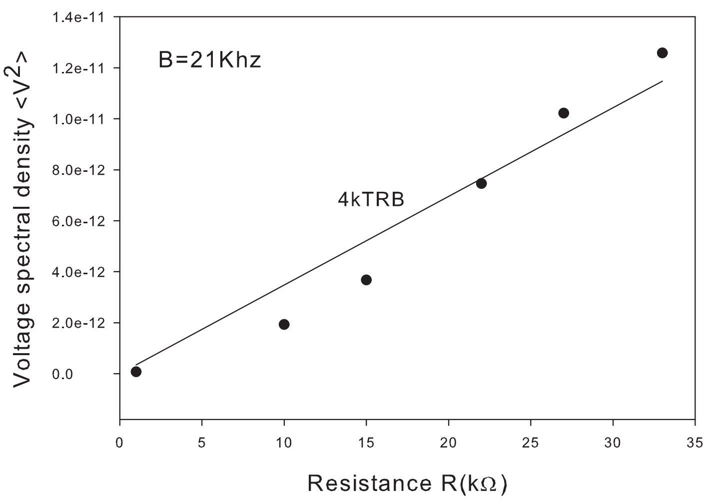

Figure 3.1: Experimental results for V^2 (obtain by correcting for amplifier noise and normalizing to gain) versus resistance R. The solid line implements the theoretical equation 4kTRB where B is the fitting parameter used.

is defined as the difference between the half-power points (-3dB points). A -3dB reduction corresponds to a loss of 50% of the power level or a voltage which is 0.707 that of the voltage at the center frequency. Noise power however exists at all frequencies and is not only constrained to the 3dB points. So ENB should be larger then the conventional bandwidth. From the expression for B_N we see that it is defined as the frequency span of a rectangular shaped power gain curve equal in area to the area under the actual power gain versus frequency curve. It is the area of the power gain curve divided by the peak amplitude of the curve.

So the measurement procedure is as follows: Measure G(f) at a range of frequencies and find the 3dB point. Then we measure $< V_o^2(R + A) >$ using a true rms meter, and then subtract away the noise of the amplifier. The measurement setup we constructed for this purpose is as follows: The resistors and the differential amplifier were housed in a metallic enclosure. The resistors were mounted on a rotary switch.By turns of the knob, different resistances were placed at the input of the differential amplifier. The differential amplifier output was fed to a oscilloscope as well as to a computer where measurements were taken using Labview. The differential amplifier circuitry was soldered onto a printed circuit board. By doing so,the leads were kept as short as possible in order to minimize problems of electrical interference and capacitance. Care was taken to keep the setup away from magnetic sources such as the oscilloscope monitor. The amplifier we used was the AD625 instrumentation amplifier which was set for a gain of 1000 according to the formula[46] $G = \frac{2R_F}{R_G} + 1$ where $R_F \approx 19k\Omega$ and $R_G \approx 39k\Omega$ were chosen.We followed the datasheet recommendation for the resistor choices since bandwidth, stability and output noise are affected by them. With these settings, the output noise of the measurement setup was in the millivolt range.

Before the measurements were taken, a calibration step was performed wherein a sinusoidal test signal in the range of 100mV to 1V from a function generator was fed into the differential stage(set for a unity gain). The RMS output was measured on a oscilloscope. Once this step was verified, for a fixed voltage on the function generator V_i, the frequency was varied from 100Hz to 25Khz and the output voltage V_o was observed on the scope.The gain can be found as $G(f) = \frac{V_o}{V_i}$ which over the frequency range was 1000. The 3dB point was found to be $25kHz$ which agreed with the gain-bandwidth product of the amplifier. The roll-off was around 15dB per decade which was less than the 20dB roll-off expected of a single pole filter.If we assume it to approximately a single pole filter the ENB can be calculated as $B_N = 39kHz$ Now we have both $G(0)$ which is 1000 and B_N. Finally we connected the setup to the computer and the true rms voltages were measured using a Virtual Instrument designed for making noise measurements in Labview.

The input of the differential amplifier was shorted and the noise contribution of the amplifier stage was measured($\langle V_{rms}^2 \rangle$) to be around 0.6mV. Next noise voltages of resistances from a few ohms to $1M\Omega$ were measured. Note that the datasheet[46] specified the input capacitance of the differential amplifier as around $4pF$. Together with the input resistance R this forms a low pass filter with a cutoff frequency of $\approx \frac{1}{2\pi RC}$. For the maximum resistance used which is $1M\Omega$, this cutoff is around 39.8Khz which is beyond the 3dB bandwidth $f_{3dB} = 25kHz$ of the amplifier. If this is smaller we have to account for it in the gain integral of Eq. (3.3) by modifying it as $\int_0^\infty \frac{|G(f)|^2}{1+(\omega RC)^2} df$. Since all contributions to the measured RMS voltage are statistically uncorrelated, the amplifier and resistor noises add in quadrature. The measurement of the Johnson noise without the amplifier noise was calculated as $V_o^2(R) = V_o^2(R+A) - V_o^2(A)$. We obtained 1000 data points for each resistor value and averaged them. The resultant points are plotted in Fig. (3.1). The points are normalized to $G(0)^2$.The solid line is the theoretical curve which was used to fit the data and the fitting parameter used was the effective noise bandwidth-ENB.

There are a few points to notice. Conventionally, a low pass filter is used after the amplifier stage to set the bandwidth[47]. Here we have used the amplifier response itself. The National instruments data acquisition card(DAQ) used has a maximum sampling rate of around 22kS/s which is another bandwidth limit. The original experiment was carried out by setting the DAQ to 50kS/s and the Labview program did not produce any error which was surprising. If the DAQ sampling rate was 50kS/s. the amplifier would serves as a gain as well as an antialiasing prefilter to the DAQ card[48] and we could take the ENB of 39kHz which we measured earlier. So the ENB in this regard will have to be smaller(around 25kHz) , and we estimate it from the slope of the experimental data. When the output from the amplifier is hooked up to the oscilloscope, we obtain a noise pattern which is Gaussian distributed in voltage. This is seen in Fig. (3.2a) .This is characteristic of all white noise including shot noise. The Gaussian character depends on the bandwidth limit(around 20kHz) and resistance. In the oscilloscope,we observed a definite increase in 3σ deviation of the Gaussian distribution as the resistances were increased from $10k\Omega$ to $1M\Omega$. Below this value the amplifier noise would swamp the readings and we were not able to identify any variations. Also the type of meter used is very important. Voltmeters are peak responding devices calibrated to show the rms values of a sine signal. So if Gaussian voltages are to measured they are to be multiplied by 1.13[49].In our case we measured the voltages by means of a Labview program which was in essence an integrating true rms voltmeter. We had options to choose windows but we did not use them since we are dealing with broadband noise[48]. There is another important difference between taking a peak measurement versus rms values: An averaging voltmeter would result in zero voltage in an infinite integration time,whereas the rms meter would measure a nonzero value.This is quite similar to sine wave measurements where a single frequency would be squared and then averaged for the rms. Noise may be considered as a number of sine wave power amplitudes(V^2) of different

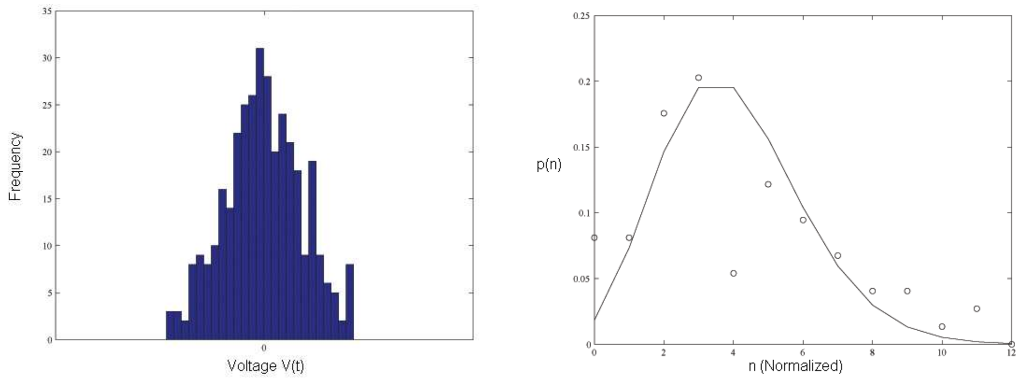

Figure 3.2: (a) Histogram of thermal noise for a 1MΩ source (b) PDF of shot noise obtained from a thermionic noise vacuum diode. The solid line is the the theoretical Poisson distribution obtained by fitting the average $< n >$ to the data(points)

frequencies and the net square voltage can be obtained by adding them all up.

We notice that the datapoints in Fig. (3.1) show slight deviations from the theoretical plot for values of $10k\Omega$ and $15k\Omega$. This may be due to several factors. 1. The resistors used are close to the noise of the amplifier stage. 2.The resistors may have excess noise(some of the resistors used were carbon composition). 3. Insufficient averaging prompting measurement of more datapoints. 4. From looking at Eq. (3.3) , a more exact procedure would be to measure the gains to very large frequencies and integrating them using a numerical procedure. However we do see that there is a linear relationship between the mean square noise voltage and the resistance as expected and the effective noise bandwidth obtained by fitting the theoretical curve to the datapoints is equal to 21kHz and is close to the ENB of 25kHz-39kHz dictated by the measurement setup.

We obtained Fig. (3.2a) by collecting about 8000 data points from a $1M\Omega$ thermal source which was fed into an oscilloscope virtual instrument in Labview. We divided the data into bins and plotted the relative frequencies. The measurement shows us that thermal noise has a Gaussian distribution as expected. Note that the histogram charts the peak-peak values. The rms value $< V_{rms}^2 >$ which we measured in the above using the rms meter is essentially the $1\sigma^2$ variance of the histogram. Typically for Gaussian limited noise,instantaneous values like between 0 and σ 68% of the time and between 0 and 3σ 99.6% of the time[49]. Fig. (3.2b) was obtained in the same way except we used a bandwidth limited noise source which housed a vacuum noise diode which is a good shot noise source. The instantaneous shot noise diode current results in a Gaussian probability density function(pdf) which shows us that the probability at any time for the current to lie between I and $I + dI$ is $p(I)dI$. The variance is the mean square shot noise current given as $\sigma^2 = 2qI_{dc}\Delta f$. The bandwidth of the noise source was adjusted to be 10Khz and the voltage around $2V_{rms}$ through the front panel controls. We measured the noise current using a Labview ammeter module. We were measuring an integrated current $I = \int_t^{t+T} i(t)dt$ over the measurement time interval T set by the DAQ and datapoints were continually obtained in intervals of T. Note that even though the pdf of shot processes are actually Poisson, at large currents we can approximate the curve to be Gaussian. We then normalized the currents to the electron number n by the relation $n = \frac{I}{e}$. The electron number was divided into bins and the probability was obtained after normalizing the relative frequency plot. The noise source produced 0 centered values which resulted in $< n >= 0$. But from our understanding of shot noise, the mean square noise current is proportional to the dc current. We fit the theoretical Poisson curve $p(n) = \frac{e^{-<n>} <n>^n}{n!}$ to the above data by estimating $< n >$ by trial and error . This method of obtaining the pdf of shot noise is also a method of calibrating it precisely and has been used to determine the optical shot/subshot noise of LEDs and feedback stabilized lasers[4]. We however use another method for the optical noise measurements, where we calculate the noise powers from the photocurrents of the detector.

3.3 Experimental setup for subshot noise measurement

In the previous section we measured the rms voltage of thermal noise and verified its probability distribution. We could have obtained the shot noise rms current using the above measurement setup,but there are a number of issues that prompted an alternate design:

1.We are more interested in the noise spectral densities(the power per hertz) and not in an integrated current or voltage. In other words, a sound spectral analysis needs to be performed, so we can compare noise levels relative to one another. The spectral densities are often referred to as 'spot noise'.

2.The AD625 amplifier noise is quite large at $4nV/\sqrt{Hz}$. This would ultimately limit the spot noise measured values.

3.The frequency range of measurement should be equal to the electrical modulation bandwidth of the LEDs used ie. 100kHz to 40Mhz , which is beyond the range of the thermal noise measuring system.

The experimental setup is shown in Fig. (3.3) .The heart of the subshot experiment is the light emitting diodes which are the L2656 and L9337 from Hamamatsu. These are high efficiency GaAlAs semiconductor heterojunction light emitters with a typical quantum efficiencies of .22 and 0.32 photons-per electron respectively at a center wavelength of 890nm specified at a forward current level of 50mA. We shall treat the L2656 as a pn homojunction device since many papers have done the same and the differences between applying the thermionic current or diffusion current model is usually imperceptible. The LEDs are mounted on a faceplate attached to a movable post. The photodiodes used are S5107 and S3997 which have large active area of 10*10 mm with specified internal quantum efficiencies as high as 0.93 electrons per photon. The photodiodes as well as the load resistance R_L and battery are housed in a metal box which is in turn mounted on a post. The posts are placed on a movable slide allowing us to adjust the distance between the LED-photodiode. But usually we placed the LED and photodiode in a face-face configuration in order to allow maximum light collection efficiency. The light from the photodiode is converted to a voltage by means of the load resistance R_L which could be switched between 50Ω and 5080Ω. The batteries used were originally 9V which were later switched to 24V. So some of the initial experiments were done at low currents so as not to saturate the PD. If the PD got saturated we could change R_L to 50Ω and get a larger maximum photocurrent range given approximately by $\frac{V_B}{R_L}$ where V_B is the battery voltage but the gain would be reduced. The maximum reverse voltage of these detectors is -50V. The photovoltage developed across R_L is amplified by a low noise 40dB gain Analog Modules(AM) 322-6 voltage amplifier whose output is fed to a HP8568B spectrum analyzer(SA) which displays the noise power. This SA is capable of measuring noise levels as low as -135dBm and has very good low frequency drift,good stability, and accuracy. A GPIB driver was used to extract the data from the spectrum analyzer onto a computer for further processing. A voltmeter or oscilloscope can be switched in place of the Analog Modules-Spectrum Analyzer(AM-SA) chain to read the photovoltage for each measurement. We opted for a discrete component design where each element can be modified easily. The LEDs could be switched in and out easily and for some experiments such as the shot noise measurement the post could be replaced with another fitted with a lamp.The LED,PD and amplifier stages were placed inside a shielded box with external BNC connections to meters and current sources.

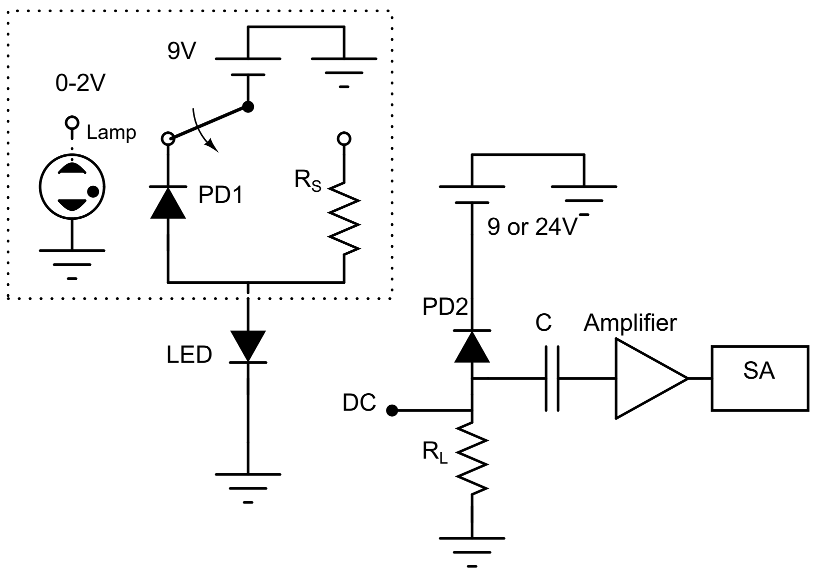

Figure 3.3: Overview of the experimental apparatus: By switching from resistor R_S to photodiode PD1 subpoisson and Poisson light can be produced which is detected by photodiode PD2. The DC voltage is measured across R_L with a multimeter and AC is passed on to the amplifier and the spectrum analyzer(SA). PD1, R_S and battery are housed in a shielded box(as indicated by the dotted lines). The rest of the components(except the SA) are housed in a RF cage.

The LED itself is driven by either a shot noise source(SNS) or a constant current source(CCS) by means of a switch. The SNS consists of a lamp which illuminates a reverse biased photodiode which was from UDT sensors. Most of the current produced by the SNS is due to optical power of the lamp and so the measured variance can be expressed as $< \Delta i_{sn}^2 >= 2e < i > B$. The goal of the experiment is to generate a light field which is below the shot noise level.The need for the SNS is to generate a light field with Poissonian statistics from the LED. This is done in order to compare the shot noise level against other measured fields. The Fanofactor of the noise from the SNS PD is given by Eq. (??) which we rewrite here as

$$F_{ph} = \eta_0 F_p + (1 - \eta_0) \tag{3.4}$$

where η_0 is the dc efficiency(the effect of differential efficiency as discussed in the previous chapter is ignored for the time being) and F_p is the Fanofactor of the LED drive current(This was referred to as the pump Fanofactor in the previous chapter and we either infer this value from experimental results or relate it to experimental quantities). Typically lamps have efficiency close to 0 and so $F_{ph} = 1$ therefore approximating the shot noise level. Alternatively, the same result could have been obtained by setting $F_p = 1$. This PD in turn drives the LED which has the same Fanofactor relationship except now the photodetector's F_{ph} is the F_p of the LED. So in general we have a series of optoelectronic LED-detector stages, where the statistics is transferred from one stage to another using the general expression[50] $F_{M+1} = F_1 \Pi \eta_i + (1 - \Pi \eta_i)$. For example,the case i=2, has led to the construction of an approximate quantum non demolition device [44] provided the efficiencies are close to 1. The CCS consists of a large series resistance R_S and a 9V battery. As seen in the previous chapter, the series resistance R_S should be greater than the diode differential resistance R_d in order to establish high impedance pump suppression conditions. The SNS and CCS were housed together in a separate box and were connected to the shielded box and to the LED inside it by means of short shielded coax cables. In addition, we used the ILX Lightwave LDX3620(referred to as ILX from here on) low noise current source to set the LED drive current to calibrated levels. In order to be assured that the experiments outlined in this chapter are valid, each stage of the experimental setup discussed above will need to calibrated and factors that may affect the squeezing results will be studied in the following sections.

3.3.1 Spectrum Analyzer Calibration

The Spectrum Analyzer(SA) is the most important tool in our arsenal to measure noise and it is important that the analyzer is properly calibrated and correction factors if any, should be included in all future extractions of data from the SA noise measurements. A classic superheterodyne SA consists of a mixer stage, several IF filter stages with an effective center frequency f_{IF}, a log amp,an envelope detector and the video filters. The mixer is a nonlinear device which receives as input the external signal of frequency(frequencies)f_{sig} and the local oscillator signal of frequency f_{LO} and produces an output which includes the original signal frequency f_{sig} as well as the sum$(f_{sig} + f_{LO})$ and difference frequencies$(f_{sig} - f_{LO})$. If for some reason, the signal frequency is below the LO by the IF frequency(f_{IF}) then one of the mixing products will lie within the passband of the IF filter and would be detected. In other words, there exists a tuning equation given by $f_{sig} = f_{LO} - f_{IF}$ which the signal frequency satisfies. This is best described with an example. Let us introduce a sine wave of 500Mhz into the SA with a tuning range of 0-1Ghz. Assume that the f_{IF} is fixed at 3Ghz and a ramp generator sweeps the frequency variable local oscillator f_{LO} from f_{IF} up to $f_{IF}+1Ghz$ thus covering the entire tuning of 1Ghz. For the 500Mhz signal the LO frequency should be $f_{LO} = f_{sig} + f_{IF} = 3.5Ghz$. In other words when the local oscillator sweeps through the frequency $f_{LO} = 3.5Ghz$, the output from the mixer(f_{IF}) is at 3Ghz and is within the passband of the IF filter and therefore registers a spike on the display. The signal has been translated or upconverted to the IF frequency according to the superheterodyne principle. The IF stage has the ability to resolve two nearby equal amplitude frequency signals according to its resolution bandwidth(RBW) which is stated as the 3dB bandwidth of the IF filter chain. The envelope detector converts the IF signal to video by following the changes in the envelope of the IF signal ie. baseband signal and not the instantaneous variation of the IF carrier itself. The video filter is a low pass filter that follows the envelope detector. If the cutoff frequency or video bandwidth(VBW) is setup to be much less than the RBW, then the video system no longer follows the rapid variations of the signal envelope passing through the IF chain. In other words, the displayed signal will be smoothed out and for noise in particular, the peak to peak variations are reduced(any sine wave present in the noise remains unaffected). The noise levels themselves are unchanged since we use the normal detection algorithm in the SA Labview program. The SA does not display all the frequency points that it sweeps. It displays a small bandwidth of frequencies(also known as a bucket) as one point on the display. The normal or rose'n'fell detection algorithm essentially displays the maximum value in its bucket if its an odd numbered data point and minimum value if it is an even numbered data point and is the best choice for viewing both signals and noise. If we had used the positive peak detection method(which displays only the maximum value in each bucket) then for the case $VBW < RBW$,changing the video bandwidth would affect the average noise level. The normal detection method is seen in Fig. (3.4a), where the RBW is kept constant but the VBW is varied from 10Khz to 3Hz. The noise levels are unchanged(characteristic of the rose'n'fell algorithm) whereas the variance is reduced. The noise powers are obtained by connecting the amplifier and PD combination without any input signal onto the photodetector. This implies that the noise on the spectrum analyzer is the resistor noise of the load resistor R_L of the PD paralleled with the amplifiers internal resistance.

Even though the spectrum analyzer (SA) works well with ac signals, the main requirement is to display the spot noise quantities of the test signals accurately. When the SA input is terminated with a 50Ω resistor, the noise indicated on the screen is nothing but the SA's own noise floor also known as the Display Averaged Noise Level or DANL. The DANL is calibrated to reflect a fictitious noise level at the SA's input in order to compare it with the other noise signals inserted into the SA. This DANL is due to the shot noise amplified through the various gain stages of the system and finally referred back to the 50Ω input. So any noise signal we insert has to have a larger magnitude than the DANL to be displayed on screen. Note that both the input noise as well as the DANL are affected by various stages in the SA such as the attenuator, mixer, IF and video filter stages. Our attenuation was set to auto. The lowest SNR can be obtained by setting 0dB attenuation. The RBW also affects the sensitivity of the system. The DANL as well as the signal noise passes through the IF bandwidth filters and the total noise power displayed is dependent on the effective noise bandwidth(ENB) of these filters. For example,a signal of 10nV/$\sqrt{Hz}$, and a IF filter of RBW≈ENB=30kHz, causes the SA to display(without corrections) an integrated noise of 10nV/$\sqrt{Hz}$*$\sqrt{30kHz}$=$1.732\mu V$. Since the spot noise values are required for the experiments, all the displayed noise measurements will be converted to 1Hz by effectively dividing by the RBW. Also when one changes from one RBW setting to another, the displayed noise changes as $10 \log \left(\frac{RBW_2}{RBW_1} \right)$ie. the input is normalized to 1Hz followed by inserting it into another RBW setting. Fig. (3.4b) illustrates the variation of RBW, with VBW kept constant at 3Hz. When the RBW is changed from 3Khz to 10Khz, a change of 5.22dB is expected but only 4.1dB is seen, which is an uncertainty of nearly 1.1dB. The inset of the Fig. (3.4b) displays the noise over a wider frequency range and as the RBW is changed from 10kHz to 100kHz an increase of 10dB is expected, but only 8.9dB is seen, which is once again an uncertainty of 1.1dB. This uncertainty will affect the absolute noise measurements if it is not properly accounted for as a correction factor. Most instruments typically have a transfer function(defined as ratio of the output to input) which do not follow the datasheets explicitly. This does not indicate that the measurements are incorrect, but rather the gains in the system have changed(perhaps due to miscalibration). On the other hand, the spectrum analyzer(SA) perfectly reproduces a well calibrated sine wave at all frequencies with no spurious responses. The SA produced a flat white noise characteristic over its entire frequency range of 100Hz-1Ghz. A similar test done on amplifiers where one or more gain stages were not working, produced a frequency varying spectrum with spurious responses which indicated its nonlinear behavior. The SA was free from some observations. Our conclusion was that the SA worked perfectly, but was slightly miscalibrated. We have found our absolute measurements to agree very well with the theoretical results once this 1.1dB is accounted for in all our calculations. Section 3.5 which deals with subshot experiments, relies on relative measurements(the ratio of one level to another). Relative measurements do not require any correction since each level is affected the same and the net effect cancels out.

So why does this 1.1dB uncertainty occur in the first place? Fig. (3.4b) indicates an anomaly when the RBW is switched from 3Khz to 1Khz. We should expect a drop of 4.77dB but we notice only 1dB change. We believe that one of the IF gain stage or filter(in particular the 1kHz RBW filter) may be miscalibrated. This may also be the reason for the 1.1dB uncertainty in the other RBW settings and thus the gain change. Notice that the 3kHz and 10kHz noise levels have the same rolloff characteristic whereas the 1kHz

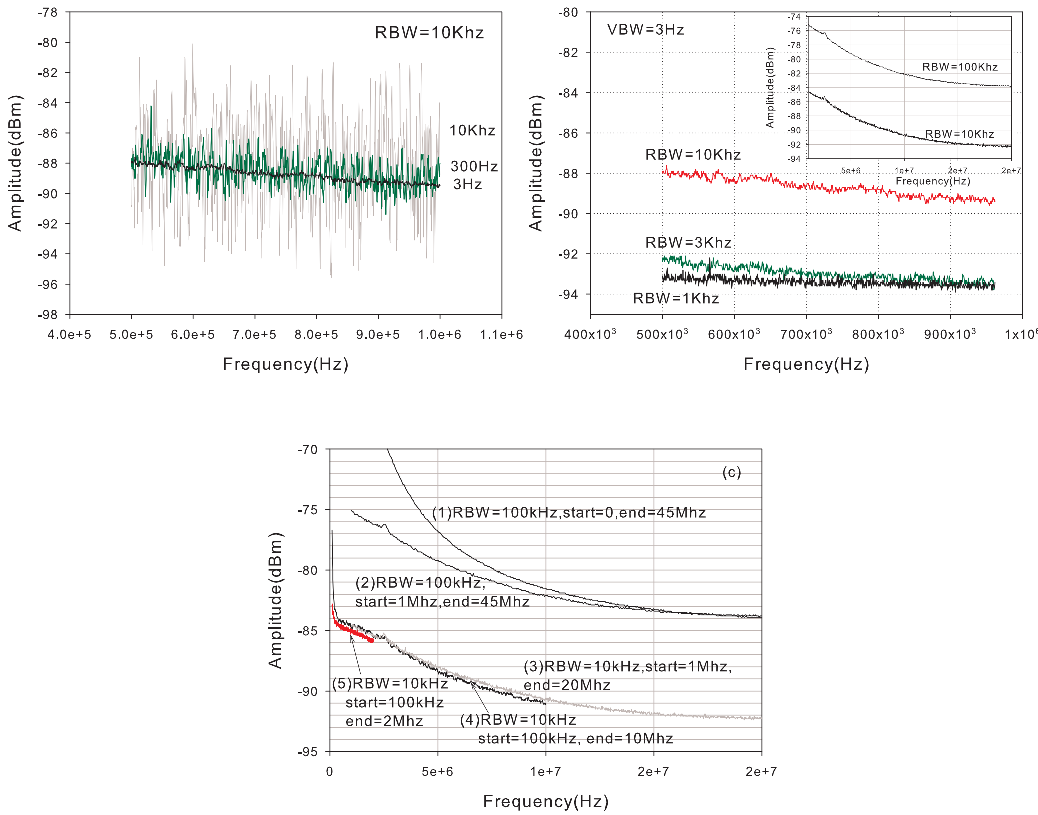

Figure 3.4: Spectra of the noise floor of setup in Fig. (3.3) measured with (a)Variation of VBW with a constant RBW of 10Khz (b)Variation of RBW with a constant VBW of 3Hz (c)Different span/center frequencies(start/stop frequencies) as a function of RBW

level seems to be flat at all frequencies similar to the DANL(The DANL actually has a 1/f characteristic as seen in the spec sheets but the SA calibrates the output in such a way that the noise looks flat on the display). The DANL from the data sheets is quoted at -112dBm at 500khz for a RBW=1kHz but due to the SA miscalibration, the noise level level may have shifted to -93dBm in Fig. (3.4b). So what is being measured may be the noise floor of the SA, and the expected resistor noise level has sunk below the DANL. This would explain why the 1kHz levels do not follow the 3kHz response at a constant difference. Most of the measurements were done at RBW of 3kHz and above and so that this discrepancy would not have to be dealt with.

Fig. (3.4c) show various measurements(performed individually on the SA and arranged on the same plot) indicating the variation in noise levels as we adjust the span and center frequency settings. If we look at measurements 4 and 5, we notice that the noise powers at 100kHz are not the same. This can be explained as follows: The total span for measurement 4 is 9.9Mhz whereas for 5, it is 1.9Mhz. Given that the total number of datapoints taken is 1000, we obtain a frequency resolution of $\Delta f = \frac{Span}{1000}$ which is 9900Hz for 4 and 1900Hz for 5. The RBW has been set to 10Khz in both cases. So during the sweep of the LO past the IF stage, the SA would give the most accurate readings when it sweeps for an integration time of nearly $1/RBW$ or a noise power equivalent to this effective bandwidth. But for the case of measurement 5, the SA needs to display a point on the screen around 2Khz before it has a chance to sweep past the 10kHz filter therefore displaying a fraction of the noise power expected. For measurement 4 on the other hand, the frequency resolution is nearly the same as the RBW, so we would expect more accurate noise powers. In actuality we should expect a 1/f dependence on the noise which is due to the LO tracing out the IF filter shape, followed by the 1/f character of the DANL in the frequency range of 0-1Mhz. In case of measurement 1 we set the start at 0Hz. The SA would obtain readouts at 0, 45kHz, 90kHz and so on integrating the 1/f nature of its own DANL since it is much larger than the noise of the resistor and PD combination. This would not affect relative measurements(such as comparing one noise level to another) but absolute measurements will be incorrect. The correct way is to set the start frequency to 1Mhz, thereby avoiding this 1/f nature completely and we notice that it has constant difference from measurements 3,4 and 5.

What is displayed on the SA screen is not the input noise spectral density but rather an integrated noise. As we have mentioned before we are more interested in the spot noise quantities and in order to convert what is displayed on the SA plots which is in dBm to dBm_{Hz}, three corrections need to applied [51, 52] which are as follows: 1.Under response due to logscale envelope detection(+2.51dB) 2.Over response due to the ratio of ENB to the -3dB bandwidth(-0.52dB) 3.Normalization to 1Hz bandwidth($-10\log RBW$). The net effect of these contributions give us

$$P_{exp}(\omega)_{dBm_{Hz}} = P(\omega)_{dBm} - 10\log(RBW) + 1.99dB \tag{3.5}$$

where P_{dBm} is the spectral power displayed on SA screen and $P_{exp}(\omega)_{dBm_{Hz}}$ is the corrected spectral density normalized to 1 Hz. Using this formula, the measured noise power can be related to the theoretical values. The noise marker feature of the SA makes these corrections automatically. We were not able to extract the noise marker values directly because the Labview drivers utilize the GPIB command KSA which essentially captures the complete trace of dBm values. It is more difficult to obtain the spot noise powers as we have to initialize the SA, followed by a complete sweep each time we need to extract the noise power for a certain frequency component. Instead, we rely on making the conversions to the dBm plots that we have acquired.

3.3.2 LED Characteristics

The LED IV characteristics are important for two main reasons:(a)For each measurement of shot and subshot noise, the drive current to the LED is inferred from the PD photovoltage. One way to ensure its accuracy is to perform IV tests with the setup of Fig. (3.3) which also serves to calibrate the setup provided the IV results agree with the specifications in the datasheet. There is no need to construct a separate IV measuring unit. (b)As we move to higher current ranges, the existence of series resistance effects, could affect the subshot noise spectra. So we need to set a boundary on the range of currents within which we would be assured of our subshot results. In Fig. (5a) ,the IV curves for the L2656 LED have been measured along with the squeezing measurements which was obtained as follows: Using the constant current source and varying the resistance we were able to vary the current according to the LED circuit equation $I_L = \frac{V-V_L}{R_S}$ and since V is the fixed battery voltage,V_L can be obtained. Note that if a voltage had been applied across the diode and the resulting current measured through a low impedance probe,we would get more error because of the exponential dependence of the current on voltage. The drive current I_L was obtained by replacing the constant current source with the current from the ILX Lightwave source and making sure that the same photovoltage was measured as using the constant current source. This way we did not have to disturb the setup of the system. The solid lines have been obtained by modeling the diode using pspice and the datasheet values. The datasheets specify currents only in excess of 10mA and so the experimental values were used to fit the IV curves for lesser current values. The L9337 should have a very similar structure to that of the L2656 which is seen by the values of ideality factor n=1.8 and bulk series resistance$r_s = 1.8\Omega$(In fact the L9337 is advertised as the replacement to the L2656). The only source of measurement inaccuracy is the ILX current source which tends to fluctuate by as much as $\pm 0.03mA$ which could explain the deviation in the Fig. (3.5a) from the solid lines. For example, the largest deviation is at 1.12V with an $I_L = 3.41mA$. If we set $I_L = 3.39mA$, we would get V=1.2V which would agree with the solid curves. The most important point to note is that we are working away from the high injection regime where bulk series resistance effects start to arise. This is also the region of backward pump processes which are responsible for squeezing under constant voltage condition[53]. Most textbooks attribute the deviation from the ideal diode equation model to only the series resistance[10] which is not true. For example, the total measured differential resistance is given by $r_{d,meas} = r_{d0} + r_{back} + r_s$ where r_{back} is the backward differential resistance(given by Eq. (2.x)) and $r_{d0} = \frac{nkT}{qI_L}$ is the standard differential resistance. At low temperatures, the authors of[] found that r_{back} which is a function of the BP process is nearly zero. Under this condition r_s can be estimated easily. At room temperature, we can extrapolate and determine r_s according to the resistivity-temperature dependence but in addition r_{back} is also present . The sum contributions will be the total resistance and not only the series resistance. When we subtract away the determined r_s from V_{meas} we obtain a diode equation which is still nonideal and is given by $I_L = I_S exp(eV_a/kT)(1 - \alpha_0(V_j))$. The ratio of this I_L to the ideal diode equation in the Fig. (3.5a) gives us the measure of the BP process ie.$1 - \alpha_0(V_j)$. It is quite hard to estimate this quantity,since we need to determine r_s which is unknown unless we know the device geometry or perform low temperature measurements. Because of the uncertainty of experiments under high injection conditions, the squeezing experiments are restricted to current levels of less than 10mA. Since the nonlinear backward pump processes would produce squeezing under constant voltage high injection current conditions, it would lead to a situation where both constant voltage and constant current bias methods produce the same subshot noise spectra, and hence the method of controlling the statistics of light between shot and subshot levels(which is an integral part of this thesis)

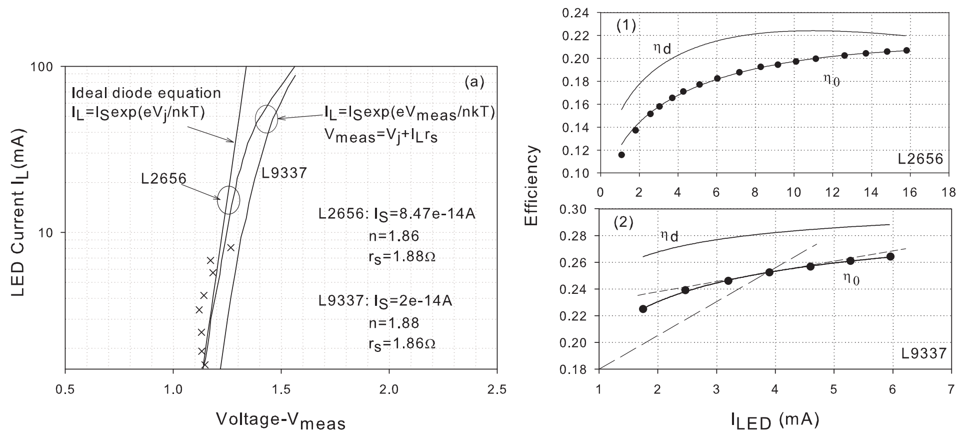

Figure 3.5: (a)Measured $I_L - V_{meas}$ characteristics of the L2656 LED which is compared with the ideal diode equation $I_L = I_S exp(qV_j/nkT)$ as well as the $I - V_{meas}$ curves obtained through pspice device modeling for both L2656 and L9337 LEDs. b)Mean quantum efficiency(η_0) and differential quantum efficiency(η_d) measured for the L2656(1) and L9337(2) LEDs.The DC operating point and tangent are shown for the L9337.

would be lost. The IV curves have also been used in the construction of LED spice models for the L2656 and L9337 LEDs and these models have been used in the calculation of certain quantities in chapter 4.

Efficiency is the most important parameter for a subshot experiment as seen in Eq. (3.4) where it can destroy any subshot characteristics even though the pump noise may be suppressed. Also the influence of non-radiative processes affect the squeezing results. Efficiencies can easily be changed with detection geometry and in order to model the experimental results accurately, a simple method is developed where the efficiency is measured once so that it can be used for all measurements. The total dc efficiency of the LED-PD system ie. $\eta_0 = \frac{I_{pd}}{I_L}$ can be defined as

$$\eta_0 = \frac{\eta_{c1}(1\backslash\tau_r)}{(1\backslash\tau_r + 1\backslash\tau_{nr})}\eta_{c2}\eta_{pd} = \eta_{int}\eta_{c1}\eta_{c2}\eta_{pd} \tag{3.6}$$

where η_{int} is the internal recombination efficiency, η_{c1} is the extraction efficiency from the LED to the output mirror through the collimating lens and photons lost at the semiconductor-air interface, η_{c2} is the coupling efficiency from the between the output photons and the photodetector and η_{pd} is the conversion efficiency of the photodetector which is dependent on the responsivity. We cannot measure η_{int} very easily, and so we rewrite the efficiency as $\eta_0 = \eta_L \eta_{c2} \eta_{pd}$ where $\eta_L = \eta_{int} \eta_{c1}$ is the total efficiency of the LED. LED injection efficiencies have been assumed to be 1. The differential efficiency is defined as $\eta_d = \eta_{c1} \eta_{c2} \eta_{pd} \frac{d\eta_{int}}{dN_C}|_{N_c=N_{C0}}$ where N_c is the electron population in the active region.In Fig. (3.5b), we have plotted the efficiencies as a function of photocurrent for the two LEDs used in our experiments. The differential efficiency has been calculated by taking the difference between the neighboring data. To get smoother results, a linear regression was done on η_0 followed by differentiation to obtain η_d. The efficiency plot obtained also coincides with typical values obtained in the squeezing experiments.Usually it is very hard to fix η_0 to be the same as we move from experiment to experiment, but any changes are only in the coupling efficiency as seen in Eq. (3.6). Hence the ratio $\frac{\eta_d}{\eta_0}$ is independent of the coupling parameter η_c and with the value of η_0 for that typical run of the experiment, we can estimate the fanofactors. Note that the efficiencies are frequency independent parameters(The authors in [42] had originally assumed it to be otherwise). From the Fig. (3.5b) we note that I_{pd} rises superlinearly with I_L and becomes more linear as drive current increases and eventually saturates. The LED saturation here is before the onset of detector saturation. If we had perfect linearity, η_{int} could have been taken as 1 and we could have determined η_{c1}. But this is not possible unless the device is cooled to low temperatures where the non-radiative channels are closed.η_d is essentially this deviation from linear behavior and characterizes the nonradiative processes. However η_{c2} can be estimated easily. The S5107 detector used has a responsivity(S) of 0.7A/W at 890nm and produces a high efficiency of $\eta_{pd} = S\frac{h\nu}{q} = 0.97$. The optical powers were measured using a calibrated Newport optical power meter from which we could obtain η_L. The dc efficiencies η_0 are determine from I_{pd} and I_L through face-face coupling between LED and PD. From these values estimated η_{c2} can be estimated. Some of these measurements have been shown in table (3.1). The L2656 has a typical flux of 15mW at 50mA[54] which gives us an efficiency of 21.5%. In the table. (3.1), at 20mA, the total efficiency is shown to be $\eta_L = 21\%$ which confirms the accuracy of the power meter. This can be used as power input to the PD, from which the

LED Current-I_L	LED Power-P_L	Photocurrent-I_{ph}	Efficiency $\eta_L = \frac{P_L}{1.39 I_L}$	Efficiency $\eta_0 = \frac{I_{pd}}{I_L}$
5mA	1.236mW	0.7716mA	0.1778	0.1542
10mA	2.740mW	1.706mA	0.1971	0.1705
15mA	4.278mW	Saturated	0.2051	-
20mA	5.838mW	Saturated	0.21	-
10mA(LE)	1.195mW	0.561mA	0.0895	0.06525
20mA(LE)	2.630mW	1.22mA	0.0917	0.06445

Table 3.1: Experimental values of optical power P_L and photocurrent I_{ph} for the L2656.The efficiencies η_L, η_0 have been calculated for two similar LEDs where LE characterizes the LED with low internal efficiency.

responsivity can be calculated as$R = \frac{I_{pd}}{P_L} = 0.62$,a value smaller than the expected 0.7A/W. This is nothing but the loss in coupling efficiency at the detector which is calculated to be $\eta_{c2} = 0.89$ and is quite high even without the aid of an integrating sphere. Such high η_{c2} is possible since the LED is outfitted with a collimating lens. Note that $\frac{\eta_d}{\eta_0}$ takes on values as large as 1.24 for the L2656, whereas it is close to 1.08 for the L9337. This implies that there fewer nonradiative mechanisms in the L9337 thus increasing the efficiency. A typical flux at 50mA is 23mW[54] which gives an efficiency of 32.2% at a center wavelength of 870nm,which is almost a decade larger than the L2656. The last two rows of table show results at 10mA and 20mA drive currents where the LED efficiencies calculated are 8% and 9%. These are efficiency measurements performed for a L2656 LED for which squeezing was observed initially but had later vanished. If the efficiencies are inserted into the Fanofactor relation of Eq. (3.4) under constant current conditions($F_p = 1$), one should theoretically see some squeezing but this is not the case. Since the coupling geometry was not drastically changed, the loss of efficiency in this case is due to the LED which had have been operated previously at peak currents of 80mA, causing joule heating and a decrease in internal efficiency. At 10mA, the total efficiency is 8% which is far below the 19% expected. This loss can be traced back to the radiative processes and injection mechanisms which are responsible for squeezing. Even though the LED was usable, squeezing was lost because the internal drive fanofactors reverted to their Poisson states. This is an interesting conclusion,since it shows that a constant current is not the only condition to establish squeezing.

3.3.3 Photodetector Nonlinearity

The S5107 PD used in the experiments must show good linearity at all ranges of optical powers used, since many experiments in the past have shown squeezing characteristics only to be later attributed to the photodetector nonlinearities[3]. So it is important to experimentally verify this nonlinearity and make sure it is at a minimum for the range of photocurrents detected. An integrated optical power P_L that is incident on the PD is related to the photocurrent by $P(I) = \frac{P_L}{I_{ph}} = Gh(I)$ where $h(I)$ is the nonlinearity function of the detector with a certain response $P(I)$ and G is a constant of the photodetection process[**?**].The important assumption here is that at very low currents, the detector is linear giving h(0)=1 and the response $P(I) = G$. Now define

$$f(I) = \frac{dh(I)}{dI} = \frac{1}{G}\frac{dP(I)}{dI} \tag{3.7}$$

where f(I) can be interpreted as the rate of change of the nonlinearity with photocurrent. We can define the small signal ac quantities $\Delta P = p_{ac}$ and $\Delta I = i_{ac}$ as follows:

$$\frac{\Delta P}{\Delta I} = \frac{dP}{dI} \rightarrow p_{ac} = Gf(I)i_{ac}(I) \tag{3.8}$$

from which the function f(I) save for the extra constant of G is the inverse responsivity function g(I) of the PD and is given as

$$f(I) = \frac{1}{g(I)} = \frac{i_{ac}(0)}{i_{ac}(I)} \tag{3.9}$$

where the constant G has been removed by assuming that f(0)=1 and that gives $G = \frac{p_{ac}}{i_{ac}(0)}$ which was substituted back in Eq.(3.8) to give Eq. (3.9). The above function was experimentally determined using the ac-dc technique[55] which is carried out by inserting two optical signals into the PD; 1) A small periodic optical square wave from the L2656 using a function generator having an amplitude of 0.7V in order to turn the LED on and a zero OFF(LOW) amplitude and 2) A time invariant dc optical signal from a 650nm Luxeon LED. The dc power is first set to zero ie P(0)=0 and the on amplitude of the ac photocurrent $i_{ac}(0)$ was measured to be around 0.024mA. Next the ac photocurrent was measured as a function of the dc optical power with a lockin amplifier and the ratio $i_{ac}(0)/i_{ac}(I)$ was calculated from the lockin readings. The lockin is a phase sensitive detector similar in operation to the SA except the mixer inputs are the signal and a square wave instead of the sine wave from the LO as for the SA. The square wave reference voltage is fed into the lockin as well as the LED in order to match its phase. The lockin 'locks' on to a frequency component or harmonic of the square wave in this case and downconverts and amplifies it such that the output is a dc voltage with very small noise(In other words signal to noise is large). The dc component of the photocurrent was obtained from a voltmeter which measured $J = I + < i_{ac}(I) >$from which I was obtained. For a square wave we have $< i_{ac}(I) >= \gamma i_{ac}(I)$ where $\gamma = 50\%$ is the duty cycle of the square wave.

The inverse response function $g(I) = \frac{i_{ac}(I)}{i_{ac}(0)}$ has been plotted in Fig. (3.6) since this is a measure of the responsivity of the system. The results are quite similar to relative responsivity $\delta = \frac{R(I)}{R(0)}$measured in [?]. In addition,a 3-6th order polynomial fitting procedure was also performed to calculate the relative responsivity and the error uncertainties in our measurements, but the results were not accurate, since we had taken only a few data points. However g(I) by itself is a very good indicator and is more sensitive to the nonlinearity variation than the responsivity[55]. We note that g(I) changes sublinearly about 1% from 0-1.5mA and at larger current detector saturation sets in. Actually $i_{ac}(0)$ still has a small time averaged dc voltage of 0.35V which the square wave rides on,but we assume it to be negligible to the dc optical powers generated by the Luxeon LED. We can now see what happens to noise if we interpret g(I) in small signal transfer terms: the slight change in linearity can cause changes in the fanofactors. If we shine a coherent beam of light on the PD for which the shot noise is dependent on the photocurrent , at larger photocurrents the shot noise should be smaller than expected. So we should obtain $F < 1$. A 1% error as the Fig. (3.6) dictates, is sufficient to cause 0.04dB change which is very small and can be neglected. So for all purposes, we assume that the PD is linear. In fact, experimental results have confirmed this PD to be linear to about 40mA photocurrent[13].

3.3.4 Amplifier Characteristics

The Analog Modules 322-6(AM) is our principal amplifier which provides the gain for the detectors. The design specs for this amplifier(Appendix.X) cites a gain of 40.7dB

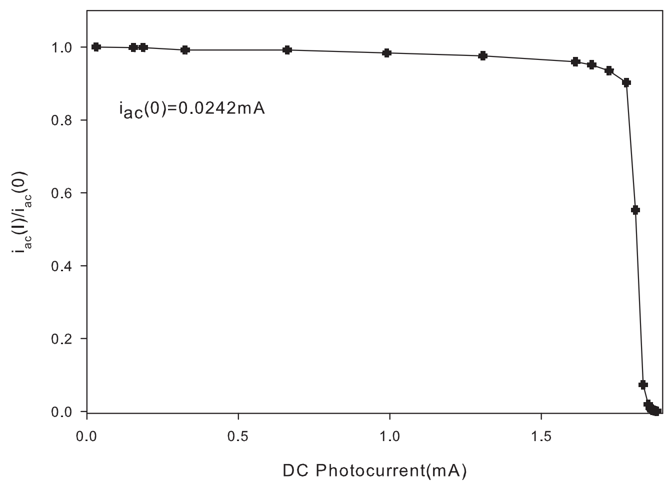

Figure 3.6: Normalized function g(I) versus photocurrent I_{ph} measured for the S5107 PD in photoconductive mode along with the interpolated curve

with a noise as low as 316pV/$\sqrt{Hz}$. The exact conditions under which these parameters were measured by the company were unknown. For example, at what frequency was the measurement made, or was the amplifiers impedance matched for gain measurements. We have measured the transfer function of the AM amplifier by feeding an input of -60dBm from a HP 8660 signal generator(which has a frequency range of 1-2600Mhz) into the amplifier. The difference between -60dBm and output measured on the SA gives us Fig. (3.7a). The lab function generators(HP 8116A) could not be used as the output rolled off at 50Mhz.This measurement strategy would seem quite obvious as we find out the 'system' gain $K_t = V_o/V_i = D_v A_v$ where D_v is the voltage divider and A_v is the voltage gain. But there is an impedance mismatch between the 50Ω generator resistance and the 200Ω input resistance of the AM. This input resistance is a physical resistor in parallel with the infinite input impedance of a FET stage. The -60dBm reading of the signal generator is specified for a 50Ω load. So if we subtract the gain of the amplifier from the output of SA, we find the power in dBm such that the source and load are matched. We don't have to worry about impedance mismatch. In fact if we plug in a 50Ω resistance into the mismatched amplifier and subtract the gain we should measure around -174dBm(actually the noise power should be higher if we consider the input impedance noise and the amplifier noise) according to the maximum power transfer theorem. This -174dBm noise power is hard to measure using only

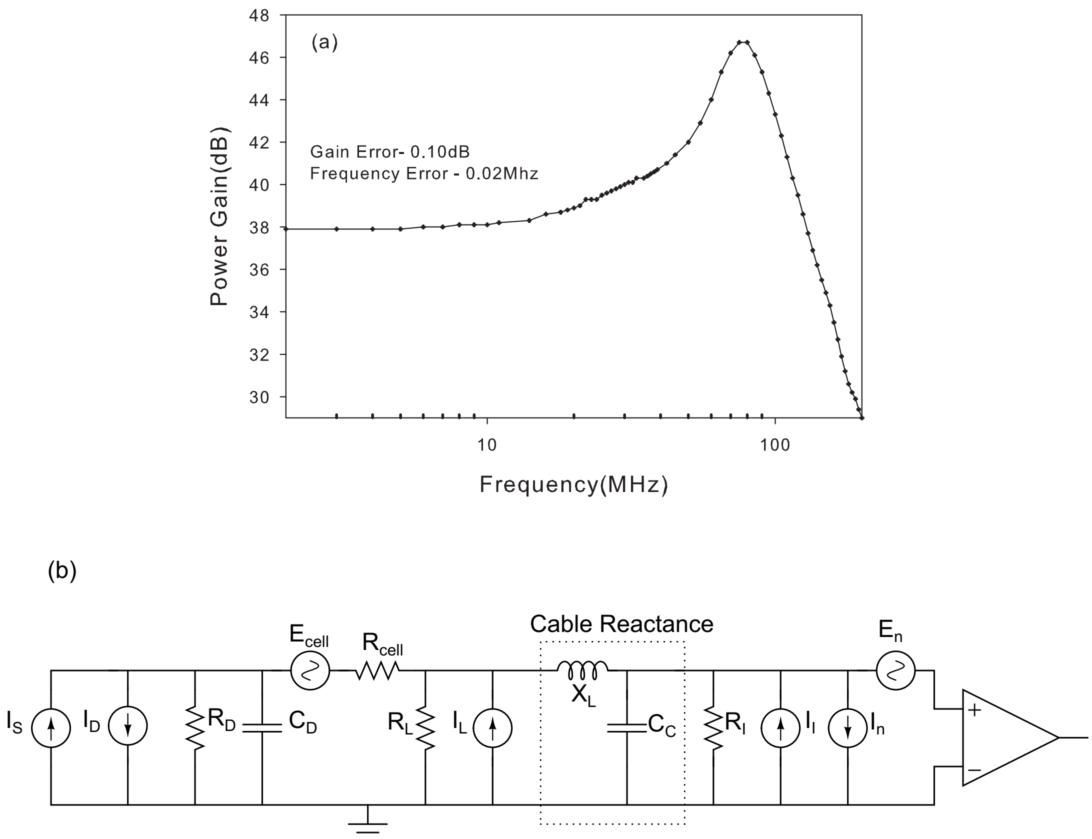

Figure 3.7: (a)System gain $K_t = \frac{V_o}{V_i}$ measured for the Analog Modules 322-6 amplifier with an input power of -60dBm (b)Noise equivalent circuit model of the entire measurement chain including PD equivalent circuit, cable reactances and input impedance of the amplifier

the single AM stage, but this value has been observed by cascading 3 amplifier stages(which will be discussed later in this section).

On the other hand when we couple a photodiode to the input,we are more interested in the shot noise of the photogenerated current. The load resistance is usually set at 5080Ω and the gain curves will not be valid if they are used as such. In such a case,we calculate the shot noise voltage across the 200ohm resistor(V_{200}) and find the output voltage as $V_{o,rms} = A_v V_{200}$ .To find A_v we used a 650kHz sine wave of 10mV peak voltage.The oscope measured it at 11.25mV which was corroborated by the SA giving -35dBm which can be verified using $10 * log(\frac{11.25mV*0.5*0.707}{50*1mW})$ where 0.5 is the voltage divider ,0.707 is the rms conversion factor ,and is divided by 50 to find power across 50ohm referred to 1mW.

Thus $11.25mV$ actually represents $V_{200} = 6.28mV$ at the 200ohm input impedance of the amplifier. The output at the SA for this input 3.10dBm or is $V_{o,rms} = 0.319V$ from which $A_v = 50$. At other frequencies A_v rises slowly and the peaking at high frequency as seen in the Fig. (3.7a) is probably due to the impedance mismatch and inductive behavior of the cables. The only source of error in this calculation is the voltage divider at the input which we have assumed based upon our understanding of the amplifier design. We also note that the spec sheet does not state any capacitance at the input which could change the voltage division picture. Also transmission line effects are neglected since we deal with maximum frequencies of 40Mhz and our cables between PD and AM are quite short($< 1m$) ie. the transmission line can be treated as a wire. However, the noise spectra demonstrate a frequency dependent behavior at higher frequencies($> 10Mhz$) which we later attributed to the reactances in these cables. This issue will be discussed when the optical noise spectra of the L9337 LEDs are studied. In our shot noise experiments, we find that using a gain of 70(a difference of nearly 1.5dB) helped to get more accurate results, which could be because of the SA miscalibration and the reactances of the cable. This value of 70 is equivalent to the total gain from the signal input into the amplifier to that which is being displayed on the SA screen. Hence the gain curves are used when we insert any 50ohm input source and for the photodetector experiments, we choose $A_v = 70$ to give us correct measurements. Also we note that the gain reaches the manufacturer's gain of 40.7dB only at frequencies beyond 10Mhz which would affect A_v as well. This would imply that the input noise voltage is specified at the same frequency since it too is a function of gain ie. $\frac{E_{no}}{K_t}$ where E_{no} is the output voltage noise.

The simplest way to determine the input noise of the AM(E_n) is to short the input(which removes the 200ohms input impedance) and then measure the output. The output divided by gain gives the E_n. Looking at the circuit diagram in Fig. (3.7b), the output noise is given by

$$E_{no}^2 = A_v^2(4kTR_p + I_n^2R_p^2 + E_n^2) \tag{3.10}$$

where $R_p = R_1 \parallel R_2 = \frac{R_1R_2}{R_1+R_2}$. We neglect I_n since its value is quite small unless $R_p > 1k\Omega$ at source[56]. Let us outline a few noise measurement cases:

Case 1.The PD was connected to the AM and the noise was measured at 20Mhz which led to -132dBm/$\sqrt{Hz}$(which can be seen in a few of subshot noise plots later on) whereas the calculation using gain of $A_v = 70$ as described above and $R_p = 5080//200 = 192\Omega$ should give us a noise power of -125dBm , a difference of 7dB. The noise signal actually rolls off which we have not accounted for. At low frequencies we would expect the resistor to show full thermal noise but at high frequencies we have kT/C noise ie. the resistors roll-off as $\frac{E_t^2}{1+(\omega RC)^2}$ leaving only the amplifier noise behind. Of course, there is still some resistor noise which is why the result is still above the amplifier noise cited at 416nV/$\sqrt{Hz}$

Case 2.Terminating with a 50ohm resistor:The noise was -125.57dBm at 650Khz which disagrees with the expected value by nearly a difference of 9dB. We may reason that the sensitivity of the SA itself is close to this limit but the spec sheets show that this is not the case[57]. Also there is the possibility that the SA is uncalibrated at low ranges or excess noise being added in some input stage. 1/f noise is usually present at low frequencies but most good amps based on FET designs have the corner frequency at couple of hundred Hertz, well below the frequency of 650kHz. So we conclude that we cannot measure resistor noise at low frequencies unless we have a larger amplification. At 10Mhz, we found a value of -131dBm_{Hz} which is very close to the expected result of -131.8dBm_{Hz} with a gain of 70 and $R_p = 40\Omega$. The first thought that one might have is that this looks like the SA noise floor, but from our knowledge of the SA, the noise floor should theoretically be -148dBm at the 1-1000Mhz range. So the value measured should be the correct result for the resistor noise. Of course it is also specified that the SA measures noise accurately for signals 10dB above the noise floor which the above value satisfies.

Case 3. Finally when terminated with a short the value remained around -136dBm suggesting that the difference between 50ohm and input noise was smaller by 2dB. Going backwards to the input this time by dividing by the gain we find around 0.506nV/$\sqrt{Hz}$. An AM technician has measured this to be 0.416$nV/\sqrt{Hz}$. This is ultimately the resolution of our experiments and often we deal with noise levels larger than this and we can apply the 10:1 rule ie. we can neglect the smaller of the two noise signals when the rms value of one is 10 time the other.

Case 4.When we open circuited the AM, we saw a increase of 5dB above the base noise floor. Normally an open load implies that we are measuring I_n in the Eq. (3.10). But in this case,we still have the 200ohm resistor which puts the value close to measurement 1 above.

Since we are working so close to the SA noise floor, one might wonder why not just increase the amplification by chaining a number of such amplifier modules. Some of the initial experiments coupled the AM with 2 Minicircuits 500ZLN voltage amplifiers with a gain of 20dB each to create as many as three stage amplifier blocks with theoretical power gains reaching 80dB. The NF of the 500ZLN minicircuit amplifier is around 2.9dB[58]. The AM amplifier noise figure can be calculated from the measured input noise voltage density as [59] $NF_{AM} = 10 * log(\frac{E_{200}^2+(416pV/\sqrt{Hz})^2}{E_{200}^2}) = 0.22dB$ which is quite small compared with the 500ZLN and hence it will have to be used as the first stage in the amplifier chain. The total noise figure obtained by using the Friis formula[49] is NF=0.25 which is a small change from the first stage NF ie. it implies that most of the noise of the measurement chain is from the first stage only. In Fig. (3.8a), we note the power spectrum at -30dBm when the three stage amplifier was terminated at the input with a 50Ω resistor. Using an input of -100dBm, the measured gain at 10Mhz was 101.6dB. The noise of the 50Ω can be calculated using the values from Fig. (3.8a) as -30dBm-101.6dB-44.77dB+1.99dB=-174.38dBm which is what we expect for a resistor. The 44.77dB is due to a 30Khz RBW filter used and the 1.99dB is the SA corrections as detailed earlier. This system gives similar values when terminated with a PD with 50ohm load provided no voltage was applied. When we increased the reverse bias to the PD,the noise levels went down as shown in Fig. (3.8b),something we could not explain for this 3 amplifier measurement setup. In other words, the degree of reverse bias set the noise floors at the SA and any light applied to the PD increased the noise level proportionally from this noise floor. We also experienced issues regarding ground noise and return paths in the system particularly when the photodetectors were connected. With such large gain, the inputs were sensitive to how the amplifiers were placed in the shielded box,wiring of cables and even movement of hands. For the above reasons, we decided to use just the single stage AM amplifier for our shot/subshot measurements. We would be

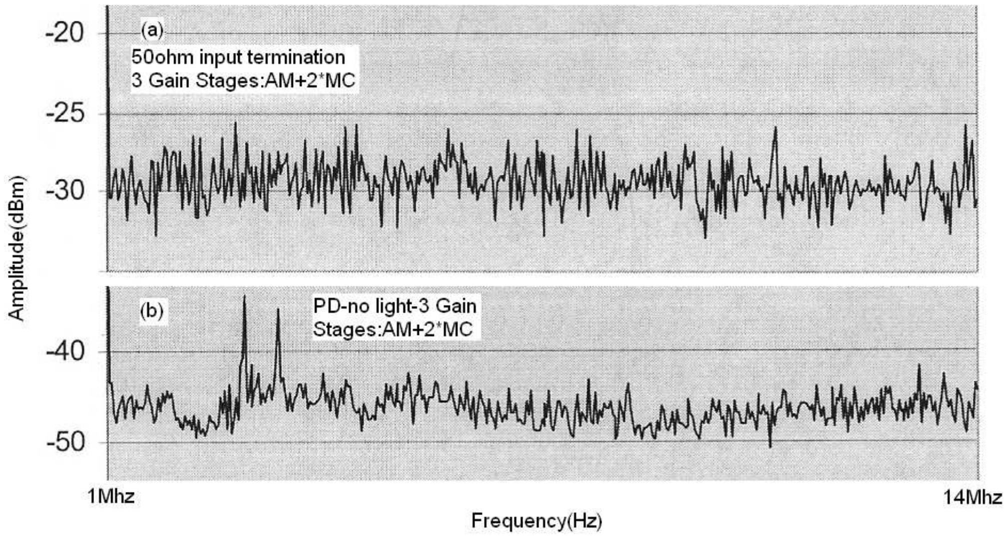

Figure 3.8: (a)Thermal Noise Power of a 50Ω resistor obtained with a 3 gain stage amplifier chain (b)Dark current + 50Ω noise power for the PD reverse biased at 10V with the same 3 gain stage amplifier.

working quite close to the spectrum analyzer noise floor but we would be able to discern or measure with sufficient accuracy at the range of current levels we used.

With the noise figure of the analog modules amplifier (AM) determined, the maximum sensitivity limits can now be established in the form of system noise figure(NF_{sys}) of the AM-SA combination and the noise equivalent power(NEP) of the overall system ie. PD-AM-SA combination. The noise figure of the AM-SA is essential so we know the fundamental limits for the smallest photocurrent noise that can be detected on the spectrum analyzer. When we connect a preamp to the SA, the noise levels either go up or remain unchanged. For example,if they increase by at least 15dB, then the noise figure of the AM-SA system is given by $NF_{sys} = NF_{pre} - NF_{SA}$ [52] where NF_{SA} is the spectrum analyzer's noise figure and NF_{pre} is the noise figure of the preamp. Our case is different in that the noise levels do not change all that much when we connect the AM. For the SA, the DANL changes in the 100kHz-1Mhz range. So we choose to evaluate the system noise figure NF_{sys} at 500-600kHz since our shot noise measurements were performed at this frequency whereas the system noise figure is constant in the range 1-1000Mhz range. Based on frequency range we can define two noise figures.

1.500kHz: From the spec sheets[57], we see that at 500kHz and an RBW=10kHz , the DANL is -102dB. The NF_{SA} can be calculated using the formula[52]

$$NF_{SA_1} = DANL - 10 * log(RBW) - kTB_{B=1} \tag{3.11}$$

Here $kT = -174dBm_{Hz}$ and we can estimate $NF_{SA_1} = 32$. Now we need to calculate $NF_{AM} + G_{AM} - NF_{SA_1} = 0.22 + 40 - 32 = 8.22dB$ and using the charts provided in [52] we can determine NF_{sys_1} to be at 0.4dB

2.1-1000Mhz: From the spec sheet, we see that at RBW=10kHz, DANL is -110dB. Then $NF_{SA_2} = 24$ and $NF_{AM} + G_{AM} - NF_{SA_1} = 16.2$. From the chart in [52] ,we obtain $NF_{sys_2} = 0.2dB$.

The NF_{sys} is usually specified to see how much above -174dBm_{Hz} we need the signal noise to be in order to be displayed on screen. In the case of AM, even -174+NF_{sys_2} gives -173.8 and so it should be able to measure the thermal noise of a 50 ohm resistor which we have measured. The minicircuits 500LN preamp on the other hand provides a $NF_{sys} = 8.2dB$ in the 1-1000Mhz range which is quite large when compared to the AM. So -174+8.2=165.8dBm_{Hz} is the minimum noise it can measure. We initially tried to reproduce results from[60] using the Luxeon LXHL-ND98 light emitter and the ZFL500LN amp but we found that unless we drove our LEDs hard enough,we had a difficult time trying to change the noise levels. Note that the DANL does not change at all and still remains at -110dBm for RBW=10kHz. For example, with an input of -174dBm at the AM amplifier, the output at the SA becomes $-174dBm + G_{AM} + 10 * log(RBW) = -110dBm$ and hence equals the noise floor or DANL. Note that at 650kHz, the result is nearly identical to the $> 1Mhz$ range. But our measured results showed that noise levels were about 10dB higher than expected.

Similar to the noise figure of the system, a noise equivalent power(NEP) can also be defined as[61, 62] $NEP = \frac{I_t}{S}$ where $S = \frac{\eta e}{h\nu}$ is the responsivity in A/W and $I_t = \sqrt{2q(I_D + I_b + I_L) + \frac{4kT}{R_L}}$ is the total noise current for the detector without the amplifiers, I_D is the photodiode dark current noise, I_b is the noise due to background radiation, I_L is the photocurrent due to incident light and R_L is the load resistance. NEP represents the smallest optical noise power that we can measure with the present photodetector, AM

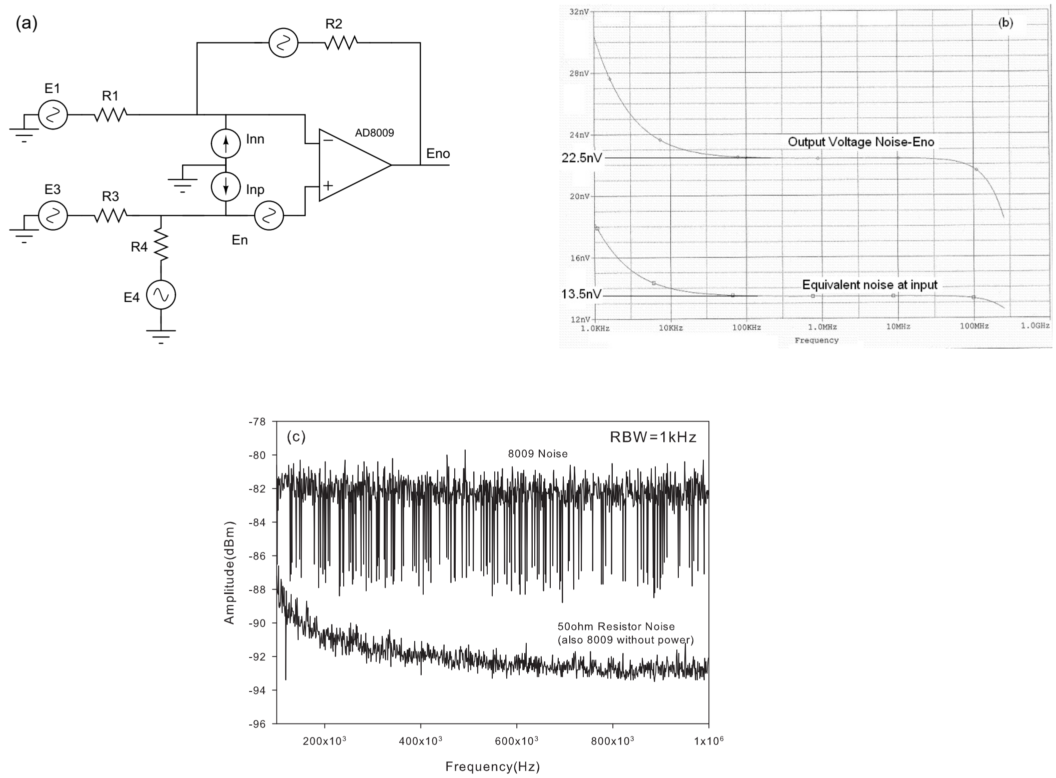

Figure 3.9: (a)Noninverting Equivalent circuit noise model of the Analog Devices AD8009 opamp (b)Input and Output noise spectral densities of the circuit in (a) calculated using pspice (c)Experimental noise power obtained for the unity gain opamp which is obtained by amplifying using the Analog Modules 322-6 amplifier. A 50Ω terminated resistor noise is also shown as reference.

amplifier and the spectrum analyzer combined. Generally NEP is defined for a PD which is not connected to any additional stages. With the introduction of the amplifier, the total current noise is then defined as $I_t = I_n$[63] (here I_n refers to the input current noise of the amplifier) since the amplifier noise would then have to be the minimum value for an equivalent optical power. For the PD-AM setup we cannot use the above relation exactly since it is more amenable for current and transimpedance amplifiers where the input current noise is much larger than the voltage noise component. So we calculate the NEP as the signal power equal to noise at the infinite input impedance of the amplifier as follows

$$\frac{\eta e}{h\nu} NEP = \left(\frac{E_n^2}{R^2} + I_n^2 + I_t^2 \right)^{1/2} \tag{3.12}$$

Using a value of $S = 072\,A/W$ for the S5107 PD and R=192Ω,and with the measured $E_n = 506pV/\sqrt{Hz}$ and $I_t = \sqrt{\frac{4kT}{R}} = 9.28pA/\sqrt{Hz}$,the NEP is $13.39pW/\sqrt{Hz}$. Most of the experiments have dc optical powers in the range of several mW and the photocurrent in mA. For example, the smallest drive current(to the LED) in the subshot experiments was at $I_L = 1.57mA$ which produced a photocurrent of 0.2066mA. The corresponding equivalent noise power is $11.2pW/\sqrt{Hz}$ which is very close to the NEP. This is infact the smallest drive current that can be used for the LEDs without the optical powers going below the noise floor of the PD-AM-SA system. In fact if we addup the powers(the noise power at 1.57mA LED drive current with the background noise) we should expect a 2.3dB rise from the NEP but in our experiments the noise spectra increased by about 1.6dB from the noise floor at 600kHz which is quite reasonable considering the coupling efficiency is not maximum and this would affect the responsivity.

Next we designed an AD8009 amplifier for the purpose of amplifying the average in the stochastic modulation method. The AD8009 voltage amplifier was constructed using SMT components on the evaluation boards supplied by Analog Devices. The design is a typical non-inverting configuration. We set the gain to unity to perform noise measurements and later changed the gain to 20 to give a bandwidth of around 50Mhz. The noise features can be calculated from the formula[64] which can be obtained using the superposition theorem from each source and then adding the square of them since each source is uncorrelated.

$$E_{no}^2 = (1+\frac{R_2}{R_1})^2(E_{n1}^2 + E_{n2}^2 + E_{tp}^2 + I_{n2}^2R_p^2) + (\frac{R_2}{R_1})^2(E_{R_1}^2) + E_{R_2}^2 + I_{n2}^2R_2^2 \tag{3.13}$$

In our calculations we have tabulated a noise 'budget' in order to calculate the total output noise which is essentially Eq (3.13). except the individual contributions are noted and can be optimized.

The total noise at the output E_{no} can be obtained from taking the square root of the sum of squares of column 4 in Table. (3.2). From which we get the noise as $E_{no} = 21.208nV/\sqrt{Hz}$. The fifth column represents the noise reflected back at the input of the noninverting amplifier pin which is obtained by dividing column 4 by $1+\frac{R_2}{R_1}$. The output noise is further voltage divided by the 200//50ohm load of the AM and the AD8009 which gives a $E_{200} = 9.42nV/\sqrt{Hz}$. If we use $A_v = 70$ as defined above the noise power at the SA is -110.6dBm_{Hz}.We measured noise powers at 10Mhz(using the noise marker feature) ranging from -112.9 to -112.2dBm in a RBW of 1kHz to 10kHz whereas at 600Khz(where the gain of 70 is valid) we can see from Fig. (3.9c) ,the noise power using a RBW=1kHz is around -110dBm_{Hz}.This is a difference of 0.6dB to the theoretical values. The same discrepancy existed when we measured the thermal noise using this amplifier. If we had chosen a gain of 75 instead, we would have measured -110.1dBm_{Hz}. Since all our measurements have uncertainties of around 0.4-0.5dB, we may not be able to explain the variation from 70 to 75,a difference of nearly 0.3dB. The total input noise is obtained from column 5 of Table. (3.2) to be 10.675nV/$\sqrt{Hz}$ which is much larger than the AM input noise. The AD8009 requires the design of a properly shielded custom PCB board at Ghz frequencies. This would eliminate the negative going spikes in the noise spectra of Fig. (3.9c). Since the AD8009 showed good low noise input, it was used in tandem with the AM to amplify square waves in our modulation experiments such that the input noise which is quite low does not propagate and affect other noise levels in the measurement chain. For example, if we use a T-connector to route a signal to both the oscope and the AM at the same time, there is a return path for the noise from the scope which gets amplified by the AM. In such cases, the AD8009 would be used as a low noise buffer with small amplification.

Noise Source	Value(nV or pA/$\sqrt{Hz}$)	Gain Multiplier	Noise at output(nV$\sqrt{Hz}$)	Noise at input
R1=499Ω	2.83nV	1	2.83	1.415
R2=499Ω	2.83nV	1	2.83	1.415
Rp=8.33Ω	0.366nV	2	0.7324	0.366
En1	1.9nV	2	3.8	1.9@10Mhz
En2	1.9nV	2	3.8	1.9@10Mhz
In1	41pA	499Ω	20.45	10.229
In2	46pA	16.66Ω	0.766	0.383

Table 3.2: Noise contributions of the various noise sources in the calculation of the total output noise voltage of the AD8009 non-inverting opamp

Also from the table we note that the noise is large primarily because of the I_n contribution which could be reduced by lowering R_2 resistor. So if we are to go to a gain of 20, and still preserve the same input noise approximately we should change R_1 to 26Ω.We used 25Ω resistor to set the gain. From Fig. (3.9c) we see that the noise is white in nature but there are certain negative peaks which seem to change the variance. When we measured the noise powers, we used averaging features and these spikes did not appear. In other words,if an averaging filter had been applied any spurious amplitude pickups would not have disappeared. When we measured the noise, the AD8009 had no shielding which could explain the pickup.The input/output terminators(SMB connectors) were not so tight and the voltage of 5V was applied without any voltage regulation, only relying on supply bypass capacitors.

3.3.5 Shielding

Our interest is in the device noise sources and in order to study them, we have to minimize all external sources of interference(such as EMI from wireless phones, power supplies, and light sources). For proper shielding, it is important to first identify the noise source, the receiver and the coupling medium. First shielding can be used to confine noise to a small region and prevent it from getting into a nearby critical circuit. Second, If noise is present in the system, shields can be placed around the critical circuits. These shields can consist of metal boxes or cables with shields around the conductors. We minimized the spurious noise until the optical shot noise spectra could be clearly observed. Even though shielding has a sound scientific basis, most of the time we felt as if we were chasing a naughty child with a stick. In general it is a good rule to avoid loopy interconnections and minimize cross overs. However there are common sources of interference noise which we can avoid using shielding. The experiments reported in this thesis observed the following design rules to reduce the ambient noise levels.

1.Capacitive Interference: Capacitive interference occurs when a fringing electric field associated with a noise source is large enough to produce a displacement current in an electric circuit. Consider an equivalent circuit made up of a noise source affecting a receiver of impedance Z through the C defined above.Then the noise voltage at the receiver in the electronic circuit is given as $V_{on} = \frac{V_n}{1+\frac{Z_C}{Z}}$ where V_n is the noise voltage of the source and

Z is the effective impedance of the electronic circuit. From the above equation, it can be seen that the magnitude of the noise voltage increases with the frequency of the source and effective impedance Z. This effect is very critical when constructing systems that operate at reduced power level(high values of Z), higher speed(implying faster frequencies) and higher resolution(much less output noise permitted). When a shield is added, we have split the equivalent circuit into two loops, where there is a noise current in loop 1 is proportional to the driving voltage source V_n whereas in loop 2 , there is no current since there is no driving source in that loop(ie. the shield has isolated the source). Hence the sensitive circuit has been shielded from the noise source. In our system for example, we encountered this problem between LED and PD face to face coupling. The LED metal plate carried noise currents from the power supply which would capacitively infringe on the detector circuit. We had constructed shielded twisted pair to connect the LED to the current source and grounded the face plate, as well as the RF cage. Later when we covered with LED with black tape, and increased the LED current, we noticed that the noise levels remained the same at -76dBm for a 2 stage gain amplifier setting effectively removing the capacitive coupling problem.

2 Magnetic Field Interference: Noise in the form of a magnetic field can induce a voltage in another conductor due to mutual inductance. Its more difficult to prevent, since it can penetrate conducting materials. For example, a shield constructed around a conductor which is grounded has little effect on the magnetically induced voltage in that conductor. As a magnetic field penetrates a shield its magnitude decreases exponentially. We can define the skin depth of a shield as the depth of penetration required for the field to attenuated to 37% of its original magnitude(in air). Since skin depth decreases with increase in frequency, high frequency magnetic noise is not that crucial and can be eliminated from the system easily. The main problem, however is the 50-60Hz line frequency which is the principal source of magnetically coupled noise at low frequency. We don't have to worry too much about 60Hz noise as the frequencies we work with are in excess of 1kHz. To avoid higher frequency magnetic interference we use a few design rules:

a) Keep the receivers are far as possible from the source of interference.

b) Use a twisted pair of wires for carrying the current that is the source of magnetic field. If the currents in the two wires are equal and opposite the net field in any direction will be zero. Alternatively, the shield of the cable can be made to carry the return current.

c) Since magnetically induced noise depends on area of the receiver loop, the induced voltage can be reduced by either reducing the loop area or the orientation of the loop to the field. This is quite similar to building a transformer where the flux linkage is increased by adding more turns to the loop.

3. Conductive Interference: These arise from currents flowing in the ground system. These currents arise from power systems, from reactive coupling and from radiation. The resulting ground potential difference can couple into the signal paths. It is usually futile to short out these potential differences. The two ground points of interest are the power supply termination and the input lead termination. This ground potential difference is usually referred to as common-mode. These were one of the greatest issues.

4. Electromagnetic field coupling: Fields from nearby transmitters are a source of interference. These fields couple voltages into the input cable in the form of a common-mode signal. The signal is proportional to loop area and the frequency. The loop area is between the cable and the earth plane. Normally these signals are out of band and do not appear as noise. They are troublesome because they can be rectified in the instrument and appear as a DC offset.

5. Transfer Impedance: Current flowing in the shield can couple voltage to the conductor pair in the cable. This is generally a high frequency phenomenon. For long lines, some form of differential filtering may be needed to attenuate this form of coupling.

In Fig. (3.10a) we see that when the RF cage was opened we found a noise power of -55dBm with the 2 stage amplifier setup and in Fig. (3.10b) the noise powers went down to -60dBm. The interference in this case is an optical noise which is white in nature since it raises the levels at all frequencies. There are also spikes at 4Mhz which is predominant with the 3stage amplifier setup since with larger gains it is more sensitive to pickup. We were able to minimize most of the noise sources but not eliminate it completely. For example the monitors which were needed to extract the plots produced conductive interference at

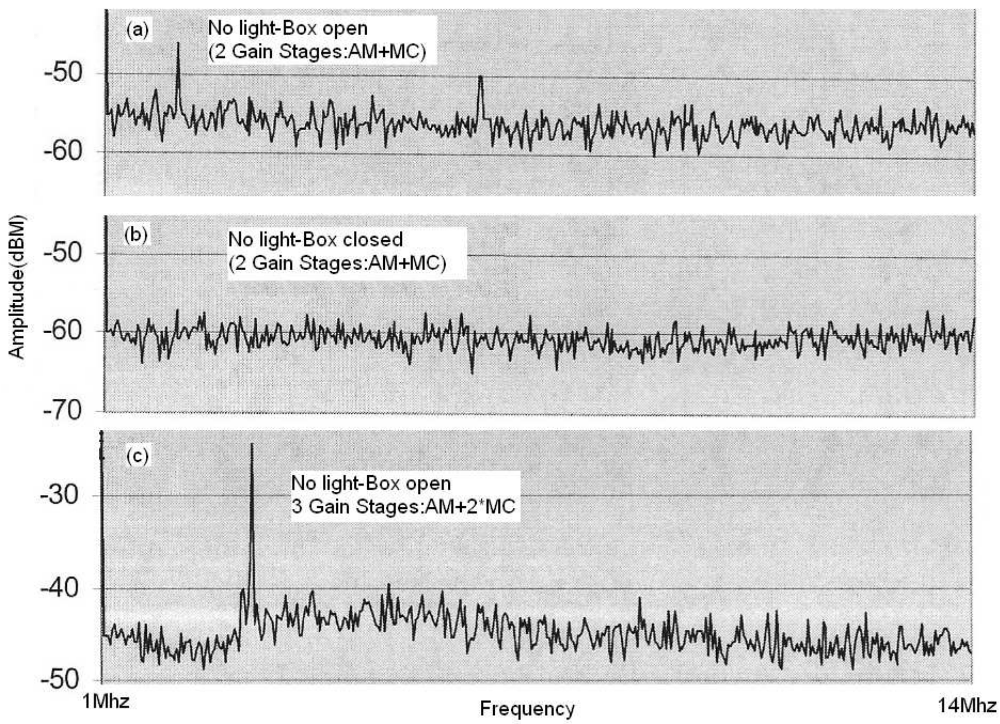

Figure 3.10: Noise power variations due to environmental and spurious optical noise obtained with the shielded RF cage open or closed. The measured noise power is the known PD2 darkcurrent+5080Ω resistor noise as well as spurious environmental RF and optical noise obtained at a RBW=30kHz.

frequencies around 30-40Mhz. So during data extraction we had to turn off the monitors.

3.4 Optical Shot Noise Source Measurements

The spectrum analyzer displays the noise power P which is a measure of the fluctuations of the photocurrent. Our goal is to obtain the frequency dependent Fanofactors given by $F(\omega) = \frac{P(\omega)}{P_{QNL}(\omega)}$ where P_{QNL} is the shot noise limited optical power from the lamp to which we choose to normalize the quantum noise. So we need to calibrate the shot noise level(SNL) precisely which in turn determines if the light statistics are indeed Poissonian. If the levels are super-Poisson for example,we will end up overestimating F or finding suppression when there isn't any. There are two ways to calibrate the SNL.

1.We focus a lamp source directly onto the PD and measure the noise power. If we know the response and gain of the measurement chain we can calculate the shot noise theoretically and compare with the SA results. This method is straightforward and accuracies to 1dB have been shown[3] .

2.Alternatively, we can estimate the slope of the power-voltage plots $\frac{dV}{dP}$, and can compare with the theoretical estimates[65] . This method is similar to 1 where we need to know the constants of the measurement chain,but its useful since if some element of the chain is unknown we can determine its values.

Our choice of using a lamp which is a a thermal source needs some clarification since the probability of finding n photons in a mode is given by a Bose-Einstein photon distribution where the total number of photons in a mode is given by $< n_{ks} >= \frac{1}{exp(\frac{h\nu}{kT})-1} \approx 10^{-3}$ for T=3000K[66]. Typical lamp photocurrents have much larger photon number than this and so the average per mode photon number is valid only when we count photons in a time less than the coherence time. The coherence time(T_c) for thermal light is extremely short(less than 1ps) and most detectors are extremely slow and hence we will not measure a Bose-Einstein statistical distribution. If we count all the modes together, the variance is obtained as[66] $< \Delta n^2 >=< n > (1 + \frac{<n>}{\mu})$ where $< n >= \Sigma_{ks} n_{ks}$ and μ is the total number of modes. We can also set $\mu = \frac{t_d}{T_c}$ where t_d is the measurement time and T_c is the coherence time. The reasoning behind this is that the single mode$< n_{ks} >$ is valid only for times less than T_c and so if end up counting a number of modes$< n >$,it should be valid for several coherence times(ie.μT_c) which is the detection interval. As $\mu \to \infty$,ie we count a large number of modes making the photocurrent large, the variance approximates a Poisson. We can see that if $\mu = 1$,the variance reverts to the form $\langle \Delta n^2 \rangle = \langle n \rangle + \langle n \rangle^2$ and if $< n >^2 \leq < n >$it still approximates a Poisson. So its very hard to get a thermal source to show its true nature which is why laser sources are scattered off randomly distributed scattering centers to create a pseudothermal source[67] .

When a LED or lamp of noise power P is incident on the PD, the quantum noise photocurrent develops a voltage across the resistor R_p which is $\Delta V_Q^2 = R_p F(\omega)(2\frac{\eta e}{h\nu}P)$ where F is the filter response factor due to the PD,cable reactances and (if any) spectrum analyzer IF stage miscalibration. In addition there is a Johnson noise component $\Delta V_J^2 = 4kTR_pF(\omega)$ due to the parallel combination of resistors and E_n^2 which is the electronic noise which we have already discussed. Putting them together the noise at the input before amplification is

$$\Delta V_i^2 = \Delta V_Q^2 + \Delta V_J^2 + E_n^2 \tag{3.14}$$

The noise power at the SA in dBm_{Hz} is given as

$$P_{th}(\omega)_{dBm_{Hz}} = 10\log(\frac{A_v^2 \Delta V_Q^2}{50 * 10^{-3}}) \tag{3.15}$$

For a gain of 50 and $R_L = 192$ we can simplify the above equation to get the theoretical noise power as

$$P_{th}(\omega)_{dBm_{Hz}} = -92.38 + 10\log(I) + 10\log F(\omega) \tag{3.16}$$

For simplicity in calculations,we have set $\Delta V_i^2 \approx \Delta V_Q^2$, using the 10:1 rule(neglect the smaller noise component if one is 10 times the other). The shape of the response function $F(\omega)$ can be seen from the electronic noise floor plots of Fig. (3.4b,c). Any noise will be displaced from this value by a constant amount. For uniformity we perform all noise power measurements at 500 and 650kHz using the noise marker feature of the SA. The experiment was carried by shining the lamp on the PD and varying the light power by means of ILX LDX-3620 current source thus changing the photocurrent. It is suggested that the lamp be spectrally filtered to the center wavelength of the LED used in the experiments ie 870 or 890nm±40nm since the response of the photodiodes are wavelength dependent[3] . We used red optical filters but we observed no variation in the measured noise. We also used a regulated power supply for the lamp which did not make a difference on the noise characteristics like it does for the LED. The spectrum of the noise power versus current is shown in Fig. (3.11a). The 50ohm resistor noise is also quite similar to the noise measurement obtained when the PD is coupled to the AM without light, which questions its validity since we should be observing a $192\Omega(200 \parallel 5080)$ resistor noise. This is the -125dBm noise we discussed earlier for 50ohms except these measurements are at 3kHz RBW. We see that the photocurrents produce a relatively flat characteristic indicating its 'white'ness. Actually there is a filter response $F(\omega)$ present in the noise spectra which can be observed in a larger frequency range. Since most of the signals are at least 10dB above the noise floor(-93dB) we can use Eq. (3.16) to calculate the noise powers at the spectrum analyzer without too much error.

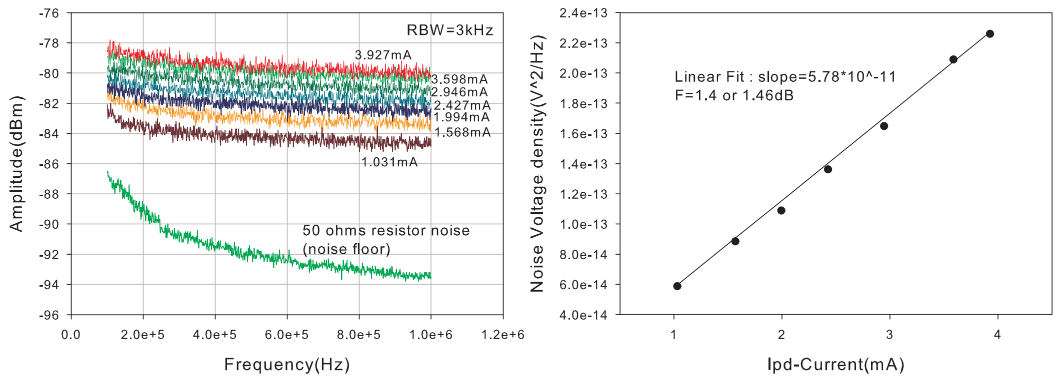

Figure 3.11: (a)Noise powers of the mean photocurrent for a red-filtered white light(from a lamp) incident on the PD which is observed at a RBW of 3kHz. (b)Noise spectral densities normalized to 1Hz(points) as well as linear regression(solid line) obtained as a function of photocurrent.The linear fit gives us the filter response function $F(\omega)$ at 650kHz.

We now demonstrate the validity of the equations . We set F=1 ie no filter response since we need to obtain this value. We obtained the experimental noise powers using the noise marker feature of the SA. It is best to use the SA noise marker feature whenever absolute measurements are required since there will be always be some error between it and reading the plots of Fig. (3.11a) using Eq. (3.5) because of the assumptions regarding the noise correction factor.

1. For $I_{pd} = 3.927mA$, we obtain $P_{exp}(650kHz)_{dBm_{Hz}} = -113.45dBm_{Hz}$. The theoretical result gives us $P_{th}(650kHz)_{dBm_{Hz}} = -116.33dBm_{Hz}$ a difference of nearly 2.88dB. This leads to F being defined as 1.4. Alternatively we could have just chosen a gain of 70 to get the right results ignoring the filter response. Either way, we end up having a consistent measure of shot noise.

2. For $I_{pd} = 2.946mA$, we obtain $P_{exp}(650kHz)_{dBm_{Hz}} = -114.82dBm_{Hz}$. The theoretical result gives us $P_{th}(650kHz)_{dBm_{Hz}} = -117.58dBm_{Hz}$ a difference of nearly 2.76dB which gives an F of 1.37.

The above measurements have been performed for 16 data points at the 500 and 650kHz frequencies and there is a consistent difference of 2.8dBm in all of them. A linear fit has been done which estimates F to be approximately 1.4. This can be seen in Fig. (3.11b) where we have plotted the currents versus voltage spectral densities. One might doubt this measurement strategy of calibrating the shot noise level since we have an unknown parameter. So we might need further tests to show that the source is indeed Poissonian. Fig. (3.11b) shows that the noise powers is a linear function of photocurrent as expected. This is by itself taken as a sufficient test for Poissonity since if there are two uncorrelated noise sources at the same frequency, they would add in quadrature causing deviation from linearity. The electronic noise is constant independent of optical power and if the noise is say quantum limited the variation is 0.5 times the optical shot noise[3] . Now if we assume that F=1, then the 2.8dB discrepancy has to accounted for. When we measured the dc photocurrents, the load resistance was 5080ohms. When we connected the AM for noise measurements, load resistance dropped to 200ohms. This would increase the reverse bias across the diode given by $V - V_{ph} = V_t \ln(\frac{S_\phi \phi_e}{I_D})$ where the photocurrent is given by $i_{ph} = S_\phi \phi_e$. But in typical PDs, the application of reverse bias does change the responsivity slightly due to improved charge collection efficiency in the photodiode[61] which is usually observed from the slope of the IV curves in the third quadrant. If we need to account for the discrepancy, the responsivity would have to change by a factor of almost 2 which seems less likely. So the response function F seems to be the most likely culprit. We also repeated the above measurements for the LED driven by the SNS and found the same linearity results at 500kHz when compared to the lamp driving the PD therefore calibrating the SNS to the shot noise level. So whenever we need to get an absolute measure of noise , we would read off 650kHz noise markers compute the noise levels with a total gain of $70(A_v * F)$ and we would be assured of computing the SNL.

Another important test for Poissonity is the Fanofactor relation. Consider the inset of Fig. (3.12) where the variation of efficiency has been plotted against current. The minimum to maximum suffers a change of less than 0.01 and so if we approximate the efficiency as nearly 0 and plug in this η_0 in Eq. (3.4), it gives us seemingly correct results(ie. $F_{ph} \approx 1$) but its usage is highly misleading. For example we may ask the question:does a lamp distinguish between the constant current or constant voltage case? If we set $F_p = 1$(CV) then $F_{ph} = 1$ and if we set $F_p = 0$(CC) then $F_{ph} = 1 - \eta_0 \approx 1$. Eq. (3.26) has been constructed specifically to link the variance from LED to PD(in some sense using stochastic

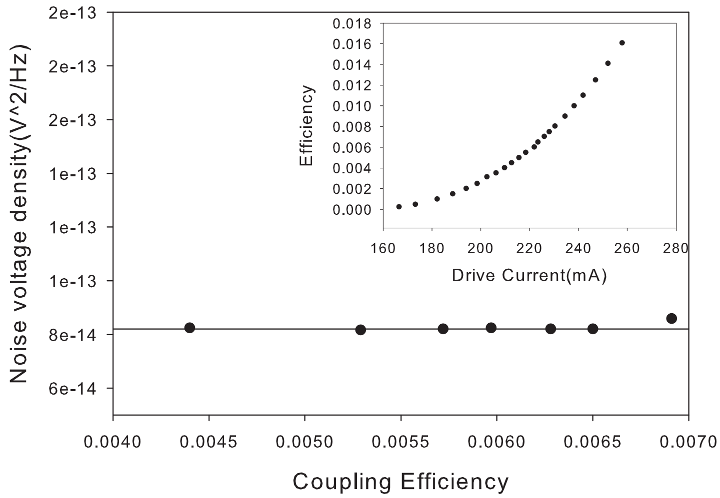

Figure 3.12: Noise power from the photocurrent obtained for the lamp(which is also representative of the LED driven by the SNS) as a function of current-current conversion efficiency. The points give the measured values whereas the straight line represents the average. The inset of the figure represents the efficiency of the lamp as a function of drive current.

ideas) but it does not have a solid quantum mechanical underpinning. In fact it has an electronic part F_p as well as an optical part F_{ph}. Consider a coherent beam of light(say from a laser) passing incident on a PD which includes loss modeled as a beam splitter with efficiency η. The output light of the beamsplitter has a mean equal to variance given by $< n >=< \Delta n^2 >= \eta|\alpha|^2$, where $|\alpha|^2$ is the average number of photons in the coherent state $|\alpha\rangle$. This implies that coherent states which are Poissonian remain so after beam-splitting. The detected photon Fanofactor becomes $F_{ph} = \frac{<\Delta n^2>}{<n>} = 1$ which is independent of the efficiency for any bias current and efficiency(not only 0). The lamp is indeed not a coherent state but the statistics are Poissonian which would make the Fanofactor definition F_{ph} valid. So whether we use the lamp or SNS ,the measured noise on the SA should remain unchanged when we vary the efficiency. Fig. (3.12) shows the measured optical shot noise spectral density which was performed by keeping the photocurrent fixed as we varied the efficiency.

The efficiency was changed by increasing the distance between the lamp and PD and the driving current was adjusted to give the same photocurrent for all the measurements.

The efficiency was determined as the ratio of driving current to the photocurrent. This differs from the inset of Fig. (3.12) since there we have kept the distance constant and varied the drive current. The lamp current was changed from 197mA to 312mA keeping the photovoltage fixed at 7V(ie 1.379mA photocurrent). The efficiencies varied from 0.0069 to 0.0044 but the noise powers remained the same at approximately -117.98dBm_{Hz} or $8.127 * 10^{-14}V^2/Hz$ indicating the light statistics are indeed Poissonian. The same experiment has been verified using the LED driven using the SNS, except in this case Eq. (3.26) is valid and $F_d = 1$ defined above is taken as the drive Fanofactor F_p.

When we place a battery of around 1.5V(assuming the battery has negligible voltage noise) across the diode(CV), we should see shot noise on the SA. But the same shot noise can be observed using our SNS where the PD inside the SNS(PD1 of Fig. (3.3)) has been calibrated to the shot noise level which in turn 'noise' modulates the LED in such a way that the output remains at a Poisson level. This method produces a Poisson photon flux similar to the CV case and hence the SNS and CV must share some similarities. Consider an equivalent circuit diagram of two back to back diodes(PD-LED), except we shall replace the equivalent circuit of the PD with a Poisson current source. From Eq. (2.77) which we rewrite here

$$\frac{dn}{dt} = \frac{i(t)}{e} - \frac{n(t)}{\tau} + i_{sn}(t) \tag{3.17}$$

where $i(t)$ is external circuit current, which is set to $i(t) = -i_{sn}(t)$. This leaves $\frac{dn}{dt} = -\frac{n(t)}{\tau}$ which we can equate to 0. In other words the number fluctuations are constant and don't change at least at the time scales we are interested in. This implies that the junction voltage does not change and the SNS is a CV source.

Since we have established the lamp as a shot noise source, we can compare it against other noise levels in Fig. (3.13). Fig. (3.13a) shows that whether we drive the lamp with a Lightwave current source or voltage source the noise levels remain fixed. This is true since the lamps do not modulate well unlike the LEDs which register huge changes based upon the type of supply. Fig. (3.13b) shows our initial experiments where we drove the LED using the photocurrent obtained from a red Luxeon LED driven by a noisy voltage source.We compare the level with the LED driven by a ILX current source. The goal of this

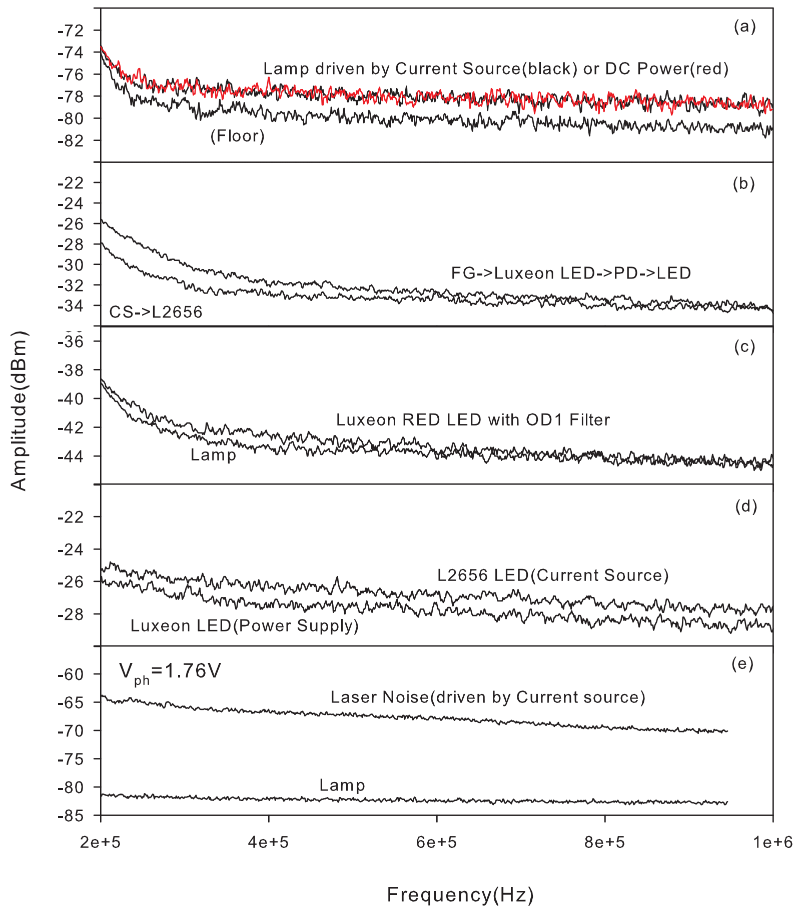

Figure 3.13: Optical noise spectra for (a)Lamp driven by voltage and current sources (b)650nm Luxeon LED driven with a noisy source (c)Attenuated spectra from Luxeon LED (d)L2656 driven by ILX current source and (d)Generic laser driven by ILX current source

experiment was to show that if we do not have a reference shot noise source such as the lamp, we could interpret the upper level as being shot noise and the lower level as being subshot since it was driven with an ILX 'constant' current source. In Fig. (3.13c) ,we note that the Luxeon driven with a ILX current source through a resistance of 330Ω at 23.25mA to produce a photovoltage of 3.49V which produces a noise level greater than the shot noise level of the lamp. This contradicts experiments done in [60] where they have observed 1.5dB squeezing with at mid-frequencies. We also tried the same experiment using a battery and 1K resistor to produce a $V_{ph} = 3.15V$. The lamp was driven at 192.27mA to produce the same photovoltage and once again the Luxeon showed super-Poisson characteristics. In Fig. (3.13d) we drive the LED with a current source and compare it with a Luxeon driven by a constant voltage of 3V. This shows a situation where the L2656 is at a noise level higher than the Luxeon which is shown to be supershot itself. This proves than the ILX current source generates a super-Poisson characteristic with the L2656 LED. Finally we compare the lamp with a laser source and we see nearly 20dB difference and at lower frequencies(not shown) the noise increases a great deal due to the relaxation oscillation. This is much larger than the noise produced in the L2656 LED with the ILX current source. It is well known that lasers driven well beyond saturation produce a coherent state, but in this case unless we use an intensity noise eater[3], and also suppress the mode partition mechanisms it would be difficult to produce subshot noise. But it should be noted that one of the largest amplitude noise reduction(nearly 75% below the SNL) have been predicted to occur in the feedback loop of a negative feedback semiconductor laser and nearly 10dB intensity squeezing has been demonstrated[4].

3.5 SubShot Noise experiments

3.5.1 Verification of High-impedance Pump suppression mechanism

Now we are in a position to carry out the subshot noise measurements, since the shot noise level(SNL) is known. This is accomplished by using a constant current source(CCS) which in our case is a 9V battery connected through a large series resistance much larger than the differential resistance of the LED. The noise current of the CCS should be well below the shot noise limit ie. $F_p = 0$ which leads the output Fanofactors to be defined as $F_{ph} = 1 - \eta_0$ ie. F_{ph} is limited by the dc efficiency η_0 of the LEDs. So we should expect variances less than the SNL. But first we shall demonstrate the concept of high impedance pump suppression. At low frequencies the diffusion capacitance can be removed from the equivalent noise circuit of Fig. (2.5) leaving behind a simple circuit with shot noise, thermal noise sources and two resistors R_s and R_d. The recombination current can be determined as $i = \frac{v_{th}+v_{sn}+v_{ps}}{R_s+R_d}$ where we have included the power supply noise v_{ps} which we do not know and varies from supply to supply.The Fanofactors can be written as

$$F_p = \frac{< i^2 >}{2qI} = \frac{(< v_{th}^2 > + < v_{sn}^2 > + < v_{ps}^2 >)}{(R_s + R_d)^2 2qI} = \frac{(4kTR_s + 2kTR_d + < v_{ps}^2 >)}{(R_s + R_d)^2 2qI} \quad (3.18)$$

Case 1. When we apply a constant voltage; we see from Eq. (3.18) that as $2R_s \ll R_d$,the Fanofactors become $F_p(CV) = \frac{2kTR_d + <v_{ps}^2>}{R_d^2 * (2qI)} = \frac{<v_{sn}^2> + <v_{ps}^2>}{<v_{sn}^2>}$ and if we assume $< v_{ps}^2 > \gg < v_{sn}^2 >$,the output noise is much above the SNL governed only by the noise of the voltage supply. If we set $v_{ps} = 0$, the junction voltage fluctuations are almost nonexistent and output light is at the full shot noise level as seen in chapter 2.

Case 2. When we increase the series resistance R_s such that $R_s \gg R_d$, then the Fanofactors become $F_p(CC) = \frac{4kTR_s + <v_{ps}^2>}{R_s^2 * 2qI} = \frac{4kT/R_s + <v_{ps}^2>/R_s^2}{2eI} = \frac{<i_{th}^2> + <i_{ps}^2>}{<i_{sn}^2>}$. If we assume that $v_{ps} \gg v_{th}$,then $F_p(CC) = \frac{<v_{ps}^2>/R_s^2}{2eIR_d^2} * R_d^2 = \frac{<v_{ps}^2>}{<v_{sn}^2>} * \frac{R_d^2}{R_S^2} = F_{CV} * \frac{R_d^2}{R_S^2}$. This tells us that the as the series resistance increases, the supply voltage noise is suppressed from the CV case and as $R_S \to \infty$, we can completely suppress the power supply noise. Now if we set $v_{th} \gg v_{ps}$, then we recover the condition $F_p = \frac{4kT/R_s}{2eI}$[6] which is always much less than 1.

In order to demonstrate high impedance pump suppression we could first determine the SNL based on the calibration method, then use various series resistances and determine the output noise level. For large series resistance, the recombination noise would be suppressed. Note that the current noise could be suppressed all the way to 0 as in case 2 for large series resistance but the light is suppressed by less than a dB because of the limited efficiencies involved as can be seen from by substituting the F_p obtained above in F_{ph}. So in order to simulate the effect of pump suppression, the power supply voltage noise is useful since for $R_s > R_d$ it establishes a recombination current given by

$$< i^2 > = < i_{th}^2 > + (< i_{sn}^2 > + < i_{ps}^2 >)(\frac{R_d}{R_S})^2 \quad (3.19)$$

The purpose of the voltage noise is to increase the noise level from the standard shot noise level (which can be seen from the Eq. (3.19)) so that the effect of pump suppression can be demonstrated over several dB. We can consider this enhanced noise as a simulated shot noise level which will be suppressed as we increase the series resistance. Otherwise it would be very hard to notice the pump suppression effect. For example if we use a 'quiet' voltage source, we will not be guaranteed a SNL(case 1), since the effect of contact and bulk resistance of the diode could well exceed the differential resistance causing the suppression to be already in effect.

Fig. (3.14a) shows us the noise levels for the various power supplies used in the experiment. The L2656 LED was driven with the following sources: 1. A current of 7.64mA from the ILX current source 2. A battery of 9V with a series resistance of 110ohms and 3.A HP 6236B power supply at 1.2V. For all these sources, the photovoltage at the multimeter was 1.52V(which indicates the same average optical power) and the coupling geometries were fixed. The noise levels from both the ILX current source and the HP power supply vary by 5-10dB when compared with the battery noise levels. We tried the experiment by running the ILX off the AC mains as well as using internal batteries. For both cases, the noise was above the battery levels at low frequency which is quite surprising since the ILX is advertised as an 'ultra-low' noise current source.We can see that the ILX generates harmonics when driven off the ac mains(these harmonics disappeared when the ILX was driven with a battery) and these harmonics are attenuated which may either be the response of the ILX itself or the modulation bandwidth of the LED which is less than 600kHz. We note that the ILX is usable as a source at frequencies greater than 800kHz since it reaches the battery noise levels. The HP supplies are normally noisy and when we used capacitors at the output terminals the noise levels went down. From the Fig. (3.14a) we see that the HP noise levels are almost white in nature and so they can be added in quadrature with the shot noise levels to verify the pump suppression effect. Also they do not modulate and roll off at frequencies less than 600kHz which suggests that noise does not respond to the modulation bandwidth of the LED and the rolloff of the ILX is due to stray pickup harmonics(which are sensitive to modulation bandwidth).

In Fig. (3.14b,c), we demonstrate the pump suppression effect for both the L2656 and the Luxeon light emitters. First we describe the effect of pump suppression for the L2656 LED shown in Fig. (3.14b). For all experiments, the DC photovoltage was set at 1.93V by adjusting the supply voltage from the HP unit. This was done so that the photon rate was the same for all cases. Then using resistors from 10Ω to $1.5\text{k}\Omega$ we noted the noise levels. The flat noise level with no spikes can be considered as a reference that other levels

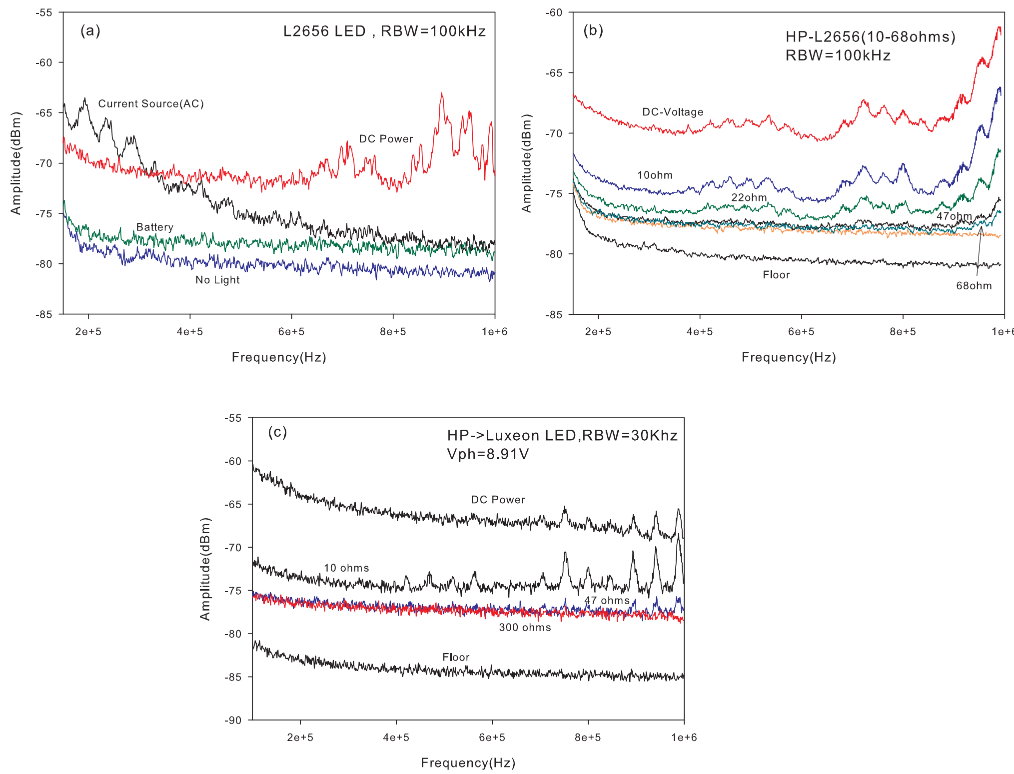

Figure 3.14: (a)Optical Noise spectra for the L2656 with different bias sources.The reference low noise source is the battery. (b) and (c) show high impedance pump suppression effect for the L2656 and for the Luxeon LED as function of series resistance R_S. Experiments were performed at a RBW of 100Khz(a,b) and 30Khz(c) with a VBW of 3Hz.

should tend towards(as they are being suppressed) and has been obtained by driving the LED with a resistor and battery source. We have only depicted the low impedance values since for resistances greater than 110Ω we noted no difference in the levels from that of the reference level. The photocurrent for all experiments is at 0.379mA(1.93V/5080Ω) which at 650kHz gives us a calculated shot noise level of -75.55dBm which is slightly above -76.5dBm obtained using the 47ohm resistor and the reference in Fig. (3.14b). The DC voltage gives us about -69.5dBm at 300kHz. At 10ohms we get -74.5dBm , a difference of nearly 10dB which can be obtained approximately as $P_{dBm}(DC) - 10\log R$. As the resistance increases to 22 ohms, we see -75.5dBm($\approx -69.5 - 10\log 22$). This shows us that the power supply voltage noise is being suppressed by a factor of R and if $v_{ps} = 0$ it would also suppress the shot noise. We also see that the noise levels do not go down arbitrarily as

R increases and the levels merge with the reference. For example at 47ohms should give us $-69.5dBm - 10\log 47 = -86.22dBm$ which should be 5dB below the reference. Instead it can be seen from Fig. (3.14b) that the noise level does not go below the reference level. This can be seen by calculating F_p. For the DC voltage case we obtain an $F_{ph} = 4.07$ and for a typical efficiency of $\eta_0 = 0.18$ we can obtain $F_p = 17.77$. When we insert a resistance of 10Ω we note an $F_p = 2.516$ which implies that the pump Fanofactors are being suppressed. For 22Ω we can obtain $F_{ph} = 0.901$ which implies that the noise is being suppressed below the shot noise level, which also implies that the drive Fanofactor is suppressed ie. $F_p = 0.453$. At larger resistance values since F_p is nearly 0 which implies that we are observing full subshot noise.

Similar results are seen for the Luxeon light emitters in Fig. (3.14c). The experiment was performed using a dc voltage of 2.15V from the HP supply and calibrating the dc photovoltage at 8.91V. Later, resistances of 10,47 and 300 ohms were inserted keeping the photovoltage constant by adjusting the dc voltage. The coupling efficiency was as high as 30% but the emitter is red and not tuned to the peak spectral wavelength of the PD. So we can expect loss and degradation of squeezing.The SNL calculated for a photocurrent of 1.75mA is -74.13dBm. Note that the RBW used for this experiment is 30kHz. At low frequency we see the 10ohm resistance registers a change of almost 10dB as expected. The Fanofactors calculated for the DC case is $F_{ph} = 6.5$ which is larger than the Fanofactors obtained for the L2656 .This may be attributed to the power supply noise which is dependent on the applied voltage. The reference level in this case is around -76.5dBm which is smaller than the shot noise level. This is rather surprising since when we compared the level of the Luxeon to a lamp in Fig. (3.13c) and we found the Luxeon level to be slightly higher. We have confirmed this source to be super-Poisson using other power supplies. This type of error can be eliminated if we place both the shot and subshot plots on the same figure to facilitate easier comparison. We will do so in all future experiments since we are interested in calculating the Fanofactors which are dependent on the relative values.

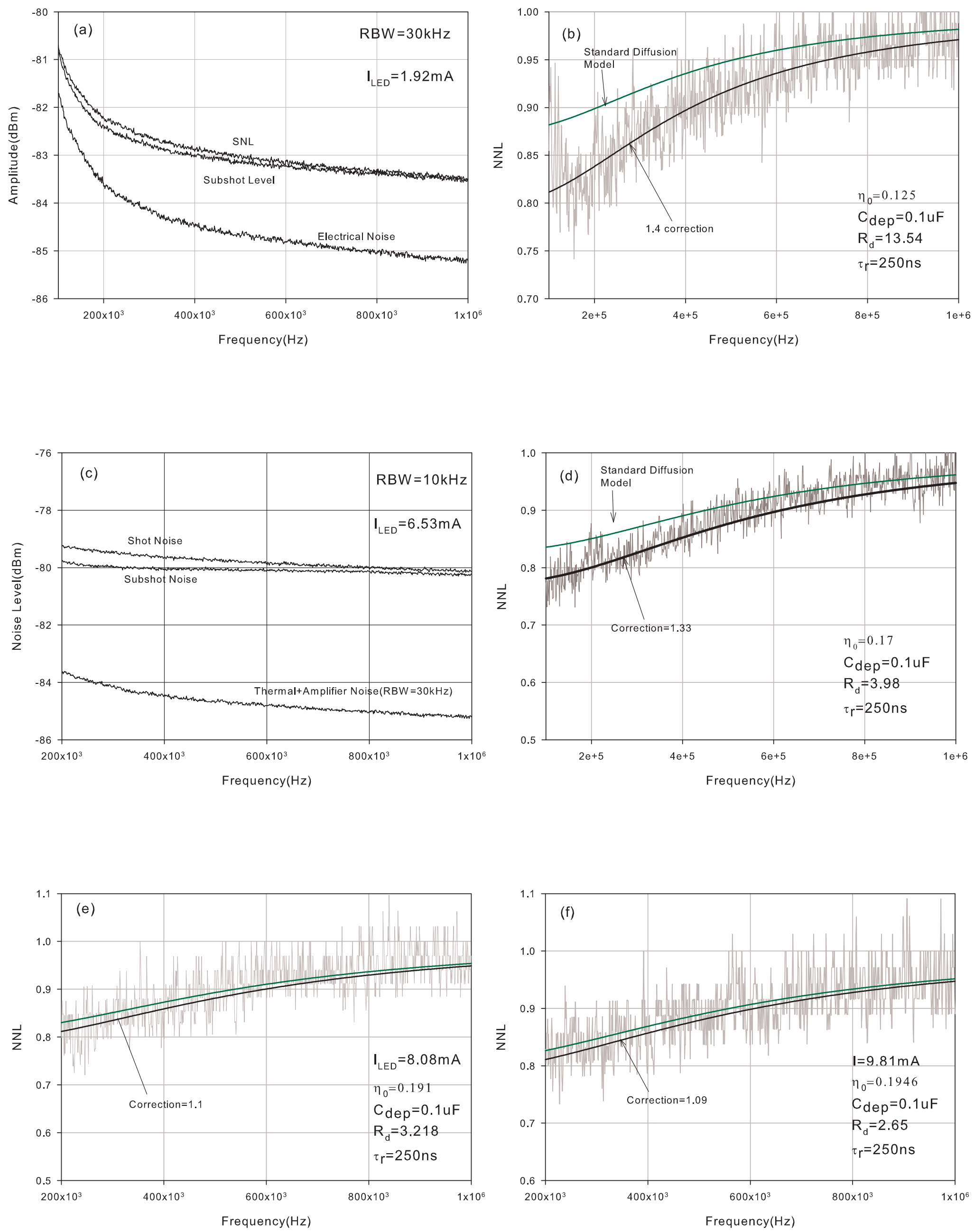

Figure 3.15: Optical noise spectra and Fanofactors of the photon fluxes from the L2656 LED obtained at (a,b)$I_L = 1.92mA$ (c,d)$I_L = 6.53mA$ (e) $I_L = 8.08mA$ and (f) $I_L = 9.81mA$. The Fanofactors were fit to the theoretical diffusion model(solid lines) which were obtained using Eq.(3.21) with various correction factors C to fit to the data better to F.The Fanofactor obtained with C=1 line has been shown for reference.The model parameters used are $C_{dep} = 0.1\mu F$ and $\tau_r = 250ns$.

3.5.2 Squeezing Results for the L2656 LED

Next we detail the results of our squeezing experiments for the L2656 which was done over a range of 1.57mA to 7mA LED drive current for a total photovoltage of 1-8V(just before photodetector saturation for a 9V supply). In each plot, the upper trace is the SNL and lower trace denotes the degree of squeezing from the SNL which is typically from 0.2-1.5dB in our experiments. The noise floor has also been included for comparison. Fig. (3.15a,b) shows the results at a LED drive current of 1.92mA with a photocurrent of 0.24mA or a total efficiency of 0.125. The calculated shot noise at a RBW=30kHz is -82.8dBm which is close to the -83.1dBm seen at 600kHz in the Fig. (3.15a). We note that the photocurrent is quite small since the power changes only by 2dB from the noise floor which is the reason we were not able to carry out the experiment at lower LED currents. The lowest currents in which squeezing has been obtained using this LED is approximately $5\mu A$ at a power levels of several μW[42]. Since smaller LED currents result in lower LED emission efficiency η_{LED}, the degree of squeezing also decreases and eventually we would reach the SNL. This can be seen for the case of the low injection LED drive current of 1.92mA in Fig. (3.15a) where the subshot noise is only 0.2dB below the shot noise level at 200kHz and merges early with the shot noise level at a frequency of around 600kHz(Note that for this figure, this is not 3dB point for squeezing). Statistically, this is explained as follows: The injection current has a high efficiency even at very low current levels. However the recombination rate or probability decreases with lower injection current. In other words the probability of emission $\eta_{LED}(\tau)$ of an photon after electron injection becomes lower where τ is the observation time. The response of the LED deteriorates as $f = \frac{1}{\tau}$ is lowered and squeezing as well as modulation is pushed down to lower frequencies.This however should not be construed as squeezing cannot take place at lower current levels. The thermionic emission regulation process is still in effect albeit it requires larger observation times(smaller frequencies) and if we can increase the efficiency of the LED at low currents we should still see squeezing. Since we are restricted by device technology,this has still not been shown for macrojunctions at low currents. Fig. (3.15b) gives us the normalized noise level or Fanofactor which has been calculated from Fig. (3.15a) as the ratio of subshot trace to the shot trace after subtracting the thermal noise from each trace which can be expressed as

$$F = \frac{10^{Subshot/10} - 10^{Floor/10}}{10^{Shot/10} - 10^{Floor/10}} \tag{3.20}$$

This ratio should be independent of the detection system parameters such as frequency response and amplifier gain since the traces follow each other. For the remainder of this chapter, F denotes the measured Fanofactors whereas the theoretical Fanofactors are written with subscripts. In Fig. (3.15a) we see that at low frequencies particularly from 0-100kHz, there appears to be little or no squeezing. This is due to the spectrum analyzer response. In order to get accurate results we have set the starting point of Fanofactor calculation at 100kHz,but we will have some error since it underestimates the squeezing. The DC values of F can be obtained by extrapolating from a low frequency point just before the Fanofactors start to rolloff(which in this case is 200kHz) to dc. If the squeezing took place over a larger frequency range, we could have made the assumption that the squeezing at 200kHz is the same as the dc since the response should be in some sense a low pass filter and some papers have used this method. If we use this assumption we find from the Fig. (3.15b) that F(200kHz)=0.85 which is somewhat close to the theoretical value of $F_{ph} = 1 - \eta_0 = 0.875$(we have got very accurate results at higher currents with differences of less than 0.01) which would have agreed well. However we note a discrepancy when we plot the theoretical frequency dependent Fanofactors in the diffusion limit given by the Eq. (**??**) which is rewritten along with an additional component C as

$$F_{ph}(\omega) = 1 - \frac{\eta_0 C}{1 + \omega^2(\tau_{te} + \tau_r)^2} \tag{3.21}$$

where we have assumed $C \propto (\frac{\eta_d}{\eta_0})^2$ is a correction factor motivated by a similar factor appearing for the thermionic emission model which will be used for the L9337 LED later on. Also this correction factor gives better agreements between theory and experiment. The thermionic emission lifetime is defined as $\tau_{te} = \frac{kTC_{dep}}{eI}$. The theoretical plots have been obtained by fitting Eq. (3.21) to the center of the variance in F. In order to be as accurate as possible, we start the fit from Fig. (3.15d) which is the normalized noise levels calculated from Fig. (3.15c). At a high current value of 6.53mA, $\tau_{te} \ll \tau_r$ and so $F_{ph}(\omega) \approx 1 - \frac{\eta_0 C}{1+\omega^2 \tau_r^2}$. As for the recombination lifetime τ_r, the datasheets do not state this parameter but other papers have measured different values ranging from 600kHz to 1Mhz[44] . When we measured this value by finding the 3dB point using AC modulating the LED from the current source, we found a frequency of approximately 600kHz(265ns). Note that this 3dB point depends on the extrinsic lifetime given by the $R_S C_{dep}$ product which could limit the modulation speeds below the intrinsic carrier lifetime τ_r. The datasheet specify a rise time of $t_r = 0.45\mu s$ at a current of 50mA. Using $t_r = 2.2(\tau_r + \frac{1.4*10^{-4} T C_{dep}}{I_{LED}})$[68] we get $\tau_r \approx 204ns$. So to get a good fit, we need to set the bounds of τ_r from 204ns to 265ns. At 6.53mA and choosing $\tau_r = 250ns$ we found a close fit to F at high frequencies. Notice that the line does not fit well at low frequencies when using the diffusion model without the correction factor. If we assume C=1, then we will have to change C_{dep} or τ_r to get a better fit. But at high injection C_{dep} should not matter unless it is made larger in which case it would cause discrepancies at low injections(A $0.01\mu F$ change is sufficient to cause drastic variations).Also τ_r can only be varied between the bounds.Otherwise it would also cause very large discrepancies. The only logical reason is to account for the deviation in C. This discrepancy has been noticed by other authors[42] , which they reasoned using the small signal transfer idea ie. As $\eta_d > \eta_0$ the transfer rate of an AC signal is larger than a DC component and so the ratio of fluctuation $\langle \Delta n^2 \rangle$ to the mean can be greater than 1, which would imply that the Poisson source is actually super-Poisson. However, η_d is a parameter associated with the LED, and it becomes a concern only when we are driving the LED using the SNS. We have verified that the SNL is nearly the same when we use a lamp directly(where η_d is not a concern since it is nearly 0), but even 0.1-0.2dB difference is sufficient to cause great variations in the Fanofactors. But super-Poissonity of the SNS which is quite small is insufficient to explain the correction factor C. So we reason that the subshot noise is also much more than expected from the simple formula $F_{ph}(0) = 1 - \eta_0$. However it serves as a good approximation for us since our results agree with it very well at 200kHz which can be seen in the Fig. (3.15d).

At low injection levels, $\tau_{te} \gg \tau_r$ and so we obtain $F_{ph}(\omega) = 1 - \frac{\eta_0 C}{1+\omega^2(\frac{kTC_{dep}}{eI_{LED}})^2}$ where C_{dep} is a fitting parameter which we estimate to have a value of $0.1\mu F$. We cannot accurately determine C_{dep} experimentally because the measured capacitance is the sum of both the diffusion and depletion capacitances at moderate voltage. After the fit,the only variable in the model is the drive current I_{LED}. We have verified the model for I_{LED} ranging from 1.5mA to 9mA and found good agreements. Fig. (15e,f) shows an example of $F_{ph}(\omega)$ at a currents of 8.08mA and 9.81mA. In the Fanofactor figures, the correction factor have been estimated to be 1.5, 1.3, 1.1 and 1.09 respectively. We notice that the correction factor C tends to 1. This can be seen since $\frac{\eta_d}{\eta_0} \propto \sqrt{C}$ gives us $\eta_d \propto .199$ for $I_L = 8.08mA$ and $\eta_d \propto .20$ for $I_L = 9.81mA$. This is less than the values shown in Fig. (3.5b) which is around 0.21 , but we see that the ratio $\frac{\eta_d}{\eta_0}$ follows the general shape of the curve. At higher currents we see that the efficiency η_0 becomes more linear from 4-9mA and then saturates from 10-16mA(Note that this is not the photodetector saturation). So slope of $\frac{\eta_d}{\eta_0}$ should decrease and be equal to 1 in the linear region and should tend to 0 in the saturation and this is what we observe for C as I_L increases. We can now see if the correction C gives us the correct DC fanofactors according to Eq. (**??**) which we rewrite here

$$F_{ph}(0) = 1 - 2\eta_0 \left(\frac{\eta_d}{\eta_0}\right) + \eta_0 \left(\frac{\eta_d}{\eta_0}\right)^2 (1 + F_{dr}(0)) \tag{3.22}$$

If we assume a Poissonian drive current $F_p = 1$ we see that $F_{ph}(0) = 1 - 2\eta_0 \left(\frac{\eta_d}{\eta_0}\right) + \eta_0 \left(\frac{\eta_d}{\eta_0}\right)^2$ and for $\frac{\eta_d}{\eta_0} > 1$ which is typical of our experiments, the optical noise is super-Poissonian. This is true only when the SNS is driving the LED and not when the lamp itself is used as the shot source. So the Fanofactor definition itself has to be renormalized to account for this new supershot noise as $F_{norm}(0) = \frac{<\Delta n^2>_{Subshgot}}{<\Delta n^2>_{Supershot}} = \frac{F_{ph}(0)_{F_{dr}=0}}{F_{ph}(0)_{F_{dr}=1}}$. This gives us the relation

$$F_{norm}(0) = \frac{1 - 2\eta_0 \left(\frac{\eta_d}{\eta_0}\right) + \eta_0 \left(\frac{\eta_d}{\eta_0}\right)^2}{1 - 2\eta_0 \left(\frac{\eta_d}{\eta_0}\right) + 2\eta_0 \left(\frac{\eta_d}{\eta_0}\right)^2} \tag{3.23}$$

which can be compared with the experimental results obtained by taking the extrapolated curves from the frequency dependent Fanofactor with the appropriate correction. For example, in Fig. (3.5b) we see that $\eta_0 = 0.17$ and $\eta_d/\eta_0 = 1.2$ which gives us $F_{norm}(0) = 0.7736$ which agrees with the Fanofactor at 100kHz. We have assumed that the value at 100khz is the same as the dc value since the curves level off at this point . We have computed $F_{norm}(0)$ for certain drive currents along with the standard definition $F_{ph}(0) = 1 - \eta_0$ in Table. (3.3) and we see that Eq. (3.23) (except for 5.72mA which shows the largest error)

Drive current $I_L(mA)$	η_0	$\frac{\eta_d}{\eta_0}$	$F_{ph}(0) = 1 - \eta_0$	$F_{norm}(0)$ (Theory)	$F(0)$ (Experiment)
1.92mA	0.125	1.264	0.875	0.815	0.815
6.73mA	0.17	1.20	0.83	0.7736	0.78
4.16mA	0.168	1.205	0.831	0.776	0.78
5.72mA	0.180	1.19	0.82	0.764	0.776
8.08mA	0.191	1.157	0.809	0.76	0.76

Table 3.3: The experimental results of η_0,η_d which are used to compute F according to Eq. (3.23) are compared with the experimental results for varying drive currents.

predicts the correct results as expected. To the best of our knowledge most of the results in the literature for the L2656 have not employed this correction and are thus misleading.

Fig. (3.15a&c) have each been averaged differently. For each trace we used a VBW=1Hz with a sweep time of several minutes. For the case of 1.9mA we took three averages and for 6.53mA we took 3-6 averages. As we know the variance goes to zero as the number of averages increases according to $\frac{\sigma^2}{N}$. When we compared 3 trace averaging for high and low currents, we found that lower currents have a larger variance in F. This is seen from Fig. (3.5a) , where the shot and subshot noise have only a 0.2dB difference and the levels are only less than 2dB above the thermal floor. The 10:1 rule cannot be used. The larger variance can be imagined as follows: Imagine we are subtracting a random value from two Gaussians which overlap a little. The resultant number has a much larger variance shared by the two pdfs. When the levels are further apart particularly at large currents we find that smaller averaging results in reasonable accuracy. For example, Figs. (3.15e,f) had no averaging done besides the video filter. Also when we perform trace averaging, the traces could shift between each measurements due to slight setup changes. For example, a typical run at say 8.08mA would see a photovoltage of 7.84V before the measurement and 7.81V after. A single run is typically 2-3minutes. But for 6 averages,we need the keep this photovoltage constant over several 10s of minutes and there might be non-negligible drift. One solution is to use TE coolers on these devices. A better option is to use cryogenic methods, but there are issues regarding the coupling of the LED with the PD. We performed a simple test to determine how much drift we would encounter by measuring the photovoltage over time which we summarize in Table (3.4). For the case of the lamp,the shot noise current

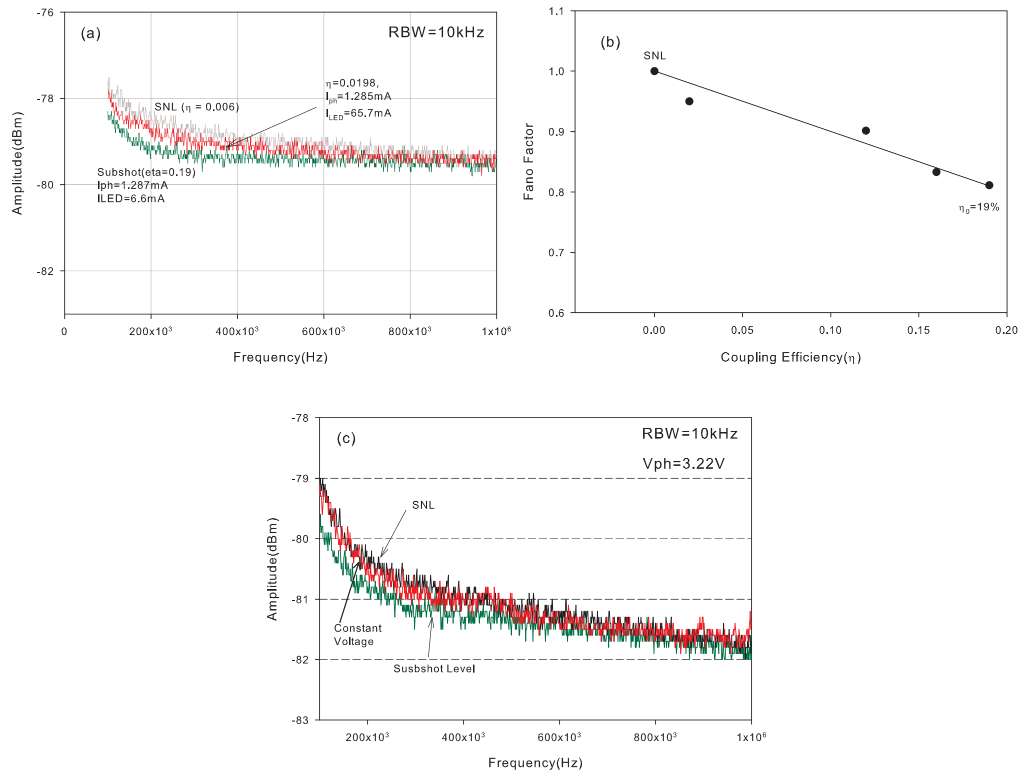

Figure 3.16: (a)Optical noise spectra for the L2656 with reduced coupling efficiency of $\eta_0 =$ 2%.The SNL has been obtained by driving the LED with the SNS (b)Experimental(points) and theoretical(solid line) Fanofactors as function of coupling efficiency (η_0) (c)Optical Noise spectra for the L2656 driven under a Constant Voltage bias of 1.26V

changes from 24.106pA/$\sqrt{Hz}$ to 24pA/$\sqrt{Hz}$ at 20 minutes which is only a difference of 0.02dB. So errors in noise powers due to drift are very negligible. The decrease in current for the lamps may be attributed to a change in responsivity due to heating up of the active area whereas for the LED, it is more likely that the battery discharges over time causing the current decrease. This is because the center wavelength of the LED lies in a range where the temperature coefficient of the PD is effectively zero.

Time(minutes)	Lamp photocurrent(mA)	LED photocurrent(mA)
0	1.816mA	1.309mA
10	1.811mA	1.295mA
20	1.799mA	1.289mA

Table 3.4: Photocurrent drift with time when driven by the shot and subshot sources

Looking at Fig. (3.15a) we see that the subshot is about 0.8dB squeezing below the SNL whereas it is 0.2dB in Fig. (3.15c). At 1.9mA the efficiency is around 0.125 which should translate to at least 0.5dB which we do not see. This is because the thermal floors have masked out the expected squeezing. At 300kHz we find the thermal noise is -84.5dBm which is $13.31\mu V$. The subshot and shot noise spectral densities are $(16.38\mu)^2V^2/Hz$ and $(16.76\mu)^2V^2/Hz$. If we calculate the ratio directly we see $F = \frac{(16.38\mu)^2}{(16.76\mu)^2} = 0.95 \rightarrow 0.2dB$. But when we subtract away the thermal noise from these values we get $F = 0.87 \rightarrow 0.56dB$ as expected. Note that at 6.53mA we see 0.7dB. Most papers specify the degree of squeezing as the difference between SNL and the subshot levels since their amplification is quite large to satisfy the 10:1 rule and some others do not. We cannot do so and need to include the thermal noise corrections. Finally in passing, we note that the SNL at 650kHz for the 6.53mA case can be obtained from the photocurrent of 1.07mA which puts it at -119dBm whereas the experimental result is -118.51dBm, a difference of 0.49dB.

Fig. (3.16a) was obtained by reducing the efficiency of the LED by moving it away from the detector but keeping the photocurrent constant. As expected the subshot noise moves towards the SNL. Fig. (3.16b) plots the variation of F versus efficiency. The first and last points are SNL($\eta_0 = 0.006$) and subshot level($\eta_0 = 0.19$) which we obtained from Fig. (3.16a). Note that the subshot is around 0.9dB below the SNL. When the efficiency is reduced to $\eta_0 = 0.0198$ we note that F is not at the SNL but rather .2dB below it leaving a value of F=0.95. This is a discrepancy of nearly 0.03 from the theoretical result expected(ie 1-0.0198=.9802). However notice that the variance of F would itself allow us to put the result closer with theory. However we refrain from doing so and use only the center of the variance as the reference. The remaining two values obtained were at 0.45dB($\eta_0 = .12$) and 0.8dB($\eta_0 = .16$) below the SNL. We can obtain only a few resolvable datapoints in this experiment unless we can increase the degree of squeezing. For example, we had difficulty resolving a 0.04 efficiency datapoint from a 0.0198 since the noise levels would merge. More averaging may be required to produce better results. The same LED has been demonstrated to produce squeezing upto 1.5dB(efficiencies reaching 30%) at temperatures of 77K. Under these conditions F varies over a larger range and better fits to the theoretical value have been obtained[27] . Also we should not raise any concern over η_d in this experiment, since we are primarily adjusting the coupling efficiency(η_c) where $\eta_0 = \eta_c \eta_{LED}$ just as we did for the shot noise experiments. So the more general Fanofactor relation given by Eq. (3.5) is in effect. The thermal noise has not been subtracted from the above results which should cause an error of 20-23% since the levels are only 6dB from the noise floor. We see closer fits without the correction results implying that the theoretical Fanofactor relation may actually be smaller validating the correction required. The most important point to note is that the Fanofactors decrease with η_o (or rather η_c) linearly. We have seen results in the literature where the theory underestimated the experimental points consistently[45] and also results where they agreed with minimal error[27]. The authors in these papers had used Eq. (3.5) for all their measurements which we have seen to be incorrect. So in summary, the sources of error that can cause F to be in error are 1.The SNL is actually super-Poisson which implies F is larger than expected. 2.No thermal correction has been assumed which implies a smaller F than expected. 3.The low frequency at which F is measured is not a measure of F(dc). We will start the experiments with the L9337 LED with these issues in mind.

3.5.3 Approximate Constant Voltage conditions

In Fig. (3.16c), we demonstrate the constant voltage operation of the LED. Ideally this would include a zero noise voltage source across the diode. This is not possible(unless we can obtain a battery source which puts out 1.5V at 10-20mA current) but we might imagine that the same effect can be reproduced by adding a large capacitor in parallel with the LED in the existing circuit. The series resistance restricts the current and after 5 RC time constants we would expect a voltage to be developed across the capacitor which would then pin the junction voltage. We have used two capacitors at 0.1mF and 0.01mF to realize this effect and both of them show similar results. Note that we are not able to distinguish between the shot and CV plots in figure. There may a slight degree of suppression from 200-400kHz. At smaller capacitance values, we do see squeezing which can be explained if we consider the internal junction dynamics coexisting with the RC charging time. The experiment was carried at a photovoltage of 3.22V(0.63mA) with $I_L = 3.705mA$. First when we include no capacitance,we see only capacitance of the junction which is $0.1\mu F$. This leads to $\tau_{RC} = 180\mu s$ at a source resistance of $R_S = 1.8k$ and $\tau_{te} = \frac{kTC_{dep}}{eI_L} = 0.7\mu s$. Thus we have constant current condition ie. $\tau_{RC} > \tau_{te}$. CV is ideally defined as $R_S \rightarrow 0$ which would put $\tau_{RC} \ll \tau_{te}$. When we placed the capacitance across the junction we are artificially enhancing the junction capacitance to $C_{dep} \approx 0.1mF$. So now we obtain $\tau_{RC} = 0.18s$ and $\tau_{te} = 0.70ms$ and we still see constant current condition. But there is negligible squeezing as seen in the plots.As C_{dep} has been made very large, the frequency cutoff given by $\frac{1}{2\pi\tau_{te}}$ decreases which in this case is around 1kHz. Since the plot has been obtained from 100kHz and above, the squeezing has not been noticed. A very large capacitance would push the 3dB to zero frequency whereas setting $R_S = 0$ would be ideal CV operation. Even though the two methods are different the end result is the same ie we reach the shot noise level. Recent experiments have used the capacitor method to achieve a constant voltage in order to study squeezing that happens under CV model[53]. This is the backward pump model which has not been studied in this thesis.

3.5.4 Issues with frequency dependent squeezing characteristics

The squeezing experiments were repeated with the L9337 which is a higher efficiency heterojunction device where the diffusion model is not valid at least at the currents we are working with. Fig. (3.17a) shows our initial experiments obtained by changing the LED but using the same general setup as Fig. (3.3). From here on, we choose to work with the relative measurements(ratio of two noise levels) instead of the absolute measurements of the noise level. The experiment was carried at a drive current $I_L = 5.96mA$ and the photovoltage obtained was 8V(1.57mA) for an expected Fanofactor of $F_{ph} = 0.73$ or a squeezing of 1.32dB below the SNL. At 1Mhz we see 1.3dB but we have not accounted for the thermal noise yet which may put it at much larger values. We see as we move to larger frequencies the squeezing increases or rather the SNL seems to increase followed by a merging of levels. The inset describes the squeezing in the frequency range from 5-6Mhz and we see a squeezing of nearly 1.7dB which is a quite a large deviation. This would imply the LED has an frequency dependent efficiency of nearly 32% at 5-6Mhz.However the LED is rated for a

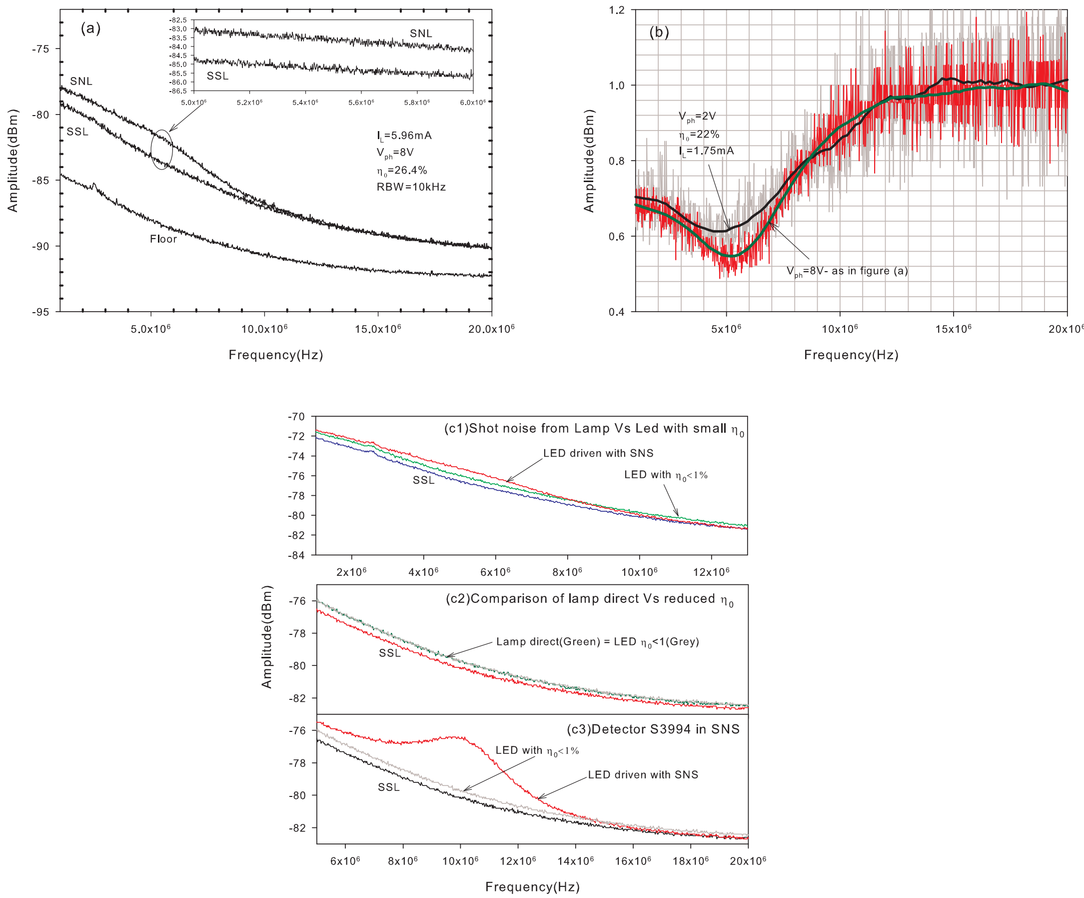

Figure 3.17: (a)Squeezing spectra for the L9337 LED highlighting the super-Poissonity at mid-frequencies when driven with the SNS (b)The overestimated Fanofactors for the low injection case of V_{ph} =2V and high injection case of V_{ph} =8V .The solid lines are the smoothing filters applied. (c)Shot noise spectra for the cases of 1.L2656 driven with SNS, 2.Reduced coupling efficiency($<$ 1%) and 3.Changing the PD1 from UDT to S3994 in the SNS. For each of these cases, the subshot noise as well as lamp noise spectra have been plotted.

modulation bandwidth of around 25-40Mhz whereas the squeezing disappears at 10Mhz. So efficiency is not the issue here. In Fig. (3.17b) the Fanofactors for $V_{ph} = 2V(I_L = 1.75mA)$ and $V_{ph} = 8V$ have been plotted. The origin of the plot is 1Mhz and we can obtain the dc value of F at this frequency since the squeezing takes place over a larger frequency range and we don't have rolloff until about 10Mhz in these plots. We see that F(1Mhz) is around 0.7(1.54dB) for 2V and 0.68(1.67dB) for 8V. There is a sizable error since the theoretical results predict 0.78(1.076dB) and 0.736(1.33dB) respectively. The shot noise source could be actually be super-Poisson in this case which we need to prove. What should be a flat response shows peaking in the Fanofactors around 3-8Mhz. This cannot be due to the measurement chain since, the levels track each other and the normalized levels should not carry any of the frequency response of the chain. Sometimes we notice an interference at lower frequencies(which we can see in the thermal trace of figure), but this is at a fixed signal strength whereas the peaking depends on the current. On a sidenote, the interference can easily be removed by interpolating between neighboring points. Nonlinearity which depends on the optical power is also not an issue here, since both shot and subshot are at the same optical power produced by the same LED. Also in typical squeezing experiments, at low injection currents, the levels merge at much earlier frequencies. Here we see that in both low(2V) and high injection(8V), the Fanofactor rolls off within the same frequency range indicating that it is a problem with the LED and not the measurement chain. Fig. (3.17c) essentially tracks down the problem to the SNS. In Fig. (3.17c1) ,we perform the comparison between SNS driving the LED and a lamp driving the PD directly. First we notice that SNS produces an error of nearly 0.2dB at 1Mhz when compared to the lamp(which we have shown to be a true Poisson source). At midfrequencies of 2-8Mhz it rises atleast 0.4dB above the lamp and rolls off around 10Mhz whereas the lamp does not rolloff. The subshot plot has been included for comparison. The vertical scale is arbitrary as we are not interested in quantitative answers. In Fig. (3.17c2) , we perform the comparison between the lamp driving the PD and an LED moved far away from the PD such that the coupling efficiency is $< 1\%$. We note that the levels are indistinguishable. This is as expected since when the efficiency of the LED is reduced, the levels should return back to the SNL as we have seen earlier for the L2656. Also there is no rolloff at 10Mhz. This tells us that the culprit is the SNS and is reasonable since we considered it only as a Poisson current source and not as an equivalent circuit of a diode connected through cables to another diode. This definitely affects the frequency response which can be explained as follows: The PD generates a current given by $I_{dc} + i_{poisson}$.The Poisson current falls off with the response of the PD-LED combination and at a certain frequency the PD becomes a constant current source which generates a subshot level at the LED. We would like to make this response 'go away' and so if we are interested in accuracy we have to use the LED to calibrate the SNL against itself by lowering the efficiency instead of relying on the SNS. Nevertheless, we find that at lower frequencies(500kHz-1Mhz) and particularly at moderate current levels, the SNS is still a viable alternative to moving the LED far away and the SNS and the lamp agree quite well. This fact has been used in our noise modulation experiments. As a final check, we replaced the detector in the SNS from the UDT model to the Hamamatsu S3994 and observed the noise characteristics of Fig. (3.17c3) . We can see that the response is the problem as the new detector causes the peaking to be more easily recognizable. Also the levels merge now at 16Mhz. When we compare with the LED level with the lamp direct, we see that an error nearly 0.4dB at 5Mhz which is quite large. We may question the validity of the SNL in the L2656 experiments based on our observations for the L9337. Note that the Fanofactors are forced to merge at the same frequency range in Fig. (3.17b)(around 10Mhz) for both low and high injection, whereas for the L2656, the response is different for each case as seen in Fig. (3.15b) (low injection) and Fig. (3.15d) (high injection). Also if we assume the SNL is super-Poisson, we should see a consistent error above the subshot level in Fig. (3.15a,c) and the levels should not merge unless its restricted by the frequency response. From this we conclude that for the L2656 the subshot levels merge with the SNL as required whereas in Fig. (3.17a), the SNL merges with the subshot level.

The bandwidth limiting mechanisms of pin detectors are 1)Diffusion time of carriers which is usually made small by placing the junction close to the surface 2)Transit time across the depletion region τ_d 3)RC product τ_{RC} of terminal capacitance C_{dep} of the PD and load resistance R_L. Since we use large area photodiodes($100mm^2$), the junction capacitance

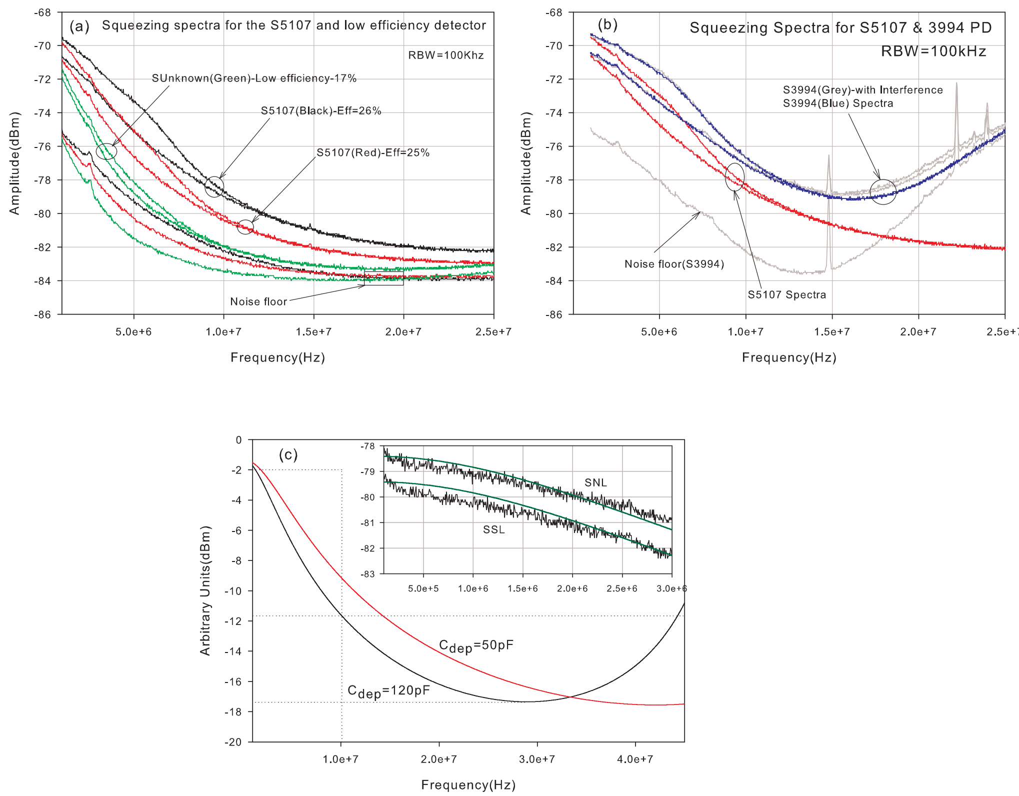

Figure 3.18: Electrical Response characteristics of photodiode-amplifier configuration (a)Optical Noise spectra of S5107 PD compared with a generic low responsivity PD (b)Optical Noise Spectra of S5107 and S3994 PDs (c) Electrical transfer function according to Eq: for S5107 and S3994 PD where the fitting parameters $L = 0.15\mu H$ and $C_C = 150pF$ have been used. The inset shows the experimental noise spectra from 1-3Mhz and the solid lines depict the theoretical model.

should be high and the bandwidth will be limited by a combination of the RC product and transit time. The S5107 PD has a quoted 3dB bandwidth of 10Mhz at $R_L = 50\Omega$ and reverse bias $V_R = 10V$ with a $C_{dep} \approx 150pF$. With the parameters of R_L and C_{dep},we should be able to calculate the cutoff frequency theoretically as[62]

$$f_{3dB} = \frac{0.35}{\sqrt{\tau_d^2 + \tau_{RC}^2}} = \frac{0.35}{\sqrt{(\frac{d^2}{\mu V_R})^2 + (2.2R_L C_{dep})^2}} \tag{3.24}$$

If we ignore the drift time, the cutoff will be 20Mhz which suggests that the drift time has to be factored in. This is around 30.7ns which is the slower time scale when compared to the RC of 16.8ns. Now if we change the resistance to 192Ω, because of adding the amplifier, we can assume that the reverse bias does not change too much and the drift time is constant.

With this the RC becomes 4 times larger or 67.2ns and we should expect a cutoff of around 5Mhz. In fact, the bandwidth will be predominantly RC limited for a certain frequency range after which it is τ_d limited. If we include the cable reactances we end up with a transfer function obtained as voltage across the $R_I = 200\Omega$ resistor to the root sum of squares of all current noise components which can be obtained from Fig. (3.7b) as

$$H(\omega) = \frac{V_{200}}{I_t} = \frac{R_D R_I}{R_D(1 + sC_C R_I) + R_I(1 + sC_D R_D) + sL(1 + sC_D R_D)(1 + sC_C R_I)} \tag{3.25}$$

The above equation does not include E_n which we shall handle separately but its different from Eq. (3.7) in that it neglects drift as per the assumption that the bandwidths are RC limited. If we set $L \approx 0$ and $C_C R_I \ll C_D R_D$ then we can expect a 20dB per decade rolloff until the next pole gets activated. Inclusion of L creates a transfer function peaking to take place at higher frequencies. Increasing C_C affects the rolloff rate of the first pole since $R_I C_C$ gets closer to $R_D C_D$ and the magnitude of the peaking as well. L and C_C affect the frequency at which resonance takes place. The low pass filter and peaking characteristics are seen in Figs. (3.18a) and (3.18b). In Fig. (3.18a) we have determined the optical noise spectra for two different S5107 detectors by varying the cable types. Note that the degree of squeezing is similar in both curves at approximately 1dB at low frequency. The midfrequency still shows the error since we used the SNS but we are more interested in the response. Even though the two detectors are the same, the low frequency pole has shifted up for the case of $\eta_0 = 26\%$ which is why it rolls off slower when compared to the case of $\eta_0 = 25\%$.All the PDs were driven such that they produced the same photovoltage, and so the noise power at 1Mhz is similar for the two cases. We have also plotted the case of a generic PD which has a low responsivity. Even though the LED is driven at a larger current(to produce the same photovoltage) which also implies a larger squeezing, the efficiency is restricted by the PD which is around 17% and hence the degree of squeezing is reduced. The 3dB of the first pole occurs at low frequencies which is why the 1Mhz noise power does not agree with the other two. The noise floors for each of the PDs have also been included and we notice the same frequency response according to Eq. (3.25). Particularly interesting is the noise floor characteristic at around 20Mhz where all the curves join. All the noise sources have a frequency dependent response except E_n which is at the input of the amplifier. So its reasonable than I_t drops below E_n leaving behind only this voltage noise component. At 20Mhz we measure -132.1dBm which when we refer to the input gives us 0.79nV/$\sqrt{Hz}$ which is less than a 50Ω resistor noise but still larger than the $E_n = 0.506nV/\sqrt{Hz}$ we measured earlier. This may be because a portion of the 200Ω input resistor noise(which was not included in the above response function) adds up with E_n. In Fig. (3.18b) the noise spectra for two different PDs are shown. The S3994 has a $C_{dep} = 40pF$ which should shift the first pole to larger frequency which is what we observe when we compare with the $C_{dep} \approx 100pF$ (at reverse bias of 20V) of the S5107 detector. The grey lines indicate the same experiment carried out with improper shielding which we believe may be due to conductive interference due to the monitor or power supply. The S3994 spectra show incorrect squeezing at higher frequencies because of this interference.

In Fig. (3.18c) we have plotted Eq. (3.25) for the parameters $R_D = 5080\Omega$, $C_D = 120pF$, $L = .15\mu H$, $C_C = 150p$ and $R_I = 200\Omega$. These curves have been fitted to the spectrum of the $V_{ph} = 4.16V$ photovoltage case which is detailed in Fig. (3.19a). Here L and C_C were the only unknown fitting parameters used and C_D was estimated from the datasheet and its value lies between 90 and 150pF(between $V_R = 10V$ and $V_R = 24V$) but we found 120pF to be a closer fit. The cable used was approximately 1foot which should put the capacitance at 10pF[**?**] but we have found a much larger value to be a better fit. Also we have used a lumped parameter model instead of the expected distributed parameter which is another source of uncertainty. But we have obtained reasonable results with the circuit model of Fig. (3.7b). As seen in Fig. (3.18c), changing the capacitance from 120pF to 50pF affects the low pass response, but it does not shift the peaking to lower frequency as it does in Fig. (3.18b). This is because the cables used were different for each of the PDs. The inset of the Fig. (3.18c) shows the squeezing spectra from 100kHz to 3Mhz and we see that the 3dB cutoff frequency is at 3Mhz. The solid line is Eq. (3.25) with the above fitting parameters.We notice that at low frequencies the SNL agrees well with the plot but the SSL level agrees well only at larger frequencies. We believe that this is an artifact of the SA, since the SNL and SSL should follow each with a difference of 1dB which is also the difference between the two solid lines. Also at 650kHz we see from the solid line it differs by 0.1dB from 100khz(or about 0.5dB if we use the noise powers) but this is not sufficient to explain the 2.8dB difference we saw for the optical shot noise. Hence the response function $F(\omega)$ we obtained there must be primarily due to the SA miscalibration. The dotted lines in the Fig. (3.18c) indicate the difference between a)1Mhz and 10Mhz which is around 9.18dB b)10Mhz and 25Mhz is 5.5dB and c)10 Mhz and 45Mhz is 0.8dB. These differences were used to obtain the fitting parameters to fit to the noise spectra plots approximately.

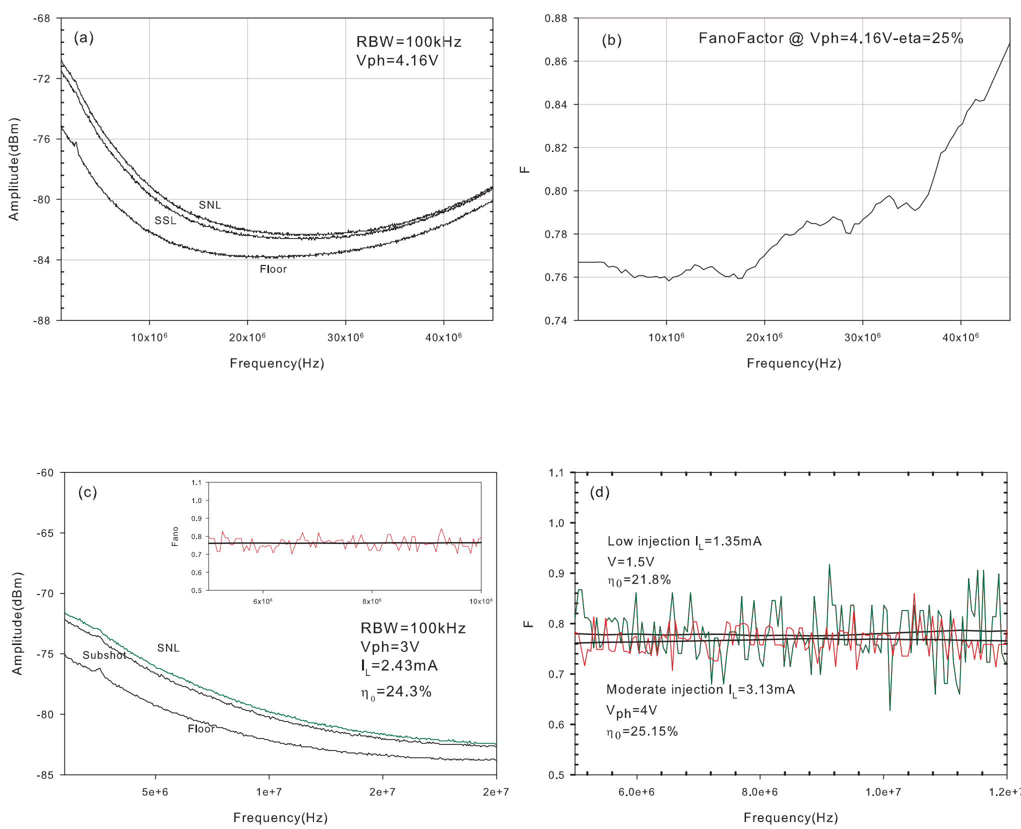

Figure 3.19: (a) and (b) shows the squeezing spectra and computed fanofactors(without the noise floor correction) for the driving current of $I_L = 3.27mA$. (c)Squeezing spectra obtained for a driving current of $I_L = 2.43mA$.The inset depicts the constant Fanofactor over a range of 1-10Mhz. (d)The Fanofactors for the low injection current($I_L = 1.35mA$) versus high injection($I_L = 3.13mA$) cases.The solid line in the fanofactors depicts the result of a smoothing filter.

Fig. (3.19a) shows the squeezing spectra for $I_L = 3.2mA$. Notice that the nonlinear increase at midfrequency is absent since we have used a LED moved far away from the

PD keeping the efficiencies to $< 1\%$ which makes it as a shot noise source. Using this method however, restricts the range of drive currents that can be used. For example, for an $I_L = 4.49mA$ the photovoltage obtained was 6V giving us an $\eta_0 = 26.3\%$. To create a SNS we have to move the LED such that $\eta_0 \approx 1\%$ and so the LED has to be driven with $I_L = 118mA$ which is beyond the maximum rating(80mA) of the LED. And if we drive the LED at high currents for too long, the LEDs lose their efficiency and squeezing and we saw such a case earlier. So we restricted our experiments to photovoltages of 4.5V with efficiencies of $< 1.5\%$ and maximum drive currents of 36mA. Next we see that from we have a difference of 1)8.2dB from 1-10Mhz and 2)1dB from 10-45Mhz. We find an error from 10-25Mhz where we see 2dB but according to Eq. (3.25) we find 5dB. This may be due to the other noise components which are present and not accounted in Eq.(3.25) or the usage of the lumped parameter model for the transmission line. However the qualitative features(low pass filtering and peaking) have been traced out in these plots. The degree of squeezing is around 1dB at low frequency and appears to rolloff around 23Mhz and eventually disappears around 40Mhz. In Fig. (3.19b) we have computed the Fanofactor from Fig. (3.19a). The cutoff frequency is found to be the frequency where $F = 1 - \frac{\eta_0}{2}$ and in this case lies beyond 45Mhz. The maximum cutoff for the L9337 LED is rated at 40Mhz which is beyond that obtained. This is an error which can be recognized by looking at Fig. (3.19a). We see that the SNL and SSL traces start to rolloff towards the noise floor around 15Mhz even though they maintain the same frequency response. This may be because of the drift time which is another bandwidth limiting mechanism which can be included in the photocurrent itself which then becomes frequency dependent(ie. $I(\omega)$). We performed the following correction to the noise floor: First we find the difference between the SSL and the noise floor(which is constant at low frequencies) and note the frequency where the difference changes. At this frequency onwards we recalculate the noise floors such that they are at a constant difference from the SSL. This way we have 'tricked' the detector into ignoring its own bandwidth limiting mechanism. The reason we can use this method is that the Fanofactor calculation subtracts away a noise floor term according to equation and we have not modified the shot or subshot noise levels themselves. This constant noise floor is a function of frequency response when there is no light and is primarily the 5080Ω resistor noise, and when we add the light, the photocurrent+resistor noise are expected to follow the same response. Hence by correcting the resistor noise by noting the constant difference and then subtracting it away, we will have the correct photocurrent noise. In Fig. (3.19c) the optical noise spectra for $I_L = 2.43mA$ has been plotted. The inset of Fig. (3.19c) shows a Fanofactor of 0.77 which is close to the calculated Fanofactor of 0.76. We notice than from 1-10Mhz the fanofactors are constant,something we could not observe for the L2656. There the 100Khz was taken as the dc point, but in this case we can take 1-10Mhz as representative of the dc point since the Fanofactor frequency characteristic tends to 1 only at frequencies greater than 10Mhz. In Fig. (3.19d) we have plotted the fanofactors for the low injection current of $I_L = 1.33mA$(which is the minimum distinguishable noise power from the noise floor in this experiment) and for high injection of $I_L = 3.13mA$. As we mentioned earlier the variance of F for smaller current is larger since it is close to the noise floor. At the low current the calculated Fanofactor is F=0.782 whereas the experimental result is 0.78 and for the high injection the calculated Fanofactor is F=0.75 and the experimental result if 0.76. We have not included the differential efficiency in these calculations since they are quite small, but nevertheless they may cause a finite error which is not discernable with the present experiment.

3.5.5 Squeezing Results for the L9337 LED

For the L9337 LEDs in the low injection regime, particularly where the backward pump process can be neglected(α_d , $\alpha_0 \approx 0$) the carrier injection process is predominantly due to thermionic emission with the frequency dependent Fanofactors given by[69]

$$F_{ph}(\omega) = 1 - \eta_d \frac{\frac{\eta_d}{\eta_0} - 2\left(\frac{\eta_d}{\eta_0} - 1\right)[1 + (\omega\tau_{te})^2]}{[1 + (\omega\tau_{te})^2][1 + (\omega\tau_r)^2]} \tag{3.26}$$

For the drive currents varying 0.5 to 3.5mA we find that $\frac{\eta_d}{\eta_0}$ varies from 1.06 to 1.09 and without incurring too much error we have set it to 1. So the above expression reduces to the much simpler Eq. (2.244) which we rewrite here as

$$F_{ph}(\omega) = 1 - \eta_0 \frac{1}{[1 + (\omega\tau_{te})^2][1 + (\omega\tau_r)^2]} \tag{3.27}$$

Fig. (3.20) shows the experimental Fanofactors obtained for $I_L = 1.54, 2.01, 2.17$ and 2.61mA respectively. In each of these cases, the dc Fanofactors have been illustrated with the straight line that passes from around 5Mhz to 0 and except for the 1.54mA case we see good agreements between experiment and theory . Note that the curves move upward at lower frequencies. This is because of the SA response which we saw earlier for the L2656. The solid lines are the theoretical models according to Eq. (3.21) and Eq. (3.27) which are used to fit the data. For the case of the diffusion model we have set C=1 since the differential efficiency is quite close to the dc efficiencies. The model parameters can have been obtained in the same way for the L2656 except in this case we could not measure the cutoff frequency since the detection bandwidth of our PDs were very small(less than 10Mhz) putting our results at a cutoff 1Mhz which is clearly incorrect and can be seen just by noticing that we have squeezing over a much larger range than 10Mhz. The datasheet specifies a cutoff of 25Mhz or $\tau_r = 6.36ns$ which is what we used to fit the curves. The remaining element is C_{dep} which we measured to be 52.4pF using a LCR meter. Using this to calculate the thermionic emission time for $I_L = 2.01mA$ we see that $\tau_{te} = 0.667ns$ which is much smaller than τ_r.In other words the thermionic emission cutoff is $f_{te} = 240Mhz$ almost ten times larger than the radiative cutoff and hence squeezing is spontaneous emission limited. We cannot use the lower current levels to obtain C_{dep} as we did for the L2656 since it seems that we already working in a high current regime. Higher currents reduce this τ_{te} further. If we try to lower the currents to try and fit C_{dep}, we will hit the noise floor of the amplifier. On a side note we can calculate the total recombination time(including nonradiative processes) by $\tau_{rec} = \tau_r \frac{\eta_d}{\eta_0}$ which is approximately 7.46ns. We notice that the model parameters fit quite well and the difference between the diffusion and thermionic emission model is quite subjective. To us, the thermionic emission model sees a better fit if we use either the center of the Fanofactor variance or the smoothed curve as reference.

Fig. (3.20e) plots the squeezing bandwidth versus driving current. The linear dashed line is the thermionic emission lifetime which is also dependent of current according to $\frac{kTC_{dep}}{eI}$ and illustrates the region where the macroscopic Coulomb blockade effects works. The horizontal dotted line is the radiative cutoff frequency of 23Mhz. The experimental

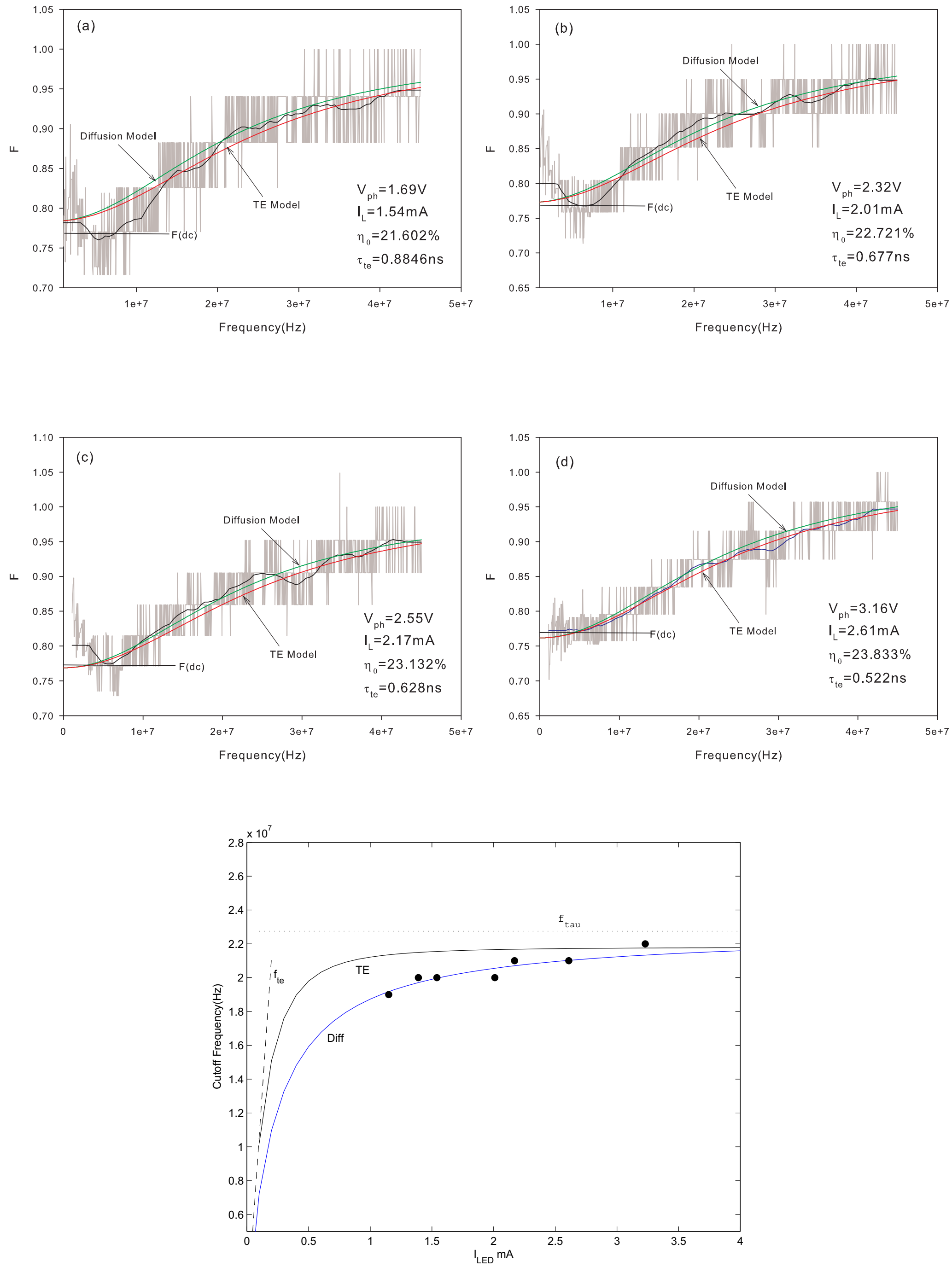

Figure 3.20: Spectral Fanofactors of the photon fluxes from the L9337 LED obtained at (a)$I_L = 1.54mA$(b)$I_L = 2.01mA$ (c) $I_L = 2.17mA$ and (d) $I_L = 2.61mA$. The Fanofactors were fit to the theoretical diffusion model and thermionic emission model(solid lines) which were obtained using Eq.(3.21)(C=1) and Eq.(3.27) with the model parameters $C_{dep} = 52.4pF$ and $\tau_r = 6.36ns$. The center dark line represents a smoothing filter applied to the raw data. (e) Pump current dependence of the squeezing bandwidth. The solid lines indicate the theoretical diffusion model and thermionic emission models. Model parameters for the diffusion model is $C_{dep} = 60pF$ and $\tau_r = 7ns$ and the thermionic emission model is $C_{dep} = 50pF$ and $\tau_r = 7.3ns$.

points have been obtained from the Fanofactors by first noting the dc values and finding the cutoff frequency at which the Fanofactors have dropped by half. The theoretical curves have been obtained by plotting the diffusion model equation from Eq.(2.243)

$$f_{Diff-3db} = \frac{1}{2\pi(\frac{kTC_{dep}}{eI_L} + \tau_r)} \tag{3.28}$$

where we have used $C_{dep} = 60pF$ and $\tau_r = 7ns$. We also compute thermionic emission model for 3dB bandwidth given by Eq.(3.17) which we rewrite here

$$f_{TE-3dB} = \frac{1}{2\pi}\sqrt{\frac{1}{2\tau_{te}^2\tau_r^2}\left\{-\left(\tau_r^2 + \tau_{te}^2\right) + \sqrt{\tau_r^4 + \tau_{te}^4 + 6\tau_r^2\tau_{te}^2}\right\}} \tag{3.29}$$

The model parameters in this case were $C_{dep} = 50pF$ and $\tau_r = 7.3n$s. We note that as we in the low current regime the squeezing bandwidth increases whether we use the TE or diffusion model. In the high current regime the squeezing bandwidth approaches the constant value limited by τ_r. Our experimental points all lie in this range. We we able to fit our results better to the diffusion model which is quite surprising since we noted that the L9337 being a heterojunction device should satisfy the TE model. We can see why just by noting that different model parameters have been used compared to the ones in Fig. (3.20a-d). This is because the experimental points were obtained using the smoothed curve, and there is a certain degree of error in interpreting its results. Also we cannot really categorize the squeezing bandwidth model until we have low injection current values which is unattainable with the present experimental setup. So in conclusion, both the TE and diffusion model seems to work well. The fit to the diffusion model should not be confused with the high injection current regime in the heterojunction where the backward pump process $\alpha_0, \alpha_d \to 1$ in which case the diffusion model given by Eq. (3.21) is once again valid. Also we note that the variance of the Fanofactors have been obtained at an VBW of 1Hz with further averaging done. The end result has a bit quantization look to it rather than the continuous form of Fig. (3.15). This is the highest level of averaging that we can achieve.

3.6 Summary

We summarize the important contribution of this chapter. A setup has been constructed to observe the subshot noise of light. Each element of this setup has been calibrated to make the errors as small as possible. The maximum uncertainty of the absolute measurements performing using this setup is around 1dB .The L2656 LED which has been previously studied has been re-investigated and accurate results have been determined. We have noted discrepancies with previous results which had ignored the role of the differential efficiency and have fit the results to theoretical models quite well. The concepts of high impedance pump suppression even though it have been well understood theoretically have not been experimentally demonstrated until now. We also see that the junction capacitance plays an important role in the constant voltage setup and introducing the large capacitor seeks to redefine the total capacitance of the junction which also affects the squeezing bandwidth. We have fitted the results of L9337 to both the TE and diffusion theoretical models and determined the pump current dependence on bandwidth. We were unable to determine which model fit better since our experiments were done at the high injection current regime. We have demonstrated maximum squeezing of nearly 1.5dB over the frequency range of 1-25Mhz. We believe that the degree of squeezing(at the time of performing this experiment) is one of the largest reported at room temperature. The experiments have shown that the light coming from the L2656 and L9337 LEDs are at the subshot noise level as postulated by the diffusion and thermionic emission Fanofactor models proving that these LEDs can be used as nonclassical light sources in quantum communication experiments.

Chapter 4

Quantum Stochastic Modulation

4.1 Introduction

Squeezed optical fields have generated considerable interest due to the possibility of reducing the quantum uncertainty in one dynamical variable (at the expense of enhanced uncertainty in the conjugate variable) in order to improve measurement accuracy. Classical methods of optical transmission achieve, as a lower limit, a Poisson distributed photon-number characteristic of the single-mode coherent state $|\alpha(t) >= \Sigma_N \alpha_N(t)|N>$ with variance $\sigma_N^2 = \bar{N}$ (shot-noise level). It has been anticipated [70] that subshot noise light ($\sigma_N^2 < \bar{N}$) with photon-number fluctuations smaller than the standard quantum limit would produce ultra-low-noise communication systems although practical ones have not been constructed. We have demonstrated that semiconductor light emitting diodes (LEDs) conveniently and inexpensively produce subshot light by means of the mechanisms for high-impedance pump-noise suppression. These states can be easily detected by semiconductor photodiodes. We demonstrate in this chapter, a novel quantum-level stochastic communicator that modulates both the average photon number $\bar{N}(t)$ (optical power) and the uncertainty in the photon number (variance) as two independent binary channels. The stochastic communicator produces random signals based on a controllable intrinsic probability distribution in contrast to the chaotic optical signals generated from lasers [71]. In principle, a stochastic communicator could be constructed that superposes M different (but fixed) Fock states to obtain M-1 independent statistical moments. The transmitter would then independently modulate the probability amplitudes to produce M-1 independent channels. However, LEDs already produce superposed number states that can be electronically controlled without using external optical modulators. Those optical states behave similar to the number-squeezed light and approach the fragile Fock states in the limit of infinite squeezing(unlike the amplitude squeezed states). The noise becomes a useful signal by making it a controllable nonstationary process $\sigma_N^2(t)$. However, the optical states can link the variance to the average such as for the Poisson distribution; this adds another source of nonstationarity and implies the two channels are not necessarily orthogonal. The technique presented here uses small modulation amplitude for the "average" signal so that it has negligible impact on the variance. The modulator section transmits the light over a low-loss medium to the highly efficient photodetector. The receiver recreates the two signals from the joint time-and-frequency (JTF) [72] information.

The modulation of noise principle has already outlined in chapter 1, but if we translate the idea into a quantum optics perspective, we see that the transmitter section of the statistical communicator uses the interaction potential $\hat{V}$ created within the LED to produce a superposed optical field represented by the density operator $\hat{\rho}$. Let the symbol v represent a parameter associated with the pn junction that controls the degree of number squeezing such as the impedance of the drive electronics and the Coulomb blockade mechanism. Suppose an external driving circuit provides slow binary modulation to the parameter v to switch between sub-Poisson and Poisson statistics so that $v(t) = \Sigma_m \Omega_m(t) v_m$, where m is "even" for subshot and "odd" for shot. The function $\Omega_m(t)$ equals 1 for $t \in ((m-1)T, mT)$ and zero otherwise, and it yields the relation $\Omega_m \Omega_n = \Omega_m \delta_{mn}$. The interaction potential can then be subdivided approximately as $\hat{V}(t) = \Sigma_m \Omega_m(t) \hat{V}_m$, where $\hat{V}_m = \hat{V}(v_m)$.The equation of motion $\partial_t \hat{\rho} = [\hat{V}, \hat{\rho}]/i\hbar$(interaction representation) indicates that the density operator decomposes as $\hat{\rho}(t) = \Sigma_m \Omega_m(t) \hat{\rho}_m$, where $\hat{V}_m$ produces the stationary field $\hat{\rho}_m$. The field $\hat{\rho}$ therefore moves between the two stationary processes. The communicator transmits the variance signal $\sigma_N^2(t) =< (N - \bar{N})^2 >$, where each process m has the Fanofactor $F_m = \sigma_N^2(v_m)/\bar{N}_m$ and the same average $\bar{N}$. Any time dependence in the average and its consequential linkage with the variance can be eliminated by using F(t) as the signal rather than the variance alone. The transmitter and receiver rely on the Fanofactor to predict changes in the squeezing level as the signal moves between system components. A component such as a reflecting interface introduces partition noise since the photons will be transmitted across the interface according to a binomial distribution with the single-photon transmittal probability p. Assuming highly efficient optical coupling and photodetection, and given that the transmitted photon number N(t) has a specific probability distribution at any particular time, the photon arrivals at the photodetector must have a nearly identical distribution as should the photocarriers comprising the photocurrent I(t). The Fanofactor F(t) for the optical state therefore transfers to the photocarriers and directly produces the time-varying spectral density $S(\omega, t) = 2eF(t)I_{dc}$ where I_{dc} is the dc photocurrent.

In chapter 1, we developed the concept of stochastic modulation and an implementation using classical signals has been included in Appendix.B . The decoding of the stochastic modulation was restricted to the time domain since it is effective for the 'hand-made' probability distributions used. Anticipating the usage of naturally arising photon number probability distributions such as the Bose-Einstein distribution for thermal light or Poisson distributions for coherent states, we introduce the idea of decoding in the frequency domain using the spectrum analyzer as a joint time-frequency analysis tool. This method is discussed in section 4.2. In section 4.3, we study the various methods of electronically modulating the noise since the optical modulation methods are quite lossy. We have performed theoretical studies for noise arising in the BJTs and MOSFETs and how it would affect the optical noise of LEDs connected to its terminals. We have been experimentally successful in producing shot and subshot noise with both of these devices connected to the LEDs, but the theoretical formulation of the BJT falls short of explaining the optical noise spectra seen in deep saturation, whereas the MOSFETs are shown to introduce very little change to the shot/subshot noise produced by LEDs, provided certain conditions are met. This is why we choose the MOSFETs for the final design of the quantum stochastic communicator, which consists of a switching circuit built of 3 such devices. After we study the switching aspects of the circuit, we demonstrate the complete system working with the average(AC) modulation and noise modulation channels together in section 4.4.

4.2 Time Frequency Analysis using the spectrum analyzer

A pulse amplitude modulation would require a cyclostationary(CS) description of the process $s(t) = \Sigma_n a_n u(t - nT)$ at the receiver where $\{a_n\}$ are a sequence of WSS random variables, and u(t-nT) is the step function. The signal s(t) in turn modulates the shot noise and if periodic square wave are assumed ie. $a_n = -a_{n-1}$, it leads to a CS shot noise process n(t). On the other hand, if the Fanofactor is controlled in time, the photocurrent from the photodiode(as seen in the previous chapter) is a constant DC current and the noise is given by $F(t)2qI_{dc}$, where F(t) is the modulated Fanofactor which changes the statistics of the distribution periodically ie. the probability $P(x_1, t_1) = P(x_1, t_1 + nT)$ where T is the period of F(t). Since the mean is constant with time, the noise modulation scheme does not fit under the CS category exactly. When both the average signal-s(t) and the noise signals-n(t) are modulated, nonstationary noise(the noise is referred to as cyclostationary when the signal is periodic and nonstationary otherwise) arises due to a)shot noise associated with signal modulation s(t) as well as b)modulating a random signal x(t) separately. In this chapter, our goal is to construct a general signal s(t)+n(t) where the signal and noise modulation can be carried out independently of one another and separately detected. The shot noise current of the diode - $i_{sh}^2 = 2qI_{dc}$ is time varying if $I_{dc} \to I(t)$ ie. it changes with a large signal excitation through $I(t)$. For simplicity we restrict ourselves to periodic signals and assume that the mechanisms for noise generation in the photon flux and photocurrent generation are sufficiently fast compared to the modulation frequency, the noise sources can be modeled as a slowly amplitude modulated noise source (CS processes).

The detection of cyclostationary noise requires the spectrum analyzer(receiver) to be configured to read the time varying nature of the power spectral density. The important elements of the SA are the local oscillator(LO), the mixer stage,the resolution bandwidth filter and video bandwidth filter and the parameters associated with these elements which are sweep time, RBW and VBW which play the role of a time base control to display the modulated spectral densities in time. The equivalent building blocks shown in Fig.(4.1) are two mixer stages and a narrow bandpass filter. The first mixer stage is representative of the way the CS process is generated by modulated noise sources. A white noise source $n_1(t)$

with unit spectral density $S_{n_1}(\omega) = 1$ is modulated by the locally time varying operating point $f(t)$. The output $n_2(t)$ is a CS process shaped in time t with spectral density $S_{n_2}(\omega) = f^2 S_{n_1}(\omega) = f^2$. Alternatively the mixer can be represented by a time varying transfer function and this represents the modulated signal path for a white stationary noise as input whose output is once again the CS process $n_2(t)$. The second mixer stage represents the SA circuitry where the inputs are the filtered(without ac modulation) photodetected light $n_2(t)$ and the LO signals and the output $n(t)$ is resolved by the RBW. In general, a process $n(t)$ is referred to as cyclostationary when the mean and the autocorrelation function are periodic in time ie. $R_{n,n}(t+\tau+T, t+T) = R_{n,n}(t+\tau, t)$. Here the t, τ dependence requires a two dimensional Fourier transform to obtain the spectral density, but if we can time average the the spectral density of a cyclostationary process $S(\omega, t)$ over a period T, we obtain

$$\frac{1}{T}\int_{-T/2}^{T/2} S(\omega, t)dt = \frac{1}{T}\int_{-T/2}^{T/2}\int_{-\infty}^{\infty} R_{n,n}(t+\tau/2, t-\tau/2)\exp(-i\omega\tau)d\tau dt \tag{4.1}$$

where we have used the time symmetric variant of the autocorrelation function. Interchanging the integrals and using the time periodic nature of the autocorrelation function, we have a time averaged power spectral density given by

$$S(\omega) = \int_{-\infty}^{\infty} \overline{R_{n,n}(\tau)}\exp(-i\omega\tau)d\tau \tag{4.2}$$

A random time shifted process $\overline{n}(t) = n(t-\theta)$ where θ is a uniformly distributed random variable in the interval [0,T] converts a cyclostationary process into a stationary process with autocorrelation given by $\overline{R}_{n,n}(\tau) =< \overline{n}(t+\tau)\overline{n}(t) >= \frac{1}{T}\int_0^T R(t+\tau, t)dt$ validating the use of Eq. (4.2). In other words if a uniformly distributed random time variable jitters the signal $n(t)$ randomly by one cycle, the output loses all phase information and the spectral density $S(\omega, t)$ becomes the time averaged power spectral density $S(\omega)$. Ex: If the cyclostationary process n(t) is applied to a system which does not track the variation of power spectral density with time, the phase information is lost. Most receivers require synchronizing pulses or timing information to obtain the exact phase of the signal which requires an exact description of CS processes. This is true for the signal s(t) and if we time average the signal spectral density $S_s(\omega, t)$ we lose the timing information which can be extracted from the received CS signals. So we divide the signal for example by a power splitter and use the averaging characteristics of the spectrum analyzer to study only the noise spectral densities. In general,the noise modulation at an operating point I(t) is given as

$$S_1(\omega, t) = F(\omega(I), t) S_n(\omega, t) \tag{4.3}$$

where $F(\omega(I), t)$ is the modulation function or Fanofactor where $\omega(I)$ denotes the dependence of squeezing bandwidth on bias current as in Fig. (3.20f) and $S_n(\omega, t)$ is the power spectral density of the noise that depends on s(t). A spectrum analyzer(SA) can be configured to read $S_1(\omega, t)$ provided it satisfies certain sweep time constraints which are dependent on the modulation frequency of the incoming signal. Since our goal is to use the SA to decode the time varying noise which appears due $F(\omega(I), t)$, we first need to remove the sensitivity of the receiver to the intrinsic signal noise variations due to s(t) and make it sensitive to the controlled noise variations imposed on n(t). One way to achieve this is If the noise modulation is performed at a much smaller frequency than the ac signal modulation, the SA would obtain the time averaged spectral density as

$$S_2(\omega, t) = \frac{1}{T} \int_{-T/2}^{T/2} F(\omega(I), t) S_n(\omega, t) dt = F(\omega(I), t) \overline{S}_n(\omega) \tag{4.4}$$

The SA is inherently a time averaging device where Eq. (4.4) can be implemented thereby making it sensitive to only the noise modulation and not the average modulation. Modulation of output noise can be described as a multiplication in the time domain or convolution in the frequency domain ie

$$n_2(\omega) = \int_{-\infty}^{\infty} f(\omega - \omega') n_1(\omega') d\omega' \tag{4.5}$$

where we can imagine for a periodic signal $f(t) = \Sigma_n f^n \exp(jn\omega_0 t) \rightarrow f(\omega) = \Sigma_n f^n \delta_T(\omega - n\omega_0)$ of natural frequency ω_0 , the white noise at the input $n_1(t)$ is replicated around each harmonic for f(t).The same is true for arbitrary PSD $S_{n_1}(\omega)$ as copies appears at $\omega + k\omega_0$ and are weighted by the strength of the harmonic $f^{(n)}$ .The output of mixer is

$$n_2(\omega) = \int_{-\infty}^{\infty} \sum_n f^n \delta_T(\omega - \omega' - n\omega_0) n_1(\omega') d\omega' = \sum_n f^n n_1(\omega - n\omega_0) \tag{4.6}$$

We have relied on the fact that δ_T is a finite delta function and T is large enough to

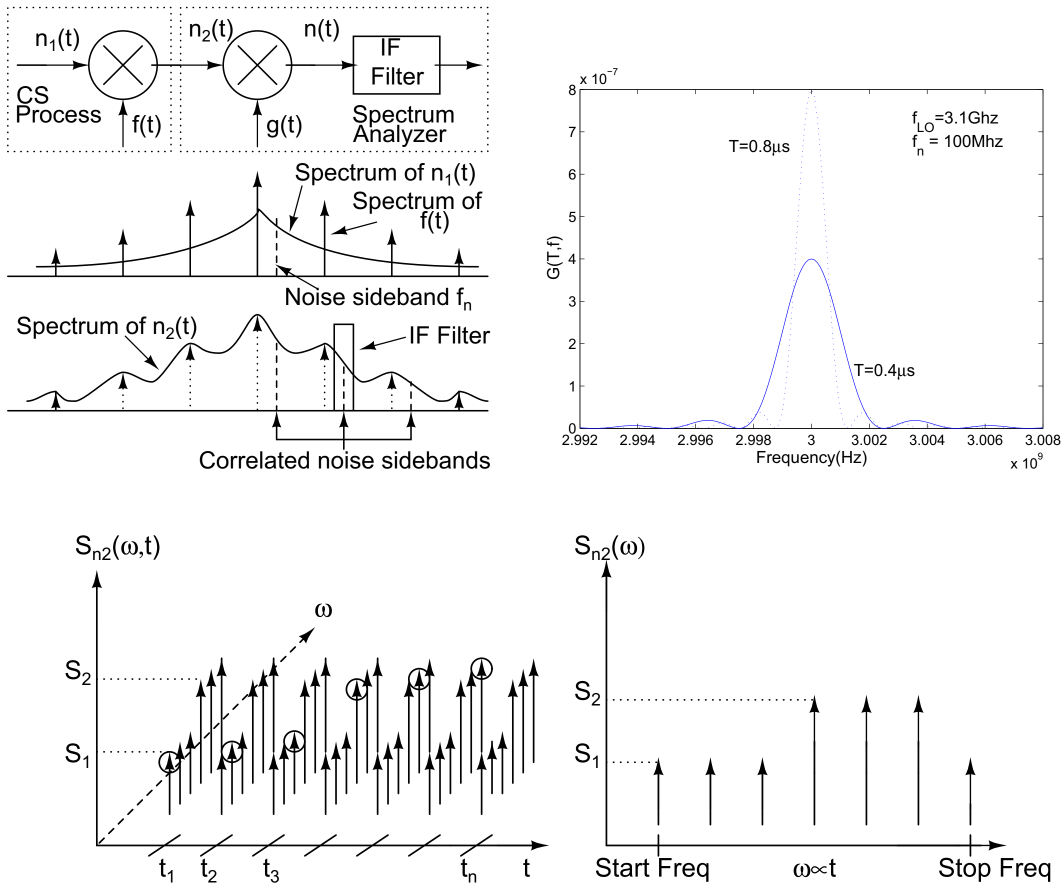

Figure 4.1: (a)The detection of cyclostationary processes by means of a spectrum analyzer (b)The finite time power spectral density $G(T, f)$ (c)The equivalent input signal description of $S_{n2}(\omega, t)$ and the corresponding time varying signal amplitudes along the line $\omega \propto t$(marked by circles) is plotted on the spectrum analyzer.

apply the singular property of delta functions. The corresponding PSD is also expressed as a convolution of the spectral density at the input with f^2 and is obtained from Eq. (4.6) as

$$
\begin{aligned}
< n_2(\omega_1) n_2^*(\omega_2) > &= \int_{-\infty}^{\infty} f(\omega_1 - \omega') f^*(\omega_2 - \omega') S_n(\omega') d\omega' \\
&= \sum_{m,n} f^{(n)} f^{(m)} \delta_T(\omega_1 - \omega_2 + (m-n)\omega_0) \qquad (4.7) \\
&= 2\pi q \sum_n I_n \delta_T(\omega_1 - \omega_2 + n\omega_0) \qquad (4.8)
\end{aligned}
$$

where $\Sigma_n f^{(n)} f^{(n+k)} = I_k$ is the harmonic of $f^2 = I(t)$. Because of the translated and replicated copies of the same PSD, noise separated by $k\omega_0$ are in general correlated. Hence for a general nonstationary process we have $< n_2(\omega_1)n_2^*(\omega_2) >= qI(\omega_1 - \omega_2)$. For the case of for $\omega_1 = \omega_2$ the time averaged PSD is

$$< n_2(\omega)^2 >= qI(0) = q\overline{I(t)} \tag{4.9}$$

So in general,the spectrum can be written as the Fourier components of the time varying PSD $S_n^{(k)}(\omega)$ where the k'th cyclic spectrum is the correlation between frequency components separated by $k\omega_0$ given by each term in the summation of Eq. (4.8) and the zero'th order is the time averaged PSD given by Eq. (4.9). $n_2(t)$ undergoes the same periodic modulation with the LO at the SA mixer stage to produce CS process $n(t)$. The output of mixer 2 has two cycle frequencies ω_0 and ω_1(where ω_1 is the frequency of the periodic LO signal of mixer 2) and if the ratio ω_0/ω_1 is a rational number, $n(t)$ can be viewed with cycle frequency equal to greatest common divisor of ω_0 and ω_1[73]. In fact, frequencies of $n(t)$ at $\omega + k\omega_1$ are 'folded' onto ω as seen in Fig. (4.1a). Simply adding these noise powers is incorrect since they are correlated which can be demonstrated as follows: Let there exist a common frequency ω_0 such that $\omega_1 = n\omega_0$ and $\omega_2 = m\omega_0$ such the ratio $\omega_1/\omega_2 = n/m$ is a rational number. In this case $m\omega_1 = n\omega_2$ and the harmonics of ω_2 which are folded onto ω are $km\omega_1$ which are themselves correlated from the previous mixing process. So when we add the noise powers we must consider the cross terms also. On the other hand if the ratio is not a rational number, there is no way we can shift ω_1 and have it equal ω_2. We can then assume that $n_2(t)$ is stationary process input to the second mixer stage without significant error. Another way to simplify the problem is to consider m or n to be large as is the case of our signal and LO frequencies of the SA. If $m \to \infty$ and n is small and finite, the harmonics created due to mixing in stage 2 are far apart from ω and its amplitude is quite small to contribute to the power spectrum and hence only a minor error is incurred by adding the correlated components. Similarly for $n \to \infty$, the same idea applies. Finally, the time averaged PSD can be used to describe the noise process $n(t)$ since the RBW filter can be adjusted to have a bandwidth less than $\omega_0/2$ such that only the noise sideband ω is selected and the correlated components as well the signal harmonic is suppressed(ie. the output noise is stationary since any two frequencies ω' and ω'' will be uncorrelated). As an example consider Fig.(4.1a), where we see that for a center frequency ω_0 and bandpass filter of bandwidth ω_0 around ω_0, we capture the stationary and second order cyclic spectra component $S^{(2)}(\omega)$ only. If the bandwidth is replaced with $\omega_0/2$, only one frequency component is captured and the resulting process is stationary with no cyclic components. The RBW filter has a Gaussian shape but if we can consider the ENB as a rectangular bandpass with the above bandwidths, the SA displays the integrated spectrum within this ENB as a single point on the display. Whether the integrated noise is calculated with or without correlations, the output looks white in nature and is modulated by the slower noise modulation factor $F(\omega, t)$. To illustrate this, consider the SA which displays a spectrum with signal harmonics and correlated components $S(\omega)$ at time t_1. This spectrum is later updated at time t_2 to display the value of $F(\omega, t_2)S(\omega)$. ie the switching process itself is not captured by the SA. The alternative possibility is to keep the LO fixed(a span of say 1Hz around the desired frequency) and track the variations of this frequency with time but it is much harder to do so.

Let us see a much simpler problem which will illustrate the modulation or translation of frequency idea as well as the finite time integration of noise as against the convolution idea presented before. Consider a WSS non-ergodic noise process

$$n_2(t) = \sum_n A_n(t) \exp(j2\pi f_n t) \tag{4.10}$$

to be demodulated at the mixer stage. Here $f_n = n/T$. The LO signal is $g(t) = A_c \cos(\omega_{LO} t)$ where A_c is the amplitude of this carrier and the output is

$$n(t) = n_2(t).g(t) = A_c \sum_n A_n \exp(j2\pi f_n t). \cos(2\pi f_{LO} t) \tag{4.11}$$

The finite time Fourier transform of the noise spectrum $n(t)$ is determined as

$$N(T, f) = \frac{A_c}{2} \sum_n A_n \{sinc[(f_{LO} + f_n - f)T] + sinc[(f_{LO} - f_n + f)T]\} \tag{4.12}$$

We notice that the modulation has shifted the frequency $f_n - f$ by $\pm f_{LO}$.The power spectrum of the signal can be calculated based on the assumption that the different frequency amplitudes are uncorrelated ie.$< A_n A_m >= 0$ and $< A_n^2 >= S(\omega_n)\Delta\omega$. This leads to

$$G(T, f) = \frac{\langle |N(T, f)|^2 \rangle}{T} = \frac{A_c^2 T}{4} \sum_n S(\omega_n)\Delta\omega \{sinc[(f_{LO}+f_n-f)T]+sinc[(f_{LO}-f_n+f)T]\}^2 \tag{4.13}$$

Note that the concept of finite time Fourier transforms can be used to define the role of the RBW after the mixing stage. In other words, the RBW filter can be suitably selected to have long integration times, to cause changes in the displayed spectrum and in this limit, the spectrum is defined as $G(\infty, f) = lt_{T\to\infty}\frac{<|N(T,f)|^2>}{T}$. If we take one of the sidebands as the signal to be detected ie. the signal frequency to be detected- $f_{sig} = f_n$, the SA will display it on screen only if it passes under the passband of the RBW centered at $f_{IF} = f_{LO} - f_{sig}$. For a particular signal frequency and time T, Eq.(4.13) is plotted in Fig.(4.1b). Note that the SA sweeps the LO between the start and stop frequencies as specified in the span settings which leads to time dependent local oscillator frequency $f_{LO} = f_{LO}(t)$. Eq. (4.10) is a simplification of the more general harmonic series representation(HSR) used to define a CS process[74] with the associated definition

$$A_n(t) = \int_{-\infty}^{\infty} w(t-\tau)x(\tau)\exp(-j2\pi f_n \tau)d\tau \tag{4.14}$$

where $w(t-\tau) = \frac{\sin(\pi(t-\tau)/T)}{\pi(t-\tau)}$. We skip the details of the calculation which can be found in Ref.[74], but the power spectrum is obtained by taking a 2D Fourier transform of the autocorrelation function $R_{x,x}(t,s)$ using Eq.(4.14) which leads to

$$R_{x,x}(t_1,t_2) = \sum_{m,n} R_{m,n}(t_1,t_2)\exp\left(\frac{j2\pi(mt_1 - nt_2)}{T}\right) \tag{4.15}$$

The corresponding spectral density is

$$S_{x,x}(\omega_1,\omega_2) = \sum_{m,n} R_{m,n}(f - \frac{m}{T})\delta\left(\omega_1 - \omega_2 + \frac{(m+n)}{T}\right) \tag{4.16}$$

where we have defined $R_{m,n}(t_1,t_2) = \langle A_m^*(t_1)A_n(t_2)\rangle$. Our interest though is the frequency domain representation of this HSR which divides $x(t)$ into bands of width $1/T$ so that the n'th component of $A_n(t)\exp(j2\pi nt/T)$ is the output of an ideal one-sided bandpass filter with input $x(t)$ and transfer function which is the Fourier transform of $w(t)$ as

$$W(t) = \begin{cases} 1, & \left|f - \frac{p}{T}\right| \leq \frac{1}{2T} \\ 0, & \text{otherwise} \end{cases} \tag{4.17}$$

Each term $A_n(*)$ is the centered version of the n'th component $A_n(*)\exp(j2\pi p*/T)$ to the frequency band [-1/2T,1/2T]. In essence the CS process is decomposed into a set of jointly WSS bandlimited process ie. the terms $\{A_n\}$ are jointly WSS if and only if $x(t)$ is CS[74]. This bandlimited-ness extends to the spectrum of our noise signal $n(t)$ in Eq.(4.11) at least for the case in which it is stationary. Looking back to Eq.(4.13) , we see that the delta functions can be defined as the limit of a sequence of ordinary functions and one such example[49] is $\delta(x) = lt_{T\to\infty}\frac{T}{\pi}sinc^2(Tx)$. This implies that in the limit of large T, the delta function picks out an element of the spectral 'fence' $S(\omega_n)$ at $f = f_n - f_{LO}$ as the output spectrum(we set $A_c = 2$ to normalize the spectrum). We notice this in Fig.(4.1b) ie. as we increase T, it moves towards a delta function. We have not discussed (besides the qualitative description of Fig.4.1a) the output spectrum obtained when two mixing steps are performed on a stationary input signal. There are two reasons for this: 1)The SA displays a time averaged PSD and with appropriate filtering, a description of sideband correlations is not required. 2)The mixer carrier frequency is usually much larger than the signal modulation frequencies which is a filtering in disguise. So in the extreme case, we may need to deal with only one mixing step which is the first stage in Fig.(4.1a). Alternatively, we can state the problem in much simpler terms: The SA performs a Fourier transform of the input cyclostationary signal and by our analysis this spectrum is modified by the presence of the second mixer stage. In fact, in the presence of stationary input the output spectrum after the second mixer stage is cyclostationary and based on sweep time settings, we should see the time varying spectrum $S(\omega, t)$ displayed. But from our experiments with the spectrum analyzer in the previous chapter, we notice that irrespective of sweep time and bandwidth parameters, the spectrum is not time varying when the input is stationary noise and this is because of the large(¿3Ghz) local oscillator modulation frequencies used. The second issue is that we might opt to track one of the bandlimited spectral elements say $S(\omega_1, t)$ with time by tuning the LO to a certain frequency, but the RBW filter must be set to 1Hz which would increase the ST drastically. So in general we select a span where the LO sweeps from the start and stop frequencies and this way we are not plotting the time varying nature of the PSD that we need, but rather $S(\omega)$ over some time. In other words,each point displayed represents a frequency range and although we don't think of time when performing a spectral analysis, each point is displayed over a time interval. By using the equivalence between time and frequency as well as the property that noise is primarily white(both shot and subshot), we propose to use the sweeping of frequencies to plot the time varying PSD at some frequency ω_1 by the assumption that $S(\omega_1, t) = S(\omega = t)$ for all ω. This in turn leads to an equivalent input signal representation for the SA which is detailed as follows.

The SA does not perform an FFT, but rather uses the envelope detector to follow the variations of the IF stage which in turn gives us the spectrum. For example when the LO is tuned to one of the spectral components of the signal, the output of the IF stage is a steady sine wave and the envelope detector output is a DC component which in turn controls the deflection plates of the display and if we can envision noise as equal power sine waves for all frequencies, the envelope detector will be flat across the frequency range. Without having to describe the envelope detection stage(which is just another mixing and filtering process), we can equivalently describe the entire detection process(including the RBW) with an FFT with the help of windows and then use it to plot the time varying densities numerically.We see that ST defines directly how much time is spent to perform a complete frequency measurement. We can imagine this as equivalent to a FFT performed on a window of width ST is placed over the input signal. Of course, there are obvious differences with the SA operations such as 1)LO can be tuned to start and stop at any frequency whereas FFT algorithm typically gives us a set of frequencies over the sampling frequency $[-\frac{f_s}{2}, \frac{f_s}{2}]$. 2)The windows select a subset of the total signal samples which further restricts the frequency range. If a signal harmonic is present then this is equivalent to multiplying the impulse with the Fourier transform of the window which is a sinc function. Note that when we use an N point FFT where N is greater than the size of the window say M, the remaining N-M points are filled with zeros. Each bucket element can itself be considered as a window. The windows can be moved over the signal in time(the short time Fourier transform) also known as the sliding window or we can take non-overlapping windows. There is no great difference between the two, but the SA processes the signal for a certain integrating time given by the time to put data into a bucket and then it processes the next bucket. So non-overlapping window would be a more exact description of the SA. But in the numerical methods used for generating macroscale signals we cannot generate a large number of random number samples(approx 10ˆ5 samples is generated in several minutes in MATLAB) to properly represent noise without issues of periodicity and processing speed cropping up. These samples are then transmitted and in such applications the sliding window idea is more applicable to obtain a running average and running standard deviation. The implementation of the macroscale communicator can be found in Appendix.B.

Note that the signal harmonics are still present in PSD , but they don't show up in our experiments as the modulation is performed below the lower cutoff frequency of the amplifier bandpass filter. If the harmonics are present, the frequency ω of the noise floor inbetween the harmonics should be selected. The simpler method is to consider a signal modulation s(t) which is quite small(in mV range) which produces a shot noise current of $2qI(t) \approx 2qI_0$ which leads to $S_n(\omega, t) \approx S_n(\omega)$. The time varying PSD due to noise modulation can be written as $S_3(\omega, t) = F(\omega(I), t)S_n(\omega)$.We adopt this method in our experiments. However when $S_3(\omega, t)$ is input to a filter with sufficiently long integration time, the resultant spectral density is an average over the Fanofactor period $\overline{S}_3(\omega) = \overline{F(\omega(I))}S_n(\omega)$ which leads to an average supershot white spectrum which we have verified in experiments. Since this case ignores the periodic statistical properties of the noise signals as well its timing information, it is of little importance and will not be dealt with.

We now determine the minimum pulse width T_{min} of $S_3(\omega, t)$ that can be displayed on the SA. We choose to define this factor as the smallest time required for two neighboring 'bucket' elements to maintain the typical up-down motion of the spectrum for a modulated shot noise process. In order to realistically use the SA as a decoder, we may need to consider a value which atleast 10 times this minimum which will be seen in the experiments to follow. The IF filters(which are typically four pole synchronous tuned filters) must need time to charge and discharge and if the mixing product is swept past too fast there will be a shift in both amplitude and frequency accuracy. Note that the amplitude inaccuracy is not really important for noise type signals, and the SA can be run in manual mode with uncalibrated settings ie.we can set RBW and sweep time(ST) settings independently. We however run the SA in AUTO mode for which the three parameters RBW,ST and VBW are coupled so that we can make use of the following calculations.The time that the mixing terms stay in the passband is proportional to RBW and inversely proportional to the ST according to [52]

$$dt_{RB} = \frac{RBW}{SP/ST} \tag{4.18}$$

If we assume that the passband is Gaussian given by $H(f) = \exp(-\pi\frac{(f-f_0)^2}{\sigma^2})$ where f is the frequency relative to the center f_0 and σ is the variance. The RBW is typically defined as the 3dB bandwidth of $H(f)$ which we can use to obtain a relation for σ. At $f - f_0 = RBW/2$, the value of the $H(f) = 0.5$. This leads to $\sigma = 1.06RBW$. Note that the corresponding time domain response is also Gaussian given by $h(t) = \sigma\exp(-\pi\sigma^2 t^2)$. At t=0, we see that $h(t) = \sigma$ which is the maximum amplitude that $h(t)$ can assume. We are interested in the time taken to charge and discharge this Gaussian filter ie. time to rise from 1/100 of its maximum value (ie. σ) to the maximum and back. When $h(t) = 0.01\sigma$,we have $0.01\sigma = \sigma\exp(-\pi\sigma^2 t_{0.01}^2)$. This gives $2t_{0.01} = 2.42/\sigma = 2.3/RBW$. HP specifies a value of 2.5 instead since the IF filters used in practice are not ideally Gaussian. Here $2t_{0.01}$ is nothing but the amount of time a signal spends in the passband of the filter that is dt_{RB} in Eq.(4.18) from which we can obtain a relation from sweep time(ST) according to

$$ST = \frac{2.5 * SP}{(RBW)^2} \tag{4.19}$$

The time spent in the IF stage in Eq.(4.18) can itself be taken as T_{min},provided that there is no following stages in the SA. Since we display the data in the SA display over a finite number of points(buckets), we are further restricted over both time and frequency. The data from the IF stage is placed into these buckets and a sample is taken from each bucket to be displayed. Each bucket contains a sample corresponding to a frequency and time interval determined by the following equations

$$\Delta f = \frac{SP}{N-1} \quad , \quad \Delta t = \frac{ST}{N-1} \tag{4.20}$$

which leads to Δt being the fundamental limit for the minimum pulse width in our receiver. We can obtain greater accuracy by either increasing the span or decreasing the sweep time, since more number of samples are taken in either case.To illustrate the role of buckets and Eq.(4.20) consider the following case of $RBW < \Delta f$: For a span of 100Mhz and 100

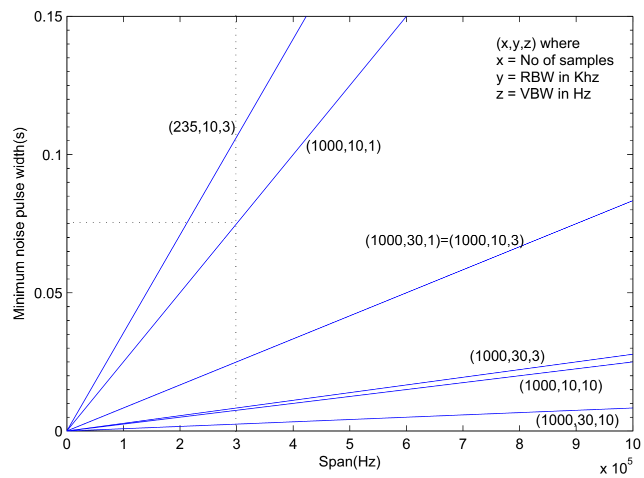

Figure 4.2: Minimum noise pulse width T_{min} as a function of span .The fixed parameters are resolution bandwidth(RBW), video bandwidth(VBW) and number of samples N.

datapoints to be displayed on screen each element corresponds to a point over 1Mhz span. Sample detection algorithm would obtain the center point in this span. Eg: A 10.5Mhz sine signal would be properly displayed in the span of 10-11Mhz. If the mixing product does not happen to be at the center of the IF when the sample is taken it will not displayed. This issue does not matter in the case of noise.

If we can somehow use the all the data within a bucket in the averaging mode of the SA, instead of a single point we may be able to reduce the fluctuations in the spectrum. Instead each point in the bucket equals the input noise integrated over the effective noise bandwidth and is the same even for the case of $RBW > \Delta f$. In order to catch the noise modulations, we need to mindful of the following: 1)A large RBW allows faster modulation speeds but also raises the DANL of the SA which makes detection of subshot noise difficult. 2) Span also affects sweep time and if increasing RBW does not follow the noise modulations, span can be reduced as an alternative but we loose some accuracy which is not of great concern. 3)If we cannot follow the noise modulations by adjusting the above parameters, the SA produces an integrated spectrum of both shot and subshot spectras and in such cases we reduce the modulation speeds. Most our experiments are restricted to less than 50Hz due to this fact but if we use DSP processors instead we can perform several FFTs over a window and average the signal very fast which in turn will allow faster modulation speeds. Further work using Analog Devices DSP chip is in progress at Nanolab group at Rutgers, with time based decoding methods akin to the classical stochastic modulator in Appendix.B already implemented.

We rely on the analog low pass filter video bandwidth filter after the envelope detector stage which performs a realtime filtering(time moving average) of the fast moving amplitudes during the sweep. The VBW filter becomes active only when the cutoff of the filter is smaller than the RBW and the ST also increases inversely with the VBW. If we assume that the VBW filter is another Gaussian, the time taken to charge and discharge is the same as the RBW filter and is given $2t_{0.01} = 2.5/VBW$. This is now the same as Eq.(4.18) which allows us to obtain an expression for the sweep time as

$$ST = \frac{2.5 * SP}{RBW * VBW} \tag{4.21}$$

We have plotted T_{min} versus the only freely controllable parameter which is the span or the start and stop frequencies in Fig.(4.2). The RBW or VBW take fixed values and rise progressively in 1,3,10 factors. The case $VBW > RBW$ has not been shown as no experiments use this setting, but it has the lowest T_{min} possible for a certain RBW setting. The traces are instantly swept, but with no averaging we cannot distinguish the relative squeezing levels. Each of the lines are linear, and we see that for a certain decreasing the number of samples N or increasing the VBW causes T_{min} to become larger. As we decrease either RBW or VBW and increase SP, the ST increases which affects the number of cycles of noise modulation displayed on screen. For example, if at a sweep time of 10secs, four cycles were displayed, cutting it to 5 secs would halve the number of cycles on screen. Since as we mentioned that VBW and RBW are rather fixed parameters, the SP may be taken as the time base control quite similar to the oscilloscope.

Fig.(4.3a) shows the case of shot noise modulation. The experiment was performed by connecting a function generator to a tungsten filament lamp and feeding a square wave of amplitude 760mV with an offset of 7.3V. The lamp was modulated at a frequency of 100mHz. The lamp could be modulated to a maximum frequency of only 10Hz beyond which it would produce a constant intensity. As we showed in the previous chapter, irrespective

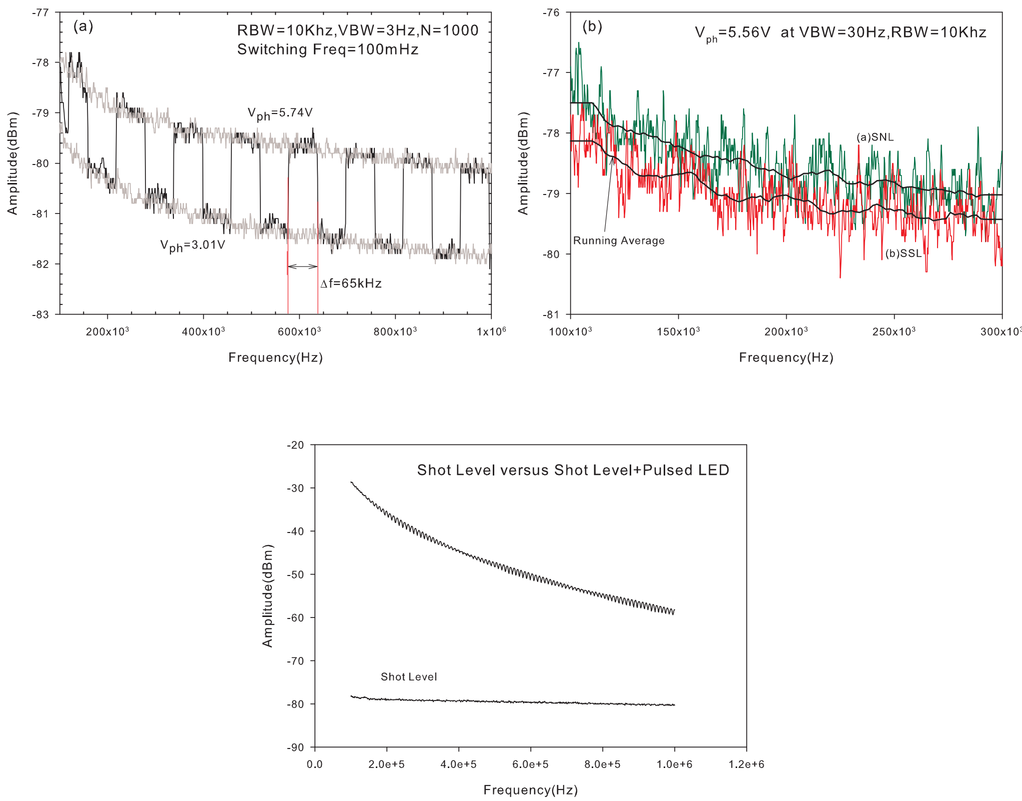

Figure 4.3: (a)Shot Noise Modulation experiment describing the time varying optical spectra $S_1(\omega, t) = F.S_n(\omega, t)$ where F=1 always (b)Shot and subshot spectra obtained with an $RBW = 10Khz$ but with low averaging of $VBW = 30Hz$. The solid dark lines indicate the negative exponential smoothing filter.

of having a noisy supply such as the function generator in this case, the light from the lamp is still shot noise limited. The dc photovoltages for the two shot noise levels were at 3.01V and 5.74V. We see in the figure that the shot noise levels during modulation agree with the calibrated shot noise levels over the entire frequency range of 100kHz-1Mhz. The square wave of 100mHz corresponds a pulse ON time of 5secs. Considering the following parameters used:span=900Khz ,the VBW=3Hz ,the RBW=10Khz,N=1000, we can find T_{min} from Fig.(4.2) to be 0.075secs which also implies that the maximum frequency of the square wave should be around 6Hz in order to see the modulation. Otherwise the signal would be averaged and a net noise would be displayed along the Fourier transform of the switching waveform and any transients. From the plot, we see that the duration the pulse is ON corresponds to a frequency interval of $\Delta f = 65Khz$. This corresponds to N1=72 sample points from which we can obtain the total ON time in the SA as $T_{min} * N1 = 0.075 * 72 = 5.4secs$ which is quite close to 5secs. In fact we have overestimated Δf which could be the source of error. Note that the difference between the two levels is around 1.7dB would allows us to clearly distinguish between the two levels as well as the pulse duration. When the difference becomes smaller(for example ¡1dB as was was seen in some squeezing experiments) both pulse width and resolution of levels become harder. We also point out this time varying spectra is an example of $S_1(\omega, t)$ of Eq.(4.3) where $F(\omega(I), t) = 1$. In Fig.(4.3b) we see a squeezing experiment carried under a higher VBW of 30Hz. With such low averaging, we cannot distinguish between the levels, and observing the switching becomes less reliable. This is typical in most communication systems where the the SNR is so small that the probability distributions between the two levels overlap causing false bit triggers. We have also shown the effects of smoothing filter applied to the raw data whereby we can ¿0.4dB of squeezing. So in order to carry reliable modulation experiments, VBW should be set to less than 10Hz. Changing the RBW did not seem to make much difference as it is the averaging in question. Reducing VBW as we have seen, increases sweep time and T_{min} and restricts the modulation frequencies. In Fig.(4.3c), we see the case where the signal is modulated at a large frequency wherein the spectrum analyzer produces a Fourier transform of the square pulse.

4.3 Design of Quantum Stochastic Modulator

Using the same methodology as the macroscopic(classical) communicator , we would like to switch between two quantum noise signals. The simplest way to do this is to switch between two sources: one calibrated at the quantum noise limit(shot noise level) and another at the sub-shot level. We can imagine focusing these two sources onto the detector and switching between them through a switch element which could be either a BJT or a FET device. The switch element in turn should not affect the statistics of the emitted light drastically(ie. it could easily raise the noise level above the SNL) and therefore we must know the noise properties of these devices beforehand. In the inset of Fig.(4.4) we show one such implementation idea. The data acquisition(DAQ) module from National instruments can serve as a function generator to provide ac modulation to the sources modulating the average. The two output lines of the DAQ, analog outputs(AO) 0 and 1 are connected to the LED and lamp respectively which are in turn focused onto the photodetector. The AO lines can both be calibrated such that the lamp and LED can both be set at the same photovoltage and we can switch between the AO lines selecting either the LED or the lamp for the noise modulation. There are three issues why this simple scheme did not work 1)The lamp draws current in excess of 300mA or a voltage of 2.5-3V. The DAQ card was able to produce voltage from 0-10V but not the amperage required. 2)In Fig.(4.4) we show the optical spectra of an L2656 LED driven the NI-DAQ card with a high impedance 10k. Even though such a resistance is sufficient to reduce the power supply noise in most cases, we see that at frequencies from 100-550kHz the noise levels exceed the SNL from the lamp by atleast 0.4dB and there are undesired harmonics. At frequencies above 600kHz squeezing disappears as is seen with the case of the the power supply driving the LED through the same resistance. These two issues itself make the DAQ card inappropriate for this experiment and we have to look for other design choices.3)Notice that the LED and lamp are to focused onto the same detector. Since the LED needs to be maintained in a face coupled configuration covering the detector, it would make it harder to focus the lamp for it to establish the same photovoltages as per the LED. This may be a simple mechanical constraint but we could not find a solution at the time.

We next tried using discrete electronic components directly driving a single LED.Even though we used many design choices(most of them by trial and error), we were restricted to a few that worked which will be described here. The central premise of subshot noise measurement is that the intensity fluctuations in the emitted light is a direct probe of the statistical fluctuations in the electron-hole recombination rate which in turn requires a high impedance suppression mechanism or pump noise suppression. Connecting a switch to the LED modifies the pump noise suppression mechanism and can be seen(or solved) in two ways:

1.By finding the spectral density of voltage or current fluctuations of the complete equivalent noise model which includes the switching element and the LED together and

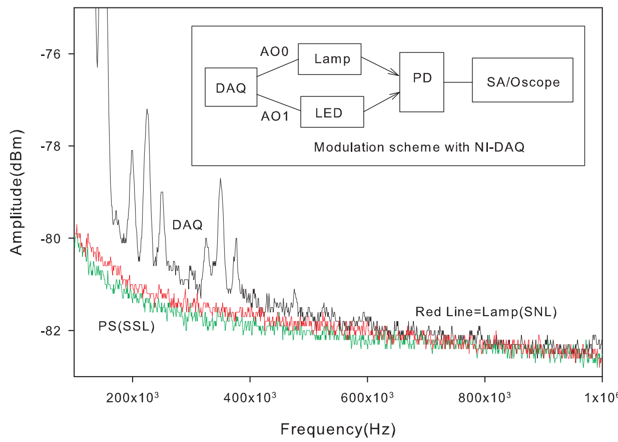

Figure 4.4: Comparison of optical spectra with LED driven with DAQ,shot and sub-shot noise sources.The inset shows a simple switching design using NI DAQ

2.Define an equivalent net impedance while looking back from the LED. If this impedance is greater than the differential resistance of the LED we will have satisfied the constraints of high impedance suppression. But this method(to us) is not theoretically sound, but has worked for most of the configurations used.

Note that the switch simply replaces the manual SPST switch which we used in the previous chapter and in order to design a successful modulator we have used the following prescription: a)Does the introduction of the switch allow us to generate a calibrated SSL and SNL level individually? If yes then b)Use this switch to construct a circuit, to modulate between these two sources c)Add the ac signal modulation as a separate channel taking care that it does not affect the statistics or adds switching noise. There are 3 methods of directly controlling the noise level using a single LED,all of which we have experimentally demonstrated in chapter 3:

1.Optical Switching: Controlling the efficiency is a simple way to switch between SNL and SSL, and can be carried out by using acousto-optic modulation(AO-cell) or by using OD filters with variable attenuation inserted in an optical chopper. An even simpler mechanical way is to mount the LED on a movable base, and by moving it close and further away we could control η_0. The main disadvantage with these methods is that efficiency is already very small in most experiments, and trying to calibrate the setup to produce SSL with additional optical elements in between the LED and PD would surely introduce partition noise and would produce SNL instead. At the present stage, it is not even possible to couple the light into a fiber unless we have much larger squeezing, and optoelectronic LED-PD-LED repeaters will have to be used over very small distances to recreate the quantum states.

2.Capacitive Switching: We had already established the difference between constant voltage and constant current. We then tried the configuration where the transistor was connected to the capacitor. By switching it on, the current would flow through the capacitor, forming the Constant voltage(CV) case which would raise it to the shot noise level. When the transistor was off, the high impedance formed would establish the Constant current case required for subshot operation.

3.Direct Modulation: In this method, a BJT or a MOSFET can be used to switch an LED between SNL and SSL cases. This method does away with some of the problems with capacitive switching such as slow modulation speeds, but we need to know the noise mechanisms of the switch itself which influences the photon noise of the LED. We shall now focus on capacitive switching and direct modulation schemes in greater detail.

4.3.1 Capacitive Switching

The capacitive switching principle is shown in the circuit diagram of Fig.(4.5a). The switch which could be a transistor or a MOSFET connects or disconnects the capacitor from the circuit. This in turn modulates the optical spectra between the shot level when the capacitor is inserted and the subshot levels when it is removed. At the same time, a signal source such as a function generator with an offset can be connected through R_S to the LED in order to perform the ac modulation. In order to establish shot noise levels, the capacitors should be quite large(around 1mF-10uF). But with the introduction of these large capacitors and the presence of $R = r_d + r_s$ (where r_s is the internal diode series resistance and r_d is the differential resistance) introduces a RC low pass filter into the problem and 3dB frequency is drastically reduced from the original modulation frequency.For example with a diode capacitance of $C = 100nF$, and R=5ohms, the 3db point is $f_c = \frac{1}{2\pi RC} = 318Khz$.

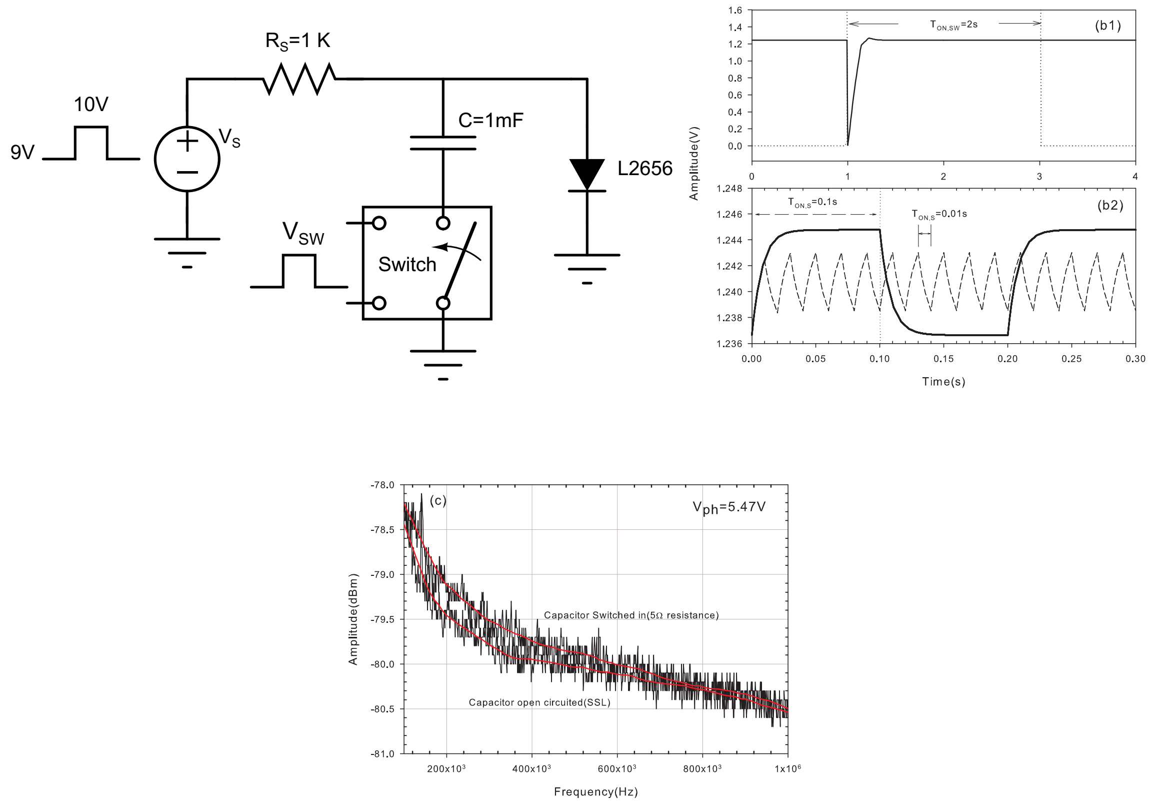

Figure 4.5: (a)Design of a capacitive switching circuit (b)Switching waveforms for MOSFET and AC switching (c)Optical spectra of true subshot noise compared with subshot spectra obtained by using a Capacitor with 5Ω in series

When we introduce a capacitor of 1mF parallel to the diode, the internal capacitance can be neglected and the 3dB cutoff frequency is now 31.8Hz. Note that the extrinsic time constant RC which determines the ac bandwidth is slightly different from the internal diode thermionic emission time constant R_dC or the recombination lifetime both of which determine the squeezing bandwidth. If the diode series resistance is negligible, then the ac modulation is governed by $r_d(C_{dep} + C_{diff}) \approx r_dC_{diff}$ which is approximately the radiative lifetime in moderate diffusion regime. The radiative lifetime predominantly depends on the doping levels and under these conditions both ac and noise modulation bandwidths may coincide. Let us now describe the switching processes taking place for a transient analysis perspective. Two square wave generators V_{SW} and V_S are applied to the switch and the LED independently with the assumption that the duration of the on time of the switch$T_{on,SW}$ is much larger than the time period of the square wave modulation to the LED. This establishes our requirement that the frequency of noise modulation is much smaller than the ac modulation.

Let us assume for the time being that V_S produces a steady dc voltage of 10V. When the switch is off, the voltage across the capacitor V_C is zero and the LED has a voltage $V_0 = 1.245V$ across it. When the switch is first turned on, a voltage across the capacitor has to be developed which can be written as $V_C(t) = V_{LED}(1 - e^{-t/RC})$. This effect is seen in the numerical simulation performed in Fig.(4.5b) where at time t=1secs when the switch is turned on, voltage across the LED is first pulled to zero followed by the exponential increase to V_{LED} again. When the switch is turned off at t=3secs, the voltage does not discharge but remains pinned to V_{LED}. In Fig.(4.5b),we show the case when V_S is modulated between 9 and 10volts when the switch is on. The voltage across the capacitor can be written as

$$V_C(t) = V_I + (V_F - V_I)(1 - e^{-t/RC}) \tag{4.22}$$

. where V_I is the voltage across the LED at time t=0 corresponding to $V_S = 9V$ and $V_F = V_0$ is the final voltage which corresponds to $V_S = 10$. We can easily test the validity of Eq.(4.22) with the numerical results. For the case of $T_{ON,S} = 0.1s$, we see that $V_F = 1.245V$ and $V_I = 1.236V$. At $t = \tau$, we can obtain $V_C(t) = 1.247s$. This corresponds to t=7.947ms. Now we can estimate the RC time constant as $\tau = RC = \frac{t}{\ln\left(\frac{1}{1-(V_C(t)-V_)/V_F-V_0)}\right)}$. Substituting the values with $C = 1mF$, we find R=8.16Ω. This agrees exactly with the sum of $r_s = 1.88\Omega$ and $r_d = 6.28\Omega$. We also point out that this method is very useful to experimentally determine the value of the series resistance, from the dc characteristics alone. As RC product decreases when the capacitor is removed, the rise time increases and the LED follows the square wave shape of the supply V_S. So as we alternate between shot and subshot modulation, we switch between two ac modulation bandwidths where only the slowest of signal frequencies are allowed to pass during the shot noise period of duration $T_{ON,SW}$. This also causes another issue which can be seen the dashed curves of Fig.(4.5b), where the faster modulation frequencies have smaller peak-peak swings since the capacitor is not allowed to fully charge and discharge.

Fig.(4.5c) shows the noise spectra for the L9337 LED with the upper plot indicating (a)capacitor in parallel with a small resistance in series and the lower plot indicating (b)When the switch is opened producing a subshot level. For the switching element,we first tried to use a Cadmium sulphide light dependent resistor since it has a large impedance when no light shines on it. Shining light on the LDR decreases the resistance but it was still large enough that high impedance pump suppression eliminated all signs of squeezing. We replaced the LDR with various resistors and found that even a 5ohm resistor produced subshot levels which we observe in Fig.(4.5c) to be quite close to the true subshot level obtained without the capacitor. Unless we could establish a nearly 0 resistance, it is very hard to produce shot noise levels using the capacitive method. Using a capacitor establishes an approximate constant voltage condition and since the L9337 is a heterojunction device based on the thermionic emission model, it is quite possible to observe squeezing under constant voltage conditions. If we measure the relative difference between the two smoothed curves, we find a result of 0.25dB at around 290kHz .Considering that the L9337 is capable of 1-1.5dB squeezing, this clearly shows that the upper plot is not at the true shot noise level. Most switches introduce some finite resistance, but we found the IRF510 to work well because of its low on resistance(approx 0.5ohms). The 2N2222 BJT and 4066 switch were also tried with small success since these elements introduced large resistances. Because of insufficient squeezing,slow ac modulations and sudden bandwidth changes between shot and subshot pulse durations, we were forced to look for an alternate design.

4.3.2 Direct Modulation with BJT

Switching mechanism of the transistor: The transistor is operated as a switch with the LED as a collector load. The low voltage $V_i \approx 0.7V$ is sufficient to cause the BJT to be in the cutoff region with a negligible base current according to the equation $i_B = \frac{V_i - V_{BE}}{R_B}$.The LED is off since collector current $i_c = 0$.For an input voltage $V_i > 0.7V$ it is sufficient to place the BJT in linear active or saturation region where $i_c \leq \beta i_b$. As the BE junction is forward biased the collector current can be obtained using KVL around CE circuit as $i_c = \frac{V_{CC} - V_{LED} - V_{CE}}{R_C}$. Hence we can operate the BJT in the cutoff region for $V_i < V_{BE}$

and linear active region $V_{BE} < V_i < V_{BE} + R_B \frac{V_{CC}-V_{LED}-V_{CE,sat}}{\beta R_C}$ and saturation regions according to $V_i \geq V_{BE} + R_B \frac{V_{CC}-V_{LED}-V_{CE,sat}}{\beta R_C}$ where in the saturation region we have $V_{CE,sat} \approx \frac{V_{BE}}{2}$. Another option is to use the LED as an emitter load. The goal is not to simply turn the LED on and off but to switch between the two quantum states ie. SNL and SSL. In order to do so, the collector or emitter current shot noise should be suppressed and should be able to assume a range of drive Fanofactors from 0 to 1. Another issue we wish to sidestep is the modulation aspects of noise in BJTs. This is within the realm of small signal large signal (SSLS) analysis and is still an open topic of research. As before we assume that the signal period is sufficiently long that noise characteristics during the transient periods such as on time,off time and storage time are unimportant.

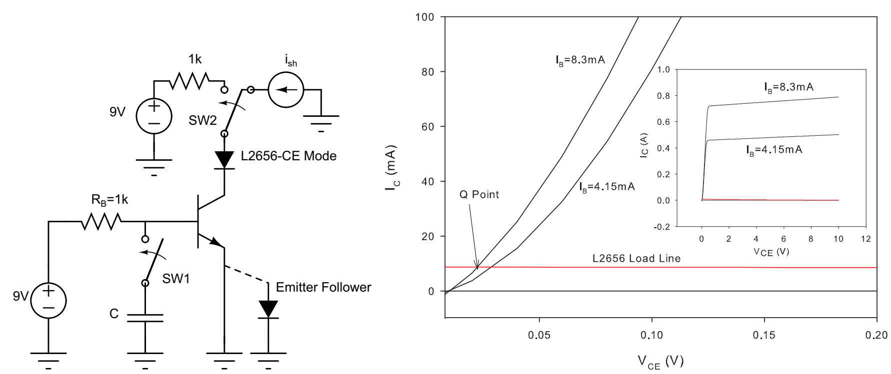

Figure 4.6: (a)Circuit Diagrams for transistor in open circuit base/closed base setups in CE and CC configurations (b)Load line of L2656 with numerical $I_c - V_{ce}$ characteristics of the 2N2222 transistor

$$S_{I_E}(\omega) = 4qI_E(\frac{G_E(\omega)}{G_E(0)} - 1/2) \approx 2qI_E \ , \ S_{I_C}(\omega) = 2qI_C \tag{4.23}$$

where $G_E(\omega)$ is the conductance of the emitter base junction and at low frequencies, $G_E \approx G_E(0)$ which leads to the forward biased emitter current showing full shot noise whereas the reverse biased collector current features full shot noise at all frequencies. The correlation between the emitter and collector terminal fluctuations Γ_{CE} can be obtained from the cross-correlation spectral densities S_{CE}[16] as

$$S_{CE}(\omega) = -2qI_C \frac{\alpha_S G_E}{\alpha_{0S} G_{E0}} \tag{4.24}$$

$$\Gamma_{CE} = \frac{S_{CE}(\omega)}{[S_{I_C}(\omega) S_{I_E}(\omega)]^{1/2}} \approx -\sqrt{\alpha_0} \tag{4.25}$$

In most modern transistors(at least in the linear active region) the common-base current gain $\alpha_0 \rightarrow 1$ over much of the frequency range. This implies that the collector and emitter current fluctuations are negatively correlated ie. An electron increase in the collector current is due to an electron decrease in the emitter current. In fact the base can be modeled as a linear beam splitter and we shall do so in the following analysis. From Eq.(4.23) it would seem reasonable that the small signal equivalent noise model of the BJT should include two current noise generators i_{esn} from the emitter to base and i_{csn} from collector to base. Notice that even though the collector features full shot noise at all frequencies, i_{csn} is correlated with the emitter current and so it should not be included. But when $\alpha_0 \rightarrow 0$ as $\beta \rightarrow 0$ the transistor is placed in deep saturation but Eq.(4.23) is still valid. It would seem then the collector current noise generator i_{csn} would have to be included. Also in order to prevent clipping and distortion when the BJT is used as an amplifier, the small signal models(eg. the hybrid-π model) are themselves only valid in the linear active region[75] or more precisely the linear region between cutoff and saturation in the voltage transfer characteristics.We shall revisit these issues later but first let us obtain the Fanofactors of the collector current in the linear active region.

FanoFactors for the hybrid-π,Van-Der Ziel T model and the Grey-Meyer model

We would like to obtain the output noise current fluctuations or the Fanofactor of the common emitter configurations (as the common collector or common base configurations can be obtained from simple rearranging of the CE circuit model). Typically this is done by using the superposition theorem by finding the square of the output noise current due to each noise source present in the small signal equivalent model and adding them up. The goal in this section is to show the hybrid-π model of Fig.(4.7a) which includes a hypothetical collector shot noise current always(not shown in figure) and the amplification of the base terminal shot noise is flawed in analyzing the output noise current and it is infact the T model of Van-derZiel in Fig.(4.7b) which includes a fraction of the base-emitter shot noise and an additive partition noise component which is valid. In fact the above assertion has already been claimed and proved experimentally by Edwards[1] by advocating the T model, but we shall do the same theoretically. Before we start. let us state some assumptions: Since we are interested in lifetimes smaller than the transit time across the base as well as thermionic emission lifetime(ie. the base emitter junction follows the same junction dynamics of the pn diode) we ignore the parameters associated with the base width modulation effect C_μ and feedback resistance r_μ on the basis that they appear in high frequency models. Losing these feedback elements limits the application of the equivalent circuit to frequencies less than $f_\beta = \frac{f_T}{\sqrt{\beta}}$ where f_β is the frequency at which the magnitude of the frequency dependent gain $|\beta(j\omega)|$ reduces by 3dB from its dc value and f_T is the transition frequency where $|\beta(j\omega)| = 1$and is a measure of the maximum useful frequency for the transistor to be used as an amplifier. The output resistance $r_0 = \frac{V_A}{I_C}$ for an Early Voltage of around 100V and collector current of 1mA is is quite large at $100k\Omega$ and so its effect can also be neglected in calculating the output voltage spectral density when the load resistance is smaller. We can also neglect its effect when obtaining the collector current which changes with v_{ce} as follows $i_c = \beta I_b + \frac{v_{CE}}{r_0} \approx \beta i_b$. These assumptions are incorporated into the hybrid-π and the T-models in Fig.(4.7). First let us compare the output noise currents of the two models and the junction voltage fluctuation obtained for the π model using nodal analysis at the node B' is

$$v_{jn} = \frac{i_{bsn} - i_{th}}{\frac{1}{r_\pi} + \frac{1}{R_S + r_b} + sC_\pi} \tag{4.26}$$

where i_{th} is the thermal noise current flowing into the base, r_b is the ohmic resistance of the lightly doped base region between the external base contact and the active base region,R_s is the source resistance(not shown in Fig.(4.7a)) but can be accommodated in r_b as an overall resistance looking backwards from the base terminal) , i_{bsn} is the base shot noise current and r_π is the base emitter dynamic resistance and $C_\pi = C_b + C_{je}$ is the sum of the base charging capacitance and emitter-base depletion layer capacitance. Applying high impedance pump suppression ie. $R_s + r_b \gg r_d$, the emitter is short circuited and the base is open circuited which leads to $i_{th} \to 0$. This leads to

$$v_{jn} = \frac{i_{bsn}}{\frac{1}{r_\pi} + sC_\pi} = \frac{i_{bsn} r_\pi}{1 + sC_\pi r_\pi} \tag{4.27}$$

The noise current flowing across the dynamic resistance r_π is obtained by first converting the Norton equivalent of $i_{bsn} - r_\pi$ to the Thevenin equivalent $v_{bsn} - r_\pi$ and then obtaining the noise current that flows through r_π.

$$i_b = \frac{v_{bsn} - v_{jn}}{r_\pi} = \frac{i_{bsn} sC_\pi r_\pi}{1 + sC_\pi r_\pi} \tag{4.28}$$

If we make the following $\pi$to T model transformation $r_\pi = (\beta + 1) r_e$ and $1 - \alpha = \frac{1}{1+\beta}$ the collector current obtained is

$$i_c = \beta i_b = \frac{\beta i_{bsn} sC_\pi r_e}{(1 - \alpha) + sC_\pi r_e} \tag{4.29}$$

The output noise current obtained using the π-model when compared with Van Der-Ziel T noise model under the same open base-grounded emitter configuration(which will be determined later) as far as the collector shot noise is concerned(ie. partition noise is neglected for the time) is given by

$$i_c = \alpha i_e = \frac{\alpha i_{esn} sC_\pi r_e}{(1 - \alpha) + sC_\pi r_e} \tag{4.30}$$

The above expression is also known as open base-shorted emitter configuration as the base terminal has a high impedance in series with it and the emitter is grounded. In order for the Eqs.(4.29 and 4.30) to yield the same result we require$\alpha i_{esn} = \beta i_{bsn}$ or rather by squaring both sides it shows that the two models are equivalent only we have the following equality $\alpha = \beta$ which is clearly incorrect. This shows that the hybrid-π model and the T model are not equivalent to each other unless the we doubt transformation of $r_\pi = \frac{kT}{qI_B}$ to $r_e = \frac{kT}{qI_E}$ or we redefine the base shot noise current as $i_{bsn} \to \frac{1}{\sqrt{1+\beta}} i_{bsn}$. Finally we would like to state the Grey and Meyer (GM) result[75] where the collector terminal is always set at the full shot noise level and the base current noise is calculated incorrectly as

$$i_b = \frac{Z R_S}{Z + R_S} i_{bsn} \approx \frac{i_{bsn} r_\pi}{1 + sC_\pi r_\pi} \tag{4.31}$$

where $Z = r_\pi // \frac{1}{sC_\pi}$.The above expression employs the same hybrid-π model of Fig.(4.7a) in order to obtain the result, but it deviates from Eq.(4.28) which we obtained using nodal analysis. This is because the base-emitter shot noise was not associated only with the differential resistance but with the net impedance Z. This model in addition includes a full shot noise current at the collector terminal and hence the total noise as predicted by the GM model is given as

$$i_c = \frac{\beta i_{bsn}}{1 + sC_\pi r_\pi} + i_{csn} \tag{4.32}$$

The GM model suggests that the collector current noise must be at least equal to the full shot noise whereas the hybrid-π and the T model indicate otherwise. Also the hybrid-π model and T model show that the collector shot noise can be suppressed under high impedance conditions and tend to the full shot noise level at large frequencies for the T model and approximately β times the full shot noise for the hybrid-π model. In order to choose the correct model, it must hold up to the scrutiny of current noise under constant voltage conditions. Most textbooks indicate[75] that the base current noise in the hybrid-π model consists of charges crossing from the base to emitter(I_{E_n}), a recombination current in the base(I_{rec}) and charges crossing from base to collector(I_{C_n}) and is known as the macroscopic description of base shot noise which claims that all these elements are individual random processes leading to a sum shot noise process which is $2q(I_{E_n} + I_{rec} + I_{C_n})$. The exact microscopic formulation however is quite different and shows us that the two processes, generation-recombination and diffusion noise in the base leads to shot noise in both the emitter and collector terminals according to Eq.(4.23) and the base terminal noise must be composed of those elements . Taking the Fourier transform of the terminal base current $I_B = I_E - I_C$ and finding its spectral density $< I_B^*(\omega) I_B(\omega) >= S_{I_B}$ by using Eq.(4.23) and Eq.(4.24) we have

$$S_{I_B} = S_{I_e} + S_{I_C} + 2Re(S_{CE}(\omega)) = 2qI_C(\frac{1}{\beta} + \frac{2G_E - (\alpha_s Y_E + \alpha_s^* Y_E^*)}{\alpha_{0s} G_{E0}} - 2\frac{(1-\alpha_{0s})}{\alpha_{0s}}) \tag{4.33}$$

At low frequencies the base current spectral density is approximately $2qI_C/\beta$. These expressions are valid only under constant voltage conditions ie. the junction voltage is pinned and the corresponding fluctuations in the minority carrier densities at the boundaries of the base are fixed(no noise) which is $p(0) = p(W_B) = 0$. So it would be reasonable that the πmodel should reproduce the results of Eq.(4.23) at the collector terminal and $2qI_B$ at the base terminal under constant voltage conditions for the model to be valid. The base-emitter circuit at low frequencies where the capacitor offers infinite impedance leads to the following base current (which can be extracted into the external base circuit)

$$< i_b^2 >= \frac{< v_{bsn}^2 > + < v_b^2 >}{(r_\pi + r_b)^2} \approx 2qI_B \tag{4.34}$$

The assumption made in Eq.(4.34) in arriving at $2qI_B$ is that r_b is quite small(which is not altogether true as it has values from 50-200Ω and is a function of current at high injection levels). If we proceed with this, the collector terminal should read $i_c^2 = \beta 2qI_C$ which is as we have stated earlier and violates Eq.(4.23) whereas the base terminal is correctly determined as per the constant voltage conditions. Next we check the T model and under constant voltage conditions. This can be seen from Fig.(4.7b) where the emitter and base are grounded. Assuming r_c, r_b are not present and at low frequency C_π offers a high impedance, the internal shot noise source $i_e = i_{esn}$ can be extracted into the external circuit validating Eq.(4.23). The collector current obtained neglecting the partition noise component since $\alpha \approx 1$ in linear active region leads to $i_c = \alpha i_e \approx i_{esn}$ validating the collector current noise spectral density of Eq.(4.23) . Thus the T model is the correct choice.

The following numerical plots are obtained using the parameters obtained from the 2N2222A datasheet[76] which was used to define the BJT model in Spice in order to obtain the small signal quantities for the linear-active and saturation regions using the modified Gummel-Poon model. From the $I_C - V_{BE}$ curve of the datasheet, we obtain $V_{BE} = 0.7V$ at $I_C = 20mA$ and choosing an ideality factor of $\eta = 1$, and using the formula $I_C = I_S[\exp(V_{BE}/\eta kT) - 1]$the saturation current is $I_S = .33fA$. The DC gain $\beta_{dc}(h_{FE}$ in the datasheet) is specified at 150mA to be from a minimum of 100 to a maximum of 300. We take the geometrical mean of 173. The gain is a widely fluctuating parameter even among various transistor samples.The emitter-base depletion capacitance is specified as $C_{je} = 25pF$ at a reverse bias of $V_{EB} = 0.5V$. The zero bias capacitance can be obtained simply using $C_{je0} = C_{je}(1 + \frac{V_{EB}}{\psi_{0E}})^{1/3}$ to be 30pF with a built in potential $\psi_{0E} = 0.75V$. Similarly the zero bias collector base capacitance is obtained to be $C_{\mu 0} = 19.4pF$ using the data that $C_\mu = 8pF$ at $V_{CB} = 10V$ and $\psi_{0C} = 0.75V$. The output resistance r_0 at $V_{CE} = 10V$

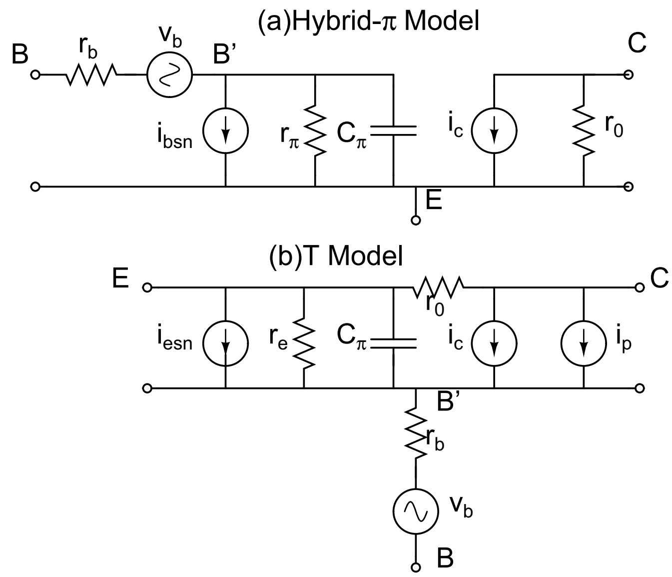

Figure 4.7: (a) Grey and Meyer hybrid-π Bipolar transistor model (b)Van-derZiel-Chenette T bipolar transistor model

and $I_C = 10m, A$ is $8.3 * 10^3\Omega$ which gives an early voltage of $V_A = r_0 I_C = 83.3V$. The most important parameter is perhaps the transit time across the base region which can be obtained from the transition frequency which is $f_T = 300Mhz$ or $\tau_T = 530.5ps$ at $I_C = 20mA$ and $V_{CE} = 20V$. The transition time is related to the base transit time τ_F as $\tau_T = \tau_F + \frac{1}{g_m}(C_{je} + C_\mu)$. We can find the corresponding $C_{je} = 25pF$ and $C_\mu = 6.5pF$ at $V_{EB} = 0.7V$ and $V_{CB} = 19.3V$ which in turn gives $\tau_F = 489.8ps$. The total capacitance is $C_\pi = C_{je} + C_b$ where $C_b = g_m \tau_F$ is the base charging capacitance.The reverse transit time is taken as approximately $\tau_R = 10\tau_F = 4.9ns$. The rest of the parameters which determine second order effects such as high injection current,base width modulation,contact resistances,etc use the conventional model parameters(from the library EVAL.LIB) present in SPICE.

T model with partition noise

Edwards[1] has claimed that both the base shot noise and the collector shot noise are unphysical quantities associated with and we have proven so in the previous section. Now we shall use the circuit diagram of Fig.(4.7b) which illustrates the Van Der Ziel-Chenette

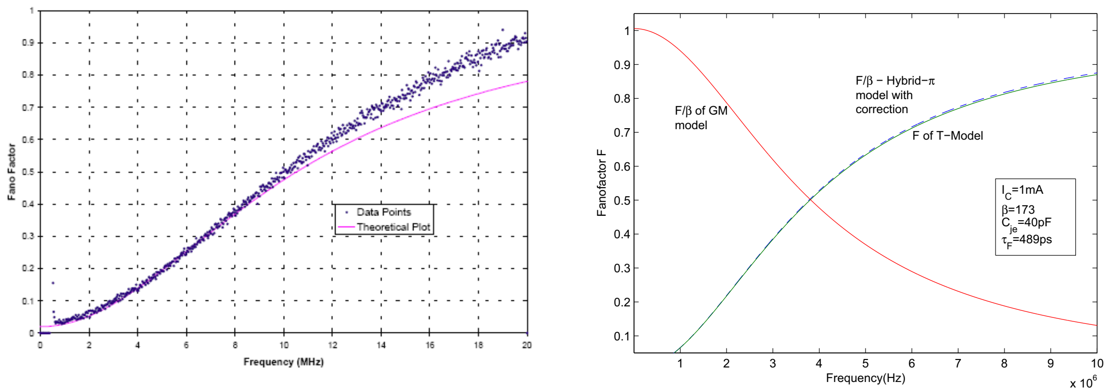

Figure 4.8: (a)Electrical Fanofactors of grounded base-open emitter Power BJT from [1](b)Comparison of Fanofactors for the hybrid-π, T and GM Models

model[77] obtained by adding an emf e_{esn} in series with the emitter or i_{esn} in parallel as we have done and a current generator i_p in parallel with the collector. The generator i_{esn} and i_p are generally correlated which can be shown to be a byproduct of the partition noise mechanism due to the $i_{esn} - i_c$ correlation of Eq.(4.24). The total collector current noise is $i_c^2 = \alpha^2 i_e^2 + i_p^2$.The partition noise current in the T model at low frequencies is written as**??**

$$i_p^2 = 2eI_E(\alpha_{dc}(1-\alpha_{dc}) + (\alpha_0 - \alpha_{dc})^2) \approx 2e(1-\alpha_{dc})I_C \tag{4.35}$$

where the last equality in Eq.(4.35) is due to the fact that $(\alpha_0 - \alpha_{dc}) \ll 1$ and can be neglected.Typically transistors have $\alpha_0, \alpha_{dc} \approx 1$ which removes this partition noise component. From Eq.(4.35) , the collector shot noise may be thought of as the output of a beam splitter with efficiency $\alpha \leq 1$ where the input is the emitter current and the partitioning process is the loss of carriers due to transit in the base We can informally arrive at expressions for $i_c$and i_p by using the Bernoulli selection process on a Poisson statistics[19] . The collector particle number variance is given as

$$\Delta m^2 = \alpha^2 \Delta n^2 + \alpha(1-\alpha)n \tag{4.36}$$

Here Δn^2 is the variance in particle number of the emitter current and n is the average. Multiplying by $e^2$and dividing by the observation time scaleΔt^2(not uncertainty) we obtain

$$\frac{e^2\Delta m^2}{\Delta t^2} \quad = \quad \alpha^2\frac{e^2\Delta n^2}{\Delta t^2} + \alpha(1-\alpha)\frac{e^2 n}{\Delta t^2}$$

$$2ei_cB \quad = \quad \alpha^2 2ei_eB + \alpha(1-\alpha)2ei_eB \tag{4.37}$$

Using the relations $\frac{en}{\Delta t} = i_e$ and the fact that the collector and emitter are shot noise limited currents ie. $\Delta m^2 = m, \Delta n^2 = n$ and the observation time is the reciprocal of twice the bandwidth-B we have obtained Eq.(4.37) from which we can infer Eq. (4.35). Now we shall calculate the collector terminal Fanofactor for 3 possible configurations of the T model obtained by either opening or shorting the emitter and base terminals. When a terminal is left open, we place a high impedance(eg. a constant current supply) source in its place and when the terminal is shorted it implies a low impedance source such as a constant voltage supply.

1.Shorted emitter-Shorted base configuration: Grounding the base and emitter terminals,and writing KCL at node E for the T model of figure(neglecting r_0), we arrive at the junction voltage fluctuation as

$$v_{jn} \quad = \quad \frac{\alpha i_e + i_p + \frac{v_{esn}}{r_e} + \frac{v_{bn}}{r_b}}{(\frac{1}{r_e} + \frac{1}{r_b} + sC_e)} \tag{4.38}$$

The emitter current which flows through the dynamic emitter resistance r_e is obtained as

$$i_e = \frac{v_{jn} - v_{esn}}{r_e} = \frac{\alpha i_e + i_p + \frac{v_{bn}}{r_b} - i_{esn}(\frac{r_e}{r_b} + sC_e r_e)}{1 + \frac{r_e}{r_b} + sC_e r_e} \tag{4.39}$$

Note that the both sides of the equality have an i_e component. This is a feedback process that corrects the emitter fluctuations from the output collector fluctuations. Collecting terms the net emitter current is

$$i_e = \frac{i_p + \frac{v_{bn}}{r_b} - i_{esn}(\delta + j\gamma)}{(1-\alpha+\delta) + j\gamma} \tag{4.40}$$

where we have set $\delta = \frac{r_e}{r_b}$ and $\gamma = \omega C_e r_e$ for notational simplicity.The total collector current noise which is the sum of the shot noise component and the partition noise is expressed as

$$i_c = \alpha i_e + i_p = \frac{\alpha\frac{v_{bn}}{r_b} - \alpha i_{esn}(\delta + j\gamma)}{(1-\alpha+\delta) + j\gamma} + \frac{\alpha i_p}{(1-\alpha+\delta) + j\gamma} + i_p \tag{4.41}$$

The noise spectral density at the collector is calculated as $< i_c^2 > = < |i_c^* i_c| >$ and we see that the two noise sources v_{bn} and i_{esn} are uncorrelated and can be added in quadrature.

The partition noise component however $<|i_p^* i_p|>$ leads to a cross term of the form $2\alpha|(1-\alpha+\delta)+j\gamma|$ and the final equation can be written as

$$< i_c^2 >= \frac{\alpha^2 < i_{esn}^2 > (\delta^2+\gamma^2) + \alpha^2 \frac{v_{bn}^2}{r_b^2}}{(1-\alpha+\delta)^2+\gamma^2} + < i_p^2 > \frac{(\alpha+\sqrt{(1-\alpha+\delta)^2+\gamma^2})^2}{(1-\alpha+\delta)^2+\gamma^2} \tag{4.42}$$

At low frequencies, the collector current noise density is given as

$$< i_{cn}^2 >= \frac{\alpha^2 < i_{esn}^2 > \delta^2 + \alpha^2 \frac{v_{bn}^2}{r_b^2}}{(1-\alpha+\delta)^2} + \frac{(1-\alpha)(1+\delta)^2 < i_{csn} >^2}{(1-\alpha+\delta)^2+\gamma^2} \tag{4.43}$$

We see that as $\alpha \approx 1$, the low frequency collector current noise tends to the full shot noise. This is the same result as predicted by Buckingham's diffusion theory for noise as per Eq.(4.23) where the emitter base and the collector base are biased in the constant voltage regime. When $\alpha < 1$, then the noise current tends to be slightly larger than the shot noise level. As we move to higher frequencies, it once again approaches the SNL. Thermal noise due to the base resistance is very significant since there are no source resistances and associated thermal noise with the supplies.

2. Shorted Emitter-Open Base: The collector current noise density can be obtained by making the base resistance very large(open circuited), thus treating it as a high impedance constant current generator,in effect removing its thermal noise contribution(along with any resistances associated with the supply).Setting $r_b, \delta \rightarrow \infty$ in Eq.(4.43) gives us

$$< i_c^2 >= \frac{\alpha^2 < i_{esn}^2 > \gamma^2}{(1-\alpha)^2+\gamma^2} + < i_p^2 > \frac{(\alpha+\sqrt{(1-\alpha)^2+\gamma^2})^2}{(1-\alpha)^2+\gamma^2} \tag{4.44}$$

At low frequencies, as $\alpha \approx 1$ the partition noise component is zero and collector noise is at the full SNL of the emitter. This result is the same as expected and is independent of the type of bias(constant current or voltage). When $\alpha \neq 1$, the collector noise raises above the SNL and is given as$< i_c^2 >=< i_{csn}^2 > \frac{1}{1-\alpha} \approx \beta < i_{csn}^2 >$ie. the collector current noise is β times the full shot noise of the collector current . At higher frequencies, the first and second terms in equation reduce as $< i_c^2 > \approx \alpha < i_{csn}^2 > + (1-\alpha) < i_{csn}^2 >$ ie. it reverts back to the SNL as in case 1.

3.Open Emitter-Shorted/Open Base: In this case, the emitter noise current is zero according to the high impedance suppression scheme. Only the internal shot noise generator

i_{esn} supplies the loop current and as in the case of the pn diode, it cannot be measured at the output emitter terminal. Also the emitter noise current has a high-pass filter characteristic and is suppressed below the shot noise at low frequencies according to

$$i_e = \frac{v_{esn}}{(r_e + \frac{1}{sC_e})} = \frac{i_{esn}\gamma}{1 + j\gamma} \tag{4.45}$$

As the frequency rises i_e tends towards the SNL since the diffusion capacitance C_e removes the negative feedback loop and the regulation mechanism is lost ie, the emitter current keeps up with the shot noise fluctuations which happens on very short observation timescales.

$$i_c = \alpha i_e + i_p \rightarrow < i_c^2 > = \frac{\alpha^2 < i_{esn}^2 > \gamma^2}{1 + \gamma^2} + (1 - \alpha) < i_{csn}^2 > \tag{4.46}$$

At low frequencies, the current noise spectral density which is primarily due to the partition noise component(as it is in the other two cases) is given by $< i_c^2 > = (1 - \alpha) < i_{csn}^2 > = \frac{1}{\beta} < i_{csn}^2 >$, ie. the partition noise component has been suppressed by β below the full shot noise collector current. This is the only case where we can expect a subshot behavior for the collector current. So if we need to switch an LED on and off with subshot drive current, the BJT has to be operated in the open emitter configuration. The small signal parameters in Table.(4.1) are used to calculate the Fanofactors by normalizing the collector current spectral density to the shot noise spectral density. In Fig.(4.9a) ,we have plotted the Fanofactors of the grounded base-grounded emitter configuration without the v_{bn}^2/r_b^2 term. This term by itself would raise the noise level and would dominate F, but if by reducing r_b (this parameter can only be changed during fabrication process) ,we can make it smaller than other elements of term-1 in Eq.(4.43). The effect of term-2 which represents the partition noise component is negligible here. Term1 by itself is subshot (approx F=0.9) at smaller frequencies but raises to the shot level at higher frequencies and the reason why the curves exhibit $F > 1$, is because of the partition term addition. For a fixed $I_B = 10\mu A$, and decreasing V_{CE} we see that F decreases. This is because as V_{CE} decreases I_C decreases causing α to decrease which reduces the amount of subshot noise transferred from emitter to collector. The partition noise component increases as $1-\alpha$ and for $V_{CE} = 1V$ it is larger than $V_{CE} = 10V$. The sum total of these components causes the Fanofactor for the $V_{CE} = 10V$ case to be larger than the $V_{CE} = 1V$ case. On the other hand,for $I_B = 1\mu A$, changing

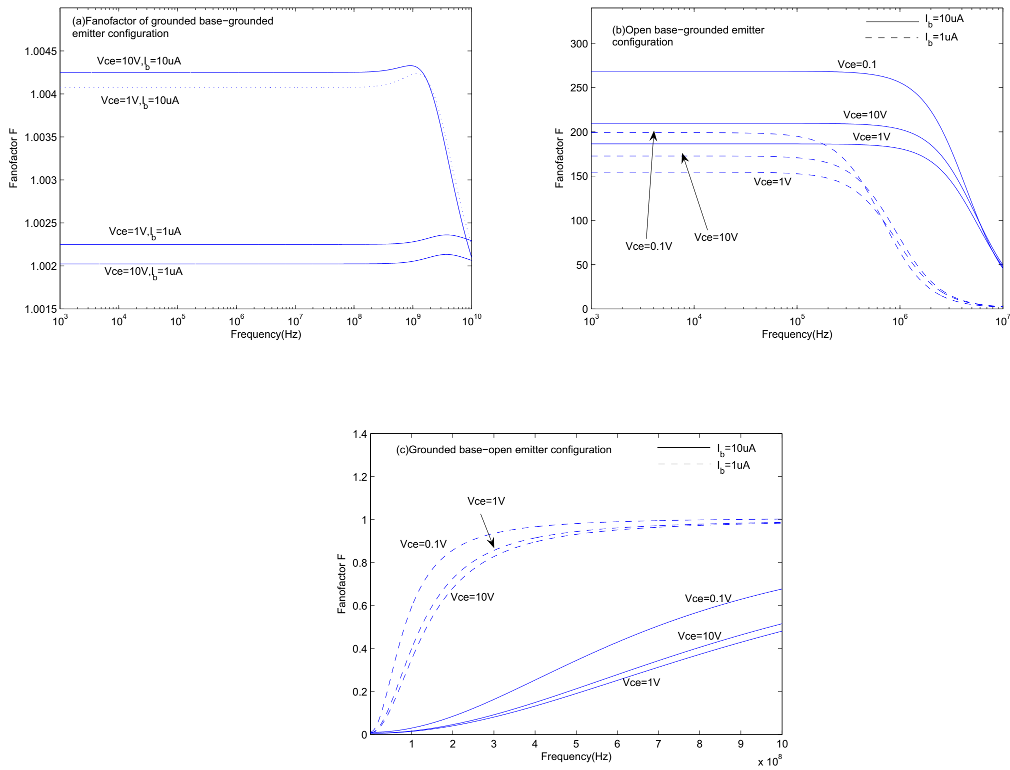

Figure 4.9: Numerical Fanofactors for the three cases of (a)grounded base-grounded emitter (b)open base-grounded emitter and (c)grounded base-open emitter configurations

V_{CE} from 10V to 0.1V increases F. Once again the partition noise term increases from 10V to 1V and the subshot term decreases but the increase in partition noise component is sufficient to raise F for $V_{CE} = 1V$ above that of $V_{CE} = 10V$. Note that by changing V_{CE},F changes by as small as 0.002 which is nearly impossible to experimentally verify and for all purposes, we can say that the collector current generates only the base thermal current with $F > 1$ at low frequencies and the shot noise current with F=1 at higher frequencies. Fig.(4.9b) plots the Fanofactors for the open base-grounded configuration. Here the emitter shot noise is completely suppressed at low frequencies and F is given by the partition noise component of term-2 in Eq.(4.44). If we assume that $(\alpha_{ac} - \alpha_{dc})^2$ is negligible then the partition noise is$< i_p^2 >\approx 2qI_E\alpha_{dc}(1 - \alpha_{dc})$. The Fanofactor at low frequencies can then be obtained as $F \approx \frac{1-\alpha_{dc}}{(1-\alpha_{ac})^2}$. By substituting the values of α_{ac}, α_{dc} from Table.(4.1) we see that F decreases from 209 to 186 and then increases to 268 as we reduce V_{CE} from 10V to

0.1V. In Fig.(4.9c) ,the Fanofactor is almost completely dependent on term-1 of Eq.(4.46) with the partition noise component negligible and at low frequencies $F \approx 0$ and at high frequencies it is $F \approx \frac{\alpha_{ac}^2}{\alpha_{dc}} \approx 1$.The method of biasing obtained by fixing the base current I_B and varying V_{CE} may appear strange particularly to the grounded emitter-grounded base configuration which is equivalent to saying that a constant voltage source applied to the base emitter junction. Spice does not make such distinctions and in fixing I_B we also fix V_{BE} and vice-versa, until we move into saturation. If we apply a constant voltage V_{BE} and decrease V_{CE} when the transistor is in saturation, the previously constant base current increases from its value in the linear active region. The small signal parameters are also completely valid in saturation and can be added straightforwardly to the T-model as we shall see in the next section.

$V_{CE}(V)$	I_B	β_{dc}	C_π	r_π	β_{ac}
10V	$10\mu A$	173	64.1pF	$2.85 * 10^3\Omega$	190
1	$10\mu A$	154	61.1pF	$2.85 * 10^3\Omega$	169
0.1	$10\mu A$	93.3	51.5pF	$4.38 * 10^3\Omega$	158
10	$1\mu A$	131	36.8pF	$2.97 * 10^4\Omega$	150
1	$1\mu A$	117	36.6pF	$2.97 * 10^4\Omega$	134
0.1	$1\mu A$	77.6	35.8pF	$4.12 * 10^4\Omega$	124

Table 4.1: Small Signal parameters used in the calculations of Fanofactors for the three configurations plotted in Fig:

Noise Model Under Saturation

If we are to switch a transistor between cutoff and saturation, we need to make sure that the above models are valid in the saturation region. We now see if the the T model can be used to predict noise in saturation.We neglect quasi-saturation region where when the collector current is high enough ,it forward biases the junction causing saturation to occur when it is supposedly linear active. We also neglect any base pushout effects where the collector epilayer is reclaimed as part of the base which causes affects the transition frequency. The analysis is ideal, ie we neglect the collector base and emitter base depletion region recombination noise and the currents are given by the Shockley diffusion model. The transistor is assumed to be $n^{++}p^{+}n$ which allows us to construct the emitter and collector current carried only by minority carrier electrons in the base region whose carrier profile is written as[10]

$$n(x) = n_{p0} + (n(0) - n_{p0})(\frac{\sinh(\frac{W-x}{L})}{\sinh\frac{W}{L}}) + (n(W) - n_{p0})\frac{\sinh\frac{x}{L}}{\sinh\frac{W}{L}}$$
$$= n(0) - (n(0) - n(W))(\frac{x'}{W}) \tag{4.47}$$

where the second equality uses the assumption that $W \ll L$.Using the same methodology as the junction diodes, the emitter current spectral density and collector current spectral density are each composed of two integrals one dealing with the diffusion component and the other with the generation recombination term each setting up relaxation current flows followed by a net charge imbalance over the entire base region.In the transistor the collector junction maintains the boundary condition but the majority carriers are supplied from the base contact to neutralize the potentials in the base region whereas in the diode the metal contact provided both these functions. The minority carrier fluctuations at the the x=0 and $x = W$ edges of the base(where W is the edge of the base-collector depletion region under zero bias) are written as[49]

$$S_{I_E} = \frac{4A}{D}\int_0^W n(x)|\frac{k_0k_2}{k_1+k_2}|^2 dx + \frac{2q^2A}{\tau_r}\int_0^W (n(x)+n_{p0})|\frac{k_0}{k_1+k_2}|^2 dx \tag{4.48}$$
$$S_{I_C} = \frac{4A}{D}\int_0^W n(x)|\frac{k_1k_W}{k_1+k_2}|^2 dx + \frac{2q^2A}{\tau_r}\int_0^W (n(x)+n_{p0})|\frac{k_W}{k_1+k_2}|^2 dx \tag{4.49}$$

where k_0, k_1, k_2, k_W are the same hyperbolic functions defined in chapter 2 and τ_n is the minority carrier lifetime. Under the low frequency condition $\omega\tau_n \ll 1$ which leads to $W \ll |L_n| \approx L_0$ (where L_n and L_0 are the ac and dc diffusion lengths) we have

$$\frac{k_0k_2}{k_1+k_2} = \frac{k_Wk_1}{k_1+k_2} \approx \frac{qD_n}{W} \tag{4.50}$$
$$\frac{k_0}{k_1+k_2} \approx 1 - \frac{x'}{W} \quad , \quad \frac{k_W}{k_1+k_2} \approx \frac{x'}{W} \tag{4.51}$$

Substituting in Eq.(4.50,4.51) and Eq.(4.47) in Eq.(4.48,4.49), we obtain

$$S_{I_E} = \frac{2q^2AD_n}{W}(n(0)+n(W)) + \frac{2q^2AW}{\tau_n}(\frac{n(0)}{4} + \frac{n(W)}{12}) \tag{4.52}$$
$$S_{I_C} = \frac{2q^2AD_n}{W}(n(0)+n(W)) + \frac{2q^2AW}{\tau_n}(\frac{n(0)}{12} + \frac{n(W)}{4}) \tag{4.53}$$

Setting $\tau_n = \frac{L_0^2}{D_n}$ and comparing the coefficients of each of the terms, we see that $2q^2AD_n\frac{W}{W^2} \gg 2q^2AD_n\frac{W}{L_)^2}$ and so we can neglect the second term in the above two equations. In modern gain transistors, the effect of recombination in the base is small, the emitter and collector fluctuations are primarily due to thermal fluctuations of minority carriers. The emitter diffusion current can be expressed as $I_E = I_{E_p} + I_{E_n} \approx I_{E_n}$ since the emitter is more heavily doped than the base and the current due to holes crossing from base to emitter I_{E_p} is negligible. The collector current is $I_C = I_{C_p} + I_{C_n}$ where in saturation where both the hole and electron currents are non-negligible. The base current is the sum of the recombination current(I_{rec}),hole current from base to emitter(I_{E_p}) and collector(I_{C_p}). These currents are obtained by solving the diffusion equation[10] using Eq.(4.47) as

$$I_E \approx I_{E_n} = \frac{qAD_n}{W}(n(0) - n(W)) \tag{4.54}$$

$$I_C = \frac{qAD_n}{W}(n(0) - n(W)) - \frac{qAD_{pC}p_{oC}}{L_{pC}}\exp(\frac{qV_{BC}}{kT} - 1) \tag{4.55}$$

$$I_B = \frac{qAW}{2\tau_n}(n(0) + n(W)) + \frac{qAD_{pE}p_{oE}}{L_{pE}}\exp(\frac{qV_{BE}}{kT} - 1) - \frac{qAD_{pC}p_{oC}}{L_{pC}}\exp(\frac{qV_{BC}}{kT} \tag{4.56}$$

where we see that the electron collector current(first term) of Eq.(4.55) evaluated from the diffusion equation at x=W is the same as the emitter current ie. $I_{C_n} = I_{E_n}$ implying negligible recombination.We can then define the transit time for a minority carrier across the base in saturation as

$$\tau_B = \frac{Q_B}{I_{C_n}} = \tau_{B0}\frac{n(0) + n(W)}{n(0) - n(W)} \tag{4.57}$$

where $\tau_{B0} = \frac{W^2}{2D_n}$ is the base transit time in the linear active region where W is the thickness of the base. Then the emitter and collector spectral density of Eq.(4.52) and Eq.(4.53) with the help of Eq.(4.57) becomes

$$S_{I_E} = S_{I_c} = 2qI_E\frac{n(0) + n(W)}{n(0) - n(W)} = 2qI_E\frac{\tau_B}{\tau_{B0}} \tag{4.58}$$

According to the above equation, we see that as we move deeper into saturation, the electron collector current decreases,and the shot noise increases or equivalently, the increase in shot noise is due to the minority carriers which take a long time to cross the base. Note that we have ignored noise at the bulk collector region which has to be included as move into saturation but is still small compared to the enhanced noise calculated in the base region at the x=0 and W planes. The above shot noise source is placed in parallel with the emitter admittance(which includes the resistance and diffusion capacitance) along with a circuit embedding procedure which includes the depletion region capacitance and parasitics.This is the same procedure followed for constructing the noise model of the diode.

Next we ask if the small signal parameters seen in the T-model are valid in 'light' saturation which would also determine the bandwidth dependence on subshot noise. Using Eq.(4.55) ,we can obtain the transconductance as

$$g_m = \frac{\partial I_C}{\partial V_{BE}} + \frac{\partial I_C}{\partial V_{BC}} = \frac{qI_C}{kT} \tag{4.59}$$

From the linear active to the saturation region, we see that g_m is proportional to the collector terminal current I_C.The small signal dynamic resistance of the BE junction in saturation does not take the form kT/qI_B and we can see this from Eq.(4.56) that

$$r_\pi = (\frac{\partial I_B}{\partial V_{BE}})^{-1} \approx \frac{kT}{q}((\frac{qAWn_{p0}}{2\tau_n} + \frac{qAD_{pE}p_{0E}}{L_{pE}})\exp(\frac{qV_{BE}}{kT}))^{-1} \tag{4.60}$$

From Eq.(4.60) we see that fixing V_{BE} also fixes r_π. As we move deeper into saturation by reducing V_{CE},the electron distribution $n(W)$ increases with increasing base-collector forward bias but n(0) remains constant because of fixed V_{BE}. This in turn increases I_B but r_π remains the same. We can however write $r_\pi = kT/qI_{BAct}$ where I_{BAct} is the current in the active region for a certain V_{BE}. Since I_{BAct} is always smaller than I_B, the actual $r_\pi > \frac{kT}{qI_B}$. We have verified g_m quantitatively through numerical simulations with minimal error but we can only qualitatively explain r_π since we don't know I_{BAct}.For example,the 2N2222 with the biasing values $I_B = 10\mu A, V_{CE} = 0.1V$ gave a current of $I_C = .933mA$ with $g_m = 3.61 * 10^{-2} mho$ and for the case of $I_B = 10\mu A, V_{CE} = 0.11V$, $I_C = 1.07mA$ and $g_m = 4.11 * 10^{-2} mho$. We see that both these cases agree with Eq.(4.59). r_π on the other hand varied for both these tests since V_{BE} varied as we changed V_{CE}.But with V_{BE} fixed at 0.645V and adjusting V_{CE} we found $r_\pi = 4.3 * 10^3 \Omega$ to be also fixed which validates Eq.(4.60). At a certain point, there would no collection of electrons by the collector causing the noise to be entirely due to the partition noise component.

As we saw in the beginning of this section,there are two biasing equations for the LED obtained by writing the KVL first at the BE and CE terminals and their parameters are important in determining the 3dB response of squeezing.

1. We can fix I_B to be a constant, by solving the BE KVL assuming the BE junction is on(0.7V). Next we can modify either R_C or V_{CC} which would in turn affect the load line causing the transistor to be placed in saturation or active regions which in turn determines both I_C and V_{CE} based on the intersection of the load line with the $I_C - V_{CE}$ characteristics . When $R_C = 0$, we are led to the absence of the loadline by keeping, the CE voltage constant which in turn fixes I_C . This is the condition under which the small signal gain β is defined. If we had a load, v_{CE} as well as i_C is allowed to fluctuate to any modulation in the base current i_B.

2.We keep V_{CE} constant, changing I_B by changing V_{BB} or R_B. This in turn changes I_C but keeping β relatively unchanged if it is in the linear active region. The above two cases can be studied in spice by using a current source at the input and voltage source at the output of the BJT and extracting their small signal parameters which can then be used to plot the three T model configurations.

The circuit of Fig.(4.6a) was designed to be switched from saturation to cutoff. The base-emitter circuit was setup to turn the transistor on, with a current of $\frac{9-0.75}{1k} = 8.25mA$.The collector current was set to be around 7.7mA by fixing a limiting resistor of 1k to the LED and adjusting the V_{CC}. This is also the drive current to the LED which leads to $V_{LED} \approx 1.2V$ and $V_{CE} \approx 0.1V$. We can see that this is well into saturation with $\beta_{dc} < 1$. Fig.(4.6b) plots the $I_C - V_{CE}$ characteristics from Spice which also validates these parameters by plotting the LED+R_C load-line onto these curves and finding the values at the Q-point.

Spectral Density Fluctuations in the LED

The above section obtained the collector current noise which is now the drive current for the LED which also determines F_{dr}. The LED can be connected as a load in the common emitter or collector mode. If $F_{dr} \approx 0$ then we know that the LED would generate subshot noise. To analyze this behavior we have to obtain the internal junction voltage fluctuation. If the noise voltage density is at the full shot noise level then the recombination current noise is below the shot noise level.

1.Common Emitter Configuration: The equivalent circuit of the diode is connected to the collector terminal and we use the following notations: i_{sn} is the internal diode shot noise generator, r_d is the diode dynamic resistance and C_d is the total capacitance. The junction voltage fluctuation at the collector terminal is

$$
\begin{aligned}
V_n(\omega)(sC_d + \frac{1}{r_d}) &= i_{sn} - i_c && (4.61)\\
S_{V_n}(\omega) &= \frac{2qI_C r_d^2 + < i_c^2 > r_d^2}{1 + \omega^2 C_d^2 r_d^2} && (4.62)
\end{aligned}
$$

The above expression is actually independent of any current limiting resistors R_S placed between the LED and the supply V_{CC}. This can be seen by superposition where the collector current source and the diode shot noise generator are opened and the thermal noise from R_S does not contribute to the junction voltage fluctuation. Note that the collector current source can be opened since it can be treated as an independent source in this problem. If the collector terminal noise is completely suppressed $< i_c^2 >= 0$, the voltage spectral density is shot noise limited at low frequencies. This of course implies that the photon flux noise is completely suppressed.The recombination current spectral density at low frequencies which is obtained by removing the capacitor C_d is given as

$$
i_{rec} = \frac{V_n - v_{sn}}{r_d} \rightarrow S_{I_{rec}} \approx < i_c^2 > \qquad (4.63)
$$

2.Emitter Follower Configuration: When we connect the LED to the emitter terminal the voltage applied across it is the difference between the voltage applied at the base minus the base-emitter voltage V_{BE}. Even if the collector current varies a small amount, V_{BE} is approximately constant which makes it a good constant voltage scheme. To obtain the spectral density we used the hybrid-π model to construct the nodal equations since it is simpler. But since we showed that the model is flawed in predicting the collector noise we make the following transformation $i_{bsn} \rightarrow \frac{i_{bsn}}{\sqrt{\beta}}$ as we stated earlier, which preserves the $T - \pi$ noise model transformations. Also the analysis is valid only in the active region, otherwise the partition noise component needs to be included and we have not found a way to incorporate it into the hybrid-π model yet. The junction voltage fluctuation at the E terminal is

$$V_n(\omega) = \frac{-i_{bsn} + i_{sn}}{(\frac{1}{r_d} + \frac{1}{r_\pi} + g_m + s(C_d + C_\pi))} \tag{4.64}$$

Since the emitter current flows through the LED, the diode parameters i_{sn} ,r_d and C_d should be dependent on it.The diode junction voltage spectral density is obtained as

$$S_{V_n}(\omega) = \frac{\frac{1}{\beta}2qI_B r_d^2 + 2qI_E r_d^2}{(1 + \frac{r_d}{r_\pi} + g_m r_d)^2 + (\omega(C_d + C_\pi)r_d)^2} \tag{4.65}$$

Since $I_B \ll I_E$,, the low frequency fluctuation is approximately $S_{V_n}(\omega)/r_d^2 = \frac{1}{4}2qI_E$ ie. it is a quarter of the full shot noise. Since the junction voltage fluctuations are slightly suppressed, we can expect a small degrees of squeezing and when the fluctuations are completely suppressed at high frequencies, we can expect full shot noise in the photon flux.

Analysis and Experiment

Since the collector current is approximately independent of base current in the saturation region with the LED load line which implies that the transistor is operating in the region of forced beta. Fig.(4.10a) shows a transistor connected in common emitter configuration. As derived in Eq.(4.63) , the LED photon noise is suppressed as it is shown below the shot noise from a calibrated lamp source. Fig.(4.10b) shows the case of an LED connected in an emitter follower configuration. It would seem that irrespective of when a constant current or constant voltage source is applied to the base-emitter terminals, the output is always shot noise limited. This is different from that of Eq.(4.65) which predicts a slight degree of suppression. It may be possible that the suppression cannot be determined with the present setup. However, we also noted in Eq.(4.58), that the transistor biased in deep saturation, the terminal noise currents increase by the base transit time which may be quite large. We should therefore expect supershot noise, which is clearly not observed. However, the linear active models seem to provide the correct answers, which is surprising. More experiments are needed to understand the transistor noise in deep saturation, which is why we chose MOSFETs as switching elements in our modulation experiments.

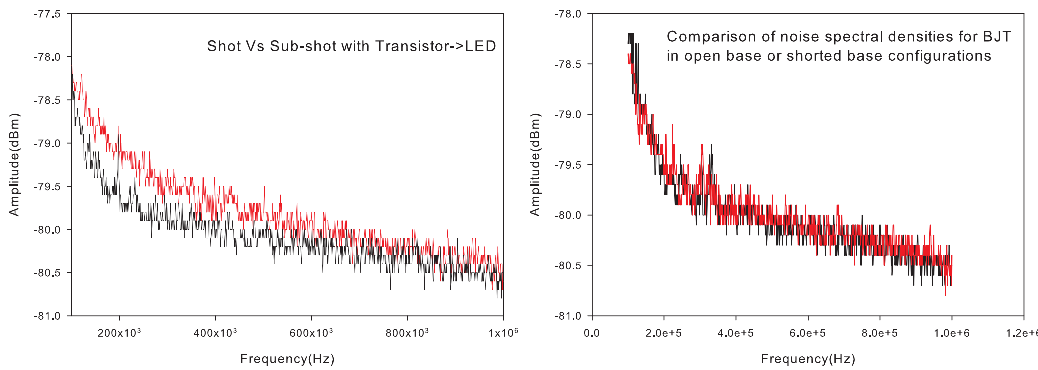

Figure 4.10: (a)Observed optical spectra for transistor in the CE deep saturation compared to shot noise obtained by driving with lamp. (b)Observed spectra for transistor with open/closed base in deep saturation

4.3.3 Direct Modulation with MOSFET

One of the main advantages of using the MOSFET instead of the BJT as a switch is due to the simplicity of the noise models involved. The MOSFET promises an ON resistance of less than an ohm, which when placed in series with a high impedance connected to the drain and a LED connected to the source should produce squeezing, ie. we can imagine the MOSFET as a non-linear resistor whose only effect is to introduce an additional negligible channel resistance which can be added without affecting the statistics of the emitted flux from the LED. We employ for our experiments, the IRF-510 and IRF-120 which are N-channel power MOSFETs. We quickly state the dc characteristics of the MOSFET. When it is in cutoff the gate to source voltage $V_{GS} < V_T$ where V_T is the threshold voltage. When $V_{GS} > V_T$, a thin inversion layer of electrons(conducting channel) is formed from source to drain in the p-type substrate. The current that flows from drain to source is still zero since we have to apply a voltage from drain to source V_{DS} which sets up an electric field causing electrons to move from source to drain. When V_{DS} increases and approaches $V_{DS} = V_{GS} - V_T$, then we may set $V_{DS} = V_{SAT}$ where the channel has been pinched on the drain side causing no further increase in current. When $V_{DS} > V_{SAT}$, the current increases very little and the pinch off region moves towards the left. There are two regions in the channel: one where the electrons are accelerated and one at pinch off where the electric field is so large that the velocity reaches saturation. The proposed circuit connection of the LED is shown in Fig .along with its output $I_D - V_{DS}$ characteristics. One thing we notice is that when the LED is driven with drain currents of even several hundred mA(which is more than it can handle) the V_{DS} is still in mV and transistor remains in the triode or non-linear region. The saturation voltage which are in volts(not shown), produce currents in amperes and so the associated equations and physics with saturation can be neglected. The drain current is given by the well known relation

$$I_D = \frac{k_p W}{2L}[2(V_{GS} - V_T)V_{DS} - V_{DS}^2] \quad \text{, where}\, V_{DS} < V_{SAT} \tag{4.66}$$

where $k_p = \mu_n C_{ox}$ is the transconductance parameter,μ_n is the electron surface mobility which is less than the mobility in the bulk due to surface states and C_{ox} is the oxide capacitance. There is a discrepancy between Eq with numerical results of Fig. For example,with an applied $V_{DS} = 2.9mV$, we can calculate a current of 25mA whereas the figure shows us only 5mA.This is because we have neglected the voltage drops across the drain and source ohmic resistances R_D and R_S. The true drain-source voltage can be obtained as$V_{DS} = I_D(R_D + R_S) - V_{D'S'}$ where $V_{D'S'}$ is the external drain-source voltage. The V_{DS} calculated with the correction is 0.5mV which when substituted in Eq leads to the current of 5mA in Fig. These dc corrections are also incorporated into the transconductance and channel conductance calculations.

Noise Analysis

To substantiate our initial claim, we first obtain a worst case estimate of the amount of the drain current noise by performing a nodal analysis on noise model of the MOSFET along with the equivalent circuit of the LED shown in Fig.(4.11a). Important small signal parameters are the channel conductance

$$g_{ds} = \frac{\partial I_D}{\partial V_{DS}}|_{V_{GS}} = \frac{k_p W}{L}(V_{GS} - V_T - V_{DS}) \tag{4.67}$$

and the transconductance which is defined as

$$g_m = \frac{\partial I_D}{\partial V_{GS}}|_{V_{DS}} = \frac{k_p W}{L} V_{DS} \tag{4.68}$$

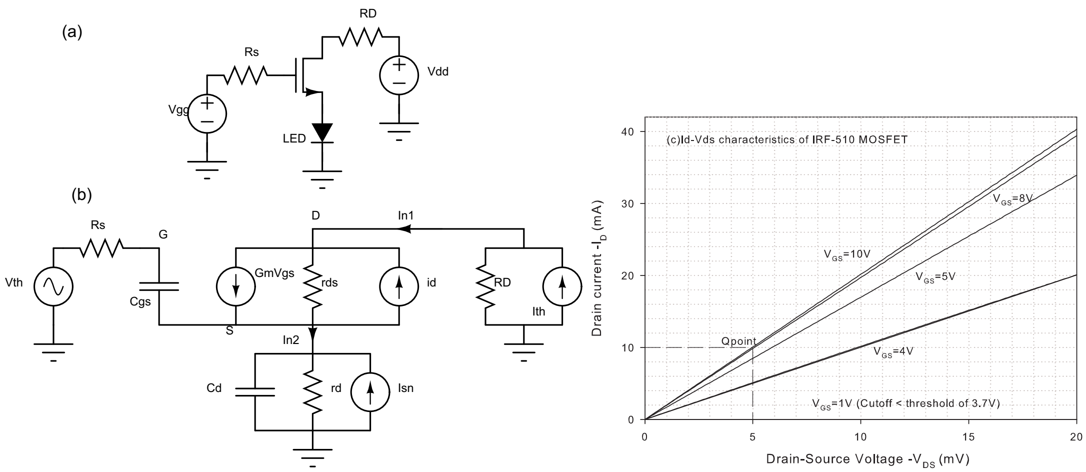

Figure 4.11: (a)Small signal noise model and large signal model of MOSFET (b)$I_D - V_{DS}$ characteristics of MOSFET in ohmic or triode region

Fig.(4.11a-b) shows the small signal equivalent of the dc circuit of Fig.(4.11a-a) . The small signal model has the following noise elements : i_{th}which is the thermal noise associated with R_D, i_d is the drain current noise which is the sum of flicker and resistive channel components, i_{sn} is the internal shot noise of the LED and v_{th} is the thermal noise of the source resistor R_S. r_{ds} is the channel resistance which can be obtained from Eq.(4.67) as $r_{ds} = \frac{1}{g_{ds}}$. The current generator $g_m v_{gs}$ can be obtained by impressing a small signal voltage v_i on V_{GS} in Eq.(4.67) and removing the dc component. The resultant ac current is $i_d = \frac{kW}{L} v_i V_{DS} = g_m v_i$ where g_m has been obtained in Eq.4.68). In the BJT case, we first obtained the collector Fanofactors followed by junction 'voltage' spectral fluctuations of the LED. For the MOSFET, we derive the drain terminal 'current' fluctuations from i_{n1} seen in Fig.(4.11a). Unlike the BJT where we had two back to back junctions which included partition noise mechanisms and the requisite inclusion of the feedback resistance r_μ in saturation, here we have here only a resistive channel r_{ds}. We make the assumptions to keep the problem tractable:

1. The gate to drain capacitance can be neglected since it is only relevant at high frequencies.

2.We even drop C_{gs} since we are interested in low frequencies where the input impedance is approximately large. The thermal current from v_{th} flows through through C_{gs} at higher frequencies contributing to the current i_{n2} at the source terminal but it is such a small component if R_S is quite large. Also at low frequencies, the inclusion of the resistor R_S causes a portion of v_{th} to be dropped across v_{gs}(which can be obtained by performing a KVL as $v_{th} = v_{gs} + v_b$ where v_b is the voltage fluctuation at the LED) but this step is not altogether necessary as we can make the resistance value low in order to eliminate its thermal noise effect, but of course the thermal current noise contribution to i_{n2} increases. Finally, we can neglect calculating the noise at the input v_{gs} from v_{th} since its amplified component $g_m v_{gs}$ is quite small. For example, from Fig.(4.11b) we see for a drain current of 2mA, $V_{DS} \approx 1mV$ which leads to $g_m = 64 * 10^{-5} A./V$.

3.We keep the junction+diffusion capacitance of the the LED C_d intact at low frequencies, since the internal regulation mechanism depends on its presence.

4.The gate leakage current is usually very small and can be neglected. For example typical value of .1pA would lead to a shot noise of $0.18 fA/\sqrt{Hz}$ whereas a 1mA drain current would lead to a LED shot noise of.

5.The drain ohmic resistance of around 20mΩ can be absorbed into R_D whereas the source ohmic resistance R_S which is 0.45Ω has been neglected in the small signal model. However they are important elements used in the calculation of g_m and r_{ds}.

Let us define the voltage at drain terminal as v_a and that at the source terminal as v_b. Writing the KCL at the corresponding nodes we obtain

$$\text{Node D: } v_a\left(\frac{1}{R_D} + \frac{1}{r_{ds}}\right) - \frac{v_b}{r_{ds}} = (i_{th} + i_d - g_m v_{gs}) \tag{4.69}$$

$$\text{Node S: } \frac{v_a}{r_{ds}} - v_b\left(\frac{1}{r_{ds}} + \frac{1}{Z}\right) = -i_{sn} - g_m v_{gs} \tag{4.70}$$

where $Z = r_d // \frac{1}{sC_d} = \frac{r_d}{1+sC_d r_d}$.Solving the above two equations, we can obtain v_a as follows

$$v_a = \frac{i_{sn} - g_m v_{gs}\frac{r_{ds}}{Z} + (i_{th} + i_d)(1 + \frac{r_{ds}}{Z})}{(\frac{1}{R_D} + \frac{r_{ds}}{R_D Z} + \frac{1}{Z})} \tag{4.71}$$

The terminal current noise entering D is then computed as $i_{n1} = i_{th} - \frac{v_a}{R_D}$ which leads to

$$i_{n1} = \frac{i_{th}(\frac{R_D}{Z}) - i_{sn} + g_m v_{gs}\frac{r_{ds}}{Z} - i_d(1 + \frac{r_{ds}}{Z})}{1 + \frac{r_{ds}}{Z} + \frac{R_D}{Z}} \tag{4.72}$$

Since we assumed that negligible current from the gate flows into the source, the above i_{n1} is also equal to i_{n2} flowing into the LED terminal at node S. Since each of the noise sources are uncorrelated the spectral density can be obtained as

$$S_{i_{n1}} = \frac{\frac{4kT}{R_D}[(\frac{R_D}{r_d})^2 + \omega^2 C_d^2 R_D^2] + 2qI_D + S_{I_d}[(1+\frac{r_{ds}}{r_d})^2 + \omega^2 C_d^2 r_{ds}^2] + (g_m v_{gs})^2[(\frac{r_{ds}}{r_d})^2 + \omega^2 C_d^2 r_{ds}^2]}{(1+\frac{R_D}{r_d}+\frac{r_{ds}}{r_d})^2 + \omega^2(C_d R_D + C_d r_{ds})^2} \tag{4.73}$$

If we assume that the drain current spectra and the channel conductance as negligible ie.$S_{I_d} = r_{ds} = 0$, we obtain Eq.(2.87) which is the expression for the external current spectral density of an LED driven with a high impedance source. For the IRF-510 MOSFET, the measured on resistance is as low as 0.5Ω. The spectral density $S_{I_d}$is unknown at this point and we shall obtain a simple analytical expression for it using the methodology employed in [78]. The thermal fluctuations in the channel of the MOSFET can be expressed as

$$S_{I_{d1}} = 4kT\frac{\mu_n}{L^2}Q_N \tag{4.74}$$

where Q_N is the total inversion layer charge. This expression is valid when the carrier temperature is equal to the lattice temperature and temperature effects become important only when we deal with hot carriers. The drain current in strong inversion is due to the drift of carriers which is written as

$$I_D = WQ_I(y)v(y) \tag{4.75}$$

where$Q_I(y)$ is the induced electron charge in the channel per unit area and $v(y)$ is the position dependent carrier drift velocity given by

$$v(y) = \frac{\mu_n E(y)}{1+\frac{E(y)}{E_C}} \approx \mu_n E(y) \tag{4.76}$$

In Eq.(4.76) we have neglected short channel effects since in the triode region, the average electric field is V_{DS}/L . Since V_{DS} is small and L is large, the average field is much smaller than the critical field E_C which reduces the denominator to unity. The electric field can be obtained from Eq.(4.75) and Eq.(4.76) as

$$E = \frac{dV}{dy} = \frac{I_d}{WQ_I(y)\mu_n} \tag{4.77}$$

The total inversion layer charge can be obtained by integrating Q_I over the entire channel length

$$\begin{aligned} Q_N &= \int_0^L WQ_I(y)dy = \int_0^{V_{DS}} WQ_I(y)(\frac{dV}{dy})^{-1}dV \\ &= \frac{W^2\mu_n}{I_D}\int_0^{V_{DS}} Q_I(y)^2 dV \end{aligned} \quad (4.78)$$

The inversion layer charge at y can be expressed as[75]

$$Q_I(y) = C_{ox}[V_{GS} - V_T - V(y)] \quad (4.79)$$

where $V(y)$is the surface potential along the channel at a distance y from the source and is equal to V_{DS} at y=L. Substituting Eq.(4.79) in Eq.(4.78) and using the resultant expression in Eq.(4.74) gives us the following drain current spectral density

$$S_{I_{d1}} = \frac{4kTW^2\mu_n^2C_{ox}^2}{I_D L^2}[(V_{GS} - V_T)^2 V_{DS} - (V_{GS} - V_T)V_{DS}^2 + \frac{V_{DS}^3}{3}] \quad (4.80)$$

The above expression is valid only for long channel devices and is a simplification of analysis done in [78] which applies to a wider range of devices. The MOSFET also has 1/f noise which occurs due the trapping and detrapping of carriers in the gate oxide or the boundary between the Si and SiO_2 interface. This noise increases with the density of surface states and can be expressed as[49]

$$S_{I_f} = \frac{2\pi K_F I_D^{AF}}{\omega C_{ox} L^2} \quad (4.81)$$

where K_F is the flicker noise coefficient and AF is a constant usually taken as 1. The total drain spectral density is $S_{I_d} = S_{I_f} + S_{I_{d1}}$ which is then used in Eq.(4.73) to obtain the external circuit current density. The parameters used to obtain the numerical results are obtained from the LEVEL-3 Spice model are tabulated in Table.(4.2). In Fig.(4.12a) we have plotted the total spectral density of Eq.(4.73) for the case of varying drain current with a constant drain load resistance R_D and supply voltage V_{GS}. We have also plotted the contribution of each of the noise components to the total spectral density. For example,the term 2qI indicates the second term of Eq.(4.73) along with the frequency dependent factors in the numerator and denominator. Even though the $2qI_D$ 'term' is the smallest component,in reality, the shot noise $2qI_D$ itself is much larger than the thermal component ie. $2qI_D \rightarrow \frac{2kT}{R_d} \gg \frac{4kT}{R_S}$ for $R_D \gg R_d$. As the drain current decreases,almost all the contribution to $S_{I_{N1}}$ is from the drain current noise S_{I_d} and if we can make its effect smaller compared to the shot noise $2qI_D$, we may be able to produce subshot light. (ie. $\frac{2kT}{R_d} \gg S_{I_d}$). However this condition is not true as we see for the low current of 2mA, where the drain component is larger than even $4kT/R_D$ and is almost the total contribution to $S_{I_{N!1}}$. The drain noise is comparable to shot noise level in which case we may observe supershot behavior. When the drain current is increased, shot noise increases whereas the drain current noise decreases and becomes smaller compared it. In that case, the total noise is due to only the thermal component $4kT/R_D$ and we will observe suppression. It may be surprising that we are predicting the output flux from the external circuit current density but $S_{I_{N1}}$ also represents approximately the internal recombination current density,which can be shown by finding the junction voltage fluctuations at V_a and then the current as $i_{rec} = \frac{V_a - v_{sn}}{r_d}$. The low frequency approximation by removing C_d and by assuming $R_D \gg r_{ds}$ and $R_D \gg r_d$, gives us

$$S_{I_{rec}} = \frac{4kT}{R_D} + 2qI_D(\frac{r_d}{R_D})^2 + S_{I_d}\left(\frac{r_d + r_{ds}}{R_D}\right) \tag{4.82}$$

The first term of Eq.(4.82) is much larger than the second but the main problem is the third term and even under large R_D,S_{I_d} can be made large that the net term-3 equals shot noise. However if $R_D \rightarrow \infty$, we see that the recombination current is completely suppressed. In Fig.(4.12b), we show the effect of increasing R_D, keeping the gate source voltage constant at 8.8V as well as the drain current at 3mA. At $10k\Omega$, we see that the noise equals the thermal component only with shot and drain component much lower. As the resistance is decreased to $1k\Omega$, the total noise is still approximately thermal, but we see S_{I_d} term coming closer. Finally at $R_D = 1\Omega$, we establish the constant voltage case, where the thermal noise component is smaller than the shot noise component at lower frequencies as expected for a diode. However, the drain current noise component dominates over the other components and equals the total noise. Note that in all cases, the thermal noise is relatively flat at all frequencies, whereas the shot and drain current noise rolloff with the cutoff frequency of the diode. In Fig.(4.12a) ,at frequencies above 1Mhz,we see that the thermal noise is the total noise irrespective of biasing conditions because of this drain current noise rolls off .

Parameters	Values
Oxide thickness t_{ox}	100nm
Surface mobility μ_n	600cm$^2/V - s$
Transconductance parameter $k_p = \mu_n C_{ox}$	$20.68\mu A/V^2$
Channel dimensions-W/L	0.64/2μ=0.32*10ˆ6
Threshold voltage V_T	3.697V
Flicker noise coefficient K_F	3.6*10ˆ-30 Coulomb$^2/Vs$
1/f Drain current constantA_F	1

Table 4.2: MOSFET model parameters used in the calculation of the drain current noise and the external terminal noise of the LED.

In Fig.(4.12c), we show the case for the total noise for varying gate-source voltage V_{GS} , with the drain current held constant at 3mA and the load resistance at $R_D = 1k\Omega$. The thermal noise current is shown as reference. For increasing gate to source voltage, the drain noise S_{I_d} increases.This also causes the total noise which is completely dependent on it to increase. So to summarize, in order to expect subshot noise, we should work with large R_D, large drain currents and preferably small gate to source voltages. Since it is possible to produce subshot noise from LED with the MOSFET inserted, the next question would be if shot noise is possible. Looking back to Fig.(4.11a), we see that the current noise flowing into the drain I_{n1} can be replaced by a photodiode based shot noise generator where $I_{n1}^2 = 2qI$. This implies that shot noise current flows into the diode since $I_{n1} = I_{n2}$. The junction voltages fluctuations are suppressed and the recombination is at the shot noise level. In Fig.(4.12d) , we show the experimental results for the IRF120 MOSFET. The experiment was performed by first inserting the MOSFET in between the LED and the shot and subshot sources, and observing the corresponding traces. Next the MOSFET was removed and the traces were recorded. The optical spectra before and after insertion were compared to see if the MOSFET generated any additional noise. Our original experiment was performed with the IRF510 whose parameters we used in our analysis. But we observed a peaking effect ie. supershot noise for both shot and subshot spectra around 1Mhz with a width of about 1Mhz, and the spectra resumed its normal behavior for the rest of the frequencies. The analysis shown in Fig.(4.12a) indicates that the drain current is capable of producing supershot noise but it does not explain why the squeezing could be observed from 2Mhz onwards,since the

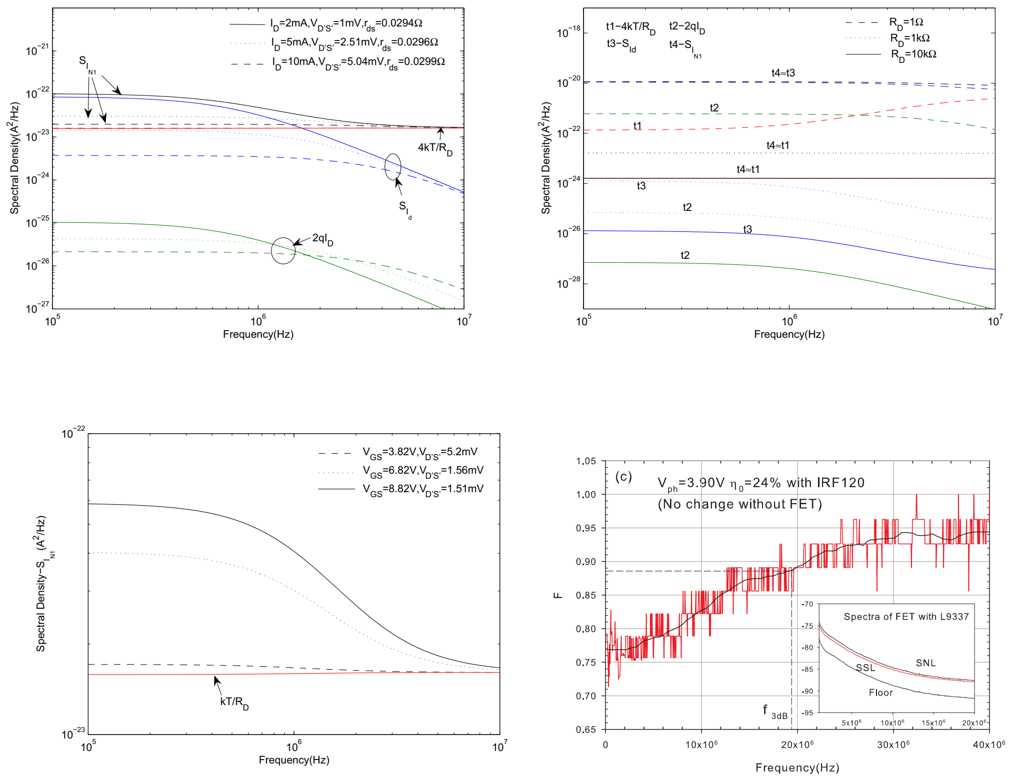

Figure 4.12: Numerical Fanofactors for the IRF511-MOSFET under (a)V_{GS} constant and $I_D - V_{DS}$ being varied (b)I_D and V_{GS} constant and R_D varied (c)$I_D - R_D$ constant andV_{GS} varied. (d) LED optical noise spectra using the IRF120 MOSFET

rolloff of the drain current density should be beyond the cutoff bandwidth of the L9337 at around 25Mhz. When we replaced the IRF510 with the IRF120 (which has on resistances as low as 0.25Ω) we observed both shot and subshot spectra agreed with the calibrated levels and we use this MOSFET hereon. The drive current to the LED is around 3.19mA which is powered by a supply of 9V through $2.45k\Omega$ resistor with gate voltages ranging from 5V-10V for this experiment. The inset of Fig.(4.12d) shows the optical spectra which agrees with the calibrated levels and the Fanofactor agrees approximately with the relation $1-\eta = 0.76$. The useful range beyond which we have negligible squeezing is 19.6Mhz. We have shown in chapter 3 that this LED is capable of larger bandwidths at higher drive currents.

Switching

Since we have now verified that the MOSFET does not affect the statistics of the emitter light when it is inserted into the circuit for both the shot and subshot sources, we can design a circuit that switches between the two sources. Much experimentation was done and we finally arrived at a design that worked which is shown in Fig.(4.13a). The basic principle is to connect one MOSFET to the shot noise source and one to the subshot source and switch between them alternately. The MOSFET M1 is connected to the photodiode which produces the shot noise of current 5.8mA at the source terminal S1 and the MOSFET M2 is connected through a high resistance R to a voltage of 7V at the drain terminal D2 to provide high impedance suppression and subshot noise. Note that the drain current in M1 flows from source to drain in an inverted fashion. Typically MOSFETs have an intrinsic diode due to its construction. In an enhancement type NMOS device, the p-channel and the n-drift layer combine to provide this diode. Reverse drain current cannot be blocked as the body is shorted to the source providing a high current path through the diode.The MOSFET symbol shows this diode connected from source to drain and can be seen in Fig.(4.13a). Finally source S1 of M1 is connected to drain D3 of M3 which is grounded. The NOR gate used here essentially performed the NOT function. Initially both M1 and M2 are off. During the first half period of the square wave, M1 is switched on, followed by shot noise to LED and in the second half-period M1 is turned off and M2 is turned on along with M3.

As we switch between the two MOSFETs, the currents should be held constant and ideally we can expect a near flat line. But in reality the switching process introduces transients and in some cases are quite large to cause the photodetector voltage to reach saturation. We have to remember that the spectrum analyzer is rated for +30dBm or 7V and transients on this scale can damage the front end stages of the SA. We show typical observations of the voltage at the output photodetector in Fig.(4.13b) for designs that were not satisfactory. In Fig.(4.13b), case (a) shows the existence of a spike only in between the subshot and shot pulses.In (b)we show the same except that the shot noise current has been increased and the levels are no longer equal and the duration of the spike has become longer.

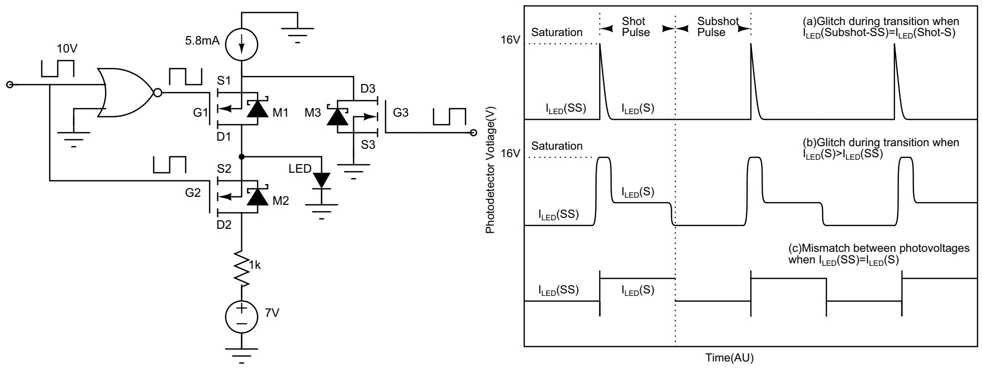

Figure 4.13: (a)Schematic for average and variance modulation using MOSFETs. M1,M2 and M3 represent the MOSFETs. The 7V battery with the 1k resistor represents the constant current source and the 5.8mA current source represents the shot noise from a photodiode. (b)Experimental Observations of the switching characteristics of the setup when switched between the shot and subshot pulses.

These experiments were observations of setup in Fig.(4.13a) without M3. It was reasoned that the shot 'current' source was primarily the problem and by replacing it with the ILX current source, we observed the same behavior. One possible explanation for the detector saturation was that when M1 was turned off, it caused a high impedance of nearly $4M\Omega$ to be developed. The photocurrent being blocked would end up flowing into the shot noise generator photodiode's own impedance effectively self-biasing itself causing a larger current to flow. When M1 is turned on, this current flows into the LED which in produced the 16V saturation voltage(at the time of performing this experiment) followed by the discharge with the time constant given by RC of the photodiode impedance and other resistances along the circuit. When the shot noise current was increased, there was the predictable change in levels, but note that the spike appears to be clipped and the duration time of the spike also increased.By adjusting the load resistor of the photodetector from $5.08k\Omega$ to 50ohms, and thus changing the gain, we could observe spike in its entirety. The increase in duration is due to the time taken to discharge from its maximum current value(which has increased from case-a) with the same discharge time constant as in case-a. Case-c shows us a situation where the photovoltage levels were offset by a certain amount even when the shot and subshot sources were calibrated to produce the same LED current. Increase in the shot noise current caused both the shot and subshot photovoltages to increase. This experiment was once again performed without M3 but with the terminals of M1 reversed. Adding M3 caused the glitches to disappear and using the circuit diagram of Fig.(4.13a) seemed to be the only possible option. The spikes due to the switching process themselves did not disappear and in such cases, the BJTs were better since they provided well rounded pulses. Since it is not a simple task to analytically study the working of Fig.(4.13a) we defer to a numerical simulation of the switching process which is shown in Fig.(4.14). The pulse voltage sources to the MOSFETs M1,M2,M3 had pulse widths of 5ms with rise and fall times of $200\mu s$. We now analyze the following 3 cases:

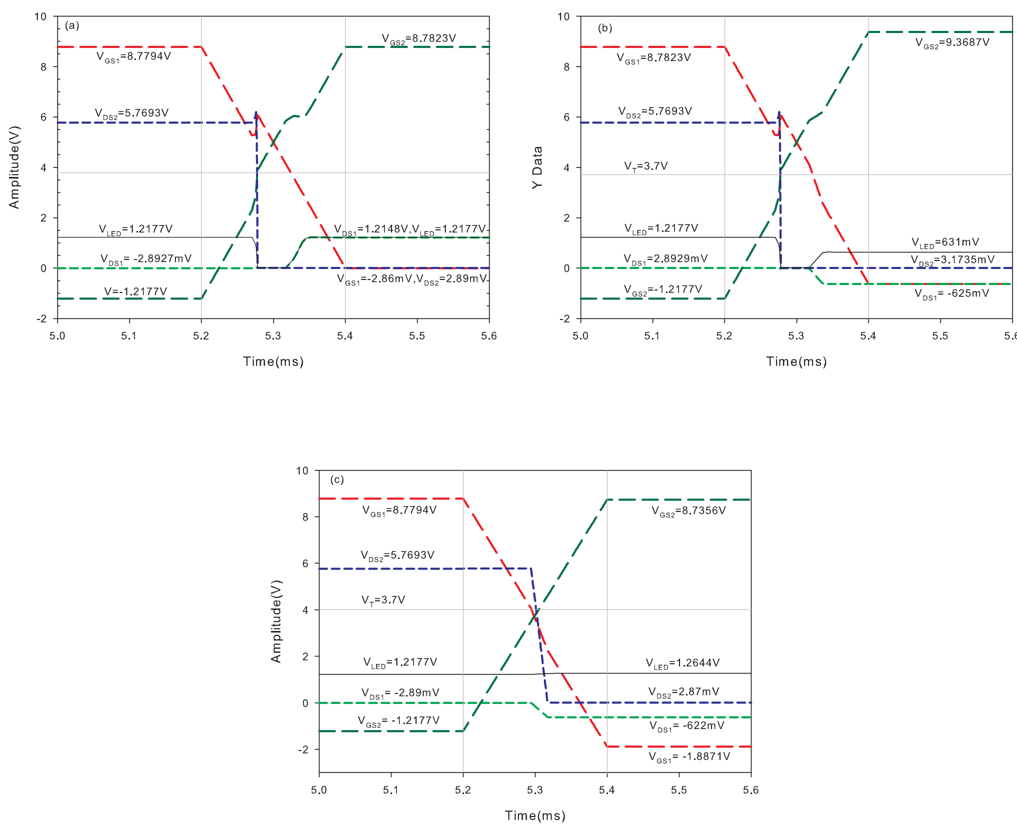

Figure 4.14: Transient analysis of MOSFETs (a)properly connected according to Fig (b)Source and Drain terminals of M1 inverted (c)M3 Removed

(a)In Fig.(4.14a), we show the transient analysis of the circuit diagram in Fig.(4.13a) .First let us assume that M1 is turned on with 10V applied to the G1 and M2 and M3 are off with 0V at G2 and G3. Since M1 is on,the current of 5.8mA flows to the LED setting a voltage of $V_{LED} = 1.2177V$. From the I-V characteristics we can see that for 5.8mA,$V_{DS1} = -2.8mV$. Note that V_{DS1} is negative because the current flows from source to drain. Since S1 and D1 are at the same potential as V_{LED}, the gate-source voltage at M2 is $V_{GS2} = -V_{LED} = -1.2177V$. In order to find the gate-source voltage at M1,we can write a KVL around the gate-source of M1 and M2 as $-10 + V_{GD1} + V_{SG2} = 0$ which gives us $V_{GD1} = 8.78V$. We can find $V_{GS1} = V_{GD1}+V_{DS1} = 8.78-2.8mV \approx 8.78V$. Since no current flows through M2, its drain to source voltage can be obtained as $V_{DS2} = 7-V_{LED} = 5.78V$. These values are approximately the same as the numerical results from 5 to 5.2ms shown in Fig.(4.14a). From 5.2 to 5.4ms , we see the transient period during which M1 starts to switch off and M2 starts to turn on. V_{GS2} starts increasing from -1.2177V and when it cross the threshold voltage $V_T = 3.7V$, the channel is formed in the MOSFET, followed by current flow.Around the same time(or slightly earlier) M3 also turns on causing the current of 5.8mA to flow through it causing $V_{DS3} = 2.8mV$. Since there is no current flow to the LED,V_{LED} is 0. Now we have a condition where both M1 and M2 are turned on at the same time.V_{DS2} drops from its high value of 5.7V to 7mV which indicates a drain current of nearly 15mA flowing through M2. This 15mA current bypasses the LED and flows from drain to source of M1 causing V_{DS1} to be positive for a small duration.The sum of 15mA and 5.8mA current is sunk at M3. Next when V_{GS1} drops below the threshold voltage,M1 is turned off. Because of the high impedance,no current flows through M1 and almost all of the current flows through the LED. We can imagine everything upwards from S2 is the load and the voltage starts to build across this load until the LED turns on drawing current and finally reaches 1.217V. Between the time M2 is turned on and M1 is turned off, V_{DS1} is continuously decreasing from 7mV and after M1 is turned off,it remains constant at 2.89mV causing a drain current of 5.8mA. The voltages around the circuit from 5.4ms and above(duration of subshot pulse width=5ms) can be obtained the same way as during the shot case. Since the V_{LED} is at the same potential as D1, $V_{DS1} = V_{LED} - V_{DS3} \approx 1.214V$. Since G1 is at 0, this leads to $V_{GD1} = -1.217V$ and the gate to source voltage of M1 can be obtained as $V_{GS1} = V_{DS1} + V_{GD1} = -3mV$. The gate to source voltage of M2 is $V_{GS2} = V_{G2} - V_{S2} = 10 - 1.217 = 8.78V$.

(b)Fig.(4.14b) shows the transient analysis for the same circuit in Fig,(4.13a), except the drain and source terminals of M1 have now been reversed. We see that the mechanisms are the same for the shot noise pulse duration and a portion of the crossover from 5.2 to 5.3ms as that of case a. The only difference is that $V_{DS1} = 2.89mV$ is now positive since the current flows from drain to source. Above 5.3ms, the M1 and M2 are both on at the same time and M3 is also on sinking 5.8mA causing $V_{DS3} = 2.8mV$. When V_{GS1} goes below threshold, it turns off M1,essentially blocking current and the voltage across the load looking upwards from S2 increases. When it reaches around 631mV from S2 to ground(which is also the voltage across LED), the body drain diode connected from source to drain terminals of M1 turns on first before the LED thus drawing current. At the same time, the current drawn through this diode is sunk at M3 which now has $V_{DS3} \approx 6mV$. Note that at this point $V_{DS1} = V_{DS3} - V_{LED} = 6mV - 631mV = -625mV$ and since source is more positive with respect to the drain the diode is forward biased. Since the LED voltage is less than the turn-on voltage of nearly 1.2V,it will not draw current and will always be off. If we increase the supply voltage,say from 7 to 20V, the voltage across the LED will change very little.

(c)Finally we remove M3 from the circuit in Fig.(4.13a) and perform the transient analysis which is shown in Fig.(4.14c). We notice that both M1 and M2 turn off and on around the same time. Since there is no M3 to short the current of 5.8mA it flows through the body drain diode forward biasing it causing a drain source voltage of $V_{DS1} = -622mV$. This current drives the LED along with the current from M2 and the net current approximately twice of 5.8mA. So even when we match the sources to produce the same LED current levels with each MOSFET individually(source or drain connected to ground), when we include them in the complete circuit, the levels would not match up. Increasing the current from 5.8mA to 10mA would produce a net current of 15.8mA during the subshot pulse.

Both the shot and subshot currents drawn into the LED can be easily controlled and made equal to each other. In the case of subshot pulse, we can adjust the supply voltage from the power supply and for the case of shot noise current, we can change the photocurrent by adjusting the light intensity from the lamp. In Fig.(4.15a) we show the current flowing into the LED corresponding to Fig.(4.14a). We notice that both shot and subshot pulses

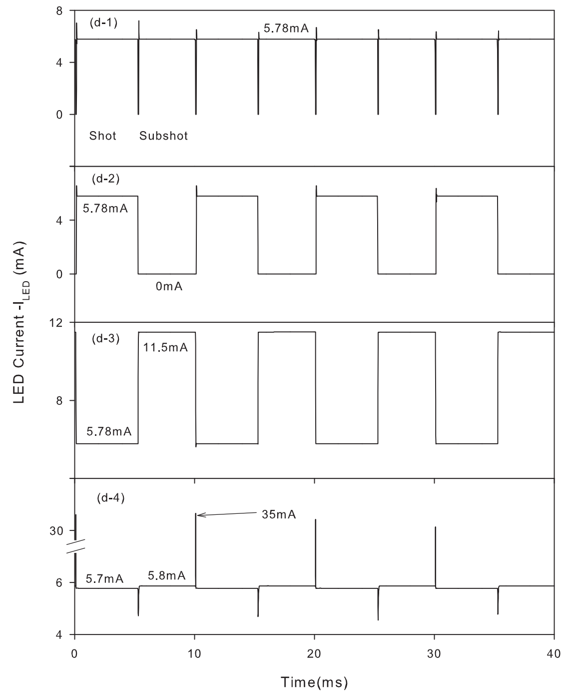

Figure 4.15: LED drive currents for the various switch configurations

are equal and the transient spikes are quite small. There is a period of time where the LED is off, as is seen in the negative going spikes. This can be minimized if we use a switching source which has fast rise times such as a microprocessor. Figs.(4.15b-c) show the cases corresponding to Fig.(4.14b and c), where the current does not flow into the LED during the subshot pulse and when the current is doubled into the LED. We have observed the current doubling case in our experiments but our observations indicate that the doubling occurs during the shot pulse. We are not sure why this occurs at this point. Finally in Fig.(4.15d), we show the case where M3 is removed and M1's terminals are reversed. We have not studied this model using transient analysis, but this is seen as the source of spiking problems in Fig.(4.13b). In this case, the current levels are the same between the shot and subshot pulses, but we notice a current of approximately 35mA which may be sufficient to cause photodetector saturation. In the end, we see that the circuit design in Fig.(4.13a) gives us the best solution ie. equal levels and small switching transients. We have attempted to use capacitors(for example-snubber circuits) to slow down the rapid turn-on of the MOSFETs, with some success, but have made no indepth study. Also, the actual experiments are carried at pulse widths of seconds, and the switching transients will not be important in spectral analysis,since the SA is configured as a time frequency device with sweep times larger than pulse width of a shot or subshot pulse.

4.4 Results

The entire experimental setup is shown in Fig.(4.16a) where the entire setup is placed in a metal enclosure to shield against environmental RF and optical noise.The RFSA and oscope are connected externally to this shield. The transmitter used is the Hamamatsu L9337 LED (L2) since it has the largest squeezing and ac modulation bandwidth of 40Mhz. A signal source (SIG) modulates the variance by switching LED L2 between a high-impedance bias source $R_1 = 2.45k\Omega$ and a shot-noise source using two power field effective transistors (FETs) Q1 and Q2 (IRFD 120); A low-noise voltage supply powers the lamp that loosely couples to a silicon photodetector D1. The signal source modulates the average photon-number by modulating the bias current to both the shot source LED L1 and subshot source resistor R1. The amplitude of the modulation is maintained at 20 mV peak-to-peak, which does not affect the power spectral density of the shot and subshot noise. Optoisolators (not shown) were employed to reduce ground noise. Also the shorting FET(not shown in Fig) discussed previously is placed across detector D1 to inhibit the detector self-bias (saturation) and thereby prevent large current transients during switching. The modulator transmits the optical signal through free space with high-efficiency coupling so as not to alter the beam statistics. The receiver uses a Hamamatsu S5107 photodetector D2 with 95% conversion efficiency at 870 nm. As a check,an estimate of the photocurrent Fano factor F=0.78 was found by supplying a constant bias current of 1.5 mA to the LED ($F_{dr} = 0$) and measuring the terminal-to- terminal efficiency of 22%. The 1.5 mA is the smallest LED bias used in the experiments and provides a well defined average rate of photon arrivals at the photodetector of $2.2 * 10^{15}/s$. Photodetector D2 which develops a signal across resistor $R_2 = 5.08k\Omega$ is reversed biased by 24 V and the incident photon rate maintains the photodetector in the linear regime away from the dark current (10 nA) and saturation (5 mA for these experiments). A minicircuits power splitter routes a portion of the signal to the RFSA through an Analog Modules, Inc. lownoise amplifier A1 (model 322-6 with 40 dB gain); the ac coupling and gain bandwidth of the amplifier help to filter out the low-frequency average signal. An HP 54111D digital oscilloscope displays the average signal and the swept-based HP 8568B RFSA displays the noise power. A personal computer (PC) can be used to save the data to file. The RF SA can display both the temporal t and frequency content of the variance signal since its internal circuitry scans the signal through a filter in a manner that mimics the action of the JTF window. By suitable choice of sweep rate, the frequency scale displays the combined time-frequency content of the noise power spectrum. The RF SA should be set to scan a range of frequencies that is small compared with that over which the noise signal has any change with frequency. Any modulation in the probability of the random signal appears on the RF SA as a time resolved signal. For the demonstration of the stochastic communicator, it is necessary to ensure the LED actually operates between the Poisson and sub-Poisson levels characteristic of the coherent and number-squeezed states, respectively. The lamp T1 is the Poisson calibration source since the photon emission is uncorrelated and they arrive independently at loosely coupled photodetector D1. The lamp and its optical coupling had efficiency less than 0.06% so that the Fano factor had a value of $F \ll 1$ to indicate the Poisson emission from the lamp. Fig.(4.16b) shows the timing waveforms applied to the MOSFETs in order to perform ac and noise modulation simultaneously. The observed photovoltage waveforms at the detectors are also detailed.

In Fig.(4.17), we attempt to determine if the subshot and shot characteristics can be determined from the time domain. The noise voltage waveforms were obtained from the photodetector connected to the amplifier and the HP54111D oscilloscope. Data was obtained at the sampling rates of 1MSPS and 25MSPS. The off pulse corresponds to shot noise and the on pulse corresponds to subshot noise. The data was tabulated as a histogram and the standard deviation was obtained. From the results, we were not able to infer with great accuracy whether the input was shot or subshot noise. So an eavesdropper using the time domain signals, will need to do much processing before he is able to discern the signals. Also, this leads to attenuation of the signals which can be easily detected by the intended receiver.

Fig.(4.18) shows only the variance modulation with both the L2656 and L9337 LEDs. The level separation is characteristic of the degree of squeezing of these LEDs. It is easy to verify that the frequency span of one pulse corresponds to the pulse duration in the time domain using the method described towards the end of Section 4.2. For the L9337 case, we see the existence of a false bit. This may be because of the spectrum analyzer unable to cope with the variations of the signal and it has retained some charge in its internal capacitors. The other possibility is that there is a sudden spike in the dc levels of the average signals, perhaps due to sudden changes in the LED-detector geometry.

The signal generator Fig.(4.16a) generates two binary signals (square waves) with different frequencies to represent two input channels. The modulation of the average optical signal shown in Fig.(4.17a) has a frequency of 10 Hz, while the optical variance signal shown in Fig.(4.17c) has a frequency of 1 Hz. The modulation frequency was limited by the characteristics of the RFSA chosen for the experiments, but it should be remembered that the squeezing bandwidth for the LED ultimately determines the modulation bandwidth for the variance channel of the stochastic modulator. The figure clearly shows that the receiver can distinguish between the two channels and that they appear to be essentially orthogonal. The modulation of the average appears skewed (with malformed bit levels) since it has a frequency lower than the lower cutoff frequency of the amplifier. The noise signal in Fig.(4.17c) is obtained with the RF SA having settings of 10 kHz for the resolution bandwidth, 3 Hz for the video bandwidth, and 4 ms for the sweep time. The oscilloscope trace in Fig.(4.17b) shows the temporal behavior of a random signal from LED L2 with only the variance modulation present; the signal was amplified at a bandwidth limitation of 5 MHz. It should be noted that there is no discernible distinction between those regions with shot or subshot modulation which thereby boosts communication security.

4.5 Summary

In conclusion,we speculate that the stochastic communicator possibly has applications to secure optical communications especially for $F \to 0$ (the Fock state limit, single mode). A tap on the optical medium that introduces partition noise would tend to collapse the squeezed-state probability distribution to the coherent-state Poisson limit. The collapse reduces the likelihood of an eavesdropper receiving any variance other than that of the Poisson limit. The receiver can detect the tap by monitoring the noise level. Quantum non-demolition measurements provide an accurate measurement of the number uncertainty [15], but the measurement introduces phase uncertainty which can also be monitored. The communicator potentially resists interference with discrete multifrequency transmitters, since each bit level for the variance contains a continuous range of frequency components. In conclusion, we have demonstrated a novel communicator that exploits statistical degrees of freedom for optical signals. The communicator modulates the probability distribution for the production of random photon emission events from a natural source. The demonstration shows that both the average and the variance can be modulated as two independent communication channels. These channels can be made orthogonal by detecting the Fano factor rather than the variance for the second channel. The statistics can be potentially modulated over the squeezing bandwidth of 22 MHz for the L9337 at room temperature. The stochastic communicator can use amplitude squeezed states from lasers by independently modulating the displacement and squeezing operators. Upon the advent of a synthesizer for arbitrary Fock states and their quantum superposition, the stochastic communicator would be capable of sustaining a larger number of channels; the variance could range from sub- to super-Poisson with macroscale magnitude.

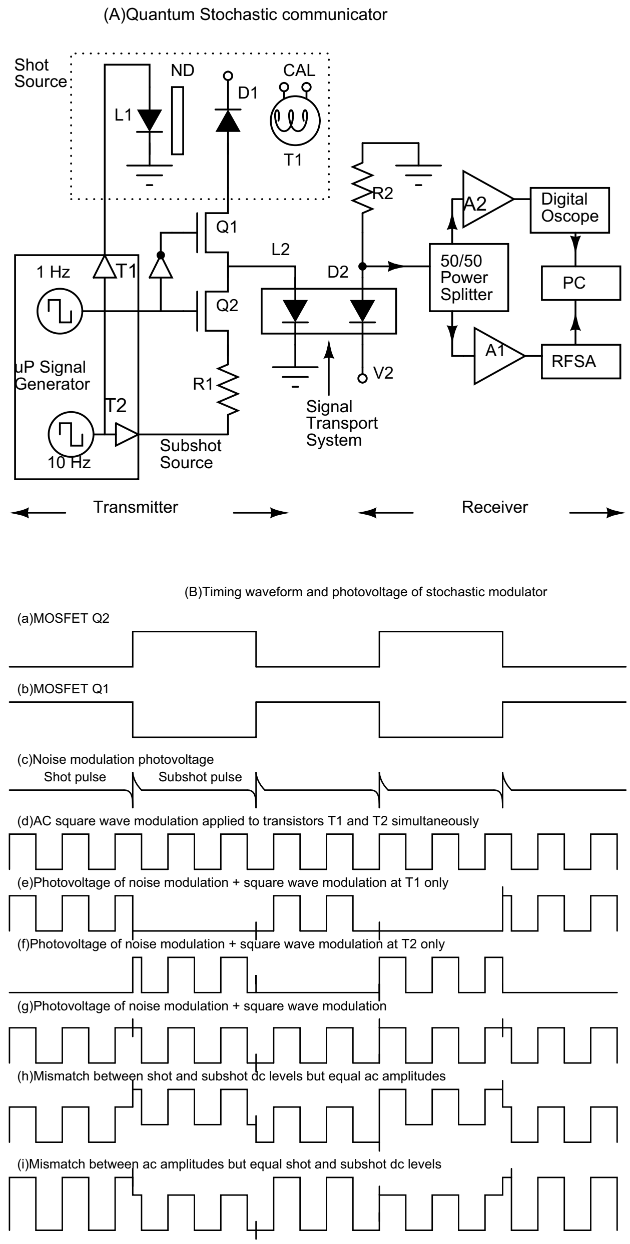

Figure 4.16: (a)The block diagram of the quantum stochastic communicator. (b)Timing diagram indicating voltages applied to MOSFETs M1,M2,M3 as well as the photovoltages observed for noise and AC modulation.

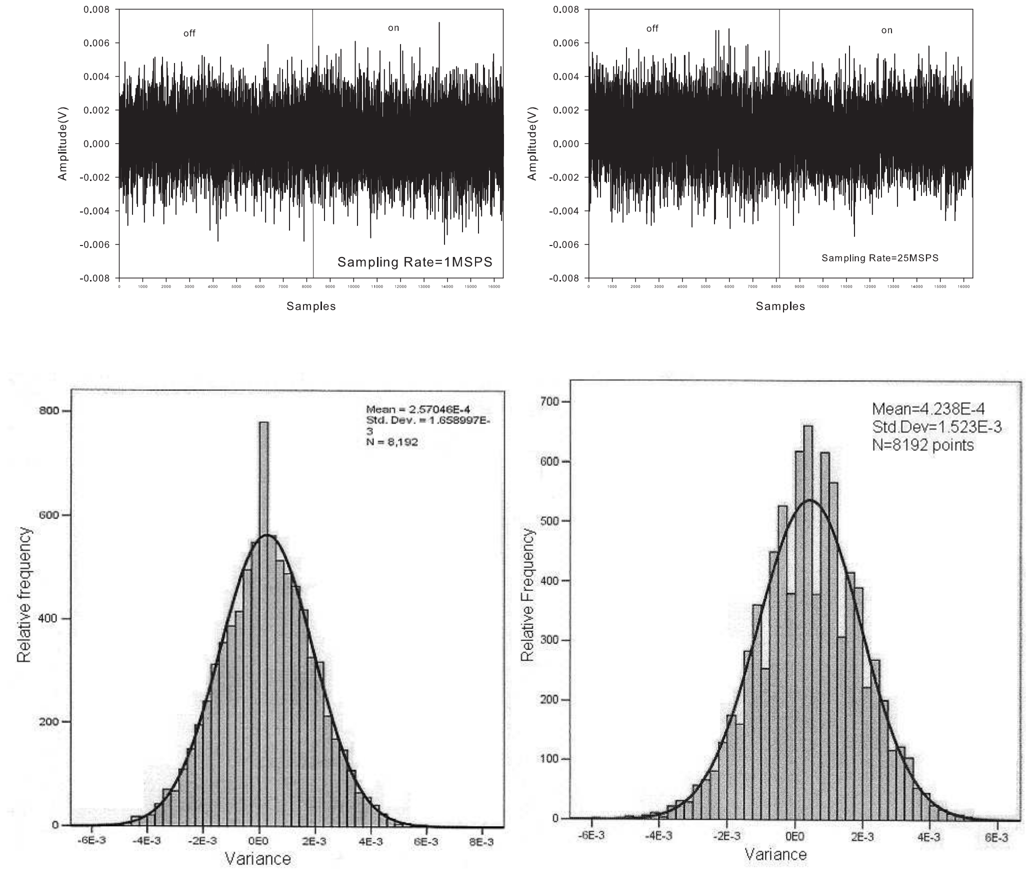

Figure 4.17: Time and Probability distribution for shot and subshot data at 5 and 25 Megasamples per second

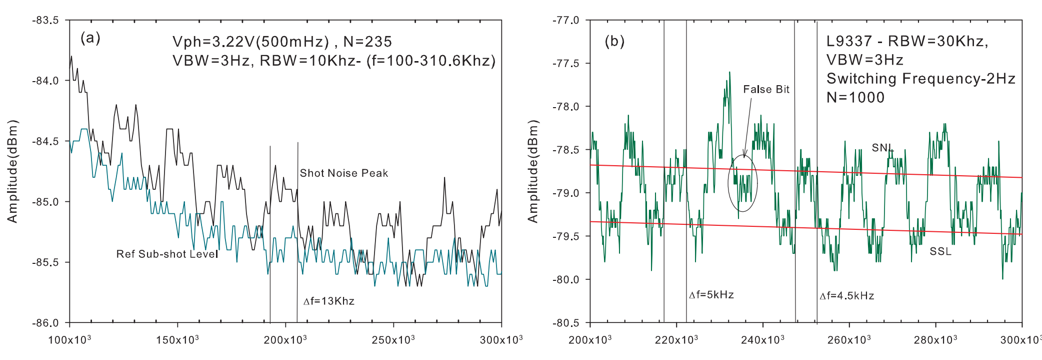

Figure 4.18: Variance Modulation between shot and subshot noise with (a)L2656 LED and (b)L9337 LED

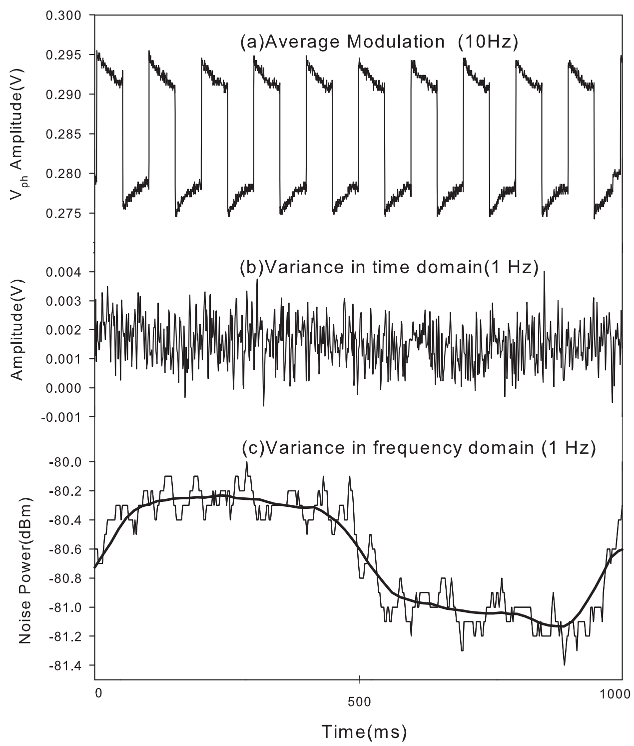

Figure 4.19: (a)The detected average signal (b)The random signal with only variance modulation and (c)The detected variance signal in the frequency domain. The smooth curve represents the moving average with an averaging time of approximately 100ms.

Chapter 5

Conclusions

The subshot noise suppression in the photon flux has been treated from a quantum mechanical perspective in Chapter 2. The pump fluctuations are treated classically but are nevertheless microscopic processes. The Fanofactors are calculated for the photon noise under constant voltage and constant current conditions from the diffusion to thermionic emission regime and the correlations between the junction voltage fluctuation and the carrier number, as well the photon number have also been studied. Most theories have neglected the photon number equations of motion within the cavity. This is made possible only under homogeneous emission conditions where the carrier number fluctuations are equal to the photon number fluctuations outside the cavity.

Next,we have validated the theory with several experiments in shot noise suppression using LEDs. One of the most important parts is to validate each section of the measurement chain. This calibration stage is very important. The nonlinearity of the photodetector or LED has led other researchers to falsely conclude that squeezing was present when there was none. We have obtained good agreements with theory when we deal with relative noise levels. For absolute levels, we have an error of 1dB which may be due to spectrum analyzer miscalibration. The L2656 LED has been re-investigated, with models fit to theory. We have also accounted for the non-radiative processes which have been neglected in previous works with this LED. We have also performed subshot experiments with the L9337 LED which has been previously unreported. We have achieved a squeezing of nearly 1.5dB at room temperature which we believe to be the largest degree of suppression at room temperature.

The stochastic communication idea has been developed for both the classical macroscale and the quantum nanoscale signals. We have studied the noise aspects of each of the switching elements and its influence on the squeezing optical spectra of the LEDs. There are certain concepts still not very clear such as the transistor noise in deep saturation. We have successfully demonstrated the two channel modulation scheme of 10Hz AC modulation and 1Hz noise modulation. The noise modulation has been decoded with the novel idea of configuring the spectrum analyzer as a time frequency analyzer. We believe that the ideas can be easily extended to other types of nonclassical states generated by parametric amplifiers and semiconductor lasers. In the ideal case, the photon number squeezed state will tend to the Fock states with zero variance of photon number. Such states are extremely hard to produce and last for very short times. In the absence of a complete error free communication,we believe that stochastic based modulation/communication methods would offer convenient alternatives.

Appendix A

A.1 Compact Noise Model of PN Junction Devices

The total correlation spectrum of current noise in the external circuit is expressed as the sum of the diffusion and GR spectra

$$\begin{aligned} S_{I_T}(\omega) &= S'_{I_T}(\omega) + S''_{I_T}(\omega) \\ &= \frac{4A}{D}\int_0^W p(x)\left|\frac{k_0k_2 - k_wk_1}{k_1+k_2}\right|^2 dx + \frac{2AD_nq^2}{L_0^2}\int_0^W [p(x)+p_{n0}]\left|\frac{k_0+k_W}{k_1+k_2}\right|^2 dx \end{aligned} \tag{A.1}$$

We first consider the diffusion noise spectra which is the first term of Eq.(A.1). Also the analysis is performed on the n-side of the pn diode where holes are the minority carriers with the DC carrier distribution $p_n(x) = p_{no} + (p(0) - p_{n0})\frac{\sinh\frac{W-x'}{L_0}}{\sinh\frac{W}{L_0}}$. Also we assume the diode base is long so that $\frac{k_wk_1}{k_1+k_2} \approx 0$. The same expressions are valid for the n side also, by appropriate change of variables such as $p_n \to n_p$. The diffusion current noise spectra is

$$S'_{I_T} = \frac{4A}{D}\int_0^W \left(p_{n0} + \frac{(p(0)-p_{n0})\sinh(W-x')/L_0}{\sin h(W/L_0)}\right)\left|\frac{\frac{qD}{L}\csc h(x'/L)\coth(W-x')/L}{\coth(x'/L)+\coth(W-x')/L}\right|^2 dx' \tag{A.2}$$

where $L = L_0/(a+jb)$ is the frequency dependent diffusion length, $a + jb = \sqrt{1+j\omega\tau}$ and τ is the minority carrier lifetime. We outline a few steps in the solution of Eq.(A.2), by considering only the $p(0)$ term for which the spectral density is

$$S_{I_T}^{p0} = \frac{4q^2A(a^2+b^2)}{L_0}\frac{p(0)}{\sinh y}\int_0^W \sinh((W-x')/L_0)\left|\frac{\cosh(\frac{W}{L})\cosh(\frac{x'}{L}) - \sinh(\frac{W}{L})\sinh(\frac{x'}{L})}{\sinh(\frac{W}{L})}\right|^2 dx' \tag{A.3}$$

where $y = W/L_0$. Furthur simplification of Eq.(A.3) leads to

$$= \frac{4q^2A(a^2+b^2)}{L_0}\frac{p(0)}{\sinh y}\int_0^W \sinh(y - \frac{x'}{L_0})\left|\frac{\cosh 2a(y-\frac{x'}{L_0}) - \cos 2b(y-\frac{x'}{L_0})}{\cosh(2ay)-\cos(2by)}\right|^2 dx \tag{A.4}$$

The above equation can be integrated to give the first four terms of the following equation. The last two terms are due to the p_{n0} components.

$$S_{I_T} = 4q^2 A\frac{D}{L_0}\frac{a^2+b^2}{\cosh(2ay)-\cos(2by)}\left\{\frac{p(0)}{\sinh y}\left[\frac{\cosh(2ay)\cosh y-1}{1-(2a)^2}-\frac{2a\sinh(2ay)\sinh y}{1-(2a)^2}+\right.\right.$$
$$\left.\left.\frac{\cos(2by)\cosh y-1}{1-(2jb)^2}+\frac{2b\sin(2by)\sinh y}{1-(2jb)^2}\right]+p_{n0}\left[\frac{\sinh(2ay)}{2a}+\frac{\sin(2by)}{2b}\right]\right\} \quad (A.5)$$

Similary the spectral density of the GR noise can be obtained as

$$S''_{I_T} = 2q^2 A\frac{D}{L_0}\frac{1}{\cosh(2ay)-\cos(2by)}\left\{\frac{p(0)}{\sinh y}\left[\frac{\cosh(2ay)\cosh y-1}{1-(2a)^2}-\frac{2a\sinh(2ay)\sinh y}{1-(2a)^2}\right.\right. \quad (A.6)$$
$$\left.\left.\frac{\cos(2by)\cosh y-1}{1-(2jb)^2}+\frac{2b\sin(2by)\sinh y}{1-(2jb)^2}\right]+2p_{n0}\left[\frac{\sinh(2ay)}{2a}-\frac{\sin(2by)}{2b}\right]\right\}$$

Eqs.(A.5) and (A.6) agree with those obtained in Ref.[26], except that the same results have been obtained using Buckingham's diffusion theory.

A.2 The Renormalized Many Body Hamiltonian for the LED system

The basis states in the Fock space are $|\{n_k\}>$ where $\{n_k\} = n_{k1}, n_{k2}, ...n_{kn}$ are the occupation numbers of the k states. If a_k can be defined as the annhilation operator,then we can define

$$a_k|n_{k1}, n_{k2}, ...0, ...n_{kn}> = (-1)^{\Sigma_{i=1}^{k-1} n_i}|n_{k1}, n_{k2}, ...0, ...n_{kn}> \quad (A.7)$$

In the second quantization representation the electron wave function in the r representation $\psi(r) = \Sigma_k \phi_{ks_z} c_{ks_z}$is replaced by the corresponding field operator

$$\psi(r) = \Sigma_{\lambda,k,s_z}\phi_{\lambda k s_z}(r)a_{\lambda k s_z} \quad (A.8)$$

where $\phi_{\lambda k s_z}$ is the single particle eigenfunction of an electron in the semiconductor and λ is the band and $a^\dagger_{\lambda k s_z}$ is the electron creation operator.From Eq.(A.7), we can see that the fermionic creation and annihilation operators satisfy the anticommutation principles which are a consequence of the Pauli exclusion principle that states that no two fermions can occupy any one state. The anticommutation relations which are defined as $[A, B]_+ = AB + BA$ can be obtained for the case of the electron operators as

$$[a_{\lambda k s_z}, a_{\lambda' k' s'_z}]_+ = [a^\dagger_{\lambda k s_z}, a^\dagger_{\lambda' k' s'_z}]_+ = 0 \quad (A.9)$$

$$[a_{\lambda k s_z}, a^\dagger_{\lambda' k' s'_z}]_+ = \delta_{\lambda\lambda'}\delta_{kk'}\delta_{s_z s'_z} \quad (A.10)$$

If the eigenstates $|1_{\lambda k s_z} >$ and $|0_{\lambda k s_z} >$ represent k-states that contain 1 or no electrons respetively, then the following are also true

$$a\left|0_{\lambda k s_z}\right\rangle = a^{\dagger}_{\lambda k s_z}\left|1_{\lambda k s_z}\right\rangle = 0 \tag{A.11}$$

$$a^{\dagger}_{\lambda k s_z} a_{\lambda k s_z}\left|n_{\lambda k s_z}\right\rangle = \mathrm{n}\left|\mathrm{n}_{\lambda \mathrm{k s_z}}\right\rangle \tag{A.12}$$

The first equation represents the fact that we cannot remove electrons from an unfilled state and also since electrons are not bosons and follow the Pauli-exclusion principle, we cannot add to an already filled state. The second describes the number operator $a^{\dagger}_{\lambda k s_z} a_{\lambda k s_z}$ whose satisfies the eigenvalue equation with corresponding eigenstates $|1_{\lambda k s_z} >$ and $|0_{\lambda k s_z} >$.We assume that the energy band structure follows a parabolic two-band model and hence we can define the hole creation operator as $d^{\dagger}_{-k,-s_z} = a_{v k s_z}$.The definition is motivated by the correspondance between the annihilation of a valence band electron with given momentum and spin and the creation of a hole with opposite momentum and spin. Also to keep the notation compact, we absorb the spin into the k variable from hereon. In the same way,the hole annihilation operator can be defined as $d_{-k} = a^{\dagger}_{v k s_z}$. For the electrons in the condutction band,the creation and annihilation operators are defined as $c^{\dagger}_{k} = a^{\dagger}_{c k s_z}$ and $c_k = a_{c k s_z}$. This notation is quite useful in representing for example,the recombination or generation mechanisms which involve simulataneous creation or annihilation of an electron hole pair. According to Eq.(A.12), the electron number operator in the valence band can be now expressed as $a^{\dagger}_{v k s_z} a_{v k s_z} = d_{-k} d^{\dagger}_{-k} = 1 - d^{\dagger}_{-k} d_{-k}$ and similarly the electron number in the conduction band is $a^{\dagger}_{c k s_z} a_{c k s_z} = c^{\dagger}_{k} c_k$. We can now obtain the Hamiltonian for N non-interacting particles in the second quantized representation as

$$H_{carriers} = \int d^3 r_1 \int d^3 r_2 ... \int d^3 r_N \psi^{\dagger}(r_N) ... \psi^{\dagger}(r_1) \sum_{N} \frac{p_n^2}{2m_e} \psi(r_1) ... \psi(r_2) \psi(r_1) \tag{A.13}$$

Here $\frac{p_n^2}{2m_e}$ represents the kinetic energy of an electron and is an operator in the first quantized representation. Substituting Eq.(A.8) in Eq.(A.13) and using the free particle wavefunction $\phi(r) = \frac{1}{\sqrt{V}} \exp(ik.r)$ we obtain

$$H_{carriers} = \sum_{k s_z} (E_{ck} a^{\dagger}_{c k s_z} a_{c k s_z} + E_{vk} a^{\dagger}_{v k s_z} a_{v k s_z}) \tag{A.14}$$

where $E_{ck} = \frac{h^2k^2}{2m_c} + E_{g0}$ and $E_{vk} = \frac{h^2k^2}{2m_v}$ is the kinetic energy of an electron and hole in the conduction and valence bands respectively. Here m_c and m_v are the effective masses of electrons in the conduction band and valence bands and E_{g0} is the bare band gap energy. Converting into the electron and hole operators we obtain

$$H_{carriers} = \sum_k ((\frac{h^2k^2}{2m_c} + E_{g0})c_k^\dagger c_k + \frac{h^2k^2}{2m_v}(1 - d_{-k}^\dagger d_{-k}) \tag{A.15}$$

$$= \sum_k ((\frac{h^2k^2}{2m_e} + E_{g0})c_k^\dagger c_k + \frac{h^2k^2}{2m_h} d_{-k}^\dagger d_{-k}) \tag{A.16}$$

where we have neglected the constant term in Eq.(A.16) and introduced the concept of hole effective mass which is the negative mass of an electron in the valence band ie. $m_h = -m_v$. This assignment allows us the notion of a particle known as the hole that is introdued when an electron is removed from the valence band and moves opposite to the direction of an electron. When the Coulomb interactions among the N particles are considered, the construction of the second quantized representation for the many body Hamiltonian is obtained as

$$H_{many-body} = \frac{1}{2}\int d^3r_1 \int d^3r_2 ... \int d^3r_N \psi^\dagger(r_N)...\psi^\dagger(r_1)V(r)\psi(r_1)...\psi(r_2)\psi(r_N) \tag{A.17}$$

where $V(r) = \sum\limits_{\substack{i,j \\ i\neq j}} \frac{e^2}{\epsilon_b|r_i - r_j|}$ is the Coulomb potential energy. Using Eq.(A.8) in Eq.(A.17) gives us

$$\begin{aligned} H_{many-body} &= \frac{1}{2V^2}\int d^3r_i \int d^3r_j \sum_{kk'} a_{k'}^\dagger a_k \exp(i(k-k').r_i) \sum_q V_q \exp(iq.(r_i - r_j)) \\ & * \sum_{kk'} a_{k'}^\dagger a_k \exp(i(k-k').r_j) \end{aligned}$$

where the following Fourier transformations $\frac{1}{V}\int d^3r_i \exp(i(k-k'+q) = \delta_{k',k+q}$ and $\frac{1}{V}\int d^3r_i \exp(i(k-k'+q) = \delta_{k,k'-q}$ transform the above equation as

$$H_{many-body} = \frac{1}{2}\sum V_q a_{k+q}^\dagger a_k a_{k'-q}^\dagger a_{k'} - \frac{1}{2}\sum a_k^\dagger a_k V_q \tag{A.18}$$

Eq.(A.18) has so far only considered only one band, and so the summation needs to be extended over the conduction and valence bands. This is followed by normal ordering the creation and destruction operators using the anticommutation relation to get

$$H_{many-body} = \frac{1}{2}\sum_{\substack{k,k',q\\q\neq 0}} V_q(a^\dagger_{c,k+q}a^\dagger_{c,k'-q}a_{c,k'}a_{c,k}+a^\dagger_{v,k+q}a_{v,k'-q}a_{v,k'}a_{v,k}+2a^\dagger_{c,k+q}a^\dagger_{v,k'-q}a_{v,k'}a_{c,k}) \tag{A.19}$$

where $V_q = \frac{1}{V}\int d^3r \exp(-iq.r)V(r) = \frac{4\pi e^2}{\epsilon_b V q^2}$ is the Fourier transform of the Coulomb potential energy V(r).

$$H_{many-body} = \sum_k V_q d^\dagger_{-k}d_{-k} + \frac{1}{2}\sum_{\substack{k,k',q\\q\neq 0}} V_q(c^\dagger_{k+q}c^\dagger_{k'-q}c_{k'}c_k + d^\dagger_{k+q}d^\dagger_{k'-q}d_{k'}d_k - 2c^\dagger_{k+q}d^\dagger_{k'-q}d_{k'}c_k) \tag{A.20}$$

We can absorb the first term into the free carrier Hamiltonian which gives us the hole energy as$E_{hk} = \frac{h^2k^2}{2m_h} = -E_{vk} + \sum_{q\neq 0} V_q$.

$$\begin{aligned} E_{hk} &= -E_{vk} + \sum_{q\neq 0} V_q + \sum_{q\neq 0}(V_{sq} - V_q) \\ &= \frac{h^2k^2}{2m_h} + \Delta E_{ch} \end{aligned} \tag{A.21}$$

The total Hamiltonian for the semiconductor system can be written as

$$\begin{aligned} H_E &= \Sigma_k((\frac{h^2k^2}{2m_e} + E_{g0})c^\dagger_k c_k + (\frac{h^2k^2}{2m_h} + \Delta E_{ch})d^\dagger_{-k}d_{-k}) \\ &+\frac{1}{2}\sum_{\substack{k,k',q\\q\neq 0}} V_q(c^\dagger_{k+q}c^\dagger_{k'-q}c_{k'}c_k + d^\dagger_{k+q}d^\dagger_{k'-q}d_{k'}d_k - 2c^\dagger_{k+q}d^\dagger_{k'-q}d_{k'}c_k) \end{aligned} \tag{A.22}$$

At this point the transition frequency can be written as

$$h\omega_k = \frac{h^2k^2}{2m_e} + E_{g0} + \frac{h^2k^2}{2m_h} + \Delta E_{ch} = \frac{\hbar^2k^2}{2m_r} + E_{g0} + \Delta E_{ch} \tag{A.23}$$

Next we obtain the dipole Hamiltonian by first expanding the the dipole operator as

$$\begin{aligned} er &= e\sum_{n,m=0}^{1} \langle nn,k|\, r\, |mm,k\rangle\, |nn,k\rangle\, \langle mm,k| \\ &= e(\langle 00,k|\, r\, |11,k\rangle\, |00,k\rangle\, \langle 11,k| + \langle 11,k|\, r\, |00,k\rangle\, |11,k\rangle\, \langle 00,k| \\ &= d_{12}\sigma_k + d_{21}\sigma^\dagger_k \end{aligned} \tag{A.24}$$

where we have written the final expression in terms of the dipole matrix elements $d_{12} = d^\star_{21}$ and the raising and lowering operators(or pseudo-spin operators from the context of magnetic transitions in spin-1/2 systems) can be defined by recognizing that the two states $|11, k\rangle$ and $|00, k\rangle$ are equivalent to the states of the a two level atom

$$\sigma_k = |00, k\rangle \langle 11, k| \equiv d_{-k} c_k \tag{A.25}$$

$$\sigma_k^\dagger = |11, k\rangle \langle 00, k| \equiv c_k^\dagger d_{-k} \tag{A.26}$$

We have assumed the diagonal terms of the dipole moment are zero which can be written as

$$\langle 00, k| \, r \, |00, k\rangle = \langle 11, k| \, r \, |11, k\rangle = 0 \tag{A.27}$$

since energy eigenstates of a wavefunction $\phi_{nk}(r)$ with a well defined parity has diagonal elements that vanish. This is true since $|\phi_{nk}(r)|^2$ is a symmetric function and r is antisymmetric and the net integratand is antisymmetric which can be written as

$$\langle nn, k| \, r \, |nn, k\rangle = \int d^3r |\phi_{nk}(r)|^2 r = 0 \tag{A.28}$$

The single mode of an the radiation field in a cavity from a collection of such fields can be written in the second quantization as

$$E(z, t)_l = iE_{0,l} u(z)(a_l - a_l^\dagger) \tag{A.29}$$

where $E_{0,l} = \sqrt{\frac{h\nu_l}{2\epsilon_0 V}}$ is the electric field of a single 'photon'. The dipole-field interaction hamiltonian is

$$H_{l,k} = -er_k E_l(z, t) = -E_{0,l} i(d_{12}\sigma_k + d_{21}\sigma_k^\dagger)(a_l - a_l^\dagger) \tag{A.30}$$

The total interaction hamiltonian including all the k states and the l modes can be written as

$$H_{dipole} = -ih(g_{l,k}\sigma_k^\dagger \exp(i\xi) + g_{l,k}^\star \sigma_k \exp(-i\xi))(a_l - a_l^\dagger) \tag{A.31}$$

where $g_{l,k} = \frac{|d_{12,k} . u(z)|}{\hbar} E_{0,l}$.When we choose a phase of $\pi/2$ and the mode function is $u(z) = \sin(kz)$ we obtain

$$H_{l,k} = \hbar(g_{l,k}\sigma_k^\dagger - g_{l,k}\sigma_k)(a_l - a_l^\dagger) \tag{A.32}$$

$$= \hbar(g_{l,k} a_l \sigma_k^\dagger + g_{l,k}^\star a_l^\dagger \sigma_k) \tag{A.33}$$

Note that we have omitted the terms σa and $\sigma^\dagger a^\dagger$ since they violate energy conservation. Here $\sigma^\dagger a^\dagger$ implies simultaneous creation of a electron-hole pair as well as the addition of a photon to the field and σa implies the annhilation of e-h pair as well as the removal of a photon from the excitation field. The total interaction hamiltonian adding together all the k states of the electronic system and the l modes of the radiation field, gives us

$$H_{dipole} = \hbar \sum_{l,k} (g_{l,k} a_l c_k^\dagger d_{-k}^\dagger + g_{l,k}^\star a_l^\dagger d_{-k} c_k) \tag{A.34}$$

The field system is modelled as a collection of oscillators with each of frequency Ω_l and the unperturbed hamiltonian of such system is

$$H_{field} = \sum_l \hbar \Omega_l a_l a_l \tag{A.35}$$

The bath is also a collection of oscillators each of frequency ω_j and the unperturbed hamiltonian of the reservoir is

$$H_{bath} = \sum_j \hbar \omega_j b_j b_j \tag{A.36}$$

Each oscillator or mode within the cavity is coupled to all the modes of the reservoir outside through the coupling coupling constant μ_{lj}.The total system(field)-reservoir(bath) interaction energy in the rotating wave approximation is obtained by summing over all modes within the cavity and is expressed as

$$H_{field-bath} = \Sigma_l H_{field-bath,l} = \hbar \sum_{l,j} (\mu_{lj} a_l^\dagger b_j + \mu_{lj}^* b_j^\dagger a_l) \tag{A.37}$$

The total Hamiltonian of the entire system can be written as

$$H_{total} = H_{carriers} + H_{many-body} + H_{dipole} + H_{field} + H_{bath} + H_{field-bath} \tag{A.38}$$

There are other terms which may be included such as the multimode phonons and the Frolich Hamiltonian which describes the longitudinal acoustic phonon interaction with carriers. Such terms can be avoided by properly accounting for their effects (for example the equilibration of the lattice and electron termperatures) in the equations of motion.

A.3 Spontaneous Emission Operator

The spontaneous emission is noted as a consequence of vacuum fluctuations stimulating the exciting the excited states to recombine. This should be readily explainable with the quantum theory. We can describe the process as annihilation of an electron-hole pair followed by creation of a photon and so we need to construct the equations of motion for $a_l^\dagger d_{-k}c_k$ which is

$$\frac{d}{dt}a_l^\dagger d_{-k}c_k = \frac{i}{\hbar}[H_{dipole} + H_{carriers} + H_{field} + H_{field-bath}, a_l^\dagger d_{-k}c_k] \tag{A.39}$$

We can evaluate three of these commutators individually and obtain $[H_{field-bath}, a_l^\dagger d_{-k}c_k] = 0$, $[H_{carriers}+H_{field}, a_l^\dagger d_{-k}c_k] = (-i\omega_k+\Omega_l)a_l^\dagger d_{-k}c_k$ .The last commutator $[H_{dipole}, a_l^\dagger d_{-k}c_k]$ involves the following commutation relation

$$\begin{aligned}[][a_l^\dagger d_{-k}c_k, c_k^\dagger d_{-k}^\dagger a_l] &= a_l^\dagger a_l[(1-d_{-k}^\dagger d_{-k})(1-c_k^\dagger c_k) - c_k^\dagger c_k d_{-k}^\dagger d_{-k}] - c_k^\dagger c_k d_{-k}^\dagger d_{-k} \\ &= a_l^\dagger a_l[(1-n_{hk})(1-n_{ek}) - n_{ek}n_{hk}] - n_{ek}n_{hk}\end{aligned}$$

The equation of motion for the operator $a_l^\dagger d_{-k}c_k$ is obtained from the Heisenburg equation of motion as

$$\frac{d}{dt}a_l^\dagger d_k c_k = -[\gamma + i(\omega_k - \Omega_l)]a_l^\dagger d_{-k}c_k + i\sum_k g_{l,k}(a_l^\dagger a_l[(1-n_{hk})(1-n_{ek}) - n_{ek}n_{hk}] - n_{ek}n_{hk}) \tag{A.40}$$

Since spontaneous emission is a slow process compared to the carrier-carrier scattering rates, the above equation can be solved in steady state leading to

$$\left\langle a_l^\dagger d_{-k}c_{-k}\right\rangle = \frac{i\sum_k \left\langle g_{l,k}(a_l^\dagger a_l[(1-n_{hk})(1-n_{ek}) - n_{ek}n_{hk}] - n_{ek}n_{hk})\right\rangle}{\gamma + i(\omega_k - \Omega_l)} \tag{A.41}$$

To see how the excited state operator $< n_{ek}n_{hk} >$ decays, we write another equation of motion

$$\frac{d}{dt} < n_{ek}n_{hk} >= -[i\sum_{l,k} g_{l,k}^\star < a_l^\dagger d_{-k}c_k > +adj] \tag{A.42}$$

Inserting Eq.(A.41) in Eq.(A.42), we obtain

$$\frac{d}{dt} < n_{ek}n_{hk} >= -\sum_k |g_{l,k}|^2 \frac{2\gamma\left\langle (a_l^\dagger a_l[(1-n_{hk})(1-n_{ek}) - n_{ek}n_{hk}] - n_{ek}n_{hk})\right\rangle}{\gamma^2 + (\omega_k - \Omega_l)^2} \tag{A.43}$$

For a state with no photons, the expectation value $< a_l^\dagger a_l >= 0$. This leads to the following decay of excited state as

$$\frac{d}{dt} < n_{ek}n_{hk} >_{vaccum} = -\sum_k |g_{l,k}|^2 \frac{2\gamma\left\langle n_{ek}n_{hk}\right\rangle}{\gamma^2 + (\omega_k - \Omega_l)^2} \tag{A.44}$$

Looking at Eq.(A.44),we see the term resembles the radiative recombination rate as $R_{sp,k} = B_k np$ where $n \equiv n_{ek}$ and $p \equiv n_{hk}$ with the spontaneous recombination coefficient given by

$$B_k = |g_{l,k}|^2 \frac{2\gamma}{\gamma^2 + (\omega_k - \Omega_l)^2} \approx \frac{1}{4\pi\epsilon_0} \frac{4\omega_k^3 |d_{12}|^2 n^3}{3\hbar c^3} \tag{A.45}$$

The last equality(which we will not derive here) is the well known Wigner-Weisskopf spontaneous emission coefficient for a semiconductor of refractive index n. The first and second terms in Eq.(A.41) imply stimulated absorption and emission respectively. Since we assume that stimulated emission is extremely small,we can neglect it. However we can include the absorption term since it is included as the intrinsic generation of carriers in the semiconductor material.

A.4 Code for evaluation of noise spectral densities

The input to this program comes from Adept, a 1D numerical Poisson equation solver, which establishes the steady state carrier densities.

```
clear all;
%obtain carrier concentrations from file:format carrV
%[labels,x1,conc]=readColData('carr9V.txt',3,0);
%load('carr9V.txt')
%p = conc(:,1);
%n = conc(:,2);
%x1 = carr9V(:,1);
%p = carr9V(:,2);
%n = carr9V(:,3);
format long;
[x1,p,n]=textread('carr9V.txt','%f %f %f');
x1 = x1 .* 10^-6; %Convert to micron width
%First obtain green functions for long diode
taur = 10^-9;
f = 10*10^3;
```

```
omega = 2*pi*f;
Na=10^16; %pp0
Nd=10^16; %nn0
ni=10^10;
np0=ni^2/Nd;
pn0=ni^2/Na;
mup = 490;
mun = 1390; % specified in cm2/V-s
Dp = mup*26*10^-3*10^-4; % Converted to meters
Dn = mun*26*10^-3*10^-4;
W = 10*10^-6; %Total thickness
wn = 5*10^-6; %Thickness of n type material
wp = 5*10^-6; %Thickness of p type material
Nx = 200; %Mesh number
%x1 = [0:W/200:W];
A = 1*10^-6; %Area of device - m^2
Lp = (Dp*taur/(1+i*omega*taur))^.5;
Ln = (Dn*taur/(1+i*omega*taur))^.5;
x=10^-15; % Really small number instead of 0 to prevent NaN
q = 1.6*10^-19;
%Depletion region widths for symetrically doped pn junction
%Calculate depletion region width and xp and xn first
Vbi=25.84*10^-3*log(Na*Nd/ni^2);
Va =0.5; %Applied voltage
Wdepl=sqrt((2*11.8*8.854*10^-14*(Na+Nd)*(Vbi-Va))/(1.6*10^-19*Na*Nd))*10^-2;
%Theoretical Depletion region widths
xp = W/2-Wdepl/2;
xn = W/2+Wdepl/2;
```

```
%Find numerical approximations
for ind=1:Nx/2
if abs(xp-x1(ind))¡0.00200*10ˆ-6
xpindex=ind;
break;
end
end
for ind=Nx/2+1:Nx
if abs(xn-x1(ind))¡0.00200*10ˆ-6
xnindex=ind;
break;
end
end
%First Calculate Scalar green functions for the p side
for m=1:Nx/2
% Calculate Hole Green functions Gp first
% First for x¡wp in the p region Gpp
Gp(m)=1;
x=wp-x1(m); %Change from wp to xp
k0 = csch((x)/Ln); % The x here ranges positive from 0 to W where W=wp-xp.
% The reason for positive x is in the derivation of the green functions.
% Here x=-xp is 0 and x=-wp is W.
k1 = coth((x)/Ln);
k2 = coth((wp-x)/Ln); %Change from wp to xp
kw = csch((wp-x)/Ln);
Gn(m)=-k0/(k1+k2);
Gnw2(m)=kw/(k1+k2); %keep backup to obtain imag components
Gpt(m)=0;
```

```
VGp(m) = 0;
VGn(m) = k0.*k2./(k1+k2).*(1/Lp); %Vector green function in p for electrons
%From xpindex to wp allow diffusion noise to go to zero smoothly
%Kdiff(m) = n(m)*Gn(m);
Kdiff(m)=4*q^2*A*Dn*n(m)*(VGn(m)*conj(VGn(m)));
Kgr(m)=q^2*A*2*(n(m)+np0)/taur*Gn(m)*conj(Gn(m));
end
%Recalculate noise in p-side of depletion region
slope1=(Kdiff(xpindex)-0)/(x1(xpindex)-wp);
slope2=(Kgr(xpindex)-0)/(x1(xpindex)-wp);
for m=xpindex:Nx/2
Kdiff(m)=slope1*(x1(m)-x1(xpindex))+Kdiff(xpindex);
Kgr(m)=slope2*(x1(m)-x1(xpindex))+Kgr(xpindex);
end
x1(Nx/2+1)=wp+10^-15; %Reinit to very small value
%Gn=Gn(end:-1:1);
Gnw = 1+Gn;
Gnt = abs(Gn - Gnw2);
%For n-side part
for m=Nx/2+1:Nx
x=x1(m)-wp;
k0 = csch((x)/Lp);
k1 = coth((x)/Lp);
k2 = coth((wp-x)/Lp);
kw = csch((wp-x)/Lp);
Gp(m) = k0/(k1+k2); % Notation is green function for holes-p in the n region -1 is to junction
Gpw(m) = kw/(k1+k2); % 2 indicates to terminal
```

```
Gnw(m) = 0;
Gnt(m) = 0;
%Gn1(m)=0;
%Remember above are green scalar functions used in computation of GR noise
%Gnp = -sinh((wp+x)/Ln)/sinh((wp-xp)/Ln);
%Gpn = sinh((wn-x)/Lp)/sinh((wn-xn)/Lp);
VGp(m) = k0.*k2./(k1+k2).*(1/Lp);
VGn(m) = 0;
%VGpn2 = k1.*kw./(k1+k2).*(1/Lp);
%x=x+increment
Kdiff(m)= 4*q^2*A*Dp*p(m)*(VGp(m)*conj(VGp(m)));
Kgr(m) = q^2*A*2*(p(m)+pn0)/taur*Gp(m)*conj(Gp(m));
end
Gpt = abs(Gpw-Gp);
%Recalculate noise in n-side of depletion region
slope1=(0-Kdiff(xnindex))/(wn-x1(xnindex));
slope2=(0-Kgr(xnindex))/(wn-x1(xnindex));
for m=(Nx/2):xnindex
Kdiff(m)=slope1*(x1(m)-x1(xnindex))+Kdiff(xnindex);
Kgr(m)=slope2*(x1(m)-x1(xnindex))+Kgr(xnindex);
end
xdata=[wp+Wdepl/2,wp+Wdepl/2];
ydata=[0,10^11];
%plot(x1,Kdiff,x1,Kgr);
%plot(x1(1:xpindex+1),imag(Gn(1:xpindex+1)),x1(xnindex:Nx),imag(Gp(xnindex:Nx)));
%plot(x1,real(Gn),x1,real(Gp));
%plot(x1,-(Gp),x1,Gnw,x1,Gnt,x1,Gpt,x1,Gpw);
plot(x1,Gp,x1,Gpw);
```

Appendix B

Classical Stochastic Communicator

B.1 Hardware Setup

The processor consists of an Atmel Mega32 using a 14.7456 MHz crystal. The processor has 32k bytes of flash memory for programs, 1k of internal RAM and 1k of EPROM. The processor executes most instructions in 1 clock cycle. The processor has four 8-bit digital IO ports that can also be assigned alternate functions for analog to digital conversion, timers and triggers and serial communications as necessary. The example transmitter uses Bascom basic for implementing the algorithm. The circuit diagram for the prototype transmitter appears in Fig.(B.1a) where the Atmel Mega32 serves as the signal processor. A 14.7456 MHz crystal provides the clock signal. The chip is programmed in compiled Bascom basic using a 25 pin parallel port from a computer. The figure shows the pin connections in the parallel cable for programming. The software supports software defined serial ports on any of the digital IO pins. However, some applications can make better use of the buffer registers associated with the built-in UART. In this case, inverters must be used as indicated for lines R and T in the figure. Port C on the Atmel processor provides an 8-bit digital output signal. Each byte from port C represents a random number generated by the software. The resistor network next to the Atmel chip (R2R network) provides the digital to analog conversion (ADC). The voltage from the R2R network can range from 0 to approximately 3.3 volts in 256 steps. The AD 625 opamp was used as an output buffer.

The receiver circuit preferably uses a fast signal processor rather than discrete components. The processor can easily perform averages and calculate the incoming moments. Fig.(B.1b) illustrates a receiver circuit suitable for extracting a modulated average (AVE) and a quantity proportional to the standard deviation (SD). The random signal is received

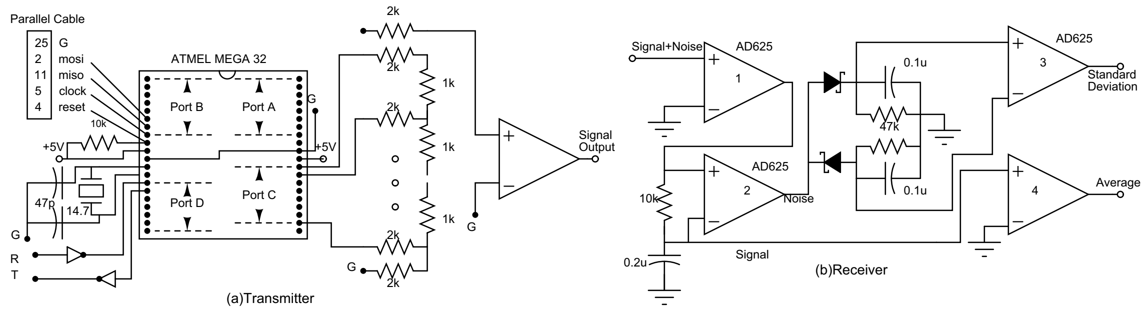

Figure B.1: Hardware realization of the classical stochastic modulator. (a)Microprocessor realization of the transmitter.The letter 'g' refers to "chassis" ground (b)Receiver for demodulating random signals using discrete components.

by instrumentation amplifier #1 (analog devices AD625). The capacitor in the 10k-0.2 charges to the average value of the input signal. AD625 #2 removes removes the modulated average from the signal and AD625 #3 buffers the modulated average. The schottky diodes with approximately 0.1 volt turn-on voltages charge the parallel RC combinations. The difference in voltages across the capacitors provides a measure of the standard deviation, which appears on the output of AD625 #4. The circuit extracts a signal SD that does not agree with the standard deviation, which requires the sum of a voltages squared. In general, the components (such as analog multipliers) necessary to raise variables to the n'th power add significant complexity to the circuit. Without the proper multiplication, the quantities related to standard deviation and skew will not be independent of one another.

The transmitter signal processor has an algorithm to generate random signals with statistical moments controlled by input data. The number of input channels matches the number of modulated statistical moments. The transmitter processor constructs the output signal using a digital to analog convert (DAC). The receiver circuit detects the signal and converts the signal into a digital signal using an analog to digital converter (ADC). A fast signal processor(not shown) then performs calculations to extract the modulated moments and therefore the channel data. The transmission medium consists of an electrical transmission line although it could well be an optical fiber or free space.

B.2 Results

The algorithm for the transmitter processor is indepedent of the type of receiver used. The overall concept consists of reading the input data from 3 channels, determining the three statistical moments of average, variance and skew, then calculating and transmiting a sequence of random numbers over the duration of the data bits consistent with the statistical distribution determined by the average, variance and skew. The channels contain binary data consisting of a sequence of 0s and 1s representing 0 and 5 volts. The test system stores 8 bits of data for channel 1, 8 bits for channel 2, and 8 bits for channel 3. The actual system would encode the bits as they arrive rather than store them in memory. The test system uses two characteristic times. The pulse width (PW) time refers to the duration during which a random number remains valid. The term pulse width reflects the appearance of the random number when viewed on an oscilloscope after the digital to analog converter DAC. The second time is the bit time which refers to the length of time that a data bit remains valid. During the bit time, multiple random numbers will be generated consistent with a probability distribution determined by the present data bits in the three channels. The algorithm implemented is as follows

1. Initialize the PW for each bit and the random number generator
2. Obtain the data bits from channel C1,C2,C3
3. If C1=0 then set Ave=AVE0 else Ave=AVE1.
   If C2=0 then choose Var=VAR0 else Var=VAR1.
   If C3=0 then choose Skew=SKW0 else Skew=SKW1
4. Generate random number based upon probability distributions from step 3. This is sent to the the DAC
5. If PW is reached then goto step 2 else send another random number.

Note that the signal processor must generate or store up to 8 different distributions. The three bits in the three data channels determine the presently active distribution. A random

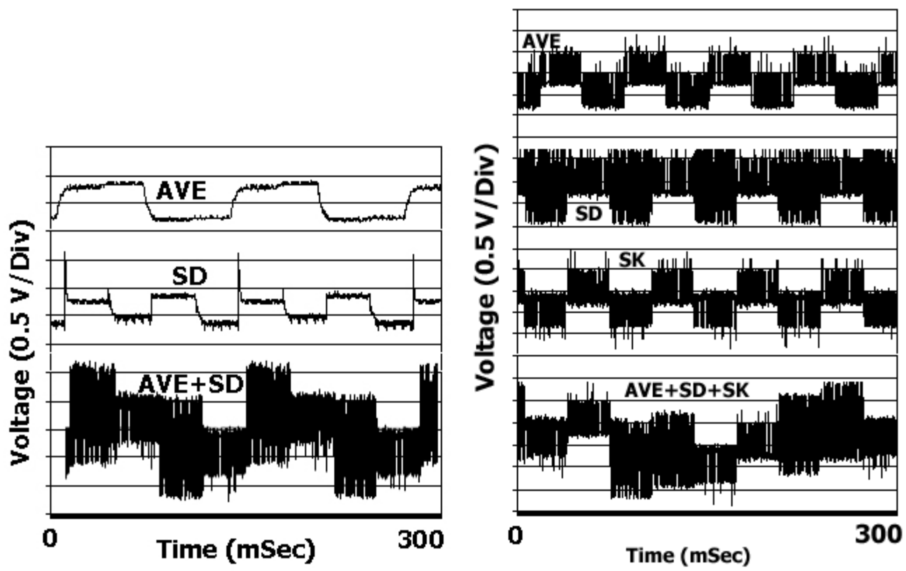

Figure B.2: Observed waveforms from the stochastic communicator. The waveforms are obtained by switching between 8 stored distributions in the microprocessor to produce time varying mean,standard deviation and skew each independent of one another.

number generator produces a random number consistent with the active probability distribution. A timer built into the signal processor ensures that the random number remains active for the the PW time (usually 2 to 5 microseconds for the Atmel Mega32 processor operating at 14.7456 MHz). During the PW time, an 8-bit DAC (an R2R ladder network in this case), sends the data over a wire to the receiver. The prototype system produces a random voltage at the output of the DAC and holds it for approximately 5-10 microseconds. These amplitude bursts may be compared to the shot noise like pulses but of different amplitudes and since the waveforms are observed on the millisecond scale they have noise like appearance. Fig.(B.2a) show the oscilloscope plots for three cases of (1) modulated average but constant variance and skew, (2) modulated variance but constant average and skew, and (3) modulated skew but constant average and variance. Fig.(B.2b) shows oscilloscope waveform of the signal for the binary modulation where starting from top we see 1)the average with constant variance and skew 2) the standard deviation varying but average constant, 3)the time varying skew and finally 4) all the three moments taking values independent of one another.

References

[1] R. F. McDonald, P. J. Edwards, and W. N. Cheung, "Shot noise-suppressed operation of bipolar junction transistors.," in *Proceeding of the Workshop on Australian Radio Science*, 2000.

[2] D.Gottesman and J.Preskill, "Secure quantum key distribution using squeezed states," *Physical Review A*, vol. 63, p. 022309, 2001.

[3] H.A.Bachor and T.C.Ralph, *A Guide to Experiments in Quantum Optics, 2nd, Revised and Enlarged Edition.* Wiley International, 2004.

[4] Y.Yamamoto, N.Imoto, and S.Machida, "Amplitude squeezing in a semiconductor laser using quantum nondemolition measurement and negative feedback," *Physical Review A*, vol. 33, pp. 3243–3261, 1986.

[5] Y.Yamomoto and S.Machida, "High impedance suppression of pump fluctuation and amplitude squeezing in semiconductor lasers," *Physical Review A*, vol. 35, pp. 5114–5130, 1987.

[6] P.J.Edwards, "Reduction of optical shot noise from light emitting diodes," *IEEE Journal of Quantum Electronics*, vol. 29, pp. 2302–2304, 1993.

[7] K.Kikuchi and M.Kakui, "Reduction of shot noise with with light emitting diodes," *IEEE Journal of Quantum Electronics,*, vol. 28, pp. 1626–1630, 1992.

[8] M.J.Martin, J.E.Valazquez, and D.Pardo, "Analysis of current fluctuations in silicon pn and pn homojunctions," *Journal of Applied Physics*, vol. 79, pp. 6975–6981, 1996.

[9] M.C.Teich, F.Capasso, and B.E.A.Saleh, "Photon number squeezed recombination radiation in semiconductors," *Journal of Optical Society of America.B*, vol. 4, pp. 1663–1666, 1987.

[10] S.M.Sze, *Physics of semiconductor devices,2nd Edition.* John Wiley and Sons, 2001.

[11] R.Landauer, "Solid state shot noise," *Physics Review B*, vol. 47, pp. 16427–16432, 1993.

[12] Kobayashi, M.Yamanishi, H.Sumitomo, and Y.Kodoya, "Influence of the backward pump process on photon number squeezing in a constant current driven heterojunction led:transition from the thermionic emission to diffusion limits," *Physical Review B*, vol. 60, pp. 16686–16700, 1999.

[13] J. Kim, H. Kan, and Y. Yamamoto, "Macroscopic coulomb-blockade effect in a constant-current-driven light-emitting diode," *Physics Review B*, vol. 52, pp. 2008–2012, 1995.

[14] H.Fujisaki and A.Shimizu, "Quantum langevin equations for semiconductor light emitting devices and the photon statistics at a low injection level," *Physical Review A*, vol. 57, pp. 3074–3083, 1998.

[15] V. D. Ziel.A, "Theory of shot noise in junction diodes and junction transistors," *Proc IRE*, vol. 43, pp. 1639–1646, 1955.

[16] M.J.Buckingham, *Noise in Electronic Devices and Systems.* Ellis Horwood Series, 1985.

[17] M.J.Buckingham and E.A.Faulkner, "The theory of inherent noise in pn junction diodes and bipolar transistors," *Radio Electron. Eng*, vol. 44, pp. 125–140, 1974.

[18] F.N.H.Robinson, *Noise in Electrical Circuits.* University Press, 1962.

[19] *Y.Yamamoto, "Fundamentals of noise processes",Appendix -A, Lecture Notes,http://www.stanford.edu/ rsasaki.*

[20] J.B.Johnson, "Thermal agitation of electricity in conductors," *Physical Review*, vol. 32, pp. 97–109, 1928.

[21] H.Nyquist, "Thermal agitation of electric charge in conductors," *Physical Review*, vol. 32, pp. 110–113, 1928.

[22] David.K.Ferry, *Semiconductor Transport.* Taylor and Francis, 2000.

[23] C. Vliet, "Macroscopic and microscopic methods for noise in devices," *IEEE Transactions on Electron devices*, vol. 41, pp. 1902–1915, 1994.

[24] F.Bonani and G.Ghione, *Noise in Semiconductor Devices:Modeling and Simulation.* Springer, 2001.

[25] A.Imamoglu and Y.Yamamoto, "Noise suppression in semiconductor p-i-n junctions:transition from macroscopic squeezing to mesoscopic coulomb blockade of electron emission processes," *Physical review Letters*, vol. 70, pp. 3327–3330, 1993.

[26] F.Bonani, D.Guerrieri, and G.Ghione, "Compact conversion and cyclostationary noise modeling of pn junction diodes in low injection-part i:model derivation," *IEEE Transactions on Electron Devices*, vol. 51, pp. 467–476, 2004.

[27] P.J.Edwards, "Sub-poissonian electronic and photonic noise generation in semiconductor junctions," *Australian Journal of Physics*, vol. 53, pp. 179–192, 2000.

[28] P.J.Edwards, "Recombination noise in semiconductor junction devices," *Noise in Devices and Circuits,IEE Proceedings-Circuit Devices and Systems*, vol. 151, pp. 175–183, 2004.

[29] A.Imamoglu and Y.Yamamoto, "Single electron thermionic emission oscillations in pn microjunctions," *Physical Review B*, vol. 46, pp. 9555–9563, 1992.

[30] E.Ben-Jacob and Y.Gefen, "Coherent versus noncoherent bloch oscillations in the presence of direct and alternating fields," *Physical Review B*, vol. 37, p. 7400, 1988.

[31] K. Hess, *Advanced Theory of Semiconductor Devices.* IEEE Press, 2000.

[32] H.Sumitomo, M.Yamanishi, and Y.Kadoya, "Theory of photon number squeezing in a heterojunction led by the nonlinear backward pump process," *Physical Review B*, vol. 65, 2002.

[33] J.Kim and Y.Yamamoto, "Theory of noise in pn junction light emitters," *Physical Review B*, vol. 55, pp. 9949–9958, 1997.

[34] K. Chow and S. III, *Semiconductor Laser Physics*. Springer Verlag, 1994.

[35] Sargent and M.O.Scully, *Laser Physics*. Westview Press, 2001.

[36] H.J.Carmichael, *Statistical Methods in Quantum Optics 1 : Master Equations and Fokker-Planck Equations*. Springer, 2003.

[37] C.W.Gardiner, *Quantum Noise*. Springer Verlag, 2002.

[38] M. Yamanishi and Y. Lee, "Scheme for generation of sub-poissonian photons: Antibunching of emission events by population-dependent spontaneous-emission lifetime in semiconductor microcavities," *Physical Review A*, vol. 48, pp. R2534 – R2537, 1993.

[39] D.C.Kilper, D.G.Steel, R.Craig, and D.R.Scifres, "Polarization dependent noise in photon number squeezed light generated by quantum well lasers," *Optics Letters*, vol. 21, pp. 1283–1285, 1996.

[40] J. Abe, T. Kuga, T. Hirano, M. Kobayashi, and M. Yamanishi, "Wideband squeezing in photon number fluctuations from a high-speed light-emitting diode," *Opt. Express*, vol. 7, pp. 215–221, 2000.

[41] K.Tanaka, A.Higashi, H.Yuji, R. Masuyama, Y.Kadoya, and M.Yamanishi, "Wideband sub-poissonian light generation in light-emitting diodes incorporating a heavily-doped active region," *Applied Physics Letters*, vol. 81, pp. 3317–3319, 2002.

[42] Hirano.T and Kuga.T, "Generation of weak sub-poissonian light by a high-efficiency light-emitting diode," *IEEE Journal of Quantum Electronics*, vol. 31, pp. 2236–2240, 1995.

[43] J.-F. Roch, J.-P. Poizat, and P. Grangier, "Sub-shot-noise manipulation of light using semiconductor emitters and receivers," *Physics Review Letters*, vol. 71, pp. 2006–2009, 1993.

[44] E.Goobar, A.Karlsson, and G.Bjork, "Experimental realization of a semiconductor photon number amplifier and a quantum optical tap," *Physics Review Letters*, vol. 71, pp. 2002–2005, 1993.

[45] A. Funk and M. Beck, "Sub-poissonian photocurrent statistics: theory and undergraduate experiment"," *American Journal of Physics*, vol. 6, pp. 492–500, 1997.

[46] *DataSheet, "Programmable Gain Instrumentation Amplifier AD625" , Analog Devices.*

[47] *Tutorial, "Johnson and Shot Noise:The Determination of the Boltzmann Constant,Absolute Zero temperature and the Charge of the Electron", MIT Department of Physics.*

[48] *Application Note 041, "The Fundamentals of FFT-Based signal Analysis and Measurement", National Instruments.*

[49] C. D. Motchenbacher and J. A. Connelly, *Low-Noise Electronic System Design*. Wiley Interscience, 1993.

[50] J.Paramanandam and M.A.Parker, "Communication via the statistics of photon-number squeezed light," *Physical Review Letters*, vol. 94, pp. 233602–1–4, 2005.

[51] *Application Note 1303, "Spectrum Analyzer Measurements and Noise", Agilent Technologies.*

[52] Agilent Technologies, *Appication Note 150, "Spectrum Analyzer Basics" , Agilent Technologies.*

[53] Sumitomo.H, Kadoya.Y, Yamanishi.M, and Abe.J, "Squeezing in photon-number fluctuations due to backward pump process without high impedance-noise-suppression in a light-emitting-diode," in *Quantum Electronics and Laser Science Conference, Technical Digest.*, 1999.

[54] *DataSheet(s), "S3994-01 Si PIN Photodiode","S5107 Si PIN Photodiode", "L2656 Infrared LED", "L9337 Infrared LED", Hamamatsu.*

[55] *Jon Geist, "Linearity and the ac/dc technique" , Tech Report , International Radiation Detectors, Inc.*

[56] *Application Note 300-1, "Amplifier Modules", Analog Modules, Inc.*

[57] *Datasheet, "Agilent 8568B RF Spectrum Analyzer Technical Specifications", http://cp.literature.agilent.com/litweb/pdf/5952-9394.pdf.*

[58] *Datasheet, "Minicircuits Low Noise Amplifiers - Broadband ,Linear 0.1-3000Mhz", www.minicircuits.com.*

[59] *Application Note 300-2, "How to measure noise in amplifier modules", Analog Modules,Inc.*

[60] P. Lynam, I. Mahboob, A. Parnell, A. Fox, and M. Krames, "Photon-number squeezing in visible-spectrum light-emitting diodes," *Electronics Letters*, vol. 39, pp. 110–112, 2003.

[61] *Application Note, "Photodiode Characteristics", UDT Sensors,Inc.*

[62] *Technical Note, "Photodiode Technical Information", Hamamatsu Photonics.*

[63] M. B. Gray, D. A. Shaddock, C. C. Harb, and H.-A. Bachor, "Photodetector designs for low-noise, broadband, and high-power applications," *Review of Scientific Instruments*, vol. 69, pp. 3755–3762, 1998.

[64] *Application Note 358, "Noise and Operational Amplifier Circuits", Analog Devices.*

[65] A. M. Bacon, H. Z. Shao, L. J. Wang, and J. E. Thomas, "Microwatt shot-noise measurement," *Applied Optics*, vol. 34, pp. 5326–5330, 1995.

[66] L. Mandel and E. Wolf, *Optical coherence and quantum optics.* Cambridge University Press, New York, 1995.

[67] P. Koczyk, P. Wiewir, and C. Radzewicz, "Photon counting statistics:undergraduate experiment," *American Journal of Physics*, vol. 64, pp. 240–245, 1996.

[68] D. K. Mynbaev and L. L. Scheiner, *Fiber-Optic Communications Technology.* Prentice Hall, 2001.

[69] R. Masuyama, A. Higashi, K. Tanaka, Y. Kadoya, and M. Yamanishi, "Broadband photon-number squeezing in light-emitting diodes at low photon-flux levels," *Applied Physics Letters*, vol. 83, pp. 1113–1115, 2003.

[70] B.E.A.Saleh and M.C.Teich, "Information transmission with photon-number-squeezed light," in *Proceedings of the IEEE*, 1992.

[71] G. D. VanWiggeren and R. Roy, "Optical communication with chaotic waveforms," *Physics Review Letters*, vol. 81, pp. 3547 – 3550, 1998.

[72] R. Vio and W. Wamsteker, "Joint time-frequency analysis: A tool for exploratory analysis and filtering of non-stationary time series," *Astronomy and Astrophysics*, vol. 388, pp. 1124–1138, 2002.

[73] M.T.Terrovitis, K.S.Kundert, and R.G.Meyer, "Cyclostationary noise in radio-frequency communication systems," *IEEE Transactions on Circuits and Systems I:Fundamental Theory and Applications*, vol. 49, pp. 1666–1671, 2002.

[74] W.A.Gardner and L.E.Franks, "Characterization of cyclostationary random signal processes," *IEEE Transactions on Information Theory*, vol. 21, pp. 4–14, 1975.

[75] P. Grey and R.G.Meyer, *Analysis and Design of Analog Integrated Circuits.* Wiley, 2001.

[76] *2N2222 Datasheet, http://www.fairchildsemi.com/pf/PN/PN2222A.html.*

[77] E.R.Chenette and A. D. Ziel, "Accurate noise measurements in transistors," *IRE Transactions on Electron Devices*, vol. 9, pp. 123–128, 1962.

[78] B.Wang, J.R.Hellums, and C.G.Sodini, "Mosfet thermal noise modeling for analog integrated circuits," *IEEE Journal of Solid State Circuits*, vol. 29, pp. 833–835, 1994.

Vita

Joshua Paramanandam

2002-2007 M.S in Electrical and Computer Engineering from Rutgers University

1998-2002 B.E in Computer Science and Engineering from University of Madras

1998 Graduated from Don Bosco Matriculation HigherSecondary School

Publications

J.Paramanandam and M.A.Parker, Communication via the Statistics of Photon-Number Squeezed Light. Phys. Rev. Lett. 94, 233602 (2005)

Patent Disclosure: Random Signal Statistical Communicator. Michael. A. Parker and Joshua Paramanandam